



Universitat Autònoma de Barcelona

**Multifunctional N,O-type Carborane-Based Materials:  
from Molecular Complexes  
to Three Dimensional Metal-Organic Frameworks**

Min Ying Tsang

TESI DOCTORAL

Programa de Doctorat en Química

**Director: Dr. José Giner Planas**

**Tutor: Prof. Agustí Lledós**

**Department de Química**

**Facultat de Ciències**

**2015**

## Conclusions

---



### Chapter 3.1 N,O-Type Carborane-Based Ligands

- 1) A whole family of mono- and di-substituted carborane-based pyridylalcohol ligands incorporating *ortho*-, *meta*- and *para*- carborane have been successfully synthesized in high yield in one pot reaction and fully characterized.
- 2) Crystallographic analysis of the racemic and enantiopure mono-substituted ligands (**CB-L1**) revealed a possible relationship between the torsion angle of the hydrogen bond donor and acceptor groups in these molecules and the helical hydrogen bonded supramolecular networks formed in the solid state.
- 3) Structural analysis for some of the crystal structures of di-substituted ligands (*syn*-**oCB-(L1)<sub>2</sub>**, *anti*-**oCB-(L1)<sub>2</sub>**, *syn*-**oCB-(L6)<sub>2</sub>** and *anti*-**oCB-(L4)<sub>2</sub>** and *syn* **oCB-(L2)<sub>2</sub>**) showed homochiral self-assembly in the supramolecular constructions.

### Chapter 3.2 Monosubstituted N,O-Type *ortho*- and *meta*-Carborane-Based Complexes

- 1) a) It has been obtained an *o*-carborane-based unsymmetric diiron (III) complex **Fe<sub>2</sub>Cl<sub>3</sub>(oCB-L1)<sub>3</sub>** that constitutes the first dinuclear iron (III) system that contains three alkoxide bridges and displays antiferromagnetic behaviour, in addition to chiroptical and second-order optical nonlinear properties. The corresponding enantiopure complexes have been also synthesized and fully characterized.  
b) Spontaneous resolution of **Fe<sub>2</sub>Cl<sub>3</sub>(oCB-L1)<sub>3</sub>** occurred on precipitation in diethyl ether and confirmed by X-ray diffraction (XRD), second harmonic generation measurement and circular dichroism.  
c) A different architecture was obtained when *o*-carborane moiety in the ligand was replaced by a phenyl ring is also demonstrated.
- 2) *m*-carborane-based diiron (III) complexes **Fe<sub>2</sub>Cl<sub>3</sub>(mCB-L1)<sub>3</sub>**, **Fe<sub>2</sub>Cl<sub>3</sub>(l-mCB-L1)<sub>3</sub>** and **Fe<sub>2</sub>Cl<sub>3</sub>(l<sub>2</sub>-mCB-L1)<sub>3</sub>** were synthesized. XRD for **Fe<sub>2</sub>Cl<sub>3</sub>(mCB-L1)<sub>3</sub>** showed a different structure, although isomeric, to that of the *o*-carborane-based complex. Similar structures for all *m*-carborane-based complexes are suggested by a combination of cyclic voltammetry, solution UV-Vis spectroscopy and NMR spectroscopy.
- 3) The comparison of the above with the iron (III) complexes with others formed with bulkier *o*-carborane-based ligands (**oCB-L4**, **oCB-L5** and **MeoCB-L1**) revealed that bulkiness is probably the dominant factor for the formation of iron complexes in this system.
- 4) Highly luminescent copper (I) complexes **Cu-oCB-L3**, **Cu-mCB-L3**, **Cu-oCB-L2** and **Cu-mCB-L2** were obtained with cubane-like Cu<sub>4</sub>I<sub>4</sub> core. Detail studies are still on-going in order to understand

the influence on incorporation of carborane clusters and the corresponding effect in the emission wavelengths.

### Chapter 3.3 Disubstituted N,O-Type *ortho*- and *meta*-Carborane-Based 2-Pyridylalcohol Complexes

- 1) a) A first family of *o*- and *m*-carborane-based NBN pincer palladium complexes **Pd-(*o*CB-(L1)<sub>2</sub>)**, **Pd-(*m*CB-(L1)<sub>2</sub>)** and **Pd-(*o*CB-(L5)<sub>2</sub>)** were obtained through B-H activation.  
b) It was found a stronger *trans* influence of the *m*-carborane than the *o*-carborane moieties in the complexes by a combination of XRD and DFT calculations.  
c) The results agree with the Pd-B bonds in all complexes exhibiting strong  $\sigma$ -electron donation, in agreement with a palladium (II), instead of palladium (0) as previously suggested for this type of complexes.  
d) Catalytic studies revealed **Pd-(*o*CB-(L1)<sub>2</sub>)** and **Pd-(*m*CB-(L1)<sub>2</sub>)** are good catalyst precursors in Suzuki coupling reactions in water and with very low amounts of catalyst loadings (10<sup>-4</sup> mmol%) and high turn-over-number (TON) for **Pd-(*o*CB-(L1)<sub>2</sub>)** ranging from 770000 to 990000.
- 2) It was found that both, *anti*-***o*CB-(L1)<sub>2</sub>** and *syn*-***o*CB-(L1)<sub>2</sub>** ligands are able to coordinate to iron (III) in a tetradentate fashion and giving diiron(III) complexes. However, whereas the former gave a complex containing two *anti*-***o*CB-(L1)<sub>2</sub>** ligands (**Fe<sub>2</sub>Cl<sub>2</sub>(*anti*-***o*CB-(L1)<sub>2</sub>)<sub>2</sub>**), the latter formed a complex containing only one *syn*-***o*CB-(L1)<sub>2</sub>** ligands (**Fe<sub>2</sub>Cl<sub>3</sub>(*syn*-***o*CB-(L1)**)(DMF)(H<sub>2</sub>O)**). **Fe<sub>2</sub>Cl<sub>2</sub>(*anti*-***o*CB-(L1)<sub>2</sub>)<sub>2</sub>** was found to show antiferromagnetic behaviour.****

### Chapter 3.4 Disubstituted N,O-Type *ortho*- and *meta*-Carborane-Based 3-Pyridylalcohol Complexes

- 1) A macrocyclic palladium (II) dimer **Pd<sub>2</sub>Cl<sub>2</sub>(*syn*-***o*CB-(L2)<sub>2</sub>)<sub>2</sub>** was obtained by using *syn*-***o*CB-(L2)<sub>2</sub>** and crystallized in a variety of polar solvents. This macrocyclic dimer showed inclusion behaviour and afforded six different inclusion compounds. The structures for all inclusion compounds have been determined by XRD and showed remarkably high/guest stoichiometric ratios (1:6 and 1:7). XRD analysis and TGA show that the solvent molecules are associated to the macrocyclic dimers by moderate (*out-guest*) and weak (*in-guest*) hydrogen bonding.**
- 2) Reaction of *syn*-***o*CB-(L2)<sub>2</sub>** with zinc or cobalt sulfate salts resulted in formation of the first coordination polymers incorporating such carborane-based ligand. This result constituted a proof of concept and showed that these di-substituted 3- and 4-pyridylalcohol ligands ***o*CB-(L2)<sub>2</sub>**, ***m*CB-(L2)<sub>2</sub>** and ***m*CB-(L3)<sub>2</sub>** can be used as bridging ligands for the construction of infinite three dimensional frameworks.

### Chapter 3.5 N,O-Type *ortho*- and *meta*-Carborane-based Metal-Organic Frameworks

It has been successfully demonstrated that the N,O-type carborane ligands prepared in this work can be easily incorporated within MOFs.

#### 1) *ortho*-carborane-based mixed ligand MOFs:

(a) *o*-carborane-based metal-organic frameworks (MOFs) ***anti*-oCB-MOF-1** have been successfully synthesized by a mixed-ligand approach with the 3-pyridylalcohol ligands ***o*CB-(L2)<sub>2</sub>** and a dicarboxylic acids (1,4-BDC). The MOF ***anti*-oCB-MOF-1** was obtained by solvothermal synthesis with Zn(NO<sub>3</sub>)<sub>2</sub>, 1,4-BDC and a racemic mixture of ***anti*-oCB-(L2)<sub>2</sub>**. The incorporation of the hydrophobic *o*-carborane cluster in the MOF provoke an increased in water stability and methane uptake. Water stability of ***anti*-oCB-MOF-1** was proven by PXRD, contact angle measurements ( $\theta_c = 138^\circ$ ) and negligible water sorption, overall showing a highly hydrophobic MOF. ***anti*-oCB-MOF-1** is also stable in a variety of organic solvents and even in pH solutions ranging from pH 2 to 12. The activated ***anti*-oCB-MOF-1** showed microporous to CO<sub>2</sub> at 195K (BET surface area: 296 m<sup>2</sup>g<sup>-1</sup>) Detailed gas sorption studies including N<sub>2</sub>, CO<sub>2</sub> and CH<sub>4</sub> are presented and discussed. The isosteric heat (Q<sub>st</sub>) of ***anti*-oCB-MOF-1** for CH<sub>4</sub> is found to be at 19.6 – 23.1 kJmol<sup>-1</sup> which is one of the highest values reported to date.

(b) Powder X-ray diffraction data showed that isostructural MOFs to that of as ***anti*-oCB-MOF-1** were formed by using enantiopure (+)/(-)-***anti*-oCB-(L2)<sub>2</sub>** or meso ***syn*-oCB-(L2)<sub>2</sub>** ligands, suggesting that there is no influence from the chirality of the ***o*CB-(L2)<sub>2</sub>** ligand towards the MOF formation.

#### 2) *meta*-carborane-based mixed ligand MOFs:

Several carborane-based MOFs with 3- and 4-pyridylalcohol ligands ***m*CB-(L2)<sub>2</sub>** or ***m*CB-(L3)<sub>2</sub>** were synthesized with different carboxylic acids (1,3,5-tris(carboxylphenyl)benzene (BTB) and 1,2,4,5-tetrakis(4-carboxyphenyl) benzene (TCPB) and metals (zinc and cobalt): ***m*CB-MOF-2**, ***m*CB-MOF-2B**, ***m*CB-MOF-3**, ***m*CB-MOF-4** and ***m*CB-MOF-5**. The structures were confirmed by Single-crystal X-ray diffraction. Only some of the *meta*-carborane-based MOFs show water stability, which reveals that not only incorporation of the carborane clusters, but also its locations around the metal cores, is crucial for the stability in water.



# Addendum

---





---

Published articles

(Comision de Doctorado de Mayo de 2015)



# Is Molecular Chirality Connected to Supramolecular Chirality? The Particular Case of Chiral 2-Pyridyl Alcohols

Min Ying Tsang,<sup>†</sup> Florencia Di Salvo,<sup>†,‡</sup> Francesc Teixidor,<sup>†</sup> Clara Viñas,<sup>†</sup> José Giner Planas,<sup>\*,†</sup> Duane Choquesillo-Lazarte,<sup>§</sup> and Nicolas Vanthuyne<sup>||</sup>

<sup>†</sup>Institut de Ciència de Materials de Barcelona (ICMAB-CSIC), Campus U.A.B. 08193 Bellaterra, Spain

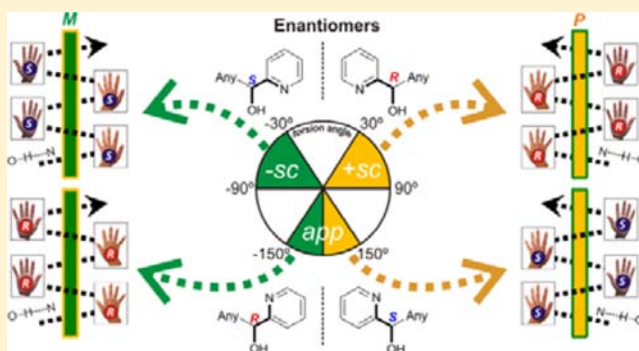
<sup>‡</sup>F.D.S: Departamento de Química Inorgánica, Analítica, y Química Física, Facultad de Ciencias Exactas y Naturales, Universidad de Buenos Aires, INQUIMAE-CONICET, Ciudad Universitaria, Pabellón 2, C1428EHA Buenos Aires, Argentina

<sup>§</sup>Laboratorio de Estudios Cristalográficos, IACT, CSIC-Universidad de Granada, Avda. de las Palmeras 4, 18100, Armilla, Granada, Spain

<sup>||</sup>Aix Marseille Université, Centrale Marseille, CNRS, iSm2 UMR 7313, 13397, Marseille, France

## Supporting Information

**ABSTRACT:** Ten structurally related racemic 2-pyridylmethyl alcohols containing an *o*-carborane core (1,2-*closo*-C<sub>2</sub>B<sub>10</sub>H<sub>10</sub>; *rac*-1a) or *m*-carborane (1,7-*closo*-C<sub>2</sub>B<sub>10</sub>H<sub>10</sub>; *rac*-2a) or *p*-carborane (1,7-*closo*-C<sub>2</sub>B<sub>10</sub>H<sub>10</sub>; *rac*-3a) and their enantiopure forms (*R*- and *S*-1a or *R*- and *S*-2a or *R*- and *S*-3a), as well as an iodo derivative of *rac*-3a (*rac*-4a) and a non-carborane derivative (C<sub>6</sub>H<sub>5</sub>; *rac*-5) have been studied by single crystal X-ray crystallography. All racemic and enantiopure structures show O–H⋯N hydrogen bonded homochiral 2<sub>1</sub>-helical networks, except that for *rac*-3a, which forms O–H⋯N hydrogen bonded trimers. A comparison of these X-ray structures with that for others found in the Cambridge Structural Database for chiral 2-pyridyl alcohols—either in racemic or enantiopure forms—that form O–H⋯N hydrogen bonded homochiral 2<sub>1</sub>-helical networks reveals a possible relationship between the torsion angle of the hydrogen bond donor and acceptor groups in these molecules and the hydrogen bonded supramolecular helices formed in the solid state.



## INTRODUCTION

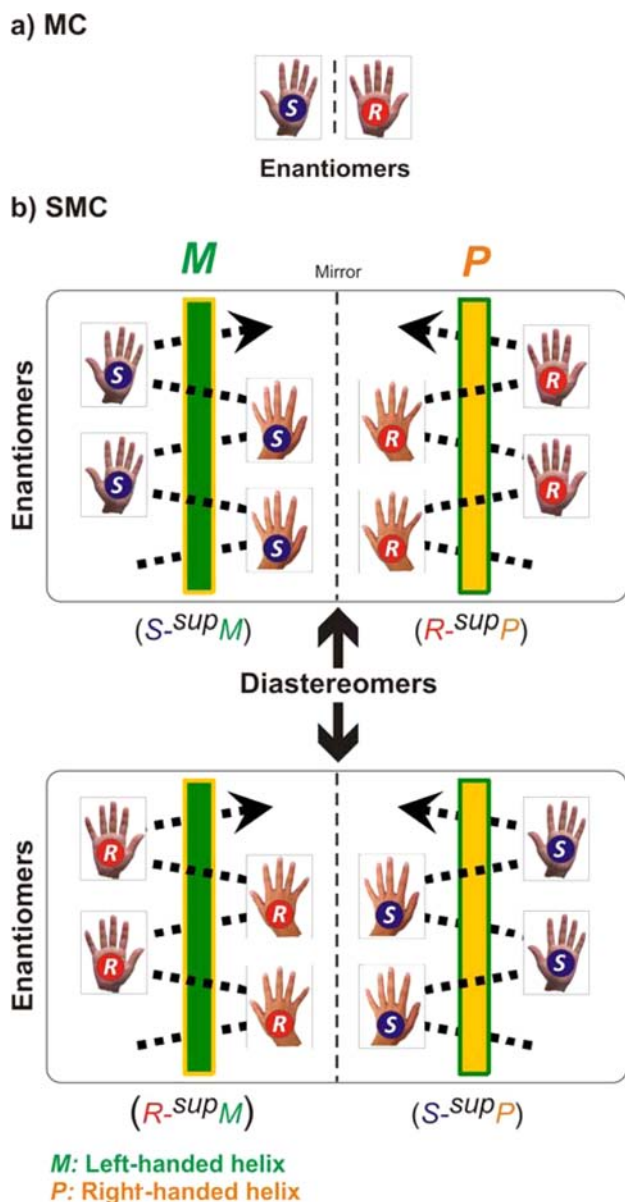
The design and self-assembly of hydrogen bond (HB) containing synthons is a very relevant research activity in supramolecular chemistry and crystal engineering.<sup>1–9</sup> One of the major challenges in these fields is to understand the parameters that control the molecular self-assembly of synthetically designed molecules that act as molecular building blocks. The motivation for preparing molecular systems with specific one- (1D), two- (2D), and three-dimensional (3D) architectures<sup>1–11</sup> is often inspired from nature where biological molecules self-assemble in unique architectural forms. For example, chiral  $\alpha$ -amino acids that are indispensable for life are found in nature as right- or left-handedness helical structures.<sup>1–9,12</sup> Molecules self-assemble noncovalently to form helical supramolecules such as, for example, those resulting from a 2<sub>1</sub> helical operation. In fact, a 2<sub>1</sub> helix is an essential motif in approximately 70% of molecular crystals, and the resultant helices exhibit chirality (right- or left-handedness).<sup>13,14</sup> However, as was already pointed out by Miyata and co-workers, from a crystallographic point of view, the handedness of 2<sub>1</sub> screw axis operation is not considered a helix as this involves a 180° rotation.<sup>13,14</sup> The same group has

developed a method (supramolecular-tilt-chirality, STC) in order to define the handedness of 2-fold helical assemblies. Using this method, the authors have shown for the first time that a correlation exists between the handedness of chiral organic salts—composed of chiral amines and achiral benzoic acid derivatives—and the handedness of the 2<sub>1</sub>-helical charge-assisted HB networks (Figure 1).<sup>14</sup> This constitutes a major breakthrough in crystal engineering as it shows that molecular chirality (MC) may be connected to supramolecular chirality (SMC), the same way that chirality in macromolecules is expressed on the supramolecular level, leading to the formation of helices.<sup>15</sup> Chiral molecules with one chiral center can adopt two configurations (*R* or *S*) and, when self-assembled into helical supramolecules, four diastereomers can be formed *R*- or *S*-<sup>sup</sup>*P* (<sup>sup</sup>*P* denotes supramolecular right-handed helix; Figure 1) and *R*- or *S*-<sup>sup</sup>*M* (<sup>sup</sup>*M* denotes supramolecular left handedness helix). Miyata's correlation has been found in helical supramolecular networks sustained by rather strong

Received: December 2, 2014

Revised: January 9, 2015

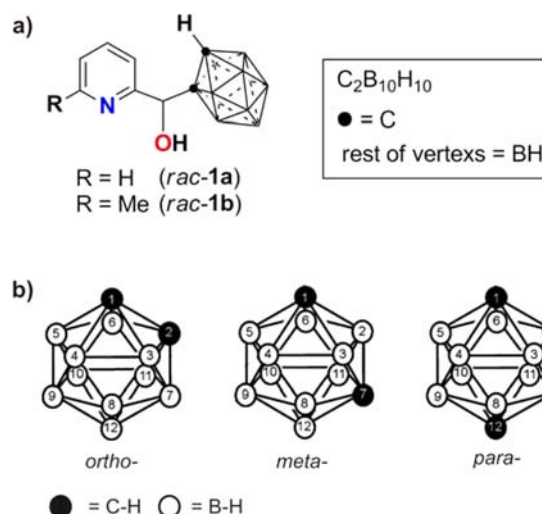
Published: January 13, 2015



**Figure 1.** Relational diagram between (a) molecular chirality (*R* or *S*) and (b) supramolecular chirality (*M* or *P*) of  $2_1$ -helical hydrogen-bonded networks. Dashed lines represent intermolecular interactions such as, e.g., hydrogen bonding (modified with permission from ref 14). Copyright 2013 Nature Publishing Group.

noncovalent interactions such as charge-assisted hydrogen bonds (15–40 kcal/mol).<sup>16</sup> The authors also present a possible mechanism for the inversion of SMC of HB helices based on steric repulsion in the achiral carboxylate anions.<sup>14</sup> Taking into account the enormous relevance of this MC–SMC relationship, it still remains challenging the possibility that much weaker intermolecular interactions might link MC and SMC or whether the relationship is extensive to other chiral molecular compounds.

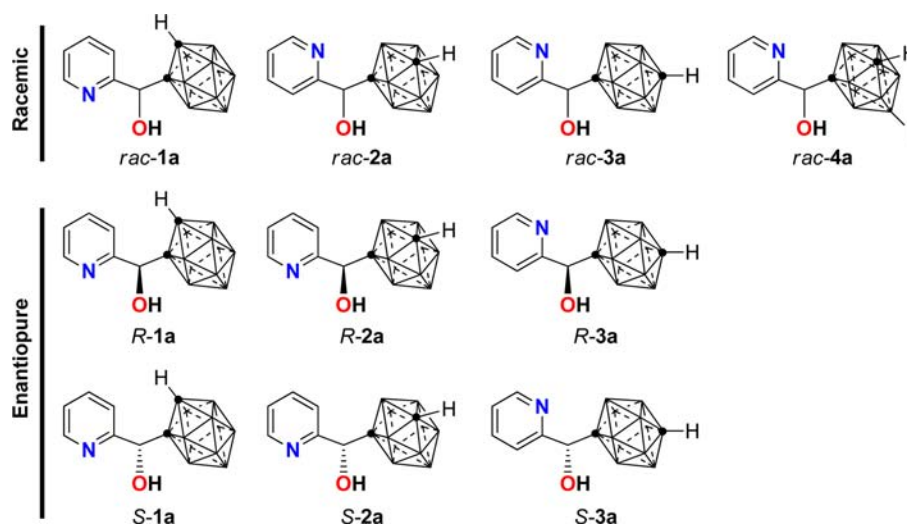
The genesis of this work was our recent studies on the syntheses and supramolecular structures of a family of chiral *o*-carboranylalcohols bearing *N*-aromatic rings (Figure 2a), which were isolated as racemic mixtures.<sup>17–19</sup> These molecules are centered around an *o*-carborane core (1,2-*closo*-C<sub>2</sub>B<sub>10</sub>H<sub>10</sub>; Figure 2) with one arm radiating out of one of the cluster carbons, containing an stereogenic center (a chiral carbon) that



**Figure 2.** (a) Previously characterized carboranyl alcohols that are related by  $2_1$ -screw to self-assemble via OH...N hydrogen bonds; (b) graphical representation of the carborane isomers (*closo*-C<sub>2</sub>B<sub>10</sub>H<sub>12</sub>) with vertex numbering.

bears an alcohol and an aromatic moiety. The icosahedral *closo* carboranes (dicarba-*closo*-dodecaboranes; C<sub>2</sub>B<sub>10</sub>H<sub>12</sub>) are an interesting class of exceptionally stable boron-rich clusters with high thermal and chemical stability, hydrophobicity, acceptor character.<sup>20–23</sup> There are however three isomers of carborane that differ in the relative position of both carbon atoms in the clusters (*ortho*-, *meta*-, and *para*- or *o*-, *m*-, and *p*-; Figure 2B). Although the volume of the three isomers of carborane is roughly the same, they show very different dipole moments as a consequence of the different arrangement of the carbon atoms in the cluster (4.53 D, 2.85 D and 0 D for *o*-, *m*-, and *p*-, respectively).<sup>24</sup> The average size of the three isomers of carborane (141–148 Å<sup>3</sup>) is comparable to that of adamantane (136 Å<sup>3</sup>) and is significantly larger (40%) than the phenyl ring rotation envelope (102 Å<sup>3</sup>). Concerning the electronic effect, all cluster carbon atoms exert an electron-withdrawing effect on attached substituents, which decreases in the order *o*- to *m*- to *p*-carborane. For example, *o*-carborane exhibits an electron-withdrawing character similar to fluorinated aryl, on a substituent at one of the cluster carbons.<sup>24–28</sup> Experimental evidence shows that the electron-withdrawing character of the carborane isomers has a clear impact in the acidity of substituents at carbon, the acidity decreasing in the same order (*o*-, *m*-, *p*-), and all being more acidic than the related phenyl moiety.<sup>23</sup> Thus, the inclusion of the three isomers of carborane in chiral pyridylmethylalcohol fragments introduces additional variables such as altering the electronics without modifying the bulkiness of the molecules that might have an impact in the supramolecular structures and crystal packing. Such control in electronic tuning without altering the steric factors is an exclusive feature of carborane based compounds.<sup>29,30</sup>

We previously found that racemic *o*-carborane 2-pyridyl derivatives **1a,b** form O–H...N hydrogen bonded homochiral chains (either *S* or *R*) with interaction energies in the range 6–7 kcal mol<sup>−1</sup> (Figure 2a).<sup>19</sup> Later we resolved the *R* and *S* enantiomers of **1a** as part of our interest in enantiopure metal complexes.<sup>31</sup> Easy resolution of enantiomers and ready crystallization prompted us to investigate the possible impact of molecular chirality and nonbonding contacts to crystal

Scheme 1. Graphical Representation of the Molecular Structures for the Carborane Isomers Analyzed in This Work<sup>a</sup>

<sup>a</sup>It is represented the rotamer found in each X-ray structure.

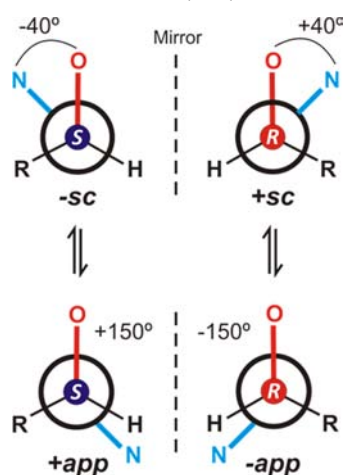
packing motifs in these 2-pyridyl alcohols. Do certain conformations translate to specific crystal motifs? Are these motifs chiral? And does the carborane isomers' nature have any impact on the solid structures? In order to get some insight into these questions we now report the molecular and supramolecular structures for a whole series of racemic and enantiopure carborane-based 2-pyridyl compounds. We have now synthesized new 2-pyridyl carboranyl alcohols containing a *m*-carborane core (1,7-*closo*-C<sub>2</sub>B<sub>10</sub>H<sub>10</sub>) or *p*-carborane (1,7-*closo*-C<sub>2</sub>B<sub>10</sub>H<sub>10</sub>) and describe in the present work the supramolecular structures for the racemic and resolved *R* and *S* enantiomers for all of them (Scheme 1). In the present paper we show that the handedness of 2<sub>1</sub>-helical HB networks observed for a series of chiral 2-pyridylalcohols can be defined by considering the torsion angles between the hydrogen bonding donor and acceptor groups in the molecules and that this does not seem to be restricted to carborane-based pyridylalcohols.

## RESULTS AND DISCUSSION

Compounds *rac-2a*, *rac-3a*, and *rac-4a* (Scheme 1) have been synthesized following a similar procedure to that used for the related *o*-carborane derivative *rac-1a*<sup>17–19</sup> and have been fully characterized by conventional spectroscopic techniques. Following their syntheses, the *R* and *S* enantiomers of *rac-1a*,<sup>31</sup> *rac-2a*, and *rac-3a* were resolved using HPLC over a chiral stationary phase (see Supporting Information (SI) for details). The molecular structures for all compounds, *R-1a*, *S-1a*, *rac-2a*, *R-2a*, *S-2a*, *rac-3*, *R-3a*, *S-3a*, and *rac-4a* have been unequivocally established by single crystal X-ray diffraction (XRD) studies (Figures S1–S2, S4–S7 in SI). Crystal and data collection details can be found in Table S1 (SI). The absolute configurations for enantiomers of **1a** showing positive or negative sign of the optical rotation at 589 nm in CH<sub>2</sub>Cl<sub>2</sub> were correlated with *R* and *S* configurations, respectively (*R*(+)**1a**, *ee* > 95.5%; *S*(–)**1a**, *ee* > 95.5%).<sup>31</sup> The absolute configurations for enantiomers of **2a** and **3a** showing negative or positive sign of the optical rotation at 589 nm in CH<sub>3</sub>Cl were correlated with *R* and *S* configurations, respectively (*R*(–)**2a**, *ee* > 99.5%; *S*(+)**2a**, *ee* > 99.5%; *R*(–)**3a**, *ee* > 99.5%; *S*(+)**3a**, *ee* > 99.5%). All enantiopure compounds crystallized in noncentrosymmetric

and chiral space groups, with Flack parameters close to zero (Table S1). Whereas racemic *rac-2a* crystallizes in the noncentrosymmetric space group *Pna2*<sub>1</sub>, *rac-3a* and *rac-4a* do in the centrosymmetric space groups *P2*<sub>1</sub>/*c* and *P2*<sub>1</sub>/*n*, respectively. The molecular structures for all these alcohols show typical icosahedrons with very similar bond distances and angles, and also similar to those in other carboranyl alcohols.<sup>17–19</sup> The pivotal role hydrogen bonding plays in the supramolecular architecture makes the accurate location of the OH hydrogen position critical. As in all our previous reports the position of the hydrogen atom was clear from examination of the difference map. In addition, powder X-ray diffraction (PXRD) analysis of crystal batches (~50 mg) for all compounds (both racemic and enantiopure) shows only one phase by comparison with the calculated patterns from the single-crystal X-ray data, with the exception of *rac-3a* (SI). The results confirm the phase purity and absence of concomitant polymorphism.

**Molecular Structures Conformations.** Rotation of the pyridine rings through the (H)(OH)C–C(pyridine) bond allows two main conformations (rotamers) in the solid state, that is, one with the pyridine nitrogen *syn-clinal* (*–sc* ~ –40° and *+sc* ~ +40°) to the alcohol oxygen or *anti-periplanar* (*–app* ~ > –150° and *+app* ~ > +150°) to it (Scheme 2). In the following *syn-* or *anti-* will refer to *syn-clinal* or *anti-periplanar*, respectively. Scheme 1 summarizes the conformations found in the solid state for each racemic or enantiopure carborane isomer, and OCCN torsion angles are listed in Table 1. For the purpose of comparison, the torsion angles for previously reported and related *o*-carborane pyridine alcohol *rac-1a* and *rac-1b* are also listed in Table 1. Detailed analyses of the torsion angles for all enantiomers in the racemic and enantiopure structures show that whereas the *o*-carborane pyridine alcohols crystallize in a *syn*-conformation, the corresponding enantiomers in *p*-carborane seem to prefer *anti*-conformations. Most interestingly is the conformations found in the *m*-carborane based structures. Whereas the racemic structures (*rac-2a* and *rac-4a*) show molecules with a *trans*-conformation, both enantiopure structures (*R-* and *S-2a*) show a *cis*-conformation (Scheme 1, Table 1 and SI). The presence of different rotamers (or conformational polymorphs) for the same molecules, in particular, for *rac-2a* and *R-2a/S-2a*, indicates that the

Scheme 2. Newman Projections for Rotamers Found in the Solid Structures for Chiral 2-Pyridylalcohols<sup>a</sup>

<sup>a</sup>The chirality at the carbon is indicated.

differences in lattice energies must be quite small.<sup>32</sup> As mentioned above, PXRD of crystal batches for these compounds show pure phases, excluding the formation of concomitant polymorphs. This is also nicely observed for *rac-2a* and the enantiopure *R-2a/S-2a* (SI). The *syn/anti* conformations found in the solid state must be related to their relative stability during crystallization and most probably due to intermolecular hydrogen bonding between our molecules or

to those with the molecules of the solvent employed.<sup>33–35</sup> We could not however influence the *syn/anti* conformations in *rac-2a* by varying the polarity of the recrystallizing solvent (acetone, hexane/EtOH (9:1)). It cannot be ruled out the possible influence of the acidity of the OH group in the intramolecular versus intermolecular hydrogen bonding and therefore in the conformations.<sup>36</sup>

**Supramolecular Structures.** The supramolecular structures for all carboranyl based alcohols in this work are dominated by hydrogen bonds involving the OH groups and the nitrogen of the aromatic rings exclusively. The geometrical parameters for all pyridylalcohols are given in Table 1. The distances of all of the observed intermolecular O–H...N hydrogen bonds are substantially shorter than the 2.75 Å distances that correspond to the sum of the van der Waals radii ( $\sum vdw$ ) of hydrogen and nitrogen atoms. Thus, they qualify as moderate hydrogen bonds.<sup>1–9</sup> In order to better understand the supramolecular structures for these molecules, we will divide the compounds into two groups: enantiopure and racemic.

**Enantiopure Carborane Pyridine Alcohols.** In the enantiopure *o*-carborane based alcohol *R-1a*, molecules with *R* configuration interact through O–H...N hydrogen bonds along the *b* axis (Figure 3a). Such interactions between molecules are related through  $2_1$  screw translation parallel to the *b* axis so that it forms a homochiral helical hydrogen bonded structure with the pitch of the helix matching the *b* axis length (6.696 Å). The handedness of the  $2_1$  helicity for all structures described in this paper are determined using the

Table 1. Selected Molecular, Supramolecular, and Crystal Parameters for Racemic and/or Enantiopure Carborane Based 2-Pyridylalcohols in Scheme 1

Comp.	SG <sup>a</sup>	Z'	OCCN torsion (°)		SMC <sup>b</sup>	P (Å) <sup>c</sup>	ON (Å)	OHN (°)
			R-isomer	S-isomer				
<i>rac-1a</i> <sup>d</sup>	<i>P2<sub>1</sub>/c</i>	1	+39.73	-	<i>R</i> - <sup>sup</sup> <i>P</i>	6.703	2.748	167.49
			-	-39.73	<i>S</i> - <sup>sup</sup> <i>M</i>			
<i>R-1a</i>	<i>C2</i>	1	+41.72	-	<i>R</i> - <sup>sup</sup> <i>P</i>	6.696	2.751	166.23
<i>S-1a</i>	<i>C2</i>	1	-	-42.89	<i>S</i> - <sup>sup</sup> <i>M</i>	6.681	2.744	164.51
<i>rac-2a</i>	<i>Pna2<sub>1</sub></i>	2	-151.50	-	<i>R</i> - <sup>sup</sup> <i>M</i>	7.049	2.808	175.20
			-146.72	-	<i>S</i> - <sup>sup</sup> <i>P</i>			
			-	+151.50			2.708	172.67
			-	+146.72				
<i>R-2a</i>	<i>P2<sub>1</sub></i>	1	+43.50	-	<i>R</i> - <sup>sup</sup> <i>P</i>	6.708	2.780	177.30
<i>S-2a</i>	<i>P2<sub>1</sub></i>	1	-	-43.44	<i>S</i> - <sup>sup</sup> <i>M</i>	6.709	2.783	173.50
<i>rac-3a</i>	<i>P2<sub>1</sub>/c</i>	3	±150.77		-	-	2.736	166.65
			±147.38				2.751	171.93
			±136.97				2.879	156.51
<i>R-3a</i>	<i>P2<sub>1</sub>2<sub>1</sub>2<sub>1</sub></i>	1	-149.82	-	<i>R</i> - <sup>sup</sup> <i>M</i>	8.962	2.836	160.19
<i>S-3a</i>	<i>P2<sub>1</sub>2<sub>1</sub>2<sub>1</sub></i>	1	-	+149.99	<i>S</i> - <sup>sup</sup> <i>P</i>	8.963	2.842	169.03
<i>rac-4a</i>	<i>P2<sub>1</sub>/n</i>	1	-151.57	-	<i>R</i> - <sup>sup</sup> <i>M</i>	7.088	2.742	172.64
			-	+151.57	<i>S</i> - <sup>sup</sup> <i>P</i>			
<i>rac-1b</i> <sup>d</sup>	<i>C2/c</i>	1	-156.72	-	<i>R</i> - <sup>sup</sup> <i>M</i>	7.138	2.713	158.19
			-	+156.72	<i>S</i> - <sup>sup</sup> <i>P</i>			

<sup>a</sup>Space groups. <sup>b</sup>Supramolecular chirality of the OHN hydrogen bonding network. <sup>c</sup>Pitches of the  $2_1$  supramolecular helices. <sup>d</sup>See ref 19.

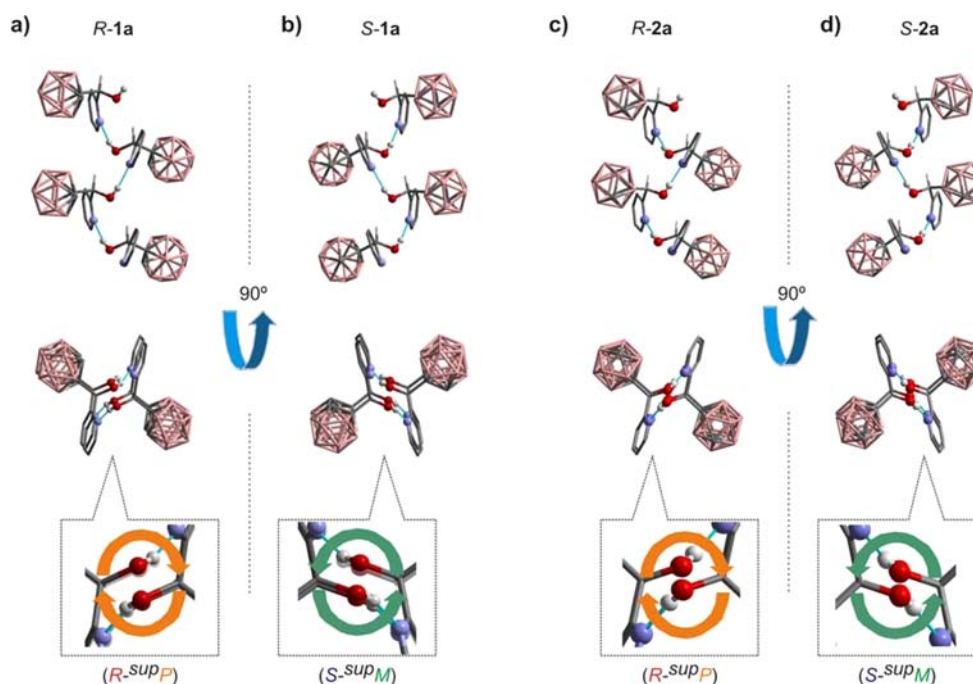


**Figure 3.** Supramolecular assemblies of enantiopure *R*-1a (a), *S*-1a (b), *R*-2a (c), and *S*-2a (d). Top: Projections showing four molecules of each enantiomer forming 1-D  $2_1$  helical hydrogen bonding columns. Bottom: a magnification of the helical hydrogen bonding networks where handedness is indicated, as determined by the supramolecular tilt chirality method.<sup>13,14</sup> See Table 1 for metric parameters. All hydrogen atoms, except those hydrogen bonded, are omitted for clarity. Color code: B pink; C gray; H white; O red; N blue.

supramolecular-tilt-chirality method (STC).<sup>13,14</sup> In brief, the STC method is as follows: Given the molecules in front of the  $2_1$  screw axis inclining to the right, the assemblies can be defined to be right-handed, or inclining to the left are defined to be left-handed. Following this method it can be seen that *R*-1a affords right-handed *P*-helices (therefore  $R\text{-}^{\text{sup}}P$ , Table 1) as illustrated in Figure 3a. Consistently with the latter, the supramolecular structure for the opposite enantiomer, *S*-1a, shows O–H $\cdots$ N hydrogen bonded homochiral left-handed *M*-helices ( $S\text{-}^{\text{sup}}M$ , Table 1) along the *b* axis (Figure 3b). The pitch of the helix also matches the *b* axis length (6.681 Å). The handedness of the  $2_1$ -helicity for all compounds is listed in Table 1, where right- or left-handedness of the supramolecular chirality (SMC) is represented as  $^{\text{sup}}P$  or  $^{\text{sup}}M$ , respectively, along with the absolute configurations (*R* and/or *S*) of the molecules. Thus, in the case of 1a, molecules with absolute *R* or *S* configurations afford right-handed ( $^{\text{sup}}P$ ) or left-handed ( $^{\text{sup}}M$ ) supramolecular structures, respectively, suggesting a possible enantiomeric relationship of the handedness of the supramolecular helices in the solid state, that is, between molecular chirality (MC) and supramolecular chirality (SMC). The same relationship is found in the structures for the enantiopure *m*-carborane based alcohols *R*-2a and *S*-2a (Figure 3, panels c and d, respectively). That is, *R* enantiomers give rise to a O–H $\cdots$ N supramolecular *P*-helix, and the *S* enantiomers afford a *M*-helix along the *b* axis, with pitches always matching the axis.

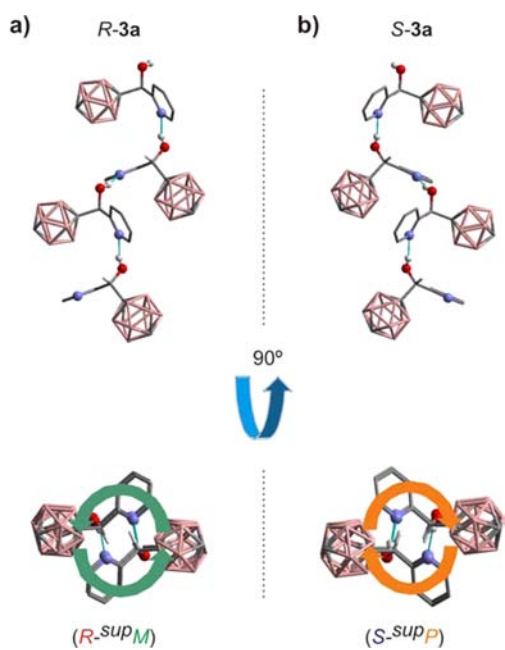
As mentioned in the previous section, molecular structures for enantiopure *R*-1a/*S*-1a and *R*-2a/*S*-2a show a *syn* conformation, with OCCN torsion angles  $\sim \pm 42\text{--}44^\circ$  (Table 1 and Scheme 1). The conformation is different in the case of the enantiopure *p*-carborane based alcohols *R*-3a and *S*-3a, showing both an *anti*-conformation (OCCN  $\approx \pm 150\text{--}157^\circ$ ). In addition, we observed that although both

enantiopure *p*-carborane based alcohols *R*-3a and *S*-3a also form O–H $\cdots$ N hydrogen bonded helices, the relationship between absolute configuration of the molecules and the handedness of the supramolecular helices in the solid state is different to those found in the *o*- and *m*-carborane enantiopure structures (Figure 4). Thus, whereas *R*-3a forms a  $R\text{-}^{\text{sup}}M$  structure, *S*-3a forms a  $S\text{-}^{\text{sup}}P$  one, in contrast to the  $R\text{-}^{\text{sup}}P$  and  $S\text{-}^{\text{sup}}M$  structures of *R*-1a/*R*-2a and *S*-1a/*S*-2a, respectively. Figure 5 shows schematically the relationship between enantiomers, torsion angles, and supramolecular helices in *R*-1a/*S*-1a and *R*-2a/*S*-2a (top) and *R*-3a/*S*-3a (bottom).

The relationship shown in Figure 5 suggests that the handedness of the  $2_1$  supramolecular hydrogen bonding networks in the enantiopure *o*-, *m*-, and *p*-carborane based pyridylalcohols is dictated by the OCCN torsion angles rather than by the absolute configuration of the molecules. In other words, different rotamers (*syn* or *anti*) for the same chiral configuration at the molecular level will provide left- or right-handed (or vice versa)  $2_1$  supramolecular networks. These results prompted us to look at the molecular and supramolecular structures for the racemic 1a, 2a, and 3a.

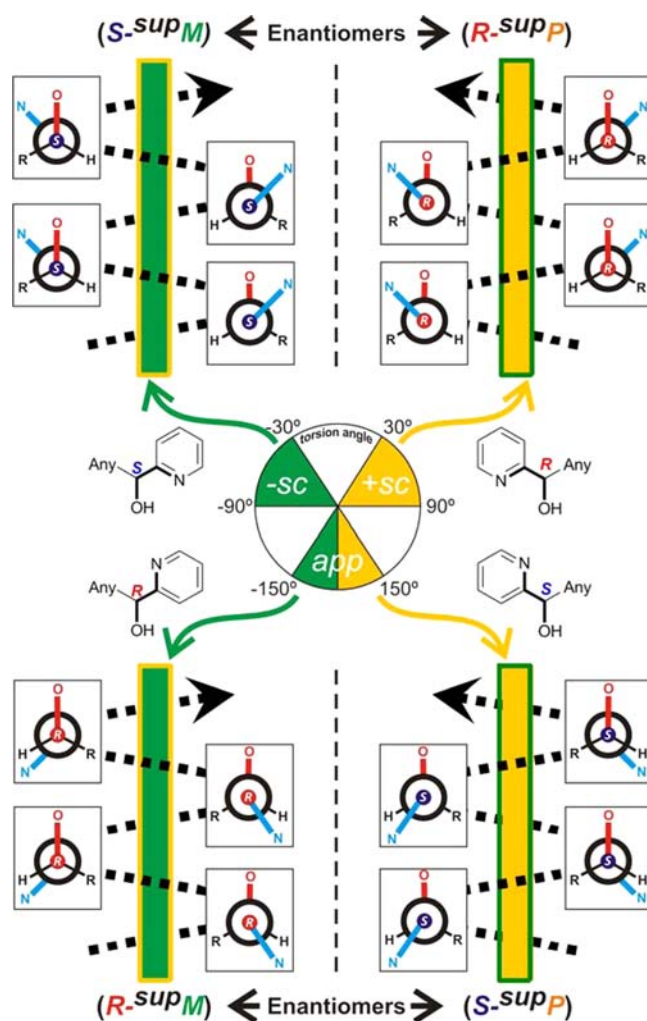
**Racemic Carborane Pyridine Alcohols.** The supramolecular structure for racemic *rac*-1a<sup>19</sup> agrees with that of the enantiopure *R*-1a and *S*-1a structures, in the sense that, both supramolecular homochiral *P*- and *M*-helices are observed in the solid state (Table 1 and Figure S8 in SI). Helices of opposite handedness pack in the solid state in *rac*-1a. Whereas *R*-isomers give rise to *P*-helices ( $R\text{-}^{\text{sup}}P$ ), *S*-isomers afford *M*-helices ( $S\text{-}^{\text{sup}}M$ ). Thus, the same relationship is found than in the structures for the enantiopure *o*-carborane based alcohols *R*-1a and *S*-1a. It is important to note that the molecular structures for this 2-pyridyl-*o*-carborane derivative are the same in the three X-ray structures determined (*rac*-1a, *R*-1a and *S*-1a), and all correspond to a *syn* configuration of the pyridine





**Figure 4.** Supramolecular assemblies of enantiopure *R*-3a (a) and *S*-3a (b). Top: Projections showing four molecules of each enantiomer forming 1-D  $2_1$  helical hydrogen bonding columns. Handedness of the helical hydrogen bonding is indicated, as determined by the supramolecular tilt chirality method.<sup>13,14</sup> See Table 1 for metric parameters. All hydrogen atoms, except those hydrogen bonded, are omitted for clarity. Color code: B pink; C gray; H white; O red; N blue.

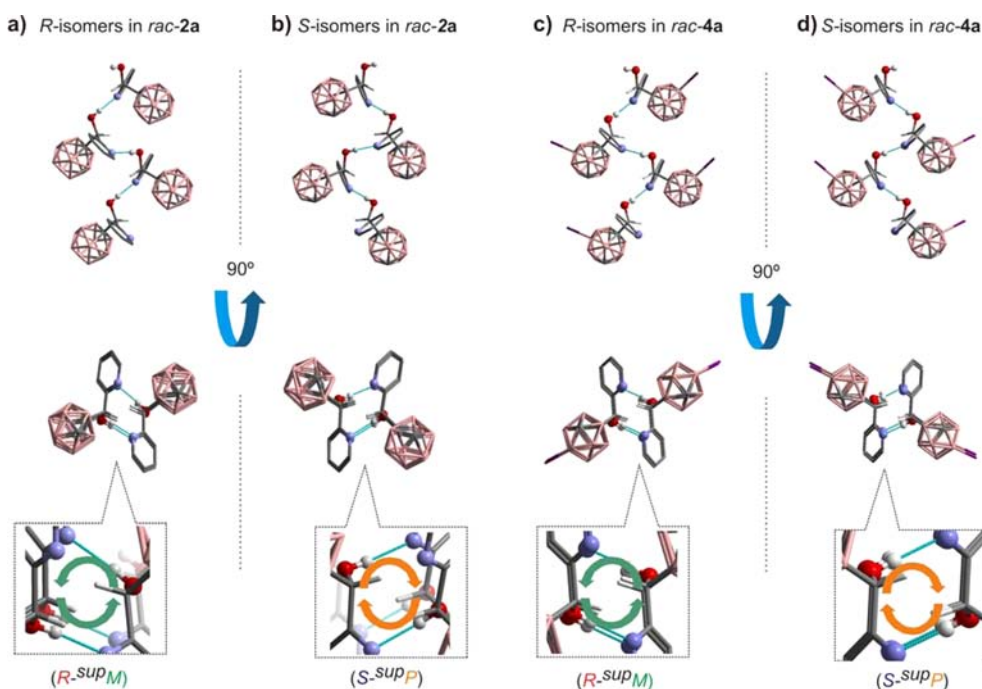
nitrogen and alcohol oxygen (Table 1) all showing OCCN torsion angles in the range of  $\sim 40^\circ$  ( $\pm sc$ ). On the contrary, whereas the *m*-carborane derivative **2a** crystallized as the *syn*-conformer in the enantiopure forms (*R*- and *S*-**2a**), it crystallized in as the *anti*-conformer in the racemic structure *rac*-**2a** (Scheme 1, Table 1 and SI). The different OCCN torsion angles in the molecules of enantiopure versus racemic structures for **2a** give us the opportunity to test the above-mentioned relationship between torsion angles and supramolecular chirality (Figure 5). Figure 6a,b and Table 1 show that the solid structure for *rac*-**2a** is formed by homochiral *P*- and *M*-helices. Most interestingly in *rac*-**2a**, the *R*-isomers give rise to *M*-helices ( $R^{supM}$ ) and the *S*-isomers afford *P*-helices ( $S^{supP}$ ), that is, the opposite to that observed in the enantiopure structures. Therefore, *m*-carborane based pyridylalcohol **2a** formed all  $S^{supM}/R^{supP}$  (in the enantiopure structures) and  $R^{supM}/S^{supP}$  (in the racemic structure) crystals as supramolecular polymorphs, indicating the formation of two pairs of true diastereomers. These results seem to corroborate the relationship in Figure 5. In view of these results, one would be able to predict the handedness of the supramolecular helices and absolute configuration of the molecules by measuring the value and sign of the OCCN torsion angle. For example, a molecule with an *anti*-configuration and negative value for the OCCN torsion angle will form a  $R^{supM}$  supramolecular structure. But if the same molecule shows a *syn*-configuration with a positive value for the OCCN torsion angle, then it will form a  $R^{supP}$  structure. This is what it is actually observed in case of compound **2a**. The same relationship found in *rac*-**2a** is also found in *rac*-**4a** (Figure 6c,d). Molecule **4a** differs from **2a** in that hydride atom bonded to B(9) has been substituted by a iodide atom.



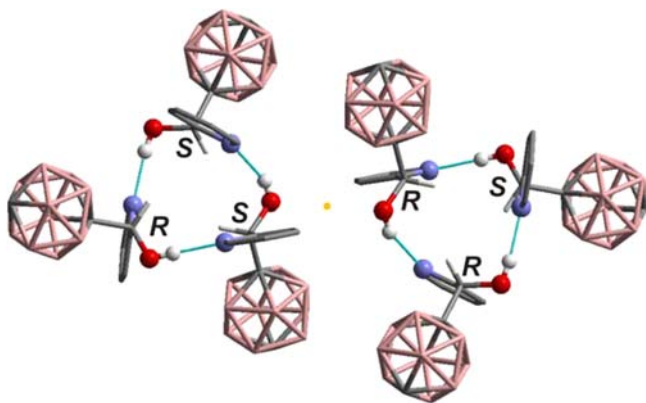
**Figure 5.** Pictorial representation of relationship between chirality-torsion angle (center) and handedness of helicity (top and bottom) of the resultant  $2_1$  supramolecular hydrogen bonding network found in this work. Specification of torsion angles is shown in Klyne-Prelog system (middle, center), in chemical drawing (middle, right and left) and Newman representation (top and bottom) each representing a molecule. Chirality at carbon (*R* or *S*) is indicated and supramolecular chirality (right -  $^{supP}$ - or left -  $^{supM}$ - handedness) is determined by the supramolecular tilt chirality method.<sup>13,14</sup>

Supramolecular structure for the *p*-carboranyl derivative *rac*-**3a** results quite surprising as it does not form the expected O $\cdots$ H $\cdots$ N hydrogen bonded helices, but hydrogen bonded trimers as shown in Figure 7. Thus, *rac*-**3a** crystallized as a different polymorph to that found in the enantiopure *R*-**3a** and *S*-**3a** and shows a supramolecular arrangement totally different from that found in all other carborane compounds in this work. As can be seen in Figure 7, hydrogen bonded trimers in the solid structure for *rac*-**3a** are formed by *RRS* and *SSR* and those are related by inversion centers. It is quite surprising that *rac*-**3a** prefers such packing as its density is significantly lower ( $1.123 \text{ g cm}^{-3}$ ) than that for the enantiopure structures *R*-**3a** and *S*-**3a** ( $1.238 \text{ g cm}^{-3}$ , both). Recrystallization of batches for *rac*-**3a** from hexane, ethanol/hexane, or acetone afforded in all cases a main phase that matched the calculated *rac*-**3a** structure (SI).

In order to prove whether the torsion angle-supramolecular helicity relationship (Figure 5) is general for other chiral 2-pyridyl alcohols, we re-examined *rac*-**1b** and synthesized and



**Figure 6.** Supramolecular assemblies of  $2_1$  helical hydrogen bonding for each enantiomer (*R*-2a in a) and (*S*-2a in b) in the racemic structure of 2a and *R*-4a (a) and *S*-4a (b) in the racemic structure of 4a. Top: Two projections showing four molecules of each enantiomer forming 1-D  $2_1$  helical hydrogen bonding columns. Bottom: a magnification of the helical hydrogen bonding networks where handedness is indicated, as determined by the supramolecular tilt chirality method.<sup>13,14</sup> See Table 1 for metric parameters. All hydrogen atoms, except those hydrogen bonded, are omitted for clarity. Color code: B pink; C gray; H white; O red; N blue.

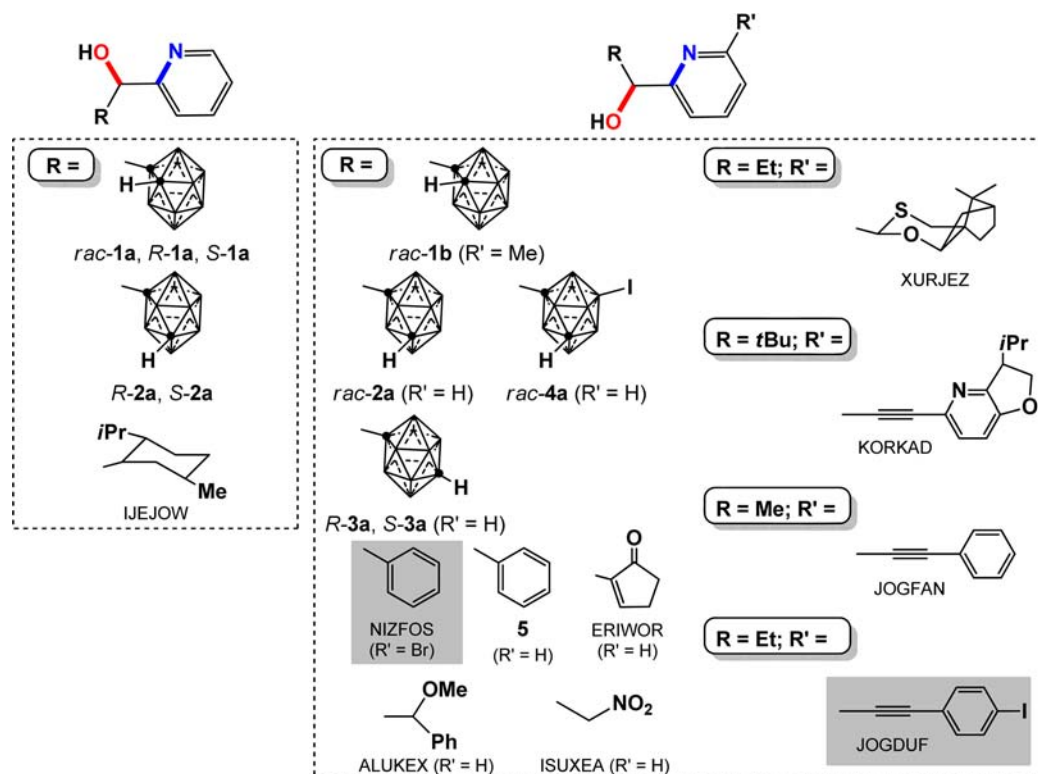


**Figure 7.** Supramolecular assembly of *rac*-3a showing six molecules forming two pairs of hydrogen bonded trimers. Configurations of stereogenic centers are indicated and inversion center is shown as an orange dot. See Table 1 for metric parameters. All hydrogen atoms, except those for the CHOH group, are omitted for clarity. Color code: B pink; C gray; H white; O red; N blue.

crystallized a non-carborane containing pyridyl alcohol *rac*-5 (Scheme 3 and SI). Whereas the former compound is the result of adding a methyl group at position-6 of the pyridine ring in 1a, the latter is the result of substituting the carborane cluster (in either 1a, 2a, or 3a) by a phenyl ring. Molecular structures for both compounds (*rac*-1b and *rac*-5) show an *anti*-periplanar ( $\pm$  *app* for *S*/*R* enantiomers) conformation (Tables 1 and 2, respectively). As previously observed for racemic structures *rac*-1a, *rac*-2a, and *rac*-4a, homochiral supramolecular helices composed of *S* or *R* enantiomer give rise to *P*-helices or *M*-helices, respectively, being in agreement with the torsion angle–supramolecular helicity relationship shown at the

bottom of Figure 5 (see Figure S9 for supramolecular assemblies of *rac*-1b and *rac*-5). We further did a search in the Cambridge Structural Database<sup>37</sup> (CSD, version 5.35 updated in February 2014) that revealed 10 other X-ray structures for chiral 2-pyridylalcohols (eight enantiopure and two racemic) with various substituents that give rise to  $2_1$ -helical networks based on moderate O–H $\cdots$ N hydrogen bonds.<sup>38</sup> Selected molecular, supramolecular, and crystal parameters for these structures can be found in Table 2. Detailed analysis of all torsion angles and supramolecular helices for the latter structures shows that the torsion angle–supramolecular helicity relationship in Figure 5 is fulfilled in 8 of the 10 structures found in the search. NIZFOS<sup>39</sup> and JOGDUF seem to show a reverse supramolecular chirality to that expected from our torsion angle correlation.

A summary of the crystal structures analyzed in this work is shown in Scheme 3. A total of 20 different crystal structures, half carborane based 2-pyridylalcohols, the other half carbon based alcohols, have been analyzed. All structures give rise to homochiral  $2_1$ -helical networks based on moderate O–H $\cdots$ N hydrogen bonds, regardless of whether the compounds crystallize in racemic or enantiopure forms. The only exception to the carborane derivatives that we have found is, as detailed above, *rac*-3a that forms O–H $\cdots$ N hydrogen bonded trimers (Figure 7). However, the enantiopure forms of this compound do form homochiral  $2_1$ -helical networks (Figure 4). This exemplifies the problem of polymorphism. Although these molecules seem to prefer a helical arrangement, there is always the possibility of polymorphism. It is however interesting that successive recrystallizations of *rac*-3a, *R*-3a, or *S*-3a in a variety of solvents always gave the same powder diffraction patterns (SI).

Scheme 3. Summary of Chemical Structures for Molecules Analyzed in This Work with Indication of Isomers Found in Their Molecular Structures Syn (Left) or Anti (Right)<sup>a</sup>

<sup>a</sup>All corresponding supramolecular structures, except those for the highlighted in grey, fulfil the correlation in Figure 5.

Table 2. Selected Molecular, Supramolecular, and Crystal Parameters for Racemic and/or Enantiopure Non-Carborane Based 2-Pyridylalcohols from the CSD<sup>36</sup>

Refcode <sup>a</sup>	SG <sup>b</sup>	Z'	OCCN torsion (°)		SMC <sup>c</sup>	P (Å) <sup>d</sup>	ON (Å)	OHN (°)
			R-isomer	S-isomer				
<b>Enantiopure Structures</b>								
ALUKEX	<i>P</i> <sub>2</sub> , <i>2</i> <sub>1</sub> <i>2</i> <sub>1</sub>	1	-	+150.37	<i>S</i> - <sup>sup</sup> <i>P</i>	8.187	2.775	- <sup>e</sup>
ERIWOR	<i>P</i> <sub>2</sub> , <i>2</i> <sub>1</sub> <i>2</i> <sub>1</sub>	1	-	+169.02	<i>S</i> - <sup>sup</sup> <i>P</i>	8.427	2.796	178.33
IJEJOW	<i>P</i> <sub>2</sub> <sub>1</sub>	1	-	-46.74	<i>S</i> - <sup>sup</sup> <i>M</i>	5.561	2.862	- <sup>e</sup>
ISUXEA	<i>P</i> <sub>2</sub> , <i>2</i> <sub>1</sub> <i>2</i> <sub>1</sub>	1	-154.46	-	<i>R</i> - <sup>sup</sup> <i>M</i>	7.145	2.720	172.55
JOGDUF	<i>P</i> <sub>2</sub> <sub>1</sub>	1	+174.77	-	<i>R</i> - <sup>sup</sup> <i>M</i>	9.387	2.831	165.60
JOGFAN	<i>P</i> <sub>2</sub> , <i>2</i> <sub>1</sub> <i>2</i> <sub>1</sub>	1	-	+171.61	<i>S</i> - <sup>sup</sup> <i>P</i>	9.635	2.927	172.52
KORKAD	<i>P</i> <sub>2</sub> <sub>1</sub>	1	-	+155.51	<i>S</i> - <sup>sup</sup> <i>P</i>	6.893	2.901	- <sup>e</sup>
NIZFOS	<i>P</i> <sub>2</sub> , <i>2</i> <sub>1</sub> <i>2</i> <sub>1</sub>	1	+177.40	-	<i>R</i> - <sup>sup</sup> <i>P</i>	8.733	2.867	168.62
XURJEZ	<i>P</i> <sub>2</sub> <sub>1</sub>	1	-	+157.10	<i>S</i> - <sup>sup</sup> <i>P</i>	6.553	2.906	151.82
<b>Racemic structures</b>								
5 (this work)	<i>P</i> <i>n</i> a2 <sub>1</sub>	1	-150.73	-	<i>R</i> - <sup>sup</sup> <i>M</i>	9.248	2.800	166.71
			-	+150.73	<i>S</i> - <sup>sup</sup> <i>P</i>			
TICPIG	<i>P</i> <sub>2</sub> <sub>1</sub> / <i>c</i>	1	-151.31	-	<i>R</i> - <sup>sup</sup> <i>M</i>	9.458	2.842	174.86
			-	+151.31	<i>S</i> - <sup>sup</sup> <i>P</i>			

<sup>a</sup>Identifiers for crystals structures in the Cambridge Structural Database. <sup>b</sup>Space group. <sup>c</sup>Supramolecular chirality of the OHN hydrogen bonding network. <sup>d</sup>Pitches of the 2<sub>1</sub> supramolecular helices. <sup>e</sup>H atoms not available.

The comparison of X-ray structures for these 20 chiral 2-pyridylalcohols reveals a possible relationship between the torsion angle of the hydrogen bond donor and acceptor groups

in these molecules and the handedness of the hydrogen bonded supramolecular helices formed in the solid state (Figure 5). Thus, chiral 2-pyridylalcohols with positive torsion angles

generally afford hydrogen bonded supramolecular *P*-helices, and negative torsion angles favor *M*-helices, in these chiral molecules. The only exception to the latter is JOGDUF (Table 2 and Scheme 2). In most of the cases (18 out of 20), the magnitude and sign of the torsion angle define the absolute configuration of the molecules in the homochiral OHN hydrogen bonding helical networks. A first inspection of Scheme 2 seems to reveal that there are more *anti* than *syn* isomers for these 2-pyridylalcohols. We should stress that this is only true when regarding those alcohols showing 2<sub>1</sub>-helical networks. Note that most of the *syn* isomers found in the CCDC will form either centrosymmetric dimers or monomers with intramolecular OHN hydrogen bonding (SI). In this sense it is interesting to observe that whereas *rac*-2a crystallized as the *anti* isomer (Figure 6a,b), their enantiopure forms *R*-2a and *S*-2a do as the *syn*-isomer (Figure 3c,d). In this case a change in the OCCN rotation angle from *syn* to *anti* (or vice versa) is followed by a change in the handedness of the helical network as summarized in Figure 5. Therefore, *m*-carborane based pyridylalcohol 2a formed all *S*<sup>sup</sup>*M*/*R*<sup>sup</sup>*P* and *R*<sup>sup</sup>*M*/*S*<sup>sup</sup>*P* crystals as polymorphs, indicating the formation of two pairs of true diastereomers. These results corroborate the relationship in Figure 5, which is fulfilled by all carborane derivatives that form OHN helical networks in Scheme 3. As previously mentioned, one is able to predict the handedness of the supramolecular helices and absolute configuration of the molecules by measuring the OCCN torsion angles of the molecules and considering the sign of the angle. The only two exceptions to this relationship seem to be the carbon based 2-pyridylalcohols NIZFOS and JOGDUF. Whereas in the former there is some doubt regarding the molecule absolute configuration,<sup>39</sup> the latter is forming *R*<sup>sup</sup>*M* whereas the relationship in Figure 5 would predict an *S*<sup>sup</sup>*P* configuration. Notice that both of these compounds show an *anti*-conformation with OCCN torsion angles near 180° (Table 2), that is, slightly wider than that found for all other *anti*-compounds in Scheme 3 (146–156°). As can be seen in Figure 5, *anti*-conformations with positive torsion angles would form *P* helices, and negative angles will afford *M* helices, the distinction being clearer the farther the angle is from 180°. It is perhaps in these intermediate cases where the correlation might not work. It seems clear to us that there is no single mechanism behind the origin of supramolecular chirality, that is, between cause and consequence. In the case of Miyata's work, it seems that molecular chirality could be the cause for the supramolecular chirality. In our case, the torsion angle between the hydrogen bonding donor and acceptor groups in the molecules seems to be the cause for the supramolecular chirality. Of course one could argue that it is the absolute configuration of the stereogenic center in these compounds that is the cause of a positive or negative torsion angle, but the magnitude of it (*syn* or *anti*) will be a consequence of intra- versus intermolecular hydrogen bonding or even more subtle forces. Thus, the answer to the title of this paper is "maybe", but it is certainly complex and probably a variety of different mechanisms are at work.

In summary, we have synthesized and crystallized nine racemic and/or enantiopure carborane based 2-pyridylmethylalcohols (*R*-1a, *S*-1a, *rac*-2a, *R*-2a, *S*-2a, *rac*-3, *R*-3a, *S*-3a, and *rac*-4a) and one phenyl derivative (*rac*-5) and compared their molecular and supramolecular structures with other previously reported carborane- and carbon-based 2-pyridylmethylalcohols. From the comparison of 20 structures, it seems clear that certain conformations of the molecules translate into OHN

helical networks with specific handedness. The analyses of the structures suggest that a correlation exists between the OCCN torsion angles of the molecules and the handedness of the supramolecular helices.

## EXPERIMENTAL DETAILS

**General Remarks.** Reactions were carried out under a nitrogen atmosphere in round-bottomed flasks equipped with a magnetic stirring bar, capped with a septum. Diethyl ether was distilled from Na/benzophenone and CH<sub>2</sub>Cl<sub>2</sub> over CaH<sub>2</sub>. All the other chemicals were commercially available and used as received. 9-*I*-1,7-*closo*-Carborane<sup>40</sup> and (2-pyridine)(phenyl)methanol –*phpmH*<sup>–41</sup> were synthesized as previously reported. TLC analyses were performed on Merck silica gel 60 F<sub>254</sub> TLC plates (0.5 mm thickness). Melting points were measured on a Stuart Scientific SMP10 and/or a Büchi Melting-Point B545. IR ATR spectra were recorded on a Perkin–Elmer Spectrum One spectrometer. <sup>1</sup>H, <sup>13</sup>C, and <sup>11</sup>B spectra were recorded respectively at 300, 75, and 96 MHz with a Bruker Advance-300 spectrometer in deuterated acetone, unless denoted, and referenced to the residual solvent peak for <sup>1</sup>H and <sup>13</sup>C NMR or to BF<sub>3</sub>·OEt<sub>2</sub> as an external standard for <sup>11</sup>B NMR. Chemical shifts are reported in ppm and coupling constants in Hertz. Multiplets nomenclature is as follows: s, singlet; d, doublet; t, triplet; br, broad; m, multiplet. Elemental analyses were obtained by a CarboErba EA1108 microanalyzer (Universidad Autónoma de Barcelona). The mass spectra were recorded in the negative ion mode using a Bruker Biflex MALDI-TOF-MS [N<sub>2</sub> laser; λ<sub>exc</sub> 337 nm (0.5 ns pulses); voltage ion source 20.00 kV (Uis1) and 17.50 kV (Uis2)] with 3,5-dimethoxy-4-hydroxycinnamic acid as matrix.

**Synthesis of (2-Pyridine)(1,7-*closo*-carboranyl)methanol 2a.** *n*BuLi (0.47 mL, 1.6 M in hexane, 0.75 mmol) was added dropwise to a diethyl ether solution (10 mL) of 1,7-*closo*-carborane (100.6 mg, 0.70 mmol) at –63 °C (chloroform/liq. N<sub>2</sub>). The mixture was stirred for 1.5 h at low temperature –63 °C, and then a diethyl ether solution (1 mL) of pyridine-2-carboxaldehyde (0.07 mL, 0.70 mmol) was added dropwise. The resulting pale yellow solution was stirred at –63 °C for 5 h. After the reaction was completed, a saturated aqueous solution of NH<sub>4</sub>Cl (10 mL) was added at –63 °C, and then the mixture was taken out of the cooling bath and stirred until reaching room temperature. The aqueous phase was then extracted with Et<sub>2</sub>O (3 × 20 mL). The organic phases were dried over MgSO<sub>4</sub> and filtered. Evaporation of the solvent afforded an oily residue that was dissolved in the minimum amount of CH<sub>2</sub>Cl<sub>2</sub> and passed through a short silica gel column, using the same solvent, to remove the unreactive carboxaldehyde that remains in the column. Slow evaporation of a concentrated solution afforded the pure desired alcohol 2a as a crystalline material (106 mg, 0.42 mmol, 60.5%); mp 133–138 °C dec <sup>1</sup>H NMR: 8.54 (d, *J* = 4.8, 1H, NC<sub>5</sub>H<sub>4</sub>), 7.84 (td, *J* = 7.8 and 1.5, 1H, NC<sub>5</sub>H<sub>4</sub>), 7.48 (d, *J* = 7.8, 1H, NC<sub>5</sub>H<sub>4</sub>), 7.38 (ddd, *J* = 7.2, 4.9 and 1.0, 1H, NC<sub>5</sub>H<sub>4</sub>), 5.48 (d, *J* = 7.2, 1H, CHOH), 5.02 (d, *J* = 7.2, 1H, CHOH). <sup>11</sup>B: –3.2 (d, *J* = 163, 1B), –6.9 (d, *J* = 182, 1B) –9.7 (brs, 4B), –11.8 (brs, 2B), –13.7 (brs, 4B). <sup>13</sup>C NMR: 160.23, 149.06, 137.50, 124.49, 122.8, 83.52, 75.27, 56.18. ATR (selected): ν = 3058 (C–H), 2595 (BH). MALDI TOF: 252.04 [M + H]<sup>+</sup>. C<sub>8</sub>H<sub>17</sub>B<sub>10</sub>ON (251.33): calcd C 38.23, H 6.82, N 5.57; found C 38.38, H 7.00, N 5.53.

**Synthesis of (2-Pyridine)(1,12-*closo*-carboranyl)methanol 3a.** The general procedure described by us for 2a was followed, using *n*BuLi (0.22 mL, 1.6 M in hexane, 0.35 mmol), diethyl ether (5 mL), 1,12-*closo*-carborane (50 mg, 0.35 mmol), and pyridine-2-carboxaldehyde (0.03 mL, 35 mmol), and an chloroform/liquid N<sub>2</sub> cooling bath (–63 °C). Work up gave a white solid (46.9 mg, 0.19 mmol, 47%); mp 122–127 °C dec. <sup>1</sup>H NMR: 8.49 (d, *J* = 3.3, 1H, NC<sub>5</sub>H<sub>4</sub>), 7.79 (td, *J* = 7.8 and 1.8, 1H, NC<sub>5</sub>H<sub>4</sub>), 7.34 (2H, NC<sub>5</sub>H<sub>4</sub>), 5.15 (d, *J* = 7.2, 1H, CHOH), 4.64 (d, *J* = 7.2, 1H, CHOH). 3.30 (br, 1H, B<sub>10</sub>C<sub>2</sub>H<sub>11</sub>). <sup>11</sup>B: –12.04 (d, *J* = 176, 5B), –14.01 (d, *J* = 176, 5B). <sup>13</sup>C NMR: 159.77, 148.64, 137.11, 124.08, 122.61, 90.39, 75.78, 62.40. ATR (selected): ν = 3052 (C–H), 2606 (BH). MALDI TOF: 252.28 [M + H]<sup>+</sup>.

C<sub>8</sub>H<sub>17</sub>B<sub>10</sub>ON (251.33): calcd C 38.23, H 6.82, N 5.57; found C 38.3, H 6.86, N 5.4.

**Synthesis of (2-Pyridine)(9-*I*-1,7-closo-carboranyl)methanol 4a.** The general procedure described by us for **2a** was followed, using *n*BuLi (0.26 mL, 1.6 M in hexane, 0.76 mmol), diethyl ether (10 mL), 9-*I*-1,7-closo-carborane (110 mg, 0.76 mmol) and pyridine-2-carboxaldehyde (0.04 mL, 0.76 mmol), and an chloroform/liquid N<sub>2</sub> cooling bath (−63 °C). Work up gave a white solid (79.8 mg, 0.21 mmol, 52%); mp 135–145 °C dec <sup>1</sup>H NMR: 8.56 (d, *J* = 4.8, 1H, NC<sub>5</sub>H<sub>4</sub>), 7.86 (td, *J* = 7.8 and 1.8, 1H, NC<sub>5</sub>H<sub>4</sub>), 7.51 (d, *J* = 7.8, 1H, NC<sub>5</sub>H<sub>4</sub>), 7.38 (ddd, *J* = 4.8 and 0.9, 1H, NC<sub>5</sub>H<sub>4</sub>), 5.61 (d, *J* = 6.9, 1H, CHOH), 5.08 (d, *J* = 6.9, 1H, CHOH), 3.80 (br, 1H, B<sub>10</sub>C<sub>2</sub>H<sub>11</sub>). <sup>11</sup>B: −2.05 (d, *J* = 165, 1B), −5.63 (d, *J* = 168, 1B) −7.40 (d, *J* = 180, 1B), −8.58 (d, *J* = 149, 1B), −9.90 (d, *J* = 127, 1B), −10.35 (d, *J* = 127, 1B), −11.60 (d, *J* = 174, 1B), −13.64 (d, *J* = 198, 1B), −15.62 (d, *J* = 186, 1B), −22.13 (s, 1B). <sup>13</sup>C NMR: 159.95, 149.16, 137.69, 124.63, 122.66, 84.87, 74.15, 57.38. ATR (selected):  $\nu$  = 3058 (C–H), 2603 (BH). MALDI TOF: 378.18 [M + H]<sup>+</sup>. C<sub>8</sub>H<sub>17</sub>B<sub>10</sub>ON (377.24): calcd C 25.47, H 4.27, N 3.71; found C 25.24, H 4.29, N 3.47.

**X-ray Diffraction (XRD) Studies.** Crystals suitable for XRD were obtained by slow evaporation of solutions of the compounds from an opened vessel in air at room temperature. It follows the solvents used in each case: **R-1a** (hexane:ethanol ~4:1), **S-1a** (hexane:ethanol ~4:1), **rac-2a** (methanol), **R-2a** (methanol), **S-2a** (acetone), **rac-3** (acetone), **R-3a** (heptane:ethanol ~9:1), **S-3a** (heptane:ethanol ~9:1), **rac-4a** (methanol), **rac-5** (acetone). Measured crystals were prepared under inert conditions immersed in perfluoropolyether as protecting oil for manipulation. Suitable crystals were mounted on MiTeGen Micro-mounts, and these samples were used for data collection. Data were collected with Bruker X8 Proteum (compounds **R-1a**, **S-1a** 120 K, CuK $\alpha$ ), Bruker D8 Venture (**R-2a**, **S-2a**, **R-3a**, **S-3a**, 100 K, CuK $\alpha$ ; **rac-2a**, 120 K, CuK $\alpha$ ; **rac-3a**, 150 K, MoK $\alpha$ ; **rac-4a**, 298 K, MoK $\alpha$ ), or Oxford Xcalibur Gemini EOS CCD (S, 293 K, MoK $\alpha$ ) diffractometers. The data were processed with APEX2<sup>42</sup> or CrysAlisPro<sup>43</sup> (S) programs and corrected for absorption using SADABS<sup>44</sup> or the SCALE3 ABSPACK algorithm implemented in CrysAlisPro. The structures were solved by direct methods,<sup>45</sup> which revealed the position of all non-hydrogen atoms. These atoms were refined on F<sup>2</sup> by a full-matrix least-squares procedure using anisotropic displacement parameters. All hydrogen atoms were located in difference Fourier maps and included as fixed contributions riding on attached atoms with isotropic thermal displacement parameters 1.2 (C–H, B–H) or 1.5 (O–H) times those of the respective atom. A summary of crystal data is reported in Table S1.

**Powder X-ray Diffraction Studies.** Powder X-ray diffraction (PXRD) was recorded at room temperature on an X'Pert PRO MPD $\theta/\theta$  powder diffractometer (PanAnalytical; configuration: convergent beam; radius: 240 nm) equipped with a focalizing mirror and a transmission geometry with a silicon sample holder, for Cu K $\alpha$  radiation ( $\lambda$  = 1.5418 Å).

## ■ ASSOCIATED CONTENT

### Supporting Information

Enantiopure separation details and crystallographic data. This material is available free of charge via the Internet at <http://pubs.acs.org>.

## ■ AUTHOR INFORMATION

### Corresponding Author

\*E-mail: [jginerplanas@icmab.es](mailto:jginerplanas@icmab.es).

### Notes

The authors declare no competing financial interest.

## ■ ACKNOWLEDGMENTS

We thank CICYT (F.D.S., M.Y.T., F.T., C.V., and J.G.P., Grant CTQ2010-16237), Generalitat de Catalunya (F.D.S., M.Y.T., F.T., C.V., and J.G.P., 2009/SGR/00279), and CSIC (JAE-doc

contract to F.D.S.) for financial support. F.D.S. thanks CONICET for support. M.Y.T. is enrolled in the UAB Ph.D. program. The project "Factoría de Cristalización, CONSOLIDER INGENIO-2010" provided X-ray structural facilities for this work.

## ■ REFERENCES

- (1) Desiraju, G. R. *Crystal Engineering. The Design of Organic Solids*; Elsevier Science Publishers B.V.: Amsterdam, 1989.
- (2) Etter, M. C. *Acc. Chem. Res.* **1990**, *23*, 120–126.
- (3) Desiraju, G. R.; Steiner, T. *The Weak Hydrogen Bond in Structural Chemistry and Biology*; Oxford University Press: Oxford, 2001.
- (4) Steiner, T. *Angew. Chem.* **2002**, *114*, 50–80; *Angew. Chem., Int. Ed.* **2002**, *41*, 48–76.
- (5) Atwood, J. L.; Steed, J. W. *Encyclopedia of Supramolecular Chemistry*; Marcel Dekker: New York, 2004.
- (6) Metrangolo, P.; Neukirch, H.; Pilati, T.; Resnatti, G. *Acc. Chem. Res.* **2005**, *38*, 386–395.
- (7) Kitagawa, S.; Uemura, K. *Chem. Soc. Rev.* **2005**, *34*, 109–119.
- (8) Britz, D. A.; Khlobystov, A. N. *Chem. Soc. Rev.* **2006**, *35*, 637–659.
- (9) Steed, J. W.; Atwood, J. L. *Supramolecular Chemistry*, 2nd edition; Wiley: Chichester, 2009.
- (10) Moulton, B.; Zaworotko, M. J. *Chem. Rev.* **2001**, *101*, 1629–1658.
- (11) Ciesielski, A.; Palma, C.-A.; Bonini, M.; Samori, P. *Adv. Mater.* **2010**, *22*, 3506–3520.
- (12) Schulz, G. E.; Schirmer, R. H. *Principles of Protein Structure*; Cantor, C. R., Eds.; Springer-Verlag: New York, 1979.
- (13) Hisaki, I.; Sasaki, T.; Tohnai, N.; Miyata, M. *Chem.—Eur. J.* **2012**, *18*, 10066–10073.
- (14) Sasaki, T.; Hisaki, I.; Miyano, T.; Tohnai, N.; Morimoto, K.; Sato, H.; Tsuzuki, S.; Miyata, M. *Nat. Commun.* **2013**, *4*, No. 1787, DOI: 10.1038/ncomms2756.
- (15) See for example: Cornelissen, J. J. L. M.; Rowan, A. E.; Nolte, R. J. M.; Sommerdijk, N. A. J. M. *Chem. Rev.* **2001**, *101*, 4039–4070.
- (16) Desiraju, G. R. *Acc. Chem. Res.* **2002**, *35*, 565–573.
- (17) Terrasson, V.; Planas, J. G.; Prim, D.; Viñas, C.; Teixidor, F.; Light, M. E.; Hursthouse, M. B. *J. Org. Chem.* **2008**, *73*, 9140–9143.
- (18) Terrasson, V.; García, Y.; Farràs, P.; Teixidor, F.; Viñas, C.; Planas, J. G.; Prim, D.; Light, M. E.; Hursthouse, M. B. *CrystEngComm* **2010**, *12*, 4109–4123.
- (19) Di Salvo, F.; Camargo, B.; García, Y.; Teixidor, F.; Viñas, C.; Planas, J. G.; Light, M. E.; Hursthouse, M. B. *CrystEngComm* **2011**, *13*, 5788–5806.
- (20) Ollid, D.; Núñez, R.; Viñas, C.; Teixidor, F. *Chem. Soc. Rev.* **2013**, *42*, 3318–3336.
- (21) Teixidor, F.; Viñas, C. In *Science of Synthesis*; Thieme: Stuttgart, 2005; Vol. 6, p 1235, and references therein.
- (22) Grimes, R. N. *Carboranes*, 2nd ed; Elsevier: Amsterdam, 2011.
- (23) Hermansson, K.; Wójcik, M.; Sjöberg, S. *Inorg. Chem.* **1999**, *38*, 6039–6048.
- (24) Scholz, M.; Hey-Hawkins, E. *Chem. Rev.* **2011**, *111*, 7035–7062 and references therein.
- (25) Núñez, R.; Viñas, C.; Teixidor, F.; Sillanpää, R.; Kivekäs, R. *J. Organomet. Chem.* **1999**, *592*, 22–28.
- (26) Schwartz, L.; Eriksson, L.; Lomoth, R.; Teixidor, F.; Viñas, C.; Ott, S. *Dalton Trans.* **2008**, 2379–2381.
- (27) Núñez, R.; Farràs, P.; Teixidor, F.; Viñas, C.; Sillanpää, R.; Kivekäs, R. *Angew. Chem., Int. Ed.* **2006**, *45*, 1270–1272.
- (28) Teixidor, F.; Núñez, R.; Viñas, C.; Sillanpää, R.; Kivekäs, R. *Angew. Chem., Int. Ed.* **2000**, *39*, 4290–4292.
- (29) Teixidor, T.; Barberà, G.; Vaca, A.; Kivekäs, R.; Sillanpää, R.; Oliva, J.; Viñas, C. *J. Am. Chem. Soc.* **2005**, *127*, 10158–10159.
- (30) Spokoyny, A. M.; Machan, C. W.; Clingerman, D. J.; Rosen, M. S.; Wiester, M. J.; Kennedy, R. D.; Stern, C. L.; Sarjeant, A. A.; Mirkin, C. A. *Nat. Chem.* **2011**, *3*, 590–596.

(31) Di Salvo, F.; Tsang, M. Y.; Teixidor, F.; Viñas, C.; Planas, J. G.; Crassous, J.; Vanthuyne, N.; Aliaga-Alcalde, N.; Ruiz, E.; Clevers, S.; Dupray, V.; Choquesillo-Lazarte, D.; Light, M. E.; Hursthouse, M. B. *Chem.—Eur. J.* **2014**, *20*, 1081–1090.

(32) Preliminary gas phase calculations for **1a**, **2a**, and **5** showed that the *syn* conformers were clearly more stable than the *anti* conformers due to intramolecular OHN hydrogen bonding. When the calculations are repeated in the corresponding deprotonated molecules, *anti* conformers were more stable.

(33) Bernardes, C. E. S.; Lopes, M. L. S.; Ascenso, J. R. *Cryst. Growth Des.* **2014**, *14*, 5436–5441.

(34) Lomas, J. S.; Cordier, C.; Adenier, A.; Maurel, A.; Vaissermann, J. *J. Phys. Org. Chem.* **2007**, *20*, 410–421.

(35) Kyruchenko, A.; Herbich, J.; Wu, F.; Thummel, R. P.; Waluk, J. *J. Am. Chem. Soc.* **2000**, *122*, 2818–2827.

(36) Huque, T. T.; Platts, J. A. *Org. Biomol. Chem.* **2003**, *1*, 1419–1424.

(37) Allen, F. H. *Acta Crystallogr., Sect. B* **2002**, *58*, 380–388.

(38) See SI for details on search criteria.

(39) The X-ray structure for (6-bromopyridin-2-yl)(phenyl)metanol [NIZFOS] shows an enantiopure *R*-isomer with a torsion angle of +177.40° and therefore does not apparently fulfill the torsion angle-supramolecular helicity relationship in Figure 5. However it is mentioned in the original publication that absolute stereochemistry of this alcohols is unknown. A simple change from the *R*-isomer to the *S*-isomer in NIZFOS shows a torsion angle of −177.41 and a *S*-<sup>sup</sup>*M*, in agreement with all other structures in Table 2. [NIZFOS]: Jen, W. S.; Truppo, M. D.; Amos, D.; Devine, P.; McNevin, M.; Biba, M.; Campos, K. R. *Org. Lett.* **2008**, *10*, 741–744.

(40) Fox, M. A. Ph.D. Thesis, University of Durham, 1991; <http://etheses.dur.ac.uk/1186/>.

(41) Doudouh, A.; Woltermann, C.; Gos, P. C. *J. Org. Chem.* **2007**, *72*, 4978–4980.

(42) *APEX2 Software*, V2013.2; Bruker AXS Inc.: Madison, Wisconsin, USA, 2013.

(43) *CrysAlisPro*, V1.171.33.55; Agilent Technologies: Santa Clara, CA, 2012.

(44) *SADABS*, V2012.1; Bruker AXS Inc.: Madison, Wisconsin, USA, 2012.

(45) Sheldrick, G. M. *Acta Crystallogr., Sect. A: Found. Crystallogr.* **2008**, *64*, 112–122.

#### ■ NOTE ADDED AFTER ASAP PUBLICATION

This paper was published ASAP on January 26, 2015, with an error in the title. The corrected version reposted on January 27, 2015.

# Synthesis, Structure, and Catalytic Applications for *ortho*- and *meta*-Carboranyl Based NBN Pincer-Pd Complexes

Min Ying Tsang,<sup>†</sup> Clara Viñas,<sup>†</sup> Francesc Teixidor,<sup>†</sup> José Giner Planas,<sup>\*,†</sup> Nerea Conde,<sup>‡</sup> Raul SanMartin,<sup>‡</sup> María Teresa Herrero,<sup>‡</sup> Esther Domínguez,<sup>‡</sup> Agustí Lledós,<sup>‡</sup> Pietro Vidossich,<sup>‡</sup> and Duane Choquesillo-Lazarte<sup>§</sup>

<sup>†</sup>Institut de Ciència de Materials de Barcelona (ICMAB-CSIC), Campus UAB, 08193 Bellaterra, Spain

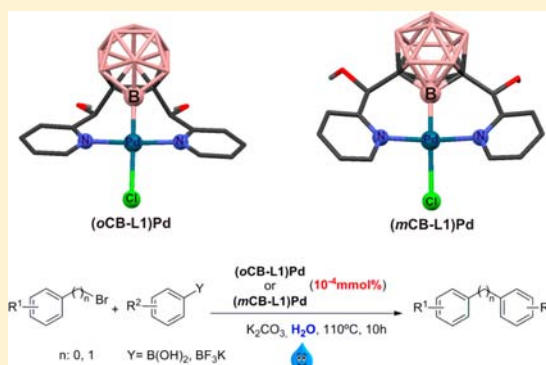
<sup>‡</sup>Department of Organic Chemistry II, University of the Basque Country, 48980 Leioa, Spain

<sup>‡</sup>Departament de Química, Universitat Autònoma de Barcelona, 08193 Bellaterra, Spain

<sup>§</sup>Laboratorio de Estudios Cristalográficos, IACT, CSIC-University of Granada, Armilla, Granada, Spain

## Supporting Information

**ABSTRACT:** *o*- and *m*-Carborane-based NBN pincer palladium complexes (*o*CB-L1)Pd, (*o*CB-L2)Pd, and (*m*CB-L1)Pd are synthesized in two steps from commercially available starting materials. The pincer complexes were prepared by the reaction of bis-[R(hydroxy)methyl]-1,2-dicarba-*closo*-dodecaborane (R = 2-pyridyl *o*CB-L1, 6-methyl-2-pyridyl *o*CB-L2) or bis-[2-pyridyl (hydroxy)methyl]-1,2-dicarba-*meta*-dodecaborane (*m*CB-L1) with [PdCl<sub>2</sub>(MeCN)<sub>2</sub>] under mild conditions. The X-ray structure determination of all carboranyl pincer complexes shows unambiguously B–H activation of the carborane cages. The results agree with the Pd–B bonds in all complexes exhibiting strong  $\sigma$ -electron donation. Theoretical calculations reveal the importance of considering the solid state intermolecular hydrogen bonding when investigating the *trans* influence in organometallic chemistry. A localized orbitals approach has also been applied to analyze the metal oxidation state in the carboranyl pincer complexes. Catalytic applications of (*o*CB-L1)Pd and (*m*CB-L1)Pd have shown the complexes are good catalyst precursors in Suzuki coupling in water and with very low amounts of catalyst loadings.



## INTRODUCTION

Pincer complexes represent an exciting platform for fundamental studies on transition metal coordination chemistry, metal mediated reactivity, and homogeneous catalysis.<sup>1</sup> Pincer ligands feature a rigid and tridentate binding pocket, usually a coordinating bridgehead position and two donor arms. Side arm functionalization and selection of the coordinating bridgehead position allow careful tuning of desired ligand physical and electronic properties, and finally the pincer complex by selection of the appropriate transition metal.<sup>1</sup> Perhaps the most attractive feature of metal pincer complexes is the unique possibility for fine-tuning the catalytic activity of the metal atom. Since the coordinating bridgehead position is usually coplanar with the coordination site available for catalysis, steric and electronic properties of the pincer ligand can be efficiently transferred to the metal center.<sup>1</sup> The coordinating bridgehead positions are, more often than not, carbon-based,<sup>1,2</sup> but also amido,<sup>3</sup> silyl,<sup>4</sup> or phosphido<sup>5</sup> units to provide heterodonor functionality. Boron was surprisingly absent in this picture until work reported by Teixidor<sup>6</sup> in 1991 and later by Nozaki<sup>7</sup> and Mirkin<sup>8</sup> in 2009. Teixidor and co-workers reported the first dithio-7,8-*nido*-carboranyl based

SBS pincer rhodium complex, although it was not recognized as such at that time. Nozaki reported the first boryl-based PBP ligand system and showed that the iridium complex of this ligand showed a stronger  $\sigma$ -donating ability, and therefore a stronger *trans* influence, than the corresponding PCP ligand.<sup>7</sup> Concomitant with Nozaki's report, Mirkin and co-workers initiated a new chapter in carborane chemistry by providing the first two *closo-meta*-carborane-based (EBE) pincer complexes **1** (E = S) and **2** (E = Se) structures with previously unobserved Pd–B boryl  $\sigma$ -coordination within a pincer ligand framework (Figure 1, top). The latter implies a strong electron-donating ability of the boron moiety and therefore a strong *trans* influence (Pd–Cl distance 2.44 Å).<sup>8</sup>

The development of pincer complexes incorporating boron as a pivotal, ligating element is important for several reasons. In contrast to the class of metallaboratranes, which feature a M(donor)–B(acceptor) bond, these ligands feature a stable, strongly  $\sigma$ -donating boryl fragment.<sup>9</sup> The incorporation of the rich carborane chemistry to the pincer type complexes has now

Received: June 13, 2014

Published: August 11, 2014

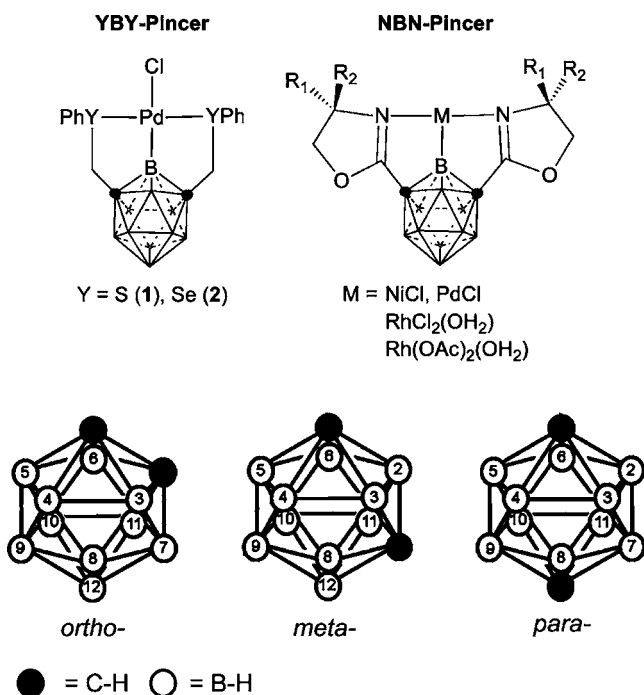
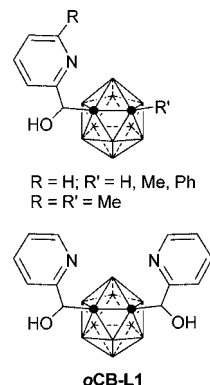


**Figure 1.** Reported *closo*-carboranyl-based pincers (top) and graphical representation of the carborane isomers (*closo*-C<sub>2</sub>B<sub>10</sub>H<sub>12</sub>) with vertex numbering.

been expanded to include possible applications as ligands in transition metal catalysis. Following Mirkin's report, Nakamura and co-workers reported the synthesis and application in asymmetric catalysis of a new family of *meta*-carborane-based (NBN) pincer complexes (Figure 1, right).<sup>10</sup> All *closo*-carborane-pincer complexes reported so far are based in the *meta*-carborane isomer (Figure 1, bottom), that is, one of the three possible isomers of carborane (*ortho*-, *meta*-, and *para*-*closo*-C<sub>2</sub>B<sub>10</sub>H<sub>10</sub>, from now on *o*-, *m*- and *p*-carborane; Figure 1). Electron density of the vertexes is strongly affected by the different electronegativities between carbon and boron atoms and by their arrangement in the three isomers. Both calculations and chemical reactivity reveal that B(3) (or 6) in *o*-carborane is more positive than the related B(2) (or 3) in *m*-carborane and B atoms in *p*-carborane are practically neutral.<sup>11,12</sup> In other words, the boron atoms attached to both carbon atoms of the cluster are more electron-withdrawing in the *o*-carborane than in the *m*-carborane isomers. The effect is known to transmit to the substituents at boron, and therefore it should also affect the metal centers in carboranyl based EBE complexes. Providing that this effect is significant, it could provide an exclusive control of electronic properties (such as *trans* influence) over the steric ones by simply selecting the desired carborane isomer for a given carboranyl based ligand and its corresponding EBE complex. Such control in electronic tuning without altering the steric factors is an exclusive feature of carborane based ligands.<sup>13</sup>

During the last few years, we have synthesized and studied the supramolecular structures of a family of mono- and disubstituted chiral *o*-carboranylalcohols (Scheme 1), which are isolated as racemic mixtures.<sup>14</sup> These molecules, which are prepared in very good yields from one-pot reactions and from readily available starting materials, are centered around an *o*-carborane core with one or two arms radiating out of one of the cluster carbons, containing a chiral carbon that bears an alcohol

## Scheme 1. Previously Synthesized Carboranylalcohols



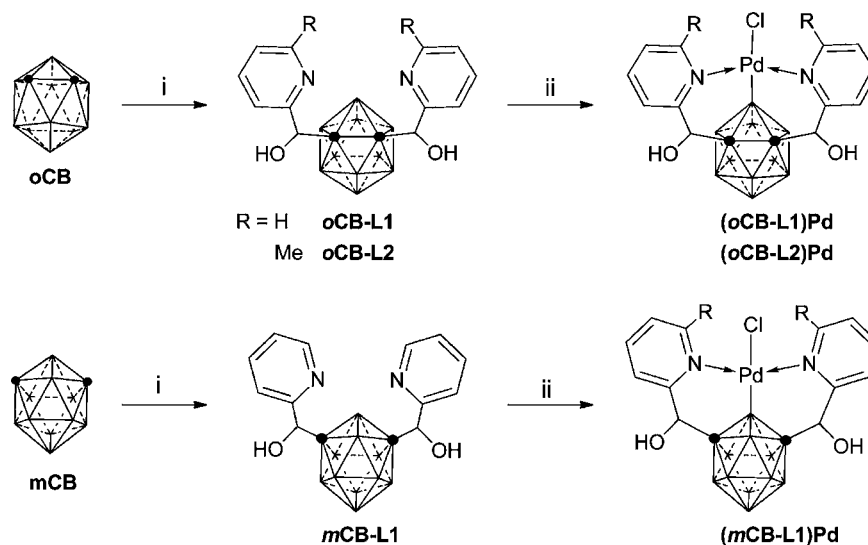
and an aromatic moiety. The high thermal and chemical stability, hydrophobicity, acceptor character, ease of functionalization, and three-dimensional nature of the icosahedral carborane clusters make these new molecules valuable ligands in coordination chemistry.<sup>9a,11b</sup> Thus, soon after we obtained our first *o*-carboranylalcohols we initiated a systematic study of the coordination chemistry of all these monosubstituted *o*-carboranylalcohol ligands, and more recently on our disubstituted ligands, with several transition metals.<sup>15</sup> We obtained a first family of *o*-carboranyl NBN based pincer palladium complexes and extended the synthesis to the corresponding *m*-carboranyl NBN analogues. Here, we report on the structural and electronic characterization of these ligands and the corresponding Pd complexes, and on catalytic properties of the latter.

## RESULTS AND DISCUSSION

**Synthesis and Characterization of Ligands.** Following our previous report,<sup>14d</sup> we have now expanded our family of bis-pyridylmethyl alcohols derived from the *o*-carborane cluster (*o*CB-L2; Scheme 2) and synthesized a new related *m*-carborane analogue (*m*CB-L1; Scheme 2). The reaction of dilithiated *o*-carborane or *m*-carborane with the corresponding aromatic aldehydes at low temperature afforded the new ligands in reasonable yields (57–79%). All new compounds have been fully characterized by standard spectroscopic and analytical techniques, and the data correlated well with that of related alcohols.<sup>14</sup> All these compounds contain two chiral centers that can adopt either *R* or *S* configuration and therefore could lead to the formation of two diastereoisomers, a *meso* compound (*RS*; OH groups in a *syn* orientation) and a racemic compound (mixture of *SS* and *RR*; OH groups in an *anti* orientation). Extensive NMR analysis for *o*-carborane *o*CB-L1 was done in the previous report and showed that *anti*- and *syn*-diastereoisomers for *o*CB-L1 showed separated NMR signals. In contrast, the mixture of *anti*- and *syn*-diastereoisomers of *m*CB-L1 showed a sole set of signals in the <sup>1</sup>H NMR spectrum. The latter might be related to free rotation of the pyridylalcohol arms in the *meta*-carborane derivatives, so that an average NMR pattern is observed for the *anti*- and *syn*-*m*CB-L1 mixture. Free rotation of pyridylalcohol arms in *ortho*-carborane derivatives is clearly not possible due to steric hindrance.<sup>14d</sup>

**Synthesis of Carborane-Based NBN Pincer Complexes.** New pincer complexes (*o*CB-L1)Pd and (*m*CB-L1)Pd were synthesized in high yield (71–76%) by reacting the corresponding ligands with [PdCl<sub>2</sub>(MeCN)<sub>2</sub>] in acetone for 15 h at rt or 2 h at 55 °C under air (Scheme 2). All



Scheme 2. Synthesis of NBN-Pincer Ligands and Complexes<sup>a</sup>

<sup>a</sup>(i) *n*-BuLi, ether (0 °C), pyridinecarboxaldehyde (−94 °C for *o*CB or −63 °C for *m*CB), 4 h, H<sub>2</sub>O, H<sup>+</sup>; (ii) PdCl<sub>2</sub>(MeCN)<sub>2</sub>, acetone, rt/55 °C.

spectroscopic data are consistent with the proposed molecular structures (Scheme 1) and are in agreement with the solid-state molecular structures determined by single crystal X-ray diffraction methods (*vide infra*). The complexes precipitated from the reaction media as air stable pale yellow solids, soluble in very polar solvents such as DMF or DMSO ((*m*CB-L1)Pd being slightly more soluble than (*o*CB-L1)Pd). It was noted that pincer formation was somewhat easier for the *o*CB-L1 ligand than that for the *m*CB-L1 one. Introduction of a methyl group in the 6-position at the pyridine moieties (*o*CB-L2) clearly decreased the reactivity of this ligand toward Pd(II), and only mixtures of a pincer complex with starting ligand were obtained. Thus, in the absence of steric hindrance, complexation to Pd(II) proceeds smoothly to enable B–H bond cleavage and biscyclopalladation to afford six-membered metallacycles, which are also typical for related aryl based Pd complexes with NCN ligands.<sup>16</sup> It is however worth noting that even though the B–H bond is inversely polarized compared to a typical C–H bond, pincer complex formation is observed after a few minutes in case of (*o*CB-L1)Pd. Similar facile B–H activation has been recently reported to occur in dicarboxylic acids of carboranes by iridium.<sup>17</sup>

**X-ray Structural Analysis.** The molecular structures for compounds (*o*CB-L1)Pd, (*o*CB-L2)Pd and (*m*CB-L1)Pd were unequivocally established by single crystal X-ray diffraction (Figure 2) and are in agreement with the NMR data (*vide infra*). Experimental crystal data and structure refinement parameters for the new pincer complex structures reported in this work are listed in Table 1. Whereas the *o*-carborane derivatives ((*o*CB-L1)Pd and (*o*CB-L2)Pd) both crystallize in the triclinic  $P\bar{1}$  space group, the *m*-carborane compound ((*m*CB-L1)Pd) crystallizes in the monoclinic  $P2_1/c$  space group. The molecular structures for all these pincer palladium complexes show typical icosahedrons with very similar bond distances and angles, and also similar to those in other *o*- or *m*-carboranyl alcohols.<sup>14</sup> The structure for the (*o*CB-L1)Pd complex shows that the *syn*-diastereoisomer (*meso*) has preferentially crystallized from the diastereoisomeric mixture (top of Figure 2). On the other hand, the (*o*CB-L2)Pd and (*m*CB-L1)Pd structures crystallized as mixtures of *syn*- and

*anti*-stereoisomers with OH groups disordered over two positions (with site occupancy factors 0.863:0.137 for (*o*CB-L2)Pd) and 0.731:0.269 for (*m*CB-L1)Pd. The Pd(II) metal atoms display a strongly distorted square planar coordination: for complex (*syn*-*o*CB-L1)Pd, maximum distances from the least-squares plane are +0.163 Å for B(6), and −0.167/−0.165 for N(20)/N(28); for complex (*m*CB-L1)Pd, corresponding distances are +0.267 Å for B(2), and −0.256/−0.260 for N(20)/N(28); for complex (*o*CB-L2)Pd, the maximum distances are −0.119 Å for Pd(1), and +0.043 for B(3). In all complexes the two pyridine rings are in a *trans* fashion and a chloride atom is *trans* to the boron atom coordinated to Pd(II). Molecular structures for the complexes show unambiguously B–H activation of the carborane cages. Activation takes place in the B–H bonds close to the carborane carbon atoms, B(3/6)H in *o*-carborane or B(2/3)H in *m*-carborane (Figure 2). A comparison of selected bond distances and angles is shown in Table 2 for all structures in this work along with those for the only other two carborane pincer structures reported so far.<sup>7</sup>

The structures of compounds (*syn*-*o*CB-L1)Pd, (*o*CB-L2)Pd, and (*m*CB-L1)Pd display exceptionally long Pd–Cl distances in the solid state, suggesting a strong *trans* influence of the carborane moieties (Table 2). Such long Pd–Cl distances are sensibly longer than similar motifs in aryl-based pincers (2.39–2.45 Å)<sup>18</sup> and are comparable with that for related alkyl-based pincer Pd complexes (2.49–2.52 Å).<sup>19</sup> The Pd–B distances (1.97–2.02 Å) are also short and are consistent with a Pd–B  $\sigma$  bond as that found in the related *m*-carboranyles 1–2.<sup>8</sup> To gain more insight into these new structural motifs, density functional theory (DFT) calculations were performed for all structures in this work and those previously reported by Mirkin.<sup>8</sup> Surprisingly, optimized structures of monomers of the compounds show systematically shorter Pd–Cl distances (and longer B–Pd distances) compared to the X-ray structures (Table 3). In the case of the related (*syn*-*o*CB-L1)Pd and (*m*CB-L1)Pd compounds, the computed Pd–Cl distances are shorter than the experimental values by 0.085 and 0.069 Å, respectively. Control calculations performed at different levels of theory (see Supporting Information) clearly indicate that the origin of this discrepancy is not due to the accuracy of the

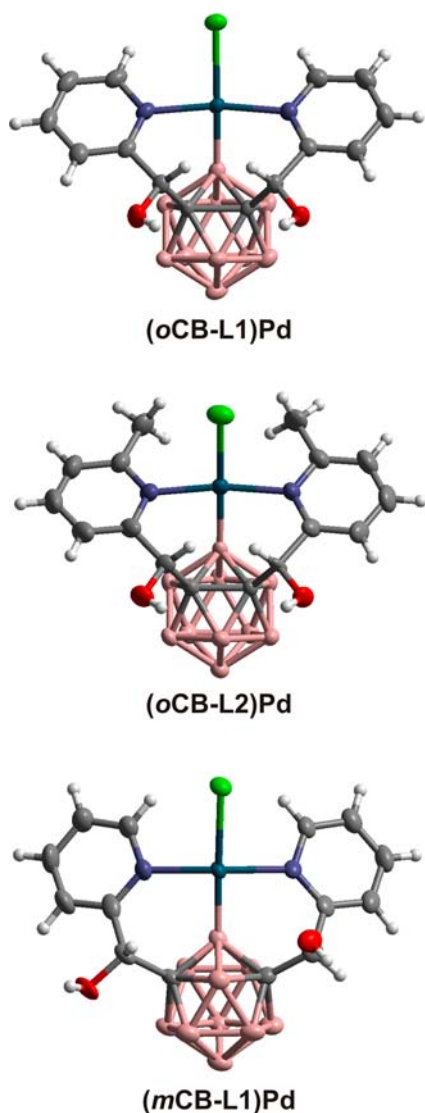


**Figure 2.** Molecular structures of  $(oCB-L1)Pd$ ,  $(oCB-L2)Pd$ , and  $(mCB-L1)Pd$ ; thermal ellipsoids set at 90%, 70%, and 80% probability, respectively, and H atoms are represented as fixed-size spheres of 0.18 Å (B–H and pyridine hydrogen atoms are omitted for clarity). Color code: B pink; C gray; H white; O red; N blue; Cl green; Pd prussian blue. Only one stereoisomer is represented in those structures with disorder of OH groups.

chosen computational setup. Further analysis of the crystal structures reveals that the hydroxyl groups of a neighboring complex form H-bonds with the chloride ligand:  $(syn-oCB-L1)Pd$  ( $(O-H)_2 \cdots Cl$ ,  $O \cdots Cl$  3.194(2)/3.098(2) Å;  $OHCl$  156.5/157.4°),  $(oCB-L2)Pd$  ( $(O-H)_2 \cdots Cl$ ,  $O \cdots Cl$  3.177(2)/3.088(3) Å;  $OHCl$  163.3/161.4°) and  $(mCB-L1)Pd$  ( $O-H \cdots Cl$ ,  $O \cdots Cl$  2.997(3)/3.172(3) Å;  $OHCl$  179.7/166.5°).<sup>20</sup> We thus set up calculations on the dimeric structure for  $(syn-oCB-L1)Pd$  (no isomerism) and for  $(mCB-L1)Pd$  (*syn* and *anti* isomers). H-bonded dimers of  $(oCB-L2)Pd$  were not considered because of the high number of isomers. The computed Pd–Cl distances for the dimeric structures are now in good agreement with the experimental solid state data (Table 3). As a means of comparison, we also computed compounds **1** and **2** from Mirkin et al.<sup>7</sup> Inspection of the crystal structures shows intermolecular C–H $\cdots$ Cl interactions which are expected to be weaker than the O–H $\cdots$ Cl H-bonds

observed in the crystal structures of  $(syn-oCB-L1)Pd$ ,  $(oCB-L2)Pd$ , and  $(mCB-L1)Pd$ . Accordingly, calculations on the monomeric and oligomeric states (a trimer for **1** and dimer for **2**; see Supporting Information for details) provide similar optimized geometric parameters, in fair agreement with the experimental data. It thus appears that two effects are operative in modulating the Pd–Cl distance in the crystal structures. One is the *trans* influence of the carborane moieties, the other being the intermolecular moderate H-bonding interactions among neighboring complexes. This finding is certainly relevant since the length of the metal–Cl bonds is often the only parameter considered for evaluating the *trans* influence in metal complexes. Calculations clearly show that in the absence of strong intermolecular interactions, like in the case of **1** and **2**, the Pd–Cl distances in the crystals can be a direct measure of the *trans* influence. The situation is however different when moderate intermolecular hydrogen bonding is taking place as it is the case of  $(syn-oCB-L1)Pd$ ,  $(oCB-L2)Pd$ , and  $(mCB-L1)Pd$ . The Cl atoms are acting as H-bonding acceptors with the consequent elongation of the Pd–Cl bond. Therefore, calculated distances for the isolated molecules in the gas phase (in the absence of intermolecular H-bonding) can be taken as a more appropriate indication of *trans* influence than the X-ray distances in our complexes. Thus, considering the Pd–Cl distances from the gas phase calculated monomers (Table 3), it can be inferred a stronger *trans* influence of the *m*-carborane than the *o*-carborane moieties in the pincer complexes, as expected. Such calculated Pd–Cl distances are therefore suggesting a *trans* influence for the carborane moieties in  $(syn-oCB-L1)Pd$ ,  $(oCB-L2)Pd$ , and  $(mCB-L1)Pd$  similar to that found in aryl-based pinners.<sup>16</sup>

We have applied an orbital localization procedure to further investigate the extent of intramolecular *trans* influence and intermolecular H-bond contribution.<sup>21</sup> Specifically, we have used the displacement of the localized orbital centroid (Wannier centers) to quantify each contribution. The approach has been successfully used in the literature to characterize environment effects<sup>22</sup> on bonding interactions and to develop ionicity scales.<sup>23</sup> Furthermore, Sit et al. proposed to use the localized orbital centroids to determine the oxidation state of transition metal ions.<sup>24</sup> Recently, we have reported that the approach is capable of providing valuable insight in the analysis of the electronic structure of organometallic compounds.<sup>25</sup> In summary, the localization procedure that we employ provides the centroid of charge (Wannier centers) and the spread of each orbital. This allows visualizing a picture of “where” electrons are and “who” they belong to. Selected localized orbitals for pincer complex  $(syn-oCB-L1)Pd$  and the corresponding free ligand *syn-oCB-L1*, with their corresponding orbital centroids, are shown in Figure 3. Table 3 collects the charges and orbital centroids for all calculated compounds.

Inspection of the localized orbital for the Pd–B bond of  $(syn-oCB-L1)Pd$  (middle of Figure 3) reveals a pear-shaped orbital centered on the boron atom of the carborane ligand, which would suggest a dative bond. However, the orbital centroid (green dot in Figure 3) for the Pd–B bond is located at about the center of the Pd–B bond, as expected for a covalent bond. On the contrary, the centroid of the Pd–Cl bond is clearly closer to the chloride, as expected for a strongly polarized bond on the basis of the respective (Pauling) electronegativities. Table 3 shows that the same is observed for all complexes. Quite interestingly, the elongation of the Pd–Cl bonds on intermolecular H-bond formation is followed by a concomitant

Table 1. Crystal Data and Refinement Details for Structures of Compounds *syn-oCB-Pd1*, *oCB-Pd2*, and *mCB-L1*<sup>a</sup>

	( <i>syn-oCB-L1</i> )Pd	( <i>oCB-L2</i> )Pd	( <i>mCB-L1</i> )Pd
empirical formula	C <sub>38</sub> H <sub>70</sub> B <sub>20</sub> C <sub>14</sub> N <sub>8</sub> O <sub>6</sub> Pd <sub>3</sub>	C <sub>16</sub> H <sub>25</sub> B <sub>10</sub> ClN <sub>2</sub> O <sub>2</sub> Pd	C <sub>17</sub> H <sub>28</sub> B <sub>10</sub> ClN <sub>3</sub> O <sub>3</sub> Pd
formula weight	1412.22	527.33	572.37
crystal system	triclinic	triclinic	monoclinic
space group	$P\bar{1}$	$P\bar{1}$	$P2_1/c$
temperature/K	100.0	100.0	100.0
wavelength/Å	0.71073	0.71073	0.71073
<i>a</i> /Å	10.6774(5)	9.9166(4)	11.0330(5)
<i>b</i> /Å	10.9800(4)	10.7176(4)	20.3495(10)
<i>c</i> /Å	13.2409(6)	12.7142(5)	11.0094(5)
$\alpha$ /deg	99.934(2)	68.9240(10)	90
$\beta$ /deg	101.468(2)	67.4490(10)	96.4690(18)
$\gamma$ /deg	102.624(2)	67.4990(10)	90
volume/Å <sup>3</sup>	1446.22(11)	1116.52(8)	2456.0(2)
<i>Z</i>	1	2	4
density (calculated)/ Mg/m <sup>3</sup>	1.622	1.569	1.548
<i>F</i> (000)	708	528	1152
theta range for data collection/deg	2.41–26.37	2.32–26.37	2.672–26.371
absorption coefficient/mm <sup>-1</sup>	1.159	0.969	0.891
goodness-of-fit on <i>F</i> <sup>2</sup>	1.080	1.065	1.123
<i>R</i> <sub>1</sub> [ <i>I</i> > 2 $\sigma$ ( <i>I</i> )]	0.0226	0.0239	0.0334
<i>wR</i> <sub>2</sub> [ <i>I</i> > 2 $\sigma$ ( <i>I</i> )]	0.0572	0.0643	0.0765
<i>R</i> <sub>1</sub> (all data)	0.0247	0.0249	0.0429
<i>wR</i> <sub>2</sub> (all data)	0.0581	0.0649	0.0810

<sup>a</sup>CCDC 1008023 (*syn-oCB-L1*)Pd, 1008024 ((*oCB-L2*)Pd), and 1008025 ((*mCB-L1*)Pd) contain the supplementary crystallographic data for this paper. These data can be obtained free of charge from The Cambridge Crystallographic Data Centre via [www.ccdc.cam.ac.uk/data\\_request/cif](http://www.ccdc.cam.ac.uk/data_request/cif).

Table 2. Comparison of Selected Distances (Å) and Angles (deg) for (*syn-oCB-L1*)Pd, (*oCB-L2*)Pd, and (*mCB-L1*)Pd and 1–2

**Y = N**

**Y = N**

**Y = S**

**Y = Se**

	Y = N		Y = N	Y = S	Y = Se
	( <i>syn-oCB-L1</i> )Pd	( <i>oCB-L2</i> )Pd	( <i>mCB-L1</i> )Pd	1	2
Pd–Cl	2.4915(5)	2.4879(6)	2.5063(8)	2.417(1)	2.4371(5)
Pd–B	2.021(2)	2.017(2)	1.974(4)	1.983(4)	1.982(3)
Pd–Y(a)	2.0557(17)	2.0490(18)	2.088(3)	2.3113(9)	2.4252(3)
Pd–Y(b)	2.0564(18)	2.0477(18)	2.087(3)	2.3204(9)	2.4340(3)
Cc(a)–B	1.718(3)	1.730(3)	1.704(5)	1.707(5)	1.714(3)
Cc(b)–B	1.723(3)	1.730(3)	1.706(5)	1.693(6)	1.720(4)
Cl–Pd–B	175.14(7)	171.85(7)	170.98(10)	173.1(1)	171.09(7)
Y–Pd–Y	166.76(7)	170.35(7)	161.55(10)	162.70(3)	162.11(1)

displacement of the Wannier centers of the Pd–Cl bonds. Thus, the intermolecular H-bonds are significantly affecting the orbitals of the Pd–Cl bonds, confirming their role on the exceptionally long distances found in the solid structures. Concerning the Pd–Cl bonds of the isolated molecules in the gas phase, we note that the longest Pd–centroid distance is displayed by (*mCB-L1*)Pd, consistent also with the idea that the *mCB-L1* ligand has the strongest *trans* influence. To further characterize the nature of the interactions, we have performed a natural bond orbital (NBO) analysis for our complexes (Table S3 in Supporting Information).<sup>26</sup> The results suggest in this

case that the Pd–B bond is better described as covalent, whereas the Pd–Cl is clearly ionic.

It was suggested that the Pd in these carbonyl pincer compounds might be formally Pd(0), based on calculated Mulliken and Löwdin charges for **2**.<sup>8</sup> The authors found a net negative charge localized on the Pd atom and a relative positive charge concentrated on the B atom bonded to it (B(2); see Figure 2 for nomenclature). However, they recognized that only the Löwdin charges showed some consistency and stressed the importance of being cautious in the choice of functional, effective core potentials and in the (quantitative) interpretation

Table 3. Calculated Geometrical, Atomic Charges and Electronic Parameters for Selected Atoms in Compounds (*syn-oCB-L1*)Pd, (*oCB-L2*)Pd, (*mCB-L1*)Pd, (*mCB-L1*)Pd, and 1–2

	( <i>syn-oCB-L1</i> )Pd	( <i>syn-oCB-L1</i> )Pd (dimer)	( <i>oCB-L2</i> )Pd	( <i>mCB-L1</i> )Pd	( <i>mCB-L1</i> )Pd (dimer)	1	1 (trimer)	2	2 (dimer)
Pd–Cl	2.406	2.502	2.430	2.437	2.497 ( <i>anti</i> ) 2.505 ( <i>syn</i> )	2.402	2.419	2.422	2.443
Pd–B	2.046	2.043	2.043	2.002	1.992 ( <i>anti</i> ) 1.987 ( <i>syn</i> )	2.004	1.998	2.012	2.011
Pd	0.280	0.248	0.241	0.247	0.237 ( <i>anti</i> ) 0.240 ( <i>syn</i> )	0.060	–0.001	0.007	–0.002
Cl	–0.616	–0.624	–0.615	–0.638	–0.639 ( <i>anti</i> ) –0.642 ( <i>syn</i> )	–0.607	–0.610	–0.608	–0.622
B	0.856	0.911	0.746	1.254	1.330 ( <i>anti</i> ) 1.345 ( <i>syn</i> )	1.205	1.318	1.238	1.374
Pd–X–Cl	1.733/0.676	1.902/0.603	1.750/0.680	1.782/0.655	1.886/0.611 ( <i>anti</i> ) 1.897/0.608 ( <i>syn</i> )	1.721/0.681	1.765/0.656	1.757/0.666	1.802/0.642
Pd–X–B	1.014/1.032	0.930/1.114	1.010/1.037	0.975/1.027	0.924/1.069 ( <i>anti</i> ) 0.919/1.069 ( <i>syn</i> )	0.946/1.059	0.929/1.069	0.951/1.061	0.925/1.086
Pd oxidation state	II	II	II	II	II	II	II	II	II

Localized Orbital Centroids

of the results. For comparison, we have therefore calculated Mulliken, Löwdin and Bader and NPA charges for ours and Mirkin's pincer complexes (Table S2 in Supporting Information). In general, Mulliken and Löwdin charges suggest a negative Pd and a positive B atom bonded to it, in line with Mirkin's findings.<sup>8</sup> On the contrary, Bader and NPA charges suggest positive charges on both Pd and boron atom. It may be appreciated that Mulliken, Löwdin and Bader's charges describe B as more positive than Pd, whereas within the NPA description Pd is more positively charged. These results suggest that interpreting the oxidation state of the metal based on calculated charges is certainly delicate. Thus, we have employed the electron counting procedure proposed by Sit et al.,<sup>24</sup> which is based on the assignment of localized orbital centroids to individual atoms, for ours and Mirkin pincer complexes. This method suggests a Pd(II) state for all carboranyl pincer complexes as eight centroids ( $d^8$  configuration) are clearly localized around the Pd atoms. Certainly, the different assignment of the Pd oxidation state depends on the nature of the Pd–B bond. Figure 3 shows the localized orbitals corresponding to the Pd–B bond in (*syn-oCB-L1*)Pd and H–B bond in the free ligand *syn-oCB-L1*. It may be appreciated the inversion of the polarity of the bond from the H–B (centroid close to H) to the Pd–B (centroid in the middle), consistent with the idea that the electrons involved in the Pd–B bond “belong” to boron. Thus, based on the above electron counting procedure and the shape of the Pd–B localized orbital, we assigned the corresponding orbital centroid to B, resulting in a Pd(II) oxidation state.

**Characterization of Carborane-Based NBN Pincer Complexes.** All spectroscopic and analytical data are consistent with the proposed molecular structures (Scheme 2) and are in agreement with the solid-state structures determined by single crystal X-ray diffraction methods (Figure 2). <sup>11</sup>B NMR spectroscopy shows a unique very broad resonance (ranging from  $\delta +10$  to  $-20$ ) centered at  $\delta \approx -6$  and  $-11$  for the (*oCB-Ln*)Pd ( $n = 1, 2$ ) and (*mCB-L1*)Pd, respectively. The broadness of the <sup>11</sup>B NMR signals, probably a consequence of the diastereomeric mixtures, prevent the direct observation of typical singlet resonance for the boron atom bonded to metals at  $\delta \approx 0$ .<sup>8</sup> Coordination of the Pd ion leads to a general downfield shift of signals of the free ligands in the <sup>1</sup>H NMR spectra, this being consistent with related Pd complexes. <sup>11</sup>B-decoupled <sup>1</sup>H NMR spectra shows also broad resonances for the hydrogen atoms at the boron atoms that are reasonable sharp, compared to the coupled spectra, so that integration is possible unless residual solvent signals overlap occurs. Thus, <sup>1</sup>H{<sup>11</sup>B} NMR for the free ligand *oCB-L1* shows broad resonances for 10 boron atoms in the range  $\delta$  3 to 1.3.<sup>14d</sup> The pattern in the related complex (*oCB-L1*)Pd changes to four resonances for nine boron atoms in a 1:3:3:2 ratio and in a larger range ( $\delta$  2.7 to 0.4). The introduction of Pd into *oCB-L1* modifies the symmetry of the carborane cluster, and this consequently modifies the observed pattern for the hydrogens at boron atoms. It is noteworthy the strongly deshielded resonance for two BH hydrogens at  $\delta$  0.4 (respect to the closest resonance at  $\delta$  1.9). The upfield signals are likely due to the shielding cone of the pyridine rings, and we tentatively assigned to hydrogens attached to B(4) and B(7). The related B(6/11) H hydrogens for (*oCB-L2*)Pd also appears upfield ( $\delta$  0.24). The situation is more complex for the *m*-carboryl pincer (*mCB-L1*)Pd since B–H activation for the mixture of *syn*- and *anti*-diastereoisomers afford four possible isomers (see Supporting

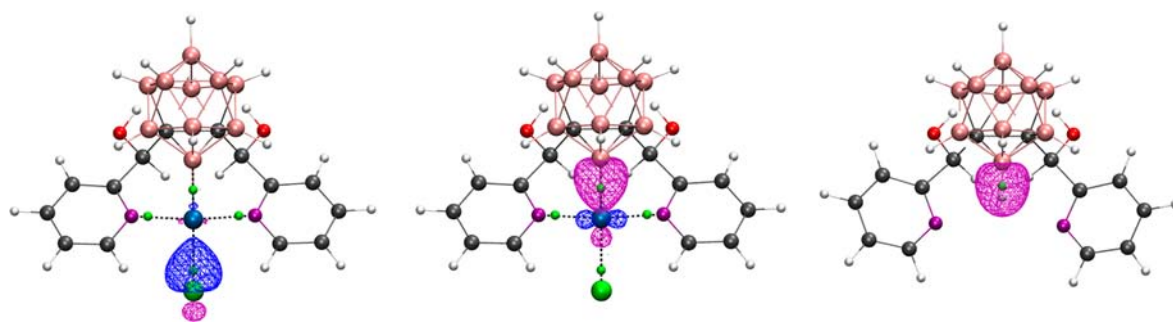


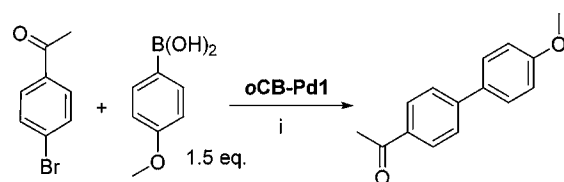
**Figure 3.** Localized orbitals corresponding to the Pd–Cl, Pd–B, and H–B bonds of (*syn*-*oCB-L1*)Pd (left and middle) and *syn*-*oCB-L1* (right), respectively. The orbital centroids of the localized orbitals at the Pd center are shown as small green dots.

Information for details). As mentioned above, the *mCB-L1* ligand is obtained as a mixture of *syn*- and *anti*-diastereomers and shows a unique set of signals in the  $^1\text{H}$  NMR, probably due to free rotation of the pyridylmethylalcohol arms around the Cc–C bonds (Cc: carbon cluster). Rotation is not possible on complexation so that diastereomers formation is evident from the  $^1\text{H}$  NMR spectrum for the Pd complex (*mCB-L1*)Pd. The  $^1\text{H}$  NMR spectrum for a mixture of *anti*- and *syn*-diastereoisomers of (*mCB-L1*)Pd, as obtained in the synthesis, shows two sets of signals for the CHOH groups in a  $\sim 1:1$  ratio as doublets at  $\delta$  5.14 and 4.96. Although pyridine and OH signals for the mixture of four diastereoisomers results in a quite complicated spectrum, integration shows the expected ratio of signals.

**Carborane-Based NBN Pincer Complexes As Catalysts.** We have initiated a systematic study on the use of the newly synthesized carboranyl NBN pincer Pd complexes as homogeneous catalysts. The catalytic profile of both (*oCB-L1*)Pd and (*mCB-L1*)Pd was evaluated in one of the most important Pd-catalyzed C–C bond-forming processes, the Suzuki–Miyaura cross-coupling reaction.<sup>27</sup> Accordingly, the coupling of two common substrates, 4-methoxyphenylboronic acid and 4-bromoacetophenone, was chosen as model reaction using (*oCB-L1*)Pd as palladium source. As displayed in Table 4, from the full range of experimental conditions assayed with a catalyst loading of 0.1 mol %, we learned that the use of water as reaction media interestingly provided better results (entry 10 vs 1–8) than those from organic solvents and partially aqueous mixtures (THF, DMF, MeOH, THF/H<sub>2</sub>O, MeOH/H<sub>2</sub>O), far more suitable to solubilize carboranyl-based pincer (*oCB-L1*)Pd. Considering the excellent conversion rate obtained, which was not improved by the use of TBAB, a known stabilizing agent for palladium nanoparticles,<sup>28</sup> we decided to further decrease the catalyst amount down to 0.0001 mol %. A quantitative result was again obtained at such a low level (entry 16), and accordingly a range of substrates were submitted to the optimized reaction conditions (K<sub>2</sub>CO<sub>3</sub>, H<sub>2</sub>O, 110 °C, 10 h) using (*oCB-L1*)Pd and (*mCB-L1*)Pd (Table 5). No coupling was observed in the absence of the pincer complex (entry 17, Table 4) and ICP-MS analysis of all the reagents employed (aryl halide, boronic acid, potassium carbonate) revealed that the palladium contents in the reaction mixture were around 10<sup>–5</sup> mol %. Therefore, the possibility of a coupling catalyzed by residual palladium traces from the reagents was ruled out.

Although more assays should be carried out in order to determine the scope of the procedure, the comparative study of the catalytic activity of both pincer complexes displayed in Table 5 reveals that not only arylboronic acids can be effectively

**Table 4.** Summary of Reactions Conditions for the Coupling between 4-Bromoacetophenone and 4-Methoxyphenylboronic Acid



entry	reaction conditions (i) <sup>a</sup>	conv (%) <sup>b</sup>
1	KOH (2.5 equiv), THF, 40 °C, 10 h	-
2	K <sub>2</sub> CO <sub>3</sub> (2.0 equiv), TBAB (1 equiv), THF, 40 °C, 12 h	10
3	K <sub>3</sub> PO <sub>4</sub> (2 equiv), DMF, 80 °C, 10 h	5
4	K <sub>2</sub> CO <sub>3</sub> (2.0 equiv), CH <sub>3</sub> OH/H <sub>2</sub> O (3:1), 70 °C, 12 h	-
5	K <sub>2</sub> CO <sub>3</sub> (2.5 equiv), TBAB (1 equiv), CH <sub>3</sub> OH, 70 °C, 10 h	68
6	K <sub>2</sub> CO <sub>3</sub> (2.0 equiv), CH <sub>3</sub> OH, 70 °C, 10 h	66
7	Cs <sub>2</sub> CO <sub>3</sub> (2.5 equiv), H <sub>2</sub> O, 100 °C, 12 h	7
8	K <sub>2</sub> CO <sub>3</sub> (2.0 equiv), THF/H <sub>2</sub> O (9:1), 80 °C, 10 h	88
9	Et <sub>3</sub> N (2.0 equiv), H <sub>2</sub> O, 80 °C, 12 h	99
10	K <sub>2</sub> CO <sub>3</sub> (2.0 equiv), H <sub>2</sub> O, 110 °C, 10 h	99
11 <sup>c</sup>	K <sub>2</sub> CO <sub>3</sub> (2.5 equiv), TBAB (1 equiv), CH <sub>3</sub> OH, 70 °C, 10 h	62
12 <sup>c</sup>	K <sub>2</sub> CO <sub>3</sub> (2.5 equiv), TBAB (1 equiv), CH <sub>3</sub> OH, 100 °C, 10 h	63
13 <sup>c</sup>	K <sub>2</sub> CO <sub>3</sub> (2.0 equiv), CH <sub>3</sub> OH, 70 °C, 10 h	60
14 <sup>c</sup>	K <sub>2</sub> CO <sub>3</sub> (2.0 equiv), THF/H <sub>2</sub> O (9:1), 80 °C, 10 h	84
15 <sup>c</sup>	Et <sub>3</sub> N (2.0 equiv), H <sub>2</sub> O, 80 °C, 12 h	95
16 <sup>c</sup>	K <sub>2</sub> CO <sub>3</sub> (2.0 equiv), H <sub>2</sub> O, 110 °C, 10 h	99
17 <sup>d</sup>	K <sub>2</sub> CO <sub>3</sub> (2.0 equiv), H <sub>2</sub> O, 110 °C, 10 h	-

<sup>a</sup>4-Bromoacetophenone, 4-methoxyphenylboronic acid (1.5 equiv), (*oCB-L1*)Pd (10<sup>–1</sup> mol %), base (2–3 equiv), solvent (1 mL per mmol of substrate), additive (when indicated). <sup>b</sup>Conversion rate measured by GC-MS. <sup>c</sup>(*oCB-L1*)Pd (10<sup>–4</sup> mol %). <sup>d</sup>Reaction performed in the absence of (*oCB-L1*)Pd.

coupled with aryl bromides but also potassium phenyltrifluoroborate (Table 5, entries 3, 5, 7, and 10). In addition, benzyl bromide can be also used as a coupling partner (entries 11–14), and both electron-withdrawing and -donating groups can be incorporated in the substrates. No byproducts were observed, and apart from the coupling products, only unreacted halides were detected in the crude reaction mixtures. With a few exceptions (entries 4, 11, and 13), a better catalytic profile was observed from (*oCB-L1*)Pd-containing aqueous solutions, since (*mCB-L1*)Pd failed to provide the corresponding biaryl compound with acceptable yields in some cases (entries 6 and 8).

Table 5. Suzuki Coupling in the Presence of Carborane-Based NBN Pincer Complexes. Functional Group Tolerance

Entry	R <sup>1</sup>	R <sup>2</sup>	n	Y	( <i>o</i> CB-L1)Pd (%) <sup>a</sup>	( <i>m</i> CB-L1)Pd (%) <sup>a</sup>
1			0	B(OH) <sub>2</sub>	99	60
2			0	B(OH) <sub>2</sub>	99	85
3 <sup>b</sup>			0	BF <sub>3</sub> K	99	93
4			0	B(OH) <sub>2</sub>	84	90
5 <sup>b</sup>			0	BF <sub>3</sub> K	92	60
6			0	B(OH) <sub>2</sub>	91	5
7 <sup>b</sup>			0	BF <sub>3</sub> K	97	69
8			0	B(OH) <sub>2</sub>	77	20
9			0	B(OH) <sub>2</sub>	66	56
10 <sup>b</sup>			0	BF <sub>3</sub> K	61	54
11			1	B(OH) <sub>2</sub>	82	99
12			1	B(OH) <sub>2</sub>	99	99
13			1	B(OH) <sub>2</sub>	87	95
14			1	B(OH) <sub>2</sub>	99	99

<sup>a</sup>Aryl or arylmethyl bromide, arylboronic acid, or aryl trifluoroborate (1.5 equiv), (*o*CB-L1)Pd or (*o*CB-L1)Pd (10<sup>-4</sup> mol %), K<sub>2</sub>CO<sub>3</sub> (2.0 equiv), H<sub>2</sub>O (1 mL per mmol of ArBr or ArCH<sub>2</sub>Br), 110 °C, 10 h. Isolated yields. <sup>b</sup>2.5 equiv of K<sub>2</sub>CO<sub>3</sub> were used.

TON values ranged from 770000 to 990000 for (*o*CB-L1)Pd, thus showing a very high catalytic activity which rivals

previous reports on Suzuki coupling performed by very low amounts of palladium catalysts, even with pincer complexes.<sup>29</sup>

Moreover, the use of water as a convenient, sustainable solvent is an added bonus that cannot be ignored.

The low catalytic loading employed prevented an analysis of the palladium species generated after the coupling reaction, including that related to possible changes in the structure of the carborane moieties. However, no palladium black or mirror was observed, even when the catalyst amount was increased at the  $10^{-1}$  mol % level (Table 4, entry 10), which is to some extent indicative of the integrity of the metal complex under the reaction conditions. Although no detailed mechanistic studies have been carried out for the present Suzuki coupling reactions, it occurs to us that the catalytic activity in water and the elongation of the Pd–Cl bonds due to intermolecular H-bond formation might be connected. It seems feasible that intermolecular H-bond between the water molecules and chloride atoms in both pincer complexes take place under the catalytic conditions. In such case, the *trans* influence of *o*- versus *m*-carborane becomes negligible, and therefore a similar catalytic activity is found in both cases. We are currently investigating other catalytic reactions that might exploit the different *trans* influence of these carboranyl pincer complexes.

## CONCLUSIONS

We report the preparation of the first family of *o*-carborane-based NBN pincer palladium complexes (**oCB-L1**)Pd and (**oCB-L2**)Pd, along with the related *m*-carborane-based NBN pincer complex (**mCB-L1**)Pd by the reaction of bis-[R-(hydroxy)methyl]-1,2-dicarba-*closo*-dodecaborane (R = 2-pyridyl **oCB-L1**, 6-methyl-2-pyridyl **oCB-L2**) or bis-[2-pyridyl (hydroxy)methyl]-1,2-dicarba-*meta*-dodecaborane (**mCB-L1**) with PdCl<sub>2</sub>(MeCN)<sub>2</sub> under mild conditions. The X-ray structures of (**oCB-L1**)Pd, (**oCB-L2**)Pd, and (**mCB-L1**)Pd shows that the Pd(II) metal atoms display a strongly distorted square planar coordination, the two pyridine rings are in a *trans* fashion and a chloride atom is *trans* to a boron atom coordinated to Pd(II). Molecular structures for the complexes show unambiguously B–H activation of the carborane cages. Activation takes place in the B–H bonds close to the carborane carbon atoms, B(3/6)H in *o*-carborane or B(2/3)H in *m*-carborane. A combined study of experimental and calculated bond distances reveals that two effects are operative in modulating the Pd–Cl distance in the crystal structures. One is the *trans* influence of the carborane moieties, the other being the intermolecular moderate H-bonding interactions among neighboring complexes. This finding is certainly relevant since the length of the metal–Cl bonds are often the only parameter considered for evaluating the *trans* influence in metal complexes. Thus, considering the Pd–Cl distances from the gas phase calculated monomers, it can be inferred a stronger *trans* influence of the *meta*-carborane than the *ortho*-carborane moieties in the pincer complexes, as expected, and similar to that found in aryl-based pinners. Calculated atomic charges and localized orbitals have been used to analyze the nature of the Pd–B bond and the metal oxidation state in our *o*- and *m*-carboranyl pincer complexes but also in the previously reported *m*-carborane-based EBE (E = S, Se) pincer Pd complexes.<sup>8</sup> The results agree with the Pd–B bonds in all complexes exhibiting strong  $\sigma$ -electron donation and suggest that the Pd atom in all these carbonyl pincer complexes bear a formal oxidation state of two, rather than zero, as previously suggested.<sup>8</sup> Catalytic applications of (**oCB-L1**)Pd and (**mCB-L1**)Pd have shown the complexes are good catalyst precursors in Suzuki coupling reactions in water and with remarkably low amounts of catalyst

loadings and with good functional group tolerance for the substrates. Complex (**oCB-L1**)Pd shows a better catalytic profile than (**mCB-L1**)Pd and with excellent conversions and TON values ranging from 770000 to 990000, thus showing a very high catalytic activity which rivals previous reports on Suzuki coupling performed by very low amounts of palladium catalysts, even with pincer complexes.

## EXPERIMENTAL SECTION

**Materials and Methods.** Reactions were carried out under a nitrogen atmosphere in round-bottomed flasks equipped with a magnetic stirring bar, capped with a septum unless noted otherwise. Diethyl ether was distilled from Na/benzophenone. All the other chemicals were commercially available and used as received. **oCB-L1** was prepared according to our previous report.<sup>14d</sup> IR ATR spectra were recorded on a Perkin–Elmer Spectrum One spectrometer. <sup>1</sup>H, <sup>13</sup>C, and <sup>11</sup>B spectra were recorded respectively at 300, 75, and 96 MHz with a Bruker Advance-300 spectrometer in deuterated chloroform, acetone or dimethyl sulfoxide, and referenced to the residual solvent peak for <sup>1</sup>H and <sup>13</sup>C NMR or to BF<sub>3</sub>OEt<sub>2</sub> as an external standard for <sup>11</sup>B NMR. Chemical shifts are reported in ppm and coupling constants in Hertz. Multiplets nomenclature is as follows: s, singlet; d, doublet; t, triplet; br, broad; m, multiplet. Elemental analyses were obtained by a CarboErba EA1108 micro-analyzer (Universidad Aut3noma de Barcelona). The mass spectra were recorded in the positive or negative ion mode using a BrukerBiflex MALDI-TOF-MS [N<sub>2</sub> laser;  $\lambda_{exc}$  337 nm (0.5 ns pulses); voltage ion source 20.00 kV (Uis1) and 17.50 kV (Uis2)] with 3,5-dimethoxy-4-hydroxycinnamic acid as matrix. ICP-MS analyses were conducted using a ICP-MS Thermo Serie X. Column chromatography was conducted on silica gel (gel (35–70 mesh, 60 Å).

**Computational Details.** DFT calculations and orbital localization were performed with the CP2K code<sup>30</sup> and based on the PBE exchange-correlation functional.<sup>31</sup> The Quickstep<sup>32</sup> algorithm was used to solve the electronic structure problem using a double- $\zeta$  plus polarization (DZVP)<sup>33</sup> basis set to represent valence orbitals and plane waves for the electron density (300 Ry cutoff). Valence-core interactions were treated by means of GTH-type pseudopotentials.<sup>34–36</sup> Wave function optimization was achieved through an orbital transformation method.<sup>37</sup> Models were treated as isolated<sup>38</sup> and optimized (until gradients were  $<5 \times 10^{-4}$  a.u.). Full details on the localization algorithm as implemented in CP2K may be found in ref 39. Atomic electron populations have been computed integrating the orbital density within the atomic basins determined according to Bader's Atom in Molecules theory.<sup>40</sup>

**Synthesis of 1,2-Bis[(6-methyl-pyridin-2'-yl)methanol]-1,2-dicarba-*closo*-dodecaborane (**oCB-L2**).** The general procedure described by us for **oCB-L1** was followed,<sup>14d</sup> using *o*-carborane (207 mg, 1.44 mmol), *n*-BuLi (1.84 mL, 1.56 M in hexane, 2.87 mmol), diethyl ether (20 mL) and 6-methyl-2-pyridinecarboxaldehyde (0.23 mL, 2.90 mmol), and an ethyl acetate/liquid N<sub>2</sub> cooling bath (–84 °C). Work up gave a light yellow solid that was dried under vacuum to afford a mixture of *syn*- and *anti*-**oCB-L2** (317.2 mg, 0.82 mmol, 57.3%); mp 175–180 °C. NMR experiments confirmed the presence of the two different diastereoisomers in a 45:55 proportion.

**NMR for anti-oCB-L2.** <sup>1</sup>H NMR (DMSO-*d*<sub>6</sub>): 7.76 (t, *J* = 7.5, 2H, C<sub>5</sub>H<sub>3</sub>N), 7.39 (d, *J* = 7.6, 2H, C<sub>5</sub>H<sub>3</sub>N), 7.24 (d, *J* = 7.3, 2H, C<sub>5</sub>H<sub>3</sub>N), 7.00 (d, *J* = 5.7, 2H, OH), 5.51 (d, *J* = 5.6, 2H, CHOH), 2.50 (CH<sub>3</sub> signals are overlapped with residual DMSO). <sup>11</sup>B NMR: –2.4 (s, 2B), –9.8 (b s, 8B).

**NMR for syn-oCB-L2.** <sup>1</sup>H NMR (DMSO-*d*<sub>6</sub>): 7.76 (t, *J* = 8.0, 2H, C<sub>5</sub>H<sub>3</sub>N), 7.35 (d, *J* = 7.8, 2H, C<sub>5</sub>H<sub>3</sub>N), 7.24 (d, *J* = 7.8, 2H, C<sub>5</sub>H<sub>3</sub>N), 6.94 (d, *J* = 5.7, 2H, OH), 5.88 (d, *J* = 6.0, 2H, CHOH), 2.50 (CH<sub>3</sub> signals are overlapped with residual DMSO). <sup>11</sup>B NMR: –2.4 (s, 2B), –9.8 (b s, 8B).

**Synthesis of 1,7-Bis[(pyridin-2'-yl)methanol]-1,7-dicarba-*closo*-dodecaborane (**mCB-L1**).** The general procedure described by us for **oCB-L1** was followed,<sup>14d</sup> using *m*-carborane (200 mg, 1.38 mmol), *n*-BuLi (1.86 mL, 1.48 M in hexane, 2.76 mmol), THF (10 mL) and 2-

pyridinecarboxaldehyde (0.27 mL, 2.83 mmol), and an chloroform/liquid N<sub>2</sub> cooling bath (−63 °C). Work up gave a light yellow solid which was dried under a vacuum to afford a mixture of *syn*- and *anti*-**mCB-L1** (369.6 mg, 1.03 mmol, 79.3%), mp 145–150 °C. IR (ATR; selected bands):  $\nu$  3379 (OH), 2613, 2595, 2554 (BH). MALDI TOF: 359.10 [M + H]<sup>+</sup>. NMR of the diastereoisomer mixture in various solvents:

(*Ac-d<sub>6</sub>*). <sup>1</sup>H NMR: 8.51 (d, *J* = 3.0, 1H, C<sub>5</sub>H<sub>4</sub>N), 7.81 (td, *J* = 9.0 and 3.0, 1H, C<sub>5</sub>H<sub>4</sub>N), 7.42 (d, *J* = 6.0, 1H, C<sub>5</sub>H<sub>4</sub>N), 7.36 (td, *J* = 6.0 and 3.0, 1H, C<sub>5</sub>H<sub>4</sub>N), 5.40 (d, *J* = 6.0, 1H, OH), 4.96 (d, *J* = 6.0, 1H, CHOH). <sup>1</sup>H {<sup>11</sup>B} NMR (*Ac-D<sub>6</sub>*): Only signals due to B–H protons are given: 2.73 (br s, 2H), 2.19 (br s, 2H), 2.15 (br s, 3H), 1.88 (br s, 3H); <sup>11</sup>B NMR: −5.34 (br s, 2B), −10.61 (br s, 6B), −12.98 (br s, 2B). <sup>13</sup>C NMR: 160.17 (s, NC<sub>5</sub>H<sub>4</sub>), 148.99 (s, NC<sub>5</sub>H<sub>4</sub>), 137.42 (s, NC<sub>5</sub>H<sub>4</sub>), 124.43 (s, NC<sub>5</sub>H<sub>4</sub>), 122.83 (s, NC<sub>5</sub>H<sub>4</sub>), 82.45 (s, cluster Carbons), 75.31 (s, CHOH).

(*DMSO-d<sub>6</sub>*). <sup>1</sup>H NMR: 8.45 (d, *J* = 5.0 Hz, 2H, C<sub>5</sub>H<sub>4</sub>N), 7.80 (t, *J* = 7.4, 1.5, 2H, C<sub>5</sub>H<sub>4</sub>N), 7.35 (d, *J* = 8.0, 2H, C<sub>5</sub>H<sub>4</sub>N), 7.30 (dd, *J* = 7.5, 4.7, 2H, C<sub>5</sub>H<sub>4</sub>N), 6.50 (d, *J* = 5.7, 2H, OH), 4.80 (d, *J* = 5.3, 2H, CHOH). <sup>1</sup>H {<sup>11</sup>B} NMR: Only signals due to B–H protons are given: 2.60 (br s, 2H), 2.06 (br s, 6H), 1.79 (br s, 2H). −5.13 (br s, 2B), −10.66 (br s, 6B).

**Synthesis of [(*oCB-L1*)PdCl] ((*oCB-L1*)Pd).** *oCB-L1* (100 mg, 0.28 mmol) and PdCl<sub>2</sub>(MeCN)<sub>2</sub> (61 mg, 0.28 mmol) were dissolved in acetone (10 mL) in a capped vial. The reaction mixture was stirred under air at room temperature for 15 h. Then a yellowish precipitate was collected by centrifugation (6000 rpm, 10 min), washed with acetone (3 × 3 mL) to remove excess of starting materials, and dried under a vacuum to provide pure (*oCB-L1*)Pd (100 mg, 0.2 mmol, 71%) as a pale yellow solid; dec pt 283 °C. Elemental analysis calculated for C<sub>14</sub>B<sub>10</sub>H<sub>21</sub>N<sub>2</sub>O<sub>2</sub>ClPd·H<sub>2</sub>O: C 32.50%, H 4.48%, N 5.42%; found C 32.52%, H 4.20%, N 5.42%. MALDI-TOF, *m/z*: M: 462.45 [M – Cl-H]<sup>+</sup>. IR (ATR; selected bands):  $\nu$  3344, 3316 (OH), 2617, 2594, 2567, 2553 (BH). <sup>1</sup>H NMR (DMSO-*d<sub>6</sub>*):  $\delta$  = 8.92 (d, *J* = 4.9, 2H, NC<sub>5</sub>H<sub>4</sub>), 8.14 (t, *J* = 7.6, 2H, NC<sub>5</sub>H<sub>4</sub>), 7.90 (d, *J* = 7.3, 2H, NC<sub>5</sub>H<sub>4</sub>), 7.55 (t, *J* = 6.7, 2H, NC<sub>5</sub>H<sub>4</sub>), 7.45 (BR s, 2H, CHOH), 6.09 (BR s, 2H, CHOH); <sup>1</sup>H {<sup>11</sup>B} NMR (DMSO-*d<sub>6</sub>*): Only signals due to B–H protons are given: 2.75 (br s, 1H), 2.17 (br s, 3H), 1.86 (br s, 3H), 0.39 (br s, 2H); <sup>11</sup>B NMR (DMSO-*d<sub>6</sub>*): +10 to −20 (br m). <sup>13</sup>C NMR (DMSO-*d<sub>6</sub>*): 161.01 (s, NC<sub>5</sub>H<sub>4</sub>), 153.39 (s, NC<sub>5</sub>H<sub>4</sub>), 139.65 (s, NC<sub>5</sub>H<sub>4</sub>), 124.49 (s, NC<sub>5</sub>H<sub>4</sub>), 123.52 (s, NC<sub>5</sub>H<sub>4</sub>), 89.93 (s, CHOH), 72.37 (s, CHB<sub>10</sub>H<sub>9</sub>).

**Synthesis of [(*oCB-L2*)PdCl] ((*oCB-L2*)Pd).** The reaction procedure of (*oCB-L1*)Pd was followed, using *oCB-L2* (10 mg, 0.028 mmol), [PdCl<sub>2</sub>(MeCN)<sub>2</sub>] (6.1 mg, 0.028 mmol), and acetone (3 mL), under air at 55 °C for 50 h. Work up gave (*oCB-L2*)Pd as an impure white solid. Recrystallization from DMF gave single crystals suitable for X-ray diffraction measurements. MALDI-TOF, *m/z*: M: 491.52 [M]<sup>+</sup>. <sup>1</sup>H NMR (DMSO-*d<sub>6</sub>*): 8.02 (t, *J* = 7.8, 2H, C<sub>5</sub>H<sub>3</sub>N), 7.71 (d, *J* = 7.2, 2H, C<sub>5</sub>H<sub>3</sub>N), 7.51 (d, *J* = 7.3, 2H, C<sub>5</sub>H<sub>3</sub>N), 7.45 (br s, 2H, OH), 6.18 (br s, 2H, CHOH), 3.15 (s, 6H, CH<sub>3</sub>). <sup>1</sup>H {<sup>11</sup>B} NMR (DMSO-*d<sub>6</sub>*): Only signals due to B–H protons are given: 2.77–2.12 (br m, overlapped with residual solvent), 1.84 (br s, 3H), 0.24 (br s, 2H); <sup>11</sup>B NMR (DMSO-*d<sub>6</sub>*): −2.41 (br s, 10B) 5 to −20 (br m). <sup>13</sup>C NMR (DMSO-*d<sub>6</sub>*): 160.28 (s, C<sub>5</sub>H<sub>3</sub>N), 153.27 (s, C<sub>5</sub>H<sub>3</sub>N), 139.41 (s, C<sub>5</sub>H<sub>3</sub>N), 124.97 (s, C<sub>5</sub>H<sub>3</sub>N), 120.55 (s, C<sub>5</sub>H<sub>3</sub>N), 90.38 (s, cluster carbon), 71.89 (s, CHOH), 27.02 (s, CH<sub>3</sub>).

**Synthesis of [(*mCB-L1*)PdCl] ((*mCB-L1*)Pd).** The reaction procedure of (*oCB-L1*)Pd was followed, using *mCB-L1* (10 mg, 0.028 mmol), [PdCl<sub>2</sub>(MeCN)<sub>2</sub>] (6.1 mg, 0.028 mmol) and acetone (3 mL), under air at 55 °C for 2 h. Work up gave pure (*mCB-L1*)Pd (10.6 mg, 0.021 mmol, 76.1%) as a light yellow solid; dec pt 282 °C. Elemental analysis calculated for C<sub>14</sub>B<sub>10</sub>H<sub>21</sub>N<sub>2</sub>O<sub>2</sub>ClPd·DMF: C 35.67%, H 4.93%, N 7.34%; found C 35.76%, H 5.08%, N 7.10%. MALDI-TOF, *m/z*: M: 462.49 [M – Cl-H]<sup>+</sup>. IR (ATR; selected bands):  $\nu$  3412, 3178 (OH), 2603 (BH). <sup>1</sup>H NMR (DMSO-*d<sub>6</sub>*): 10.02, 9.91, 9.82, and 9.68 (d, *J* = 5.7, 2H, C<sub>5</sub>H<sub>3</sub>N for four diastereomers), 8.10–7.49 (m, 6H, C<sub>5</sub>H<sub>3</sub>N), 7.08, 7.07, 6.91, and 6.83 (d, *J* = 5.9, 2H, OH for four diastereomers), 5.14 (d, *J* = 5.9, 1H, CHOH for *anti*- or *syn*-**mCB-Pd1** isomer), 4.96 (d, *J* = 5.3, 1H,

CHOH for *syn*- or *anti*-**mCB-Pd1** isomer). <sup>11</sup>B NMR (DMSO-*d<sub>6</sub>*): −11.4 (br m). <sup>13</sup>C NMR (DMSO-*d<sub>6</sub>*): 162.24, 161.16, 160.96, 157.81, 155.76, 154.69, 139.74, 139.53, 139.40, 127.32, 124.22, 123.58, 122.88, 122.61 (s, NC<sub>5</sub>H<sub>4</sub>), 76.11, 75.74, 75.35, 74.47, 73.92, 73.75 (s, CHOH and CHB<sub>10</sub>H<sub>9</sub>).

**Suzuki Coupling with Arylboronic Acids in the Presence of (*oCB-L1*)Pd. General Procedure.** A screw-capped tube equipped with a magnetic stirrer bar was charged with the aryl- or benzyl bromide (1 mmol), arylboronic acid (1.5 mmol), potassium carbonate (276 mg, 2.0 mmol), and (*oCB-L1*)Pd (0.00049 mg, 10<sup>−6</sup> mmol) and distilled water (1 mL) at room temperature. This mixture was heated to 110 °C for 10 h under stirring, allowed to cool, and extracted with diethyl ether (4 × 5 mL). The combined organic extracts were dried over anhydrous sodium sulfate and evaporated *in vacuo* to give a residue that was purified by flash column chromatography using hexane:ethyl acetate as eluent. By this procedure the following biaryls and diarylmethanes were prepared:

**4-Acetyl-4'-methoxybiphenyl<sup>41</sup> (99%).** <sup>1</sup>H NMR (CDCl<sub>3</sub>)  $\delta$ : 2.63 (s, 3H), 3.86 (s, 3H), 7.01 (d, *J* = 8.8 Hz, 2H), 7.57 (d, *J* = 8.8 Hz, 2H), 7.65 (d, *J* = 8.4 Hz, 2H), 7.99 (d, *J* = 8.4 Hz, 2H). <sup>13</sup>C NMR (CDCl<sub>3</sub>)  $\delta$ : 26.6, 55.3, 114.4, 126.6, 128.3, 128.9, 132.2, 135.2, 145.3, 159.9, 197.7.

**4-Acetylbiphenyl<sup>42</sup> (99%).** <sup>1</sup>H NMR (CDCl<sub>3</sub>)  $\delta$ : 8.03 (d, *J* = 8.0 Hz, 2H), 7.68 (d, *J* = 8.0 Hz, 2H), 7.62 (d, *J* = 7.6 Hz, 2H), 7.47 (t, *J* = 7.6 Hz, 2H), 7.41 (d, *J* = 7.6 Hz, 1H), 2.65 (s, 3H). <sup>13</sup>C NMR (CDCl<sub>3</sub>)  $\delta$ : 197.7, 145.7, 139.8, 135.8, 128.9, 128.8, 128.2, 127.2, 127.1, 26.7.

**4-Methoxybiphenyl<sup>21</sup> (84%).** <sup>1</sup>H NMR (CDCl<sub>3</sub>)  $\delta$ : 7.56–7.51 (m, 4H), 7.41 (t, *J* = 7.6 Hz, 2H), 7.30 (t, *J* = 7.6 Hz, 1H), 6.98 (d, *J* = 7.2 Hz, 2H), 3.85 (s, 3H). <sup>13</sup>C NMR (CDCl<sub>3</sub>)  $\delta$ : 159.1, 140.8, 133.7, 128.7, 128.1, 126.7, 126.6, 114.2, 55.3.

**2-Chlorobiphenyl<sup>21</sup> (91%).** <sup>1</sup>H NMR (CDCl<sub>3</sub>)  $\delta$ : 7.48–7.38 (m, 6H), 7.36–7.26 (m, 3H). <sup>13</sup>C NMR (CDCl<sub>3</sub>)  $\delta$ : 140.5, 139.4, 132.5, 131.4, 129.9, 129.4, 128.5, 128.0, 127.6, 126.8.

**2-Chloro-3',4'-dimethoxy-1,1'-biphenyl<sup>43</sup> (77%).** <sup>1</sup>H NMR (CDCl<sub>3</sub>)  $\delta$ : 3.87, 3.89 (2s, 6H), 6.94 (d, *J* = 8.4 Hz, 1H), 7.08 (d, *J* = 2.0 Hz, 1H), 7.12 (dd, *J* = 8.2, 2.2 Hz, 1H), 7.39–7.52 (m, 4H). <sup>13</sup>C NMR (CDCl<sub>3</sub>)  $\delta$ : 148.6, 148.4, 140.3, 132.6, 132.1, 131.4, 130.0, 128.3, 126.8, 121.8, 112.9, 110.8, 56.0, 55.9.

**5-Chloro-2-methoxy-1,1'-biphenyl<sup>44</sup> (66%).** <sup>1</sup>H NMR (CDCl<sub>3</sub>)  $\delta$ : 7.52 (m, 2H), 7.37 (m, 5H), 6.92 (d, *J* = 8.4 Hz, 1H), 3.81 (s, 3H). <sup>13</sup>C NMR (CDCl<sub>3</sub>)  $\delta$ : 155.9, 155.1, 137.1, 132.4, 130.4, 129.3, 128.1, 128.05, 127.4, 125.7, 112.5.

**1-Benzyl-4-methoxybenzene<sup>45</sup> (82%).** <sup>1</sup>H NMR (CDCl<sub>3</sub>)  $\delta$ : 3.81 (s, 3H), 3.96 (s, 2H), 6.86 (d, *J* = 8.5 Hz, 2H), 7.18 (d, *J* = 8.5 Hz, 2H), 7.24–7.29 (m, 3H), 7.32 (t, *J* = 7.3 Hz, 2H). <sup>13</sup>C NMR (CDCl<sub>3</sub>)  $\delta$ : 41.2, 55.4, 114.0, 126.1, 128.6, 129.0, 130.0, 133.4, 141.7, 158.1.

**1-Benzyl-naphthalene<sup>46</sup> (99%).** <sup>1</sup>H NMR (CDCl<sub>3</sub>)  $\delta$ : 4.53 (s, 2H), 7.24–7.31 (m, 3H), 7.32–7.40 (m, 3H), 7.47–7.56 (m, 3H), 7.85 (d, *J* = 8.4 Hz, 1H), 7.91–9.97 (m, 1H), 8.05–8.12 (m, 1H). <sup>13</sup>C NMR (CDCl<sub>3</sub>)  $\delta$ : 39.2, 124.4, 125.7, 126.1, 126.2, 127.5, 127.5, 128.6, 128.8, 128.9, 132.3, 134.1, 136.8, 140.8.

**1-Benzyl-3,5-difluorobenzene<sup>47</sup> (87%).** <sup>1</sup>H NMR (CDCl<sub>3</sub>)  $\delta$ : 7.33 (tt, *J* = 8.2, 1.6 Hz, 2H), 7.25 (tt, *J* = 6.2, 1.4 Hz, 1H), 7.20–7.17 (m, 2H), 6.74–6.68 (m, 2H), 6.65 (tt, *J* = 9.0, 2.3 Hz, 1H), 3.96 (s, 2H). <sup>13</sup>C NMR (CDCl<sub>3</sub>)  $\delta$ : 163.0 (dd, *J*<sub>C–F</sub> = 248.0, 12.9 Hz), 145.0 (t, *J*<sub>C–F</sub> = 8.9 Hz), 139.4, 128.9, 128.7, 126.6, 111.6 (dd, *J*<sub>C–F</sub> = 18.4, 6.5 Hz), 101.6 (t, *J*<sub>C–F</sub> = 25.4 Hz), 41.6 (t, *J*<sub>C–F</sub> = 1.9 Hz). <sup>19</sup>F NMR (376 MHz, CDCl<sub>3</sub>)  $\delta$ : −110.3 (m, 2F)

**4-Benzyl-1,2-dimethoxybenzene<sup>48</sup> (99%).** <sup>1</sup>H NMR (CDCl<sub>3</sub>)  $\delta$ : 3.84–3.87 (2 s, 6H), 3.96 (s, 3H), 6.74–6.83 (m, 3H), 7.20–7.34 (m, 5H). <sup>13</sup>C NMR (CDCl<sub>3</sub>)  $\delta$ : 41.4, 55.7, 55.8, 111.1, 111.2, 112.2, 120.7, 120.8, 125.9, 128.3, 128.6, 133.5, 141.2, 147.3, 148.8.

**Suzuki Coupling with Potassium Phenyltrifluoroborate in the Presence of (*oCB-L1*)Pd. General Procedure.** A screw-capped tube equipped with a magnetic stirrer bar was charged with the aryl bromide (1 mmol), potassium phenyltrifluoroborate (276 mg, 1.5 mmol), potassium carbonate (276 mg, 2.0 mmol), and (*oCB-L1*)Pd (0.00049 mg, 10<sup>−6</sup> mmol) and distilled water (1 mL) at room temperature. This mixture was heated to 110 °C for 10 h under



stirring, allowed to cool, and extracted with diethyl ether ( $4 \times 5$  mL). The combined organic extracts were dried over anhydrous sodium sulfate and evaporated *in vacuo* to give a residue which was purified by flash column chromatography using hexane:ethyl acetate as eluent. By this procedure the following biaryls were prepared:

- 4-Acetylbiphenyl (99%)
- 4-Methoxybiphenyl (92%)
- 2-Chloridebiphenyl (97%)
- 5-Chloro-2-methoxy-1,1'-biphenyl (61%)

**Suzuki Coupling with Arylboronic Acids in the Presence of *m*CB-Pd1. General Procedure.** A screw-capped tube equipped with a magnetic stirrer bar was charged with the aryl- or benzyl bromide (1 mmol), arylboronic acid (1.5 mmol), potassium carbonate (276 mg, 2.0 mmol), and (*m*CB-L1)Pd (0.0005 mg,  $10^{-6}$  mmol) and distilled water (1 mL) at room temperature. This mixture was heated to 110 °C for 10 h under stirring, allowed to cool, and extracted with diethyl ether ( $4 \times 5$  mL). The combined organic extracts were dried over anhydrous sodium sulfate and evaporated *in vacuo* to give a residue which was purified by flash column chromatography using hexane/ethyl acetate as eluent. By this procedure the following biaryls and diarylmethanes were prepared:

- 4-Acetyl-4'-methoxybiphenyl (60%)
- 4-Acetylbiphenyl (85%)
- 4-Methoxybiphenyl (90%)
- 2-Chloridebiphenyl (5%)
- 2-Chloro-3',4'-dimethoxy-1,1'-biphenyl (20%)
- 5-Chloro-2-methoxy-1,1'-biphenyl (56%)
- 1-Benzyl-4-methoxybenzene (99%)
- 1-Benzyl-naphthalene (99%)
- 1-Benzyl-3,5-difluorobenzene (95%)
- 4-Benzyl-1,2-dimethoxybenzene (99%)

**Suzuki Coupling with Potassium Phenyltrifluoroborate in the Presence of (*m*CB-L1)Pd. General Procedure.** A screw-capped tube equipped with a magnetic stirrer bar was charged with the aryl bromide (1 mmol), potassium phenyltrifluoroborate (276 mg, 1.5 mmol), potassium carbonate (276 mg, 2.0 mmol), and (*m*CB-L1)Pd (0.0005 mg,  $10^{-6}$  mmol) and distilled water (1 mL) at room temperature. This mixture was heated to 110 °C for 10 h under stirring, allowed to cool, and extracted with diethyl ether ( $4 \times 5$  mL). The combined organic extracts were dried over anhydrous sodium sulfate and evaporated *in vacuo* to give a residue which was purified by flash column chromatography using hexane:ethyl acetate as eluent. By this procedure the following biaryls were prepared:

- 4-Acetylbiphenyl (93%)
- 4-Methoxybiphenyl (60%)
- 2-Chloridebiphenyl (69%)
- 5-Chloro-2-methoxy-1,1'-biphenyl (54%)

**Single Crystal Studies.** Crystals of (*o*CB-L1)Pd, (*o*CB-L2)Pd, and (*m*CB-L1)Pd were kept under inert conditions and immersed in perfluoropolyether as protecting oil for manipulation. A suitable size crystal was mounted on a MiTeGen Micromount, and this sample was used for data collection. Data were collected with a Bruker D8 Venture diffractometer (MoK $\alpha$ , 100 K). Data were processed with APEX2<sup>49</sup> suite and corrected for absorption using SADABS.<sup>50</sup> The structure was solved by direct methods,<sup>51</sup> which revealed the position of all non-hydrogen atoms. These atoms were refined on F<sup>2</sup> by a full-matrix least-squares procedure using anisotropic displacement parameters.<sup>49</sup> All hydrogen atoms were located in difference Fourier maps, except those corresponding to C–H groups which were placed geometrically, and included as fixed contributions riding on attached atoms with isotropic thermal displacement parameters 1.2 (C–H, B–H) or 1.5 (O–H, methyl) times those of the respective bonded atom. The structures of *o*CB-Pd2 and *m*CB-L1 exhibit disorder of the OH groups, which was successfully refined using a two-site model with 0.863:0.137 and 0.731:0.269 occupancies for *o*CB-Pd2 and *m*CB-L1, respectively. Thermal parameter constraints were applied. The crystal of *m*CB-L1 is a nonmerohedral twin with a minor component of 12.37%. The twin law describes a rotation of 180° around the [1  $\bar{1}$  0] direction, given by

the matrix (0.109 -0.887 0, -1.114 -0.109 0, 0 -0.014 -1). Absorption correction was applied using TWINABS.<sup>52</sup>

## ■ ASSOCIATED CONTENT

### § Supporting Information

Spectroscopic and crystallographic data. DFT functional calibration, atomic charges, and optimized geometries. This material is available free of charge via the Internet at <http://pubs.acs.org>.

## ■ AUTHOR INFORMATION

### Corresponding Author

\*E-mail: [jginerplanas@icmab.es](mailto:jginerplanas@icmab.es).

### Notes

The authors declare no competing financial interest.

## ■ ACKNOWLEDGMENTS

We thank CICYT (Projects CTQ2010-16237 and CTQ2011-23336) and Generalitat de Catalunya (2009/SGR/00279) for financial support. M.Y.T. is enrolled in the UAB Ph.D. program. The project "Factoría de Cristalización, CONSOLIDER INGENIO-2010" provided X-ray structural facilities for this work. The evaluation of the catalytic activity was supported by the Basque Government (IT-774-13 and S-PC13UN018), the Spanish Ministry of Science and Innovation (CTQ2010-20703), and the University of the Basque Country (UFI QOSYC 11/12). N.C. thanks the Basque Government for a predoctoral scholarship. The authors also thank Petronor, S.A. for a generous donation of hexane.

## ■ REFERENCES

- (1) See for example: (a) Selander, N.; Szabó, K. J. *Chem. Rev.* **2011**, *111*, 2048. (b) Moreno, I.; SanMartin, R.; Inés, B.; Churrua, F.; Domínguez, E. *Inorg. Chim. Acta* **2010**, *363*, 1903. (c) *The Chemistry of Pincer Compounds*; Morales-Morales, D., Jensen, C. M., Eds.; Elsevier: Amsterdam, 2007. (d) van der Boom, M.; Milstein, D. *Chem. Rev.* **2003**, *103*, 1759. (e) Albrecht, M.; van Koten, G. *Angew. Chem., Int. Ed.* **2001**, *40*, 3750.
- (2) (a) Moulton, C. J.; Shaw, B. L. *J. Chem. Soc., Dalton Trans.* **1976**, 1020. (b) Poverenov, E.; Efremenko, I.; Frenkel, A. I.; Ben-David, Y.; Shimon, L. J. W.; Leitus, G.; Konstantinovski, L.; Martin, J. M. L.; Milstein, D. *Nature* **2008**, *455*, 1093. (c) Schuster, E. M.; Botoshansky, M.; Gandelman, M. *Angew. Chem., Int. Ed.* **2008**, *47*, 4555. (d) Goldman, A. S.; Roy, A. H.; Huang, Z.; Ahuja, R.; Schinski, W.; Brookhart, M. *Science* **2006**, *312*, 257.
- (3) (a) Liang, L. C. *Coord. Chem. Rev.* **2006**, *250*, 1152. (b) Fan, L.; Foxman, B. M.; Ozerov, O. V. *Organometallics* **2004**, *23*, 326. (c) Fryzuk, M. D. *Can. J. Chem.* **1992**, *70*, 2839.
- (4) (a) Dixon, L. S. H.; Hill, A. F.; Sinha, A.; Ward, J. S. *Organometallics* **2014**, *33*, 653. (b) Korshin, E. E.; Leitus, G.; Shimon, L. J. W.; Konstantinovski, L.; Milstein, D. *Inorg. Chem.* **2008**, *47*, 7177. (c) MacInnis, M. C.; MacLean, D. F.; Lundgren, R. J.; MacDonald, R.; Turculet, L. *Organometallics* **2007**, *26*, 6522. (d) Sangtrirunugul, P.; Tilley, T. D. *Organometallics* **2007**, *26*, 5557.
- (5) Mankad, N. P.; Rivard, E.; Harkins, S. B.; Peters, J. C. *J. Am. Chem. Soc.* **2005**, *127*, 16032.
- (6) Teixidor, F.; Romerosa, A.; Viñas, C.; Rius, J.; Miravittles, C.; Casabó, J. J. *Chem. Soc. Chem. Commun.* **1991**, 192.
- (7) Segawa, Y.; Yamashita, M.; Nozaki, K. *J. Am. Chem. Soc.* **2009**, *131*, 9201.
- (8) Spokoiny, A. M.; Reuter, M. G.; Sterm, C. L.; Ratner, M. A.; Seideman, T.; Mirkin, C. A. *J. Am. Chem. Soc.* **2009**, *131*, 9482.
- (9) (a) Spokoiny, A. M. *Pure Appl. Chem.* **2013**, *85*, 903. (b) Kameo, H.; Nakazawa, H. *Chem.—Asian J.* **2013**, *8*, 1720. (c) van der Vlugt, J. I. *Angew. Chem., Int. Ed.* **2010**, *49*, 252.

- (10) El-Zaria, M. E.; Arii, H.; Nakamura, H. *Inorg. Chem.* **2011**, *50*, 4149.
- (11) (a) Grimes, R. N. *Carboranes*, 2nd ed; Elsevier: Amsterdam, 2011). (b) Scholz, M.; Hey-Hawkins, E. *Chem. Rev.* **2011**, *111*, 7035. (c) Chizhevsky, I. T. *Coord. Chem. Rev.* **2007**, *251*, 1590. (d) Teixidor, F.; Viñas, C. In *Science of Synthesis*; Thieme: Stuttgart, 2005; Vol. 6, p 1235. (e) Xie, Z. *Acc. Chem. Res.* **2003**, *36*, 1. (f) Valliant, J. F.; Guenther, K. J.; King, A. S.; Morel, P.; Schaffer, P.; Sogbein, O. O.; Stephensen, K. *Coord. Chem. Rev.* **2002**, *232*, 173. (g) Hawthorne, M. F.; Zheng, Z.-P. *Acc. Chem. Res.* **1997**, *30*, 267. (h) Plešek, J. *Chem. Rev.* **1992**, *92*, 269. (i) Bregadze, V. I. *Chem. Rev.* **1992**, *92*, 209.
- (12) Hermansson, K.; Wójcik, M.; Sjöberg, S. *Inorg. Chem.* **1999**, *38*, 6039.
- (13) (a) Spokoynny, A. M.; Machan, C. W.; Clingerman, D. J.; Rosen, M. S.; Wiester, M. J.; Kennedy, R. D.; Stern, C. L.; Sarjeant, A. A.; Mirkin, C. A. *Nat. Chem.* **2011**, *3*, 590. (b) Teixidor, F.; Barberà, G.; Vaca, A.; Kivekäs, R.; Sillanpää, R.; Oliva, J.; Viñas, C. *J. Am. Chem. Soc.* **2005**, *127*, 10158.
- (14) (a) Terrasson, V.; Planas, J. G.; Prim, D.; Viñas, C.; Teixidor, F.; Light, M. E.; Hursthouse, M. B. *J. Org. Chem.* **2008**, *73*, 9140. (b) Terrasson, V.; García, Y.; Farràs, P.; Teixidor, F.; Viñas, C.; Planas, J. G.; Prim, D.; Light, M. E.; Hursthouse, M. B. *CrystEngComm* **2010**, *12*, 4109. (c) Di Salvo, F.; Planas, J. G.; Camargo, B.; García, Y.; Teixidor, F.; Viñas, C.; Light, M. E.; Hursthouse, M. B. *CrystEngComm* **2011**, *13*, 5788. (d) Di Salvo, F.; Paterakis, C.; Tsang, M. T.; Viñas, C.; Teixidor, F.; Planas, J. G.; Light, M. E.; Hursthouse, M. B.; Choquesillo-Lazarte, D. *Cryst. Growth Des.* **2013**, *13*, 1473–1484.
- (15) (a) Di Salvo, F.; Tsang, M. Y.; Teixidor, F.; Viñas, C.; Planas, J. G.; Crassous, J.; Vanthuyne, N.; Aliaga-Alcalde, N.; Ruiz, E.; Clevers, S.; Dupray, V.; Choquesillo-Lazarte, D.; Light, M. E.; Hursthouse, M. B. *Chem.—Eur. J.* **2014**, *20*, 1081–1090. (b) Di Salvo, F.; Teixidor, F.; Viñas, C.; Planas, J. G. *Z. Anorg. Allg. Chem.* **2013**, *639*, 1194. (c) Di Salvo, F.; Teixidor, F.; Viñas, C.; Planas, J. G.; Light, M. E.; Hursthouse, M. B.; Aliaga-Alcalde, N. *Cryst. Growth Des.* **2012**, *12*, 5720.
- (16) Albrecht, M.; van Koten, G. *Angew. Chem., Int. Ed.* **2001**, *40*, 3750.
- (17) Yaho, Z.-J.; Yu, W.-B.; Lin, Y.-J.; Huang, S.-L.; Li, Z. H.; Jin, G.-X. *J. Am. Chem. Soc.* **2014**, *136*, 2825.
- (18) Selected examples of NC<sub>aryl</sub>N-pincer palladium: (pyrido[2',3':5,6]naphtho[2,3-h]quinolin-14-yl)PdCl, Pd–Cl 2.4304(17) Å, Young, K. J. H.; Bu, X.; Kaska, W. C. *J. Organomet. Chem.* **2011**, *696*, 3992–3997. (2-(pyridin-2-yl)-6-(pyridin-2-yl)sulfanyl)phenyl)PdCl, Pd–Cl 2.4191(6) Å, Hirotsu, M.; Tsukahara, Y.; Kinoshita, I. *Bull. Chem. Soc. Jpn.* **2010**, *83*, 1058. (2,6-bis(2,6-dimethyl-5,6,7,8-tetrahydro-5,7-methanoquinolin-2-yl)phenyl)PdCl, Pd–Cl 2.451(1) Å, Soro, B.; Stoccoro, S.; Minghetti, G.; Zucca, A.; Cinellu, M. A.; Manassero, M.; Gladiali, S. *Inorg. Chim. Acta* **2006**, *359*, 1879–1888. (2,6-bis(2-pyridyl)phenyl)PdCl, Pd–Cl 2.427(1) Å, Soro, B.; Stoccoro, S.; Minghetti, G.; Zucca, A.; Cinellu, M. A.; Gladiali, S.; Manassero, M.; Sansoni, M. *Organometallics* **2005**, *24*, 53–61. (4-bromo-2,6-bis(7-azaindolyl)phenyl)PdCl, Pd–Cl 2.3867(16) Å, Song, D.; Wu, Q.; Hook, A.; Kozin, I.; Wang, S. *Organometallics* **2001**, *20*, 4683–4689.
- (19) Selected examples of NC<sub>alkyl</sub>N-pincer palladium: (3,5-Bu<sub>2</sub>pz)<sub>2</sub>PdCl(Me), Pd–Cl 2.5165(9) Å, Li, K.; Darkwa, J.; Guzei, I. A.; Mapolie, S. F. *J. Organomet. Chem.* **2002**, *660*, 108–115. (N-N')(h<sup>2</sup>-olefin)PdCl(Me), Pd–Cl 2.492(1) Å, Albano, V. G.; Casterllari, C. *Organometallics* **1990**, *9*, 1269–1276.
- (20) Intermolecular O–H...Cl hydrogen bonding for (oCB-L2)Pd and (mCB-L1)Pd have to be considered carefully due to the disorders in OH position and as a consequence of the disatereoisomeric mixtures. See SI for details.
- (21) Marzari, N.; Mostofi, A. A.; Yates, J. R.; Souza, I.; Vanderbilt, D. *Rev. Mod. Phys.* **2012**, *84*, 1419.
- (22) Alber, F.; Folkers, G.; Carloni, P. *J. Phys. Chem. B* **1999**, *103*, 6121.
- (23) Abu-Farsakh, H.; Qteish, A. *Phys. Rev. B* **2007**, *75*, 085201.
- (24) Sit, P. H. L.; Zipoli, F.; Chen, J.; Car, R.; Cohen, M. H.; Selloni, A. *Chem.—Eur. J.* **2011**, *17*, 12136.
- (25) Vidossich, P.; Lledos, A. *Dalton Trans.* **2014**, *43*, 11145–11151.
- (26) Glendening, E. D.; Landis, C. R.; Weinhold, F. *WIREs Comput. Mol. Sci.* **2012**, *2*, 1.
- (27) For an account on the relevance and widespread use of Suzuki coupling in academic, industrial research and bulky production, see: Martin, R.; Buchwald, S. L. *Acc. Chem. Res.* **2008**, *41*, 1461–1473.
- (28) See for example: *Palladium-Catalyzed Coupling Reactions: Practical Aspects and Future Developments*; Molnar, A., Ed.; Wiley: Weinheim, 2013.
- (29) (a) Beletskaya, I. P.; Cheprakov, A. V. *J. Organomet. Chem.* **2004**, *689*, 4055–4082. (b) Bolliger, J. L.; Blacque, O.; Frech, C. M. *Angew. Chem., Int. Ed.* **2007**, *46*, 6514–6517. (c) Inés, B.; SanMartin, R.; Moure, M. J.; Dominguez, E. *Adv. Synth. Catal.* **2009**, *351*, 2124–2132. (d) Rao, G. K.; Kumar, A.; Ahmedz, J.; Singh, A. K. *Chem. Commun.* **2010**, *46*, 5954–5956.
- (30) VandeVondele, J.; Krack, M.; Mohamed, F.; Parrinello, M.; Chassaing, T.; Hutter, J. *Comput. Phys. Commun.* **2005**, *167*, 103.
- (31) Perdew, J. P.; Burke, K.; Ernzerhof, M. *Phys. Rev. Lett.* **1996**, *77*, 3865.
- (32) Lippert, G.; Hutter, J.; Parrinello, M. *Mol. Phys.* **1997**, *92*, 477.
- (33) VandeVondele, J.; Hutter, J. Gaussian basis sets for accurate calculations on molecular systems in gas and condensed phases. *J. Chem. Phys.* **2007**, *127*, (11).
- (34) Goedecker, S.; Teter, M.; Hutter, J. *Phys. Rev. B* **1996**, *54*, 1703.
- (35) Hartwigsen, C.; Goedecker, S.; Hutter, J. *Phys. Rev. B* **1998**, *58*, 3641.
- (36) Krack, M. *Theor. Chem. Acc.* **2005**, *114*, 145.
- (37) VandeVondele, J.; Hutter, J. *J. Chem. Phys.* **2003**, *118*, 4365.
- (38) Genovese, L.; Deutsch, T.; Neelov, A.; Goedecker, S.; Beylkin, G. *J. Chem. Phys.* **2006**, *125*, 074105.
- (39) Berghold, G.; Mundy, C. J.; Romero, A. H.; Hutter, J.; Parrinello, M. *Phys. Rev. B* **2000**, *61*, 10040.
- (40) Bader, R. F. W. *Acc. Chem. Res.* **1985**, *18*, 9.
- (41) Liu, Q.-X.; Zhang, W.; Zhao, X.-J.; Zhao, Z.-X.; Shi, M.-C.; Wang, X.-G. *Eur. J. Org. Chem.* **2013**, 1253–1261.
- (42) Zhou, W.-J.; Wang, K.-H.; Wang, J.-X.; Huang, D.-F. *Eur. J. Org. Chem.* **2010**, 416–419.
- (43) McLean, M. R.; Bauer, U.; Amaro, A. R.; Robertson, L. W. *Chem. Res. Toxicol.* **1996**, *9*, 158–164.
- (44) Bolliger, J. L.; Frecha, C. M. *Adv. Synth. Catal.* **2010**, *352*, 1075–1080.
- (45) Molander, G. A.; Elia, M. D. *J. Org. Chem.* **2006**, *71*, 9198–9202.
- (46) McLaughlin, M. *Org. Lett.* **2005**, *7*, 4875–4878.
- (47) Burns, M. J.; Fairlamb, I. J. S.; Kapdi, A. R.; Sehna, P.; Taylor, R. J. K. *Org. Lett.* **2007**, *9*, 5397–5400.
- (48) Tsuchimoto, T.; Tobita, K.; Hiyama, T.; Fukazawa, S. *J. Org. Chem.* **1997**, *62*, 6997–7005.
- (49) Bruker, APEX2 Software, V2012.2; Bruker AXS Inc.: Madison, WI, 2012.
- (50) Sheldrick, G. M. *SADABS, Program for Empirical Absorption Correction of Area Detector Data*; University of Göttingen: Göttingen, Germany, 2012.
- (51) Sheldrick, G. M. *Acta Crystallogr.* **2008**, *A64*, 112.
- (52) Sheldrick, G. M. *TWINABS*; University of Göttingen, Germany, 2012.

## Coordination Chemistry

A Racemic and Enantiopure Unsymmetric Diiron(III) Complex with a Chiral *o*-Carborane-Based Pyridylalcohol Ligand: Combined Chiroptical, Magnetic, and Nonlinear Optical Properties

Florencia Di Salvo,<sup>[a, b]</sup> Min Ying Tsang,<sup>[a]</sup> Francesc Teixidor,<sup>[a]</sup> Clara Viñas,<sup>[a]</sup> José Giner Planas,<sup>\*[a]</sup> Jeanne Crassous,<sup>[c]</sup> Nicolas Vanthuyne,<sup>[d]</sup> Núria Aliaga-Alcalde,<sup>[e]</sup> Eliseo Ruiz,<sup>[f]</sup> Gerard Coquerel,<sup>[g]</sup> Simon Clevers,<sup>[g]</sup> Valerie Dupray,<sup>[g]</sup> Duane Choquesillo-Lazarte,<sup>[h]</sup> Mark E. Light,<sup>[i]</sup> and Michael B. Hursthouse<sup>[i, j]</sup>

**Abstract:** The design of molecule-based systems combining magnetic, chiroptical and second-order optical nonlinear properties is still very rare. We report an unusually unsymmetric diiron(III) complex **1**, in which three bulky chiral carboranylpyridinealkoxide ligands (*o*CBhmp<sup>-</sup>) bridge both metal ions and the complex shows the above-mentioned properties. The introduction of *o*-carborane into the 2-(hydroxymethyl)pyridine (hmpH) architecture significantly alters the coordination of the simple or aryl-substituted 2-hmpH. The unusual architecture observed in **1** seems to be trig-

gered by the poor nucleophilicity of our alkoxide ligand (*o*CBhmp<sup>-</sup>). A very rare case of spontaneous resolution takes place on precipitation or exposure to solvent vapor for the bulk compound, as confirmed by a combination of single-crystal and powder X-ray diffraction, second-harmonic generation, and circular dichroism. The corresponding enantiopure complexes (+)**1** and (-)**1** have also been synthesized and fully characterized. This research provides a new building block with unique geometry and electronics to construct coordination complexes with multifunctional properties.

## Introduction

The introduction of chirality into coordination compounds has attracted much attention due to their applications in such areas as enantioselective separation, catalysis, nonlinear optics, sensors, and chiral switches.<sup>[1]</sup> Of particular interest is the combination of several properties within the same chiral molecule to reveal fascinating effects, such as magnetochirality.<sup>[2]</sup> New synthetic strategies to achieve chiral coordination compounds

with unprecedented architectures and combinations of properties are, therefore, in high demand for the development of novel chiral materials. In particular, N,O ligands, such as (hydroxymethyl)pyridines (hmpH; Scheme 1), have proved to be successful building blocks for the self-assembly of metallo-supramolecular architectures with exciting physical properties.<sup>[3]</sup> However, only achiral hmpH ligands have been employed in coordination compounds. We have recently described the synthesis and molecular and supramolecular char-

[a] Dr. F. Di Salvo, M. Y. Tsang, Prof. Dr. F. Teixidor, Prof. Dr. C. Viñas, Dr. J. G. Planas  
Institut de Ciència de Materials de Barcelona (ICMAB-CSIC)  
Campus U.A.B. 08193 Bellaterra (Spain)  
E-mail: jginerplanas@icmab.es

[b] Dr. F. Di Salvo  
Departamento de Química Inorgánica, Analítica, y Química Física  
Facultad de Ciencias Exactas y Naturales, Universidad de Buenos Aires  
INQUIMAE-CONICET, Ciudad Universitaria  
Pabellón 2, C1428EHA Buenos Aires (Argentina)

[c] Dr. J. Crassous  
Institut des Sciences Chimiques de Rennes  
Campus de Beaulieu, UMR 6226 CNRS  
Université de Rennes 1, 35042 Rennes Cedex (France)

[d] Dr. N. Vanthuyne  
Aix Marseille Université, Centrale Marseille, CNRS  
iSm2 UMR 7313, 13397 Marseille (France)

[e] Prof. Dr. N. Aliaga-Alcalde  
Institució Catalana de Recerca i Estudis Avançats (ICREA)  
Institut de Ciència de Materials de Barcelona (ICMAB-CSIC)  
Campus de la UAB, 08193 Bellaterra (Spain)

[f] Prof. Dr. E. Ruiz  
Departament de Química Inorgànica and  
Institut de Recerca de Química Teòrica i Computacional  
Universitat de Barcelona, Diagonal 647, 08028 (Spain)

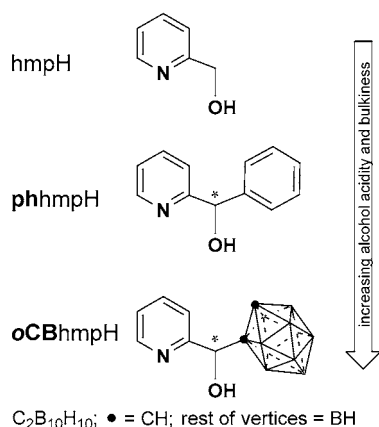
[g] Prof. Dr. G. Coquerel, Dr. S. Clevers, Dr. V. Dupray  
Unité de Cristallogénèse, Sciences et Méthodes Séparatives (SMS)  
UPRES EA 3233, IRCOF IMR 4114, Université de ROUEN  
Rue Tesnière, F-76821 Mont Saint-Aignan Cedex (France)

[h] Dr. D. Choquesillo-Lazarte  
Laboratorio de Estudios Cristalográficos  
IACT-CSIC, Armilla, Granada (Spain)

[i] Dr. M. E. Light, Prof. Dr. M. B. Hursthouse  
School of Chemistry, University of Southampton  
Highfield, Southampton. UK SO17 1BJ (UK)

[j] Prof. Dr. M. B. Hursthouse  
Department of Chemistry, Faculty of Science  
King Abdulaziz University, Jeddah 21588 (Saudi Arabia)

Supporting information for this article is available on the WWW under <http://dx.doi.org/10.1002/chem.201303037>.



Scheme 1. 2-(Hydroxymethyl)pyridine (hmpH)-related ligands.

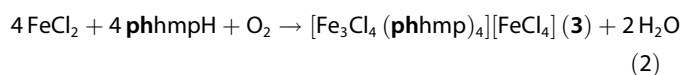
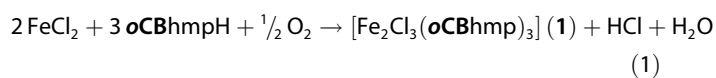
acterization of a series of chiral nitrogenated aromatic carboranyl alcohols, such as (*o*-carboranyl)(2-hydroxymethyl)pyridine (**oCBhmpH**; shown in Scheme 1).<sup>[4]</sup> These new compounds, which are prepared in very good yields from one-pot reactions in racemic form, can be regarded as a hmpH ligand in which one of the H atoms at the CH<sub>2</sub> position of the alcohol arm has been replaced by an *o*-carboranyl fragment (*closo*-1,2-C<sub>2</sub>B<sub>10</sub>H<sub>11</sub>) to give *o*-carboranyl-hmpH (**oCBhmpH**; Scheme 1). The icosahedral *closo* carboranes (dicarba-*closo*-dodecaboranes; C<sub>2</sub>B<sub>10</sub>H<sub>12</sub>) are an interesting class of exceptionally stable boron-rich clusters that can be modified at different vertices through chemical reactions.<sup>[5]</sup> The high thermal and chemical stability, hydrophobicity, acceptor character, and three-dimensional nature of the icosahedral carborane clusters make these new molecules valuable ligands in coordination chemistry. The average size of the *o*-carborane (148 Å<sup>3</sup>) is comparable to that of adamantane (136 Å<sup>3</sup>) and is significantly larger (40%) than the phenyl ring rotation envelope (102 Å<sup>3</sup>).<sup>[6]</sup> Regarding the electronic effect, *o*-carborane behaves as a strong electron-withdrawing group (similar to fluorinated aryl) on a substituent at one of the cluster carbons.<sup>[6,7]</sup> Thus, introduction of *o*-carborane into the hmpH backbone is expected to exert a higher decrease of the alcohol p*K*<sub>a</sub> value with respect to the related phenyl-hmpH (**phhmpH**) derivative (Scheme 1). On the other hand, introduction of *o*-carborane leads to an increase in the size and hydrophobicity of **oCBhmpH** with respect to **phhmpH**. Importantly, the alterations provoked by the introduction of *o*-carborane into hmpH cannot be considered individually because usually a number of properties are influenced simultaneously. For example, we have recently published our first results on the metallosupramolecular chemistry of **oCBhmpH** with cobalt, which gives a rare example of an anti-ferromagnetic complex with porous channels.<sup>[8]</sup> The porosity in this complex seems to be triggered by the self-assembly of staggered carborane fragments along hydrogen-bonding networks. It also appears that the chirality in conjunction with the bulky carborane favors *RR/SS* alternation in the supramolecular chains as a more compact packing arrangement.

Following our previous results, the next challenge is to resolve the enantiomers of our ligand or the related metal complexes with the expectation that novel properties would add to those found in the racemic complexes.<sup>[8]</sup> Herein, we focus our interest on iron complexes. Although iron is inexpensive, non-toxic, very abundant, and environmental friendly, known chiral enantiopure iron-based molecular materials are very limited.<sup>[9]</sup> We now report the synthesis of a dinuclear chiral iron complex, both in racemic and enantiopure forms, with unusual asymmetry triggered by the *o*-carborane-based ligand **oCBhmpH** and compared with the corresponding phenyl-hmpH (**phhmpH**) derivative. Structural, chiroptical, and magnetic properties of the **oCBhmpH** complexes are reported and discussed. Molecular materials that combine magnetic, chiroptical, and second-order optical nonlinear properties are still very rare.<sup>[10]</sup>

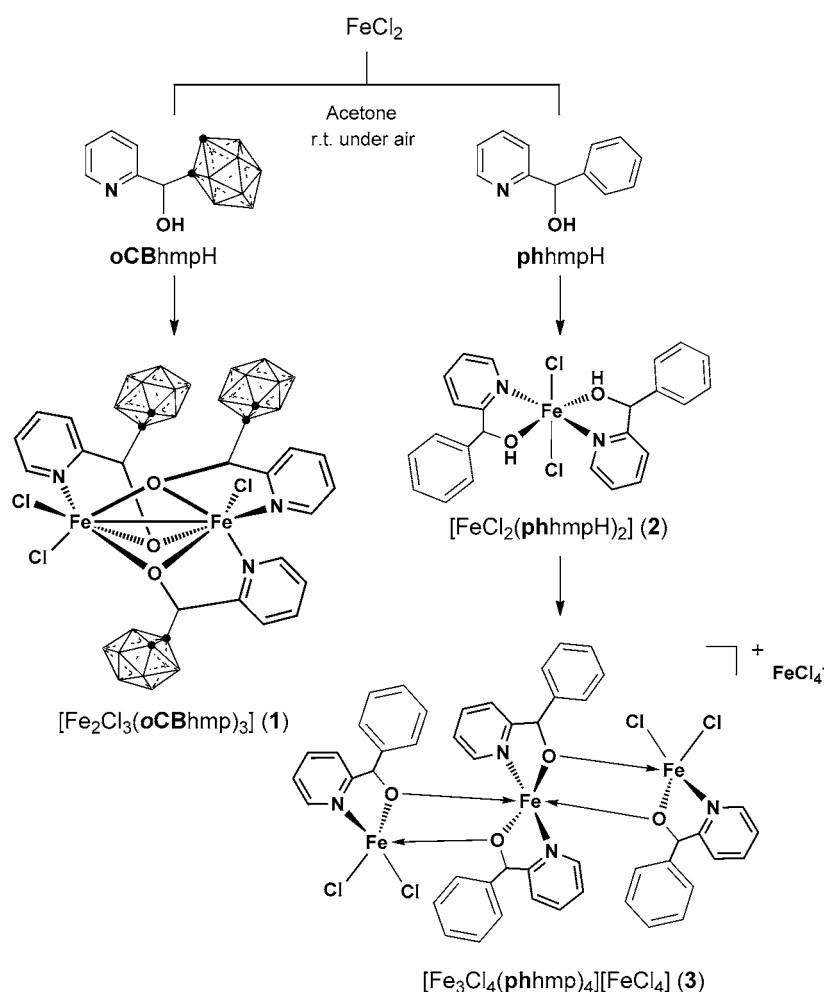
## Results and Discussion

The reaction of **oCBhmpH** with FeCl<sub>2</sub> in a 1.5:1 ratio in acetone gave a clear yellowish golden solution from which the Fe<sup>III</sup> complex [Fe<sub>2</sub>Cl<sub>3</sub>(**oCBhmp**)<sub>3</sub>] (**1**) was subsequently isolated in nearly quantitative yield (Scheme 2). Small variations in the Fe<sup>II</sup>/**oCBhmpH** ratio also gave complex **1**. When the same reaction was carried out with the phenyl-modified ligand **phhmpH**, initial formation of the mononuclear Fe<sup>II</sup> complex [FeCl<sub>2</sub>(**phhmpH**)<sub>2</sub>] (**2**) was observed, followed by its conversion to the trinuclear Fe<sup>III</sup> complex [Fe<sub>3</sub>Cl<sub>4</sub>(**phhmp**)<sub>4</sub>][FeCl<sub>4</sub>] (**3**). A comparison of the reactions with **oCB**- and **phhmpH** is shown in Scheme 2.

Clearly, Fe<sup>III</sup> complexes **1** and **3** are the preferred products of the reactions under these conditions. The stability of complex **3** is further confirmed in a recent report in which its formation was shown by hydrolysis and reduction of the related phenylpyridine-2-yl-methanone oxime ligand in the presence of FeCl<sub>3</sub> under solvothermal conditions.<sup>[11]</sup> We have confirmed the structure of **3** by using single-crystal X-ray diffraction (XRD) studies (Figure S11 in the Supporting Information) and the phase purity of the final product by using elemental analysis. The formation of these complexes is summarized in Equations (1) and (2), assuming atmospheric O<sub>2</sub> is the oxidizing agent.



Note that no base is added to abstract the alcohol protons in these two related ligands. However, in the final complexes (**1** and **3**) the ligands are both deprotonated. An increasing tendency to deprotonation of alcohols upon coordination is expected with increasing hardness of the metal ion.<sup>[12]</sup> Group 7 and 8 transition metals are in an intermediate situation in which either protonated or deprotonated coordinated alcohols



Scheme 2.

are found. It is in these intermediate situations that the acidity of the alcohols might make a difference. As previously mentioned, our carborane-based ligand **oCBhmpH** is expected to be more acidic than the related **PhhmpH** due to the greater electron-withdrawing character of the *o*-carboranyl than that of the phenyl moiety.<sup>[6,7]</sup> This is indirectly confirmed by the isolation and single-crystal XRD studies of the intermediate mononuclear Fe<sup>II</sup> complex [FeCl<sub>2</sub>(**phhmpH**)<sub>2</sub>] (**2**), in which the alcohol moieties remain protonated (Figure S13 in the Supporting Information). No such reaction intermediate was observed during the formation of [Fe<sub>2</sub>Cl<sub>3</sub>(**oCBhmp**)<sub>3</sub>] (**1**) even under an N<sub>2</sub> atmosphere by using NMR spectroscopy.

Racemic complex **1** was characterized by using elemental analysis, IR, cyclic voltammetry, and UV/Vis spectrometry. The molecular structure for complex **1** was unequivocally established by single-crystal XRD. Two crystal structures have been determined from racemic [Fe<sub>2</sub>Cl<sub>3</sub>(**oCBhmp**)<sub>3</sub>] (**1**), an acetone solvate [Fe<sub>2</sub>Cl<sub>3</sub>(**oCBhmp**)<sub>3</sub>]·acetone (**1**-acetone; Figure 1) and an ether solvate [Fe<sub>2</sub>Cl<sub>3</sub>(**oCBhmp**)<sub>3</sub>]·ether (**1**-ether; Figure S10 in the Supporting Information). The molecular structure for compound **1** shows a dinuclear Fe<sup>III</sup> system with rather unusual asymmetry. Both solvated structures of complex **1** show the

same arrangement of ligands and consist of two distorted octahedral metal ions bridged by three **oCBhmp**<sup>-</sup> ligands, each of which uses its alkoxide functionality to link the two Fe<sup>III</sup> ions. The remaining pyridine rings on each of the carborane-based ligands are also coordinated in a monodentate fashion, so that the octahedral coordination of one Fe<sup>III</sup> ion is completed by two pyridine nitrogen atoms and a terminal Cl<sup>-</sup> ion and the other Fe<sup>III</sup> is completed by one pyridine nitrogen and two terminal Cl<sup>-</sup> ions. The **oCBhmp**<sup>-</sup> ligands thus feature a μ-κ<sup>1</sup>O: κ<sup>2</sup>N,O bonding mode, which leads to a unique unsymmetrical dinuclear Fe<sup>III</sup> complex with three alkoxide bridges. Due to the unsymmetric nature of complex **1**, the Fe–O bonds show some differences. The average length of the three Fe1–O bonds (2.017 Å) is 0.085 Å shorter than the related Fe2–O bonds (2.102 Å) in structure **1**-acetone. This difference is less pronounced in the ether solvate **1**-ether (0.022 Å). The three Fe–N bonds and three Fe–Cl bonds have similar lengths and are in agreement with values found in other Fe<sup>III</sup> complexes.

The geometrical constraints imposed by the chelating and bridging coordination modes of the three **oCBhmp**<sup>-</sup> ligands in **1** (**1**-acetone/**1**-ether mean chelation N–Fe–O angle: 78.1/77.4°, mean O–Fe–O angle: 88.4/88.5°) result in a significant distorted octahedral geometry for both metal centers (with the

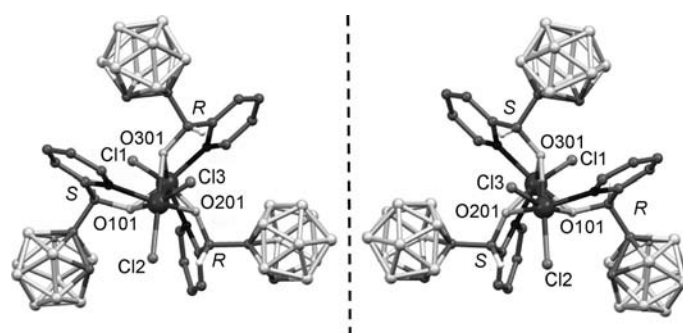
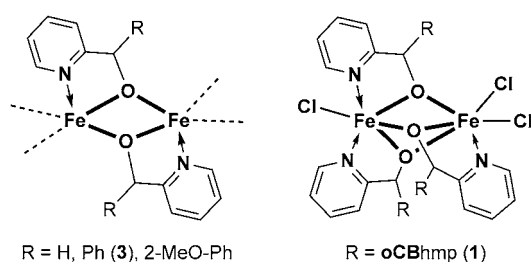


Figure 1. Ball-and-stick representation (Mercury 3.0)<sup>[16]</sup> of the molecular structure of **1**-acetone, showing both enantiomers in the racemate. All hydrogen atoms, except those for the CHOH group, are omitted for clarity. Black spheres = N, light grey spheres = B, dark grey spheres = C, larger spheres = Fe, other atoms labeled.

largest deviation of the axial angle from the ideal 180° being for N101-Fe2-O201 at 150.8(3)° and N201-Fe2-O301 at 150.2(1)° in **1**-acetone and **1**-ether, respectively). The Fe–Fe separations of 2.8722(15) Å and 2.8843(8) Å are short enough to be consistent with a bonding interaction between the metals. Fe<sup>III</sup> complexes with short Fe–Fe contacts have been reported in the literature,<sup>[13]</sup> the shortest bond being 2.714 Å.<sup>[14]</sup> A search in the CCDC shows only one example of a dinuclear Fe<sup>III</sup> compound with three citrate bridges but the complex is symmetric.<sup>[15]</sup>

The deprotonation of the alcohol functionalities in hmpH and its derivatives is known to favor bridging ( $\mu$ - $\kappa^1$ O:  $\kappa^2$ N,O) over chelating (N,OH) bonding modes and this is a widely used strategy for fostering formation of polynuclear complexes.<sup>[3b]</sup> Introducing substituents of controllable bulk near the alkoxide functional group seems to affect the polynuclearity of the related complexes in the sense of lowering the nuclearity for bulkier substituents and vice versa. This could also explain the formation of a dinuclear Fe<sup>III</sup> complex in the case of **1** (*o*-carboranyl-substituted) against a trinuclear complex in the case of **3** (phenyl-substituted). However, it is worth noting that regardless of the nuclearity of the iron complexes formed, in all other reported noncarboxylate Fe<sup>III</sup> complexes in the literature with hmpH or any related derivatives, two alkoxide pyridylalcohol ligands always bridge two close Fe<sup>III</sup> ions (Scheme 3, left).<sup>[12,17]</sup> Or in other words, all reported Fe<sup>III</sup> complexes with 2-pyridylalcohol ligands contain (in the absence of



**Scheme 3.**  $\mu_2$ -O versus  $\mu_3$ -O bridging of hmpH in Fe complexes.<sup>[18]</sup>

carboxylate ligands) an even number of alkoxide bridges, regardless of the nuclearity. This is in sharp contrast with dinuclear complex **1**, which has three alkoxide bridges, that is, an odd number of chiral pyridylalcohol ligands (Scheme 3, right). The expected higher acidity of our ligands compared with other hmpH-related ligands makes our alkoxide ligand (**oCBhmp**<sup>−</sup>) less basic and, therefore, less nucleophilic and consequently less coordinating at oxygen.<sup>[18]</sup> In such a case, a third alkoxide pyridylalcohol ligand might compensate the electron densities at the metals better. We cannot however rule out the possible role that the bulky carborane fragments might have in the entropy of the reaction. The presence of three alkoxide bridges in **1** is rather surprising owing to the size of the carborane cages and it has important structural consequences. Each of the pyridylalcohol ligands can adopt an *R* or *S* configuration, so that *RRR*, *SSS*, *RRS*, and *SSR* could all be expected in complex **1**. However, only *RRS* and *SSR* combinations are found

in the structure for **1** (Figure 1). Careful examination of the structures for **1** suggests that *RRR* or *SSS* ligand combinations would not fit around a dinuclear Fe<sup>III</sup> core due to the steric hindrance imposed by the handedness of the ligands. To confirm the latter assumption, the direct stereoselective synthesis of an enantiopure complex **1** from pure *R* and *S* enantiomers of **oCBhmpH** was investigated.

The *R* and *S* enantiomers of **oCBhmpH** were resolved by using HPLC over a chiral stationary phase (see the Supporting Information) and the absolute configurations were determined by using single-crystal XRD (*(R)*-(+)-**oCBhmpH**, *ee* > 95.5%; *(S)*-(-)-**oCBhmpH**, *ee* > 95.5%).<sup>[19]</sup> Addition of FeCl<sub>2</sub> to *(R)*-(+)-**oCBhmpH**/*(S)*-(-)-**oCBhmpH** mixtures (1:0.5 equiv or 0.5:1 equiv per 1 equiv of Fe) in acetone quantitatively produced the corresponding enantiopure complexes [Fe<sub>2</sub>Cl<sub>2</sub>((*RRS*)-**oCBhmp**)<sub>3</sub>] ((*RRS*)-(-)-**1**) or [Fe<sub>2</sub>Cl<sub>2</sub>((*SSR*)-**oCBhmp**)<sub>3</sub>] ((*SSR*)-(+)-**1**)<sup>[27]</sup> and have been characterized by using IR and XRD (Figures S11 and S12 in the Supporting Information). Both enantiopure metal complexes crystallize in the chiral space group *P*2<sub>1</sub>, with Flack parameters of 0.028(7) ((*RRS*)-(-)-**1**) and 0.033(8) ((*SSR*)-(+)-**1**); the latter is isostructural to **1**-ether. When only one of the enantiomers was employed (*(R)*-(+)-**oCBhmpH** or *(S)*-(-)-**oCBhmpH** with FeCl<sub>2</sub> in a 1.5:1 ratio), a mixture of a dinuclear [Fe<sub>2</sub>Cl<sub>2</sub>((*RR*)-**oCBhmp**)<sub>2</sub>]-acetone (**4**-acetone) and mononuclear [Fe((*SSS*)-**oCBhmp**)<sub>3</sub>] (**5**) were formed and have been characterized by using XRD (Figure 2) and PXRD (Figure S9 in the Supporting Information). Complexes **4**-acetone and **5** crystallize in the chiral space groups *P*4<sub>1</sub>,2

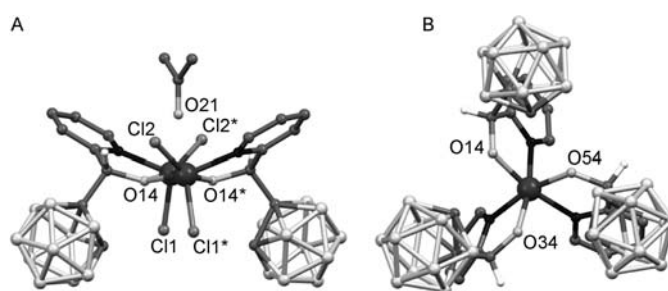


**Figure 2.** Ball-and-stick representation (Mercury 3.0)<sup>[16]</sup> of the molecular structures of A) [Fe<sub>2</sub>Cl<sub>2</sub>((*RR*)-**oCBhmp**)<sub>2</sub>]-acetone (**4**-acetone) and B) [Fe((*SSS*)-**oCBhmp**)<sub>3</sub>] (**5**). All hydrogen atoms, except those for the CHO group, are omitted for clarity. Black spheres = N, light grey spheres = B, dark grey spheres = C, larger spheres = Fe, other atoms labeled; \* = *x*, *y*, *z*.

(Flack parameter 0.008(4)) and *P*2<sub>1</sub> (Flack parameter 0.009(2)), respectively. Unlike complex **1**, complexes **4** and **5** show symmetrical structures. Whereas in complex **4** two **oCBhmp**<sup>−</sup> ligands with a  $\mu$ - $\kappa^1$ O:  $\kappa^2$ N,O bonding mode led to a symmetrical dinuclear Fe<sup>III</sup> complex with two alkoxide bridges, mononuclear complex **5** consists of a *fac*-Fe(**oCBhmp**)<sub>3</sub> molecule in which three **oCBhmp**<sup>−</sup> ligands coordinate through the N and O atoms in a bidentate fashion (Figure 2). It is particularly interesting to compare the X-ray structures for the acetone solvated structures **1**-acetone and **4**-acetone in Figures 1 and 2. The average length of the four Fe–O bonds (2.012 Å) in **4**-acetone is 0.048 Å shorter than the related average length of the six

Fe–O bonds (2.0595 Å) in 1-acetone. However, the Fe–Fe separation in 4-acetone (3.1205(6) Å) is significantly larger (0.248 Å) than the related distance for 1-acetone. Most remarkable is the position of the solvated acetone molecules in both structures. Whereas the acetone molecules are clearly out of the metal coordination spheres in 1-acetone, each acetone molecule in the solid structure for 4-acetone is interacting with the Fe<sup>III</sup> centers as shown in Figure 2. The acetone interaction mode is unprecedented and can be described as η<sup>1</sup>-O coordination of the acetone to the Fe–Fe bond (C=O...Fe<sub>2,centroid</sub> separation 2.138 Å; angle 180°). It is known that η<sup>1</sup> coordination of ketones to metal centers is preferred over η<sup>2</sup> for electron-deficient metals.<sup>[20]</sup> This data clearly supports our hypothesis that our alkoxide ligand (oCBhmp<sup>-</sup>) is a poor nucleophile and, therefore, a third oxygen, either from an alkoxide pyridylalcohol ligand or a solvent molecule, better compensates the electron densities at the metals. In addition, the data also show that dinuclear complexes with RRR or SSS ligand combinations cannot be formed due to the steric hindrance imposed by the handedness of the oCBhmp<sup>-</sup> ligands.

The circular dichroism (CD) spectra were recorded in solution in CH<sub>2</sub>Cl<sub>2</sub> for ligands (R)-(+)-oCBhmpH/(S)-(–)-oCBhmpH and the corresponding metal complexes [Fe<sub>2</sub>Cl<sub>3</sub>((SSR)-oCBhmp)<sub>3</sub>] ((SSR)-(+)-1)/[Fe<sub>2</sub>Cl<sub>3</sub>((RRS)-oCBhmp)<sub>3</sub>] ((RRS)-(–)-1) (Figure 3). In all cases, they display mirror-image values for the (+) and (–) enantiomers within experimental error. Regarding the ligands, their mirror-image CD spectra display structured bands of moderate intensity with Δε values of around –9.3 M<sup>-1</sup> cm<sup>-1</sup> at λ = 260 nm for (R)-(+)-oCBhmpH (see dashed lines in Figure 3) that are typical of chiral secondary alcohols with an aromatic substituent.<sup>[20,21]</sup> The solution CD spectra for Fe<sup>III</sup> complexes (RRS)-(–)-1 and (SSR)-(+)-1 are mirror images and display bands at λ = 260, 310, and 350 nm (Δε = –6.4, +1.6, –2.1 M<sup>-1</sup> cm<sup>-1</sup>, respectively, for the (RRS)-(–)-1 enantiomer<sup>[20]</sup>), which reveals the chiral environment around the iron centers. The CD spectra show that the enantiopure complexes are chemically and configurationally stable in solution. Because the two iron centers show configuration stability, a stereochemical assignment can be proposed for this uncommon chirality around the metal centers by using the A<sup>Fe</sup> and C<sup>Fe</sup> stereochemical descriptors to finally give (S,S)-A<sup>Fe</sup>A<sup>Fe</sup>-(+)-1 and (R,R)-C<sup>Fe</sup>-(S)-C<sup>Fe</sup>-(–)-1 (see the Supporting Information).

As previously mentioned, two crystal structures have been determined for racemic [Fe<sub>2</sub>Cl<sub>3</sub>(oCBhmp)<sub>3</sub>] (*rac*-1), that is, an acetone solvate ([Fe<sub>2</sub>Cl<sub>3</sub>(oCBhmp)<sub>3</sub>]-acetone (1-acetone); Figure 1) and an ether solvate ([Fe<sub>2</sub>Cl<sub>3</sub>(oCBhmp)<sub>3</sub>]-ether (1-ether); Figure S10 in the Supporting Information). The structural analysis of the two solvated

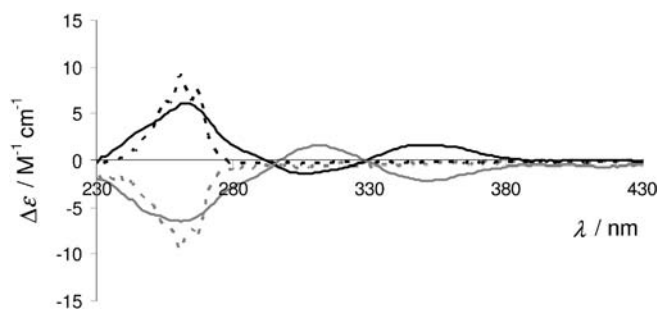


Figure 3. CD spectra of (R)-(+)-oCBhmpH (----), (S)-(–)-oCBhmpH (----), (R,R)-C<sup>Fe</sup>-(S)-C<sup>Fe</sup>-(–)-1 (—), and (S,S)-A<sup>Fe</sup>-(R)-A<sup>Fe</sup>-(+)-1 (—).<sup>[20]</sup>

structures for 1 revealed that whereas 1-acetone (centrosymmetric *P*<sub>2</sub><sub>1</sub>/*c* space group) is a racemate and, therefore, contains both enantiomers ((*RR*)-Fe:(*S*)-Fe and (*SS*)-Fe:(*S*)-Fe; Figure 1), 1-ether is formed by only one of these enantiomers and crystallizes in the non-centrosymmetric and chiral space group *P*<sub>2</sub><sub>1</sub> ((*SS*)-Fe:(*S*)-Fe, Flack parameter 0.004(15)).<sup>[22]</sup> Therefore, the latter is the result of spontaneous resolution and conglomerate formation on crystallization (i.e., a physical mixture of enantiomorphous (*RR*)-Fe:(*S*)-Fe and (*SS*)-Fe:(*R*)-Fe crystals).<sup>[23]</sup> Because the loss of centrosymmetry is at the origin of the appearance of numerous interesting optical and electrical properties,<sup>[24]</sup> we further explored whether total spontaneous resolution or conglomerate formation was possible in entire crystalline batches (i.e., bulk solids). Thus, a crystalline powder obtained by slow evaporation of solutions of 1 in acetone during the workup of the reaction (Figure 4A) could be identified from comparisons of XRPD patterns as a racemic compound (*rac*-1) with the *P*<sub>2</sub><sub>1</sub>/*c* space group, isomorphous to 1-acetone (Figure 4B). However, when diethyl ether was added to a solution of *rac*-1 in acetone, a new phase immediately precipitated (virtually no material remained in solution) and was subsequently identified as a conglomerate-forming monoclinic *P*<sub>2</sub><sub>1</sub> form (*co*-1) that was isomorphous to 1-ether (Figure S10 in the Supporting Information). To our knowledge, this is the first switch from a racemic

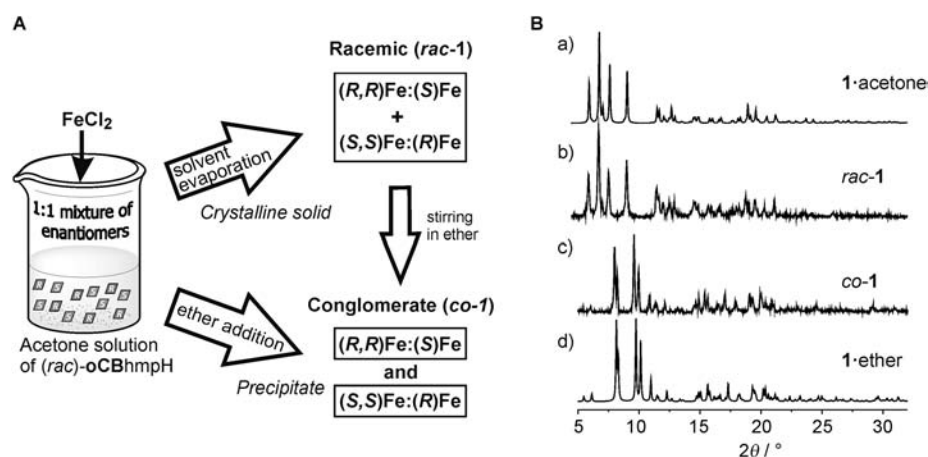


Figure 4. A) Schematic representation of racemic (*rac*-1) and conglomerate (*co*-1) formation for bulk samples of 1, see the text for details. B) XRPD of 1: a) calculated XRPD obtained from the crystal structure of 1-acetone, b) racemic mixture *rac*-1, c) conglomerate *co*-1, d) calculated XRPD obtained from the crystal structure of 1-ether.

compound solvate to a conglomerate solvate on precipitation.<sup>[25]</sup> These unexpected results encouraged us to study the possibility of solvent-mediated conglomerate formation in the solid state. The ability of *rac*-1 to take up solvent vapor and convert into *co*-1 has been demonstrated experimentally. Freshly made dried powdered *rac*-1 converts to conglomerate *co*-1 when left in contact with diethyl ether vapor for 3 d (Figure S8 in the Supporting Information). The identity of the products was confirmed by using XRPD, which matched the calculated diffraction patterns from the single-crystal X-ray structures. Thus, the transition from a racemic compound to a conglomerate either on precipitation or exposition to solvent vapor is of particular interest because it corresponds to a spontaneous resolution. We are further investigating the conglomerate formation mechanism.

To confirm the chiral nature of conglomerate solid phase *co*-1, its nonlinear optical activity has been measured by using second-harmonic generation (SHG) measurements. The SHG method is currently used to prescreen conglomerates.<sup>[26]</sup> Complex *co*-1 shows a clear positive SHG signal (about 25% quartz; Figure 5) that is consistent with the structure of 1-ether crystallized in the non-centrosymmetric and chiral space group  $P2_1$  (see Figure S8 in the Supporting Information). Complex *co*-1 exhibits a relatively poor damage threshold under laser irradiation and remains stable up to 110 °C. The decay of the time-resolved second-harmonic generation (TR-SHG) curve between 110 °C and the decomposition temperature of the complex ( $\approx 200$  °C) could be due to the thermal expansion of the crystal lattice and/or degradation of the sample. Consistent with solid-phase *co*-1 being a conglomerate, that is, a 1:1 mixture of enantiomorphous crystals, the CD spectrum in solution shows no signal.

Solid-state, variable-temperature (2–300 K) magnetic susceptibility data under applied external magnetic fields of 0.03 and 0.5 T were collected for polycrystalline samples of compound 1. The data shows behavior characteristic of an antiferromagnetic species, in which  $\chi_M T$  values decrease on lowering

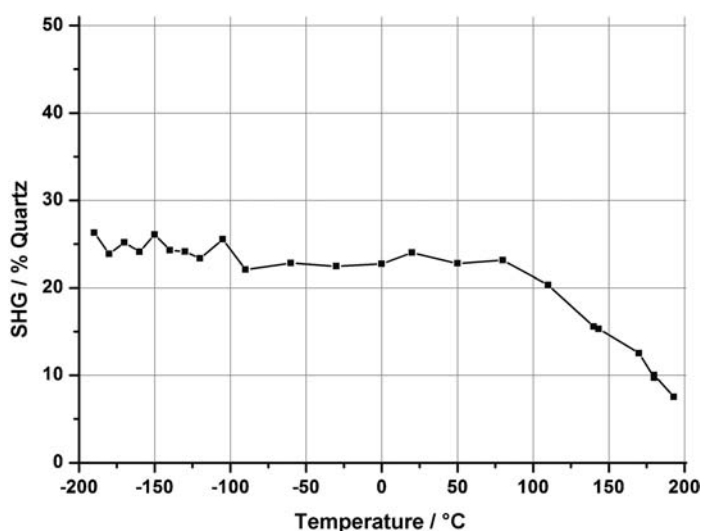


Figure 5. SHG intensity of *co*-1 versus temperature between –200 and 200 °C.

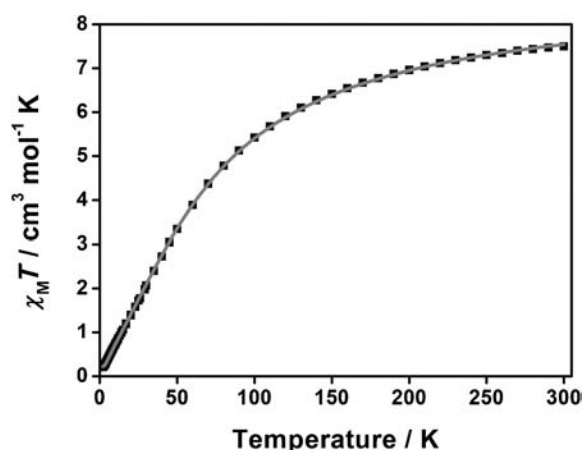


Figure 6. Fitting of the  $\chi_M T$  versus  $T$  of *rac*-1 between 2 and 300 K. The experimental data are shown as ■ and — corresponds to the fitting values.

the temperature and give a value of  $7.50 \text{ cm}^3 \text{mol}^{-1} \text{K}$  at 300 K (Figure 6). This is lower than expected for two independent high-spin  $\text{Fe}^{\text{III}}$  centers of  $8.75 \text{ cm}^3 \text{mol}^{-1} \text{K}$  with a  $g$  value of 2.00, and is evidence of a significant antiferromagnetic interaction. The graph shows a decrease in the magnetic susceptibility to nearly zero at 2 K ( $0.21 \text{ cm}^3 \text{mol}^{-1} \text{K}$ ). Magnetic susceptibility data were analyzed by using the Van Vleck equation derived from the spin-exchange Hamiltonian  $H = -JS_1S_2$ ,<sup>[27]</sup> in which  $S_1 = S_2 = 5/2$ . The best fit matches well with experimental data and gives values of  $g = 2.05$ ,  $J = (-10.22 \pm 0.03) \text{ cm}^{-1}$ ,  $TIP = 280 \times 10^{-6} \text{ cm}^3 \text{mol}^{-1}$ ,  $\rho = 0.05\%$ , and  $R = 1 \times 10^{-5}$  (see Experimental Section). Overall, the analysis of the data agrees with the shape and values observed in the experimental measurement, in which the exchange coupling for both  $\text{Fe}^{\text{III}}$  atoms is significantly antiferromagnetic. The present data confirm compound 1 as the first dinuclear  $\text{Fe}^{\text{III}}$  system that contains three alkoxide bridges and displays antiferromagnetic behavior. DFT calculations by using B3LYP functional are in agreement with the experimental data, giving a calculated  $J$  value of  $-6.0 \text{ cm}^{-1}$ . The analysis of the calculated  $J$  values for other complexes with similar bridging ligands corroborates the idea that the Fe–O separation could be the main parameter that controls the magnetic behavior and the longest Fe–O separation of 1 gives an understanding of the antiferromagnetic coupling (see the Supporting Information).

## Conclusion

We report an unusually unsymmetric diiron(III) complex 1 in which three bulky chiral carboranylpyridinealkoxide ligands ( $\text{oCBhmp}^-$ ) bridge both metal ions; this complex combines magnetic, chiroptical, and second-order optical nonlinear properties. Complex 1 constitutes the first dinuclear  $\text{Fe}^{\text{III}}$  system that contains three alkoxide bridges and displays antiferromagnetic behavior. DFT calculations have corroborated this behavior and show that the Fe–O separation is the main parameter that controls the magnet-



ic behavior. We showed that the introduction of the bulky *o*-carborane into the 2-(hydroxymethyl)pyridine (hmpH) architecture significantly alters the coordination of the simple or aryl-substituted 2-hmpH. Whereas all other examples in the literature always show two alkoxide pyridylalcohol ligands bridging two close Fe<sup>III</sup> ions, our dinuclear complex **1** contains three alkoxide bridges. This unusual architecture seems to be triggered by the poor nucleophilicity of our alkoxide ligand (**oCBhmp**<sup>−</sup>). The presence of an odd number of ligands per molecule in **1** results in a reduction of possible enantiomers with the consequent simplicity of the enantiomeric mixture. A very rare case of spontaneous resolution takes place on precipitation or exposure to solvent vapor for the bulk compound, as confirmed by a combination of XRD, XRPD, SHG, and CD measurements. The corresponding enantiopure complexes (+)-**1** and (−)-**1** have also been synthesized and fully characterized. This case study highlights the potential of combining carboranes, coordination chemistry, and chirality in conceiving new molecular materials with unprecedented properties and opens new perspectives in chiral materials.

## Experimental Section

### Materials

All manipulations were carried out in air unless otherwise noted. The reactions were carried out in glass vials equipped with a magnetic stirring bar and capped with a septum. The following chemicals were used: ethanol (distilled from CaH<sub>2</sub>), acetone (distilled from P<sub>2</sub>O<sub>5</sub>), anhydrous FeCl<sub>2</sub> (98%, Sigma Aldrich; used as received). (2-Pyridine)(*o*-carboranyl)methanol (**oCBhmpH**)<sup>[4b]</sup> and (2-pyridine)(phenyl)methanol (**phhmpH**)<sup>[28]</sup> were synthesized as previously reported.

### General procedure for the synthesis of [Fe<sub>2</sub>Cl<sub>3</sub>(**oCBhmp**)<sub>3</sub>] (**1**) and conglomerate formation

A solution of **oCBhmpH** (75.0 mg, 0.298 mmol) in acetone (0.50 mL) was added to a stirred suspension of FeCl<sub>2</sub> (16.9 mg, 0.131 mmol) in acetone (0.25 mL) in a small capped vial. The vial was closed and the orange-brown mixture was then gently warmed at about 50 °C and shaken until formation of a clear yellowish golden solution. Once the solution was at RT, it was filtered through a Celite leach and left with the cap slightly open. Evaporation of the acetone gave yellow-brown crystalline agglomerates that were dried under vacuum to give *rac*-**1** (71 mg, ≈100%; phase purity established by XRPD, FTIR (ATR), and elemental analysis). Elemental analysis calcd (%) for C<sub>28</sub>H<sub>58</sub>B<sub>30</sub>Cl<sub>3</sub>Fe<sub>2</sub>N<sub>3</sub>O<sub>4</sub>·1.5 acetone (1056.15): C 32.41, H 5.44, N 3.09; found: C 32.14, H 5.48, N 3.89.

### Transformation of *rac*-**1** into *co*-**1** by precipitation

Addition of diethyl ether (2.0 mL) to a solution of the above *rac*-**1** in acetone gave a suspension that was stirred for 3 h. The supernatant solution was decanted to give a fine pale yellow powder that was dried under vacuum to give ether solvate *co*-**1** (yield: 50 mg, 73%). Phase purity was checked by XRPD, FTIR (ATR), and elemental analysis. M.p. 231 °C (decomp.); elemental analysis calcd (%) for C<sub>28</sub>H<sub>58</sub>B<sub>30</sub>Cl<sub>3</sub>Fe<sub>2</sub>N<sub>3</sub>O<sub>4</sub> (1043.16): C 32.24, H 5.60, N 4.03; found: C 32.25, H 5.65, N 4.01.

### Transformation of *rac*-**1** into *co*-**1** by exposure to solvent vapor

A dry polycrystalline sample of complex *rac*-**1** (50 mg) was exposed to vapor of diethyl ether for 3 d. The quantitative formation of *co*-**1** was assessed by comparing the X-ray powder diffraction pattern of the crystalline product with the spectrum calculated on the basis of the single-crystal structure (Figure S8 in the Supporting Information).

### In situ NMR spectroscopy studies for formation of **1**

The reaction was performed under inert atmosphere conditions. A solution of **oCBhmpH** (15.5 mg, 0.062 mmol) in degassed [D<sub>3</sub>]-acetonitrile (0.50 mL) was added to a NMR tube containing FeCl<sub>2</sub> (5.2 mg, 0.041 mmol), with the tube kept in liquid nitrogen to avoid the reaction starting before measurement. The iced sample was then taken to an NMR spectrometer and <sup>1</sup>H and <sup>11</sup>B NMR spectra were recorded. Sharp signals observed for the free ligand became very broad and paramagnetically shifted as soon as the [D<sub>3</sub>]-acetonitrile solution melted, which indicated the fast formation of a Fe<sup>III</sup> compound.

### Synthesis of [Fe<sub>2</sub>Cl<sub>3</sub>((*RRS*)-**oCBhmp**)<sub>3</sub>] ((*RRS*)-(−)-**1**)

The general procedure was followed by using (*R*)-(+)-**oCBhmpH** (20.3 mg, 0.081 mmol), (*S*)-(−)-**oCBhmpH** (10.3 mg, 0.041 mmol), and FeCl<sub>2</sub> (10.3 mg, 0.081 mmol). Slow evaporation of the solvent gave complex (*RRS*)-**1** (39.9 mg, 96%) as brown-yellow needles suitable for single-crystal X-ray structure determination. [α]<sub>D</sub><sup>23</sup> = −35.5, [α]<sub>578</sub><sup>23</sup> = −40.0, [α]<sub>546</sub><sup>23</sup> = −48.9, [α]<sub>436</sub><sup>23</sup> = −160 (±5%; CH<sub>2</sub>Cl<sub>2</sub>, c = 0.24 g/100 mL); UV/Vis: λ = 254 (23 800), 320 (10 200), 356 nm (8000 M<sup>−1</sup> cm<sup>−1</sup>); CD (CH<sub>2</sub>Cl<sub>2</sub>, C = 2.3 × 10<sup>−3</sup> M): λ = 260 (−6.4), 310 (+1.6), 350 nm (−2.1 M<sup>−1</sup> cm<sup>−1</sup>).

### Synthesis of [Fe<sub>2</sub>Cl<sub>3</sub>((*RRS*)-**oCBhmp**)<sub>3</sub>] ((*SSR*)-(+) -**1**)

The general procedure was followed by using (*S*)-(−)-**oCBhmpH** (20.1 mg, 0.080 mmol), (*S*)-(+)-**oCBhmpH** (10 mg, 0.040 mmol), and FeCl<sub>2</sub> (10.1 mg, 0.080 mmol). Slow evaporation of the solvent gave complex (*RRS*)-**1**·acetone (52.0 mg, 125%) as brown-yellow needles suitable for single-crystal X-ray structure determination. [α]<sub>D</sub><sup>23</sup> = +34.8, [α]<sub>578</sub><sup>23</sup> = +39.1, [α]<sub>546</sub><sup>23</sup> = +47.8, [α]<sub>436</sub><sup>23</sup> = +169.6 (±5%) (CH<sub>2</sub>Cl<sub>2</sub>, c = 0.23 g/100 mL); UV/Vis: λ = 254 (22 700), 320 (10 000), 356 nm (8000 M<sup>−1</sup> cm<sup>−1</sup>); CD (CH<sub>2</sub>Cl<sub>2</sub>, C = 2.2 × 10<sup>−3</sup> M): λ = 260 (+6.0), 310 (−1.3), 350 nm (+1.6 M<sup>−1</sup> cm<sup>−1</sup>).

### Synthesis of [FeCl<sub>2</sub>(**phhmpH**)<sub>2</sub>] (**2**)

A degassed solution of **phhmpH** (20.0 mg, 0.108 mmol) in acetone (0.30 mL) was added to a stirred degassed suspension of anhydrous FeCl<sub>2</sub> (7.0 mg, 0.054 mmol) in acetone (0.25 mL) in a small vial capped with a septum and equipped with a magnetic bar. The mixture was then gently warmed at about 50 °C and stirred until a clear red-yellow solution formed. Once the solution was at RT, the solvent was partially evaporated under a nitrogen gas flow. After 24–36 h, prismatic red crystals were obtained. The identity of the compound was then established by using single-crystal X-ray diffraction. Due to the high solubility and certain instability of the compound, other characterization techniques were not performed. This compound is under further investigations.

### Synthesis of $[\text{Fe}_3\text{Cl}_4(\text{phhmp})_4][\text{FeCl}_4]$ (**3**)

The general procedure was followed by using **phhmpH** (30 mg, 0.162 mmol) and  $\text{FeCl}_2$  (20.95 mg, 0.162 mmol). Under inert conditions, the red crystalline material from  $[\text{FeCl}_2(\text{phhmpH})_2]$  (**2**) formed after 24–36 h, then slowly redissolved to give a yellow solution. Evaporation of the acetone gave yellow crystalline agglomerates that were dried under vacuum to afford **3**. The same procedure under air directly gave compound **3** (42.6 mg, 85%). Purity was established by elemental analysis. Elemental analysis calcd (%) for  $\text{C}_{48}\text{H}_{40}\text{Cl}_8\text{Fe}_4\text{N}_4\text{O}_4$  (1243.86): C 46.35, H 3.24, N 4.050; found: C 46.3, H 3.4, N 4.3.

### Reaction of $\text{FeCl}_2$ with (*R*)-(+)-**oCBhmpH** or (*S*)-(–)-**oCBhmpH**

The general procedure was followed by using  $\text{FeCl}_2$  (10.1 mg, 0.079 mmol) and (*R*)-(+)-**oCBhmpH** (29.5 mg, 0.117 mmol) or  $\text{FeCl}_2$  (9.7 mg, 0.077 mmol) and (*S*)-(–)-**oCBhmpH** (30.0 mg, 0.119 mmol). Slow evaporation of the solvent gave mixtures of single crystals and polycrystalline solids that corresponded to **4** and **5**, as determined by XRD (Figure 2) and PXRD (Figure S9 in the Supporting Information).

### Physical measurements

**Elemental analysis:** Elemental analyses (C, H, N) were performed by the Analysis Service of the Universitat Autònoma de Barcelona by using a Carlo Erba CHNS EA-1108 microanalyzer.

**FT-IR spectra:** FTIR-ATR spectra were recorded by using a Perkin-Elmer 1720X spectrometer.

**NMR spectra:**  $^1\text{H}$ ,  $^{11}\text{B}$  NMR spectra were recorded at 300 and 96 MHz, respectively, by using a Bruker ARX 300 MHz spectrometer and referenced to the solvent ( $^1\text{H}$ , residual  $[\text{D}_5]$ acetone) or  $\text{BF}_3\cdot\text{OEt}_2$  ( $^{11}\text{B}$ ). Chemical shifts ( $\delta$ ) are reported in ppm and coupling constants ( $J$ ) in Hz.

**UV/Vis spectra:** UV/Vis measurements were carried out by using a Hewlett Packard 8453 diode array spectrometer equipped with a Lauda RE 207 thermostat and a screw-capped quartz cuvette.

**Circular dichroism:** Circular dichroism (in  $\text{m}^{-1}\text{cm}^{-1}$ ) and UV/Vis were measured by using a Jasco J-815 Circular Dichroism Spectrometer (IFR140 facility, Université de Rennes 1). Specific rotations were measured in a 1 dm thermostated quartz cell by using a Perkin-Elmer-341 polarimeter.

**Cyclic voltammetry:** Cyclic voltammetry measurements were made in 0.1 M tetrabutylammonium hexafluorophosphate ( $\text{TBAPF}_6$ ) electrolyte solutions in acetonitrile. A two-compartment cell equipped with a glassy carbon working electrode, a platinum gauze as the counter electrode, and an Ag wire as the pseudo-reference electrode, properly checked against a ferrocene/ferrocenium ( $\text{Fc}/\text{Fc}^+$ ) couple before test, was used. Measurements were made by using a BASi C-3 Cell Stand. Data were obtained at a scan rate of  $100\text{ mV s}^{-1}$ .

**X-ray powder diffraction (XRPD):** XRPD data was collected by using a Siemens Analytical X-ray D-5000 diffractometer with a  $\text{Cu}_{\text{K}\alpha}$  radiation. All XRPD measurements were carried out at RT.

**X-ray diffraction studies:** Single-crystal intensity data for **1**-acetone was collected at 120 K by using a Bruker Nonius Kappa CCD area detector mounted at the window of a rotating Mo anode ( $\lambda(\text{Mo}_{\text{K}\alpha})=0.71073\text{ \AA}$ ; see Table S1 in the Supporting Information). Data collection and processing were performed by using the programs COLLECT<sup>[29]</sup> and DENZO<sup>[30]</sup> and a multi-scan absorption correction was applied by using SADABS.<sup>[31]</sup> Data for **1**-ether was collected at 100 K by using a Rigaku AFC<sub>12</sub> goniometer equipped with

an enhanced sensitivity (HG) Saturn724+ detector mounted at the window of an FR-E+ SuperBright molybdenum rotating anode generator ( $\lambda(\text{Mo}_{\text{K}\alpha})=0.71073\text{ \AA}$ ) with HF Varimax optics (100  $\mu\text{m}$  focus). Data collection and processing, including a multi-scan absorption correction, was performed by using CrystalClear.<sup>[32]</sup> The structures were solved by using direct methods<sup>[33]</sup> and refined by using full matrix least squares<sup>[34]</sup> on  $F^2$ . X-ray reflections for **2** and **3** were collected at 298 K by using an Oxford Xcalibur Gemini Eos CCD diffractometer with  $\text{Mo}_{\text{K}\alpha}$  radiation ( $\lambda=0.7107\text{ \AA}$ ; see Table S3 in the Supporting Information). Data collection and processing, including a multi-scan absorption correction, were performed by using CrysAlisPro (v. 1.171.34.55)<sup>[35]</sup> and OLEX2-1.2<sup>[36]</sup> and SHELXL97<sup>[37]</sup> were used for structure solution and refinement. For these structures, several H atoms (especially OH) were detected at approximate locations in a difference Fourier map and then refined freely. Those for BH and some CH were placed in idealized positions and refined by using a riding model, with  $\text{C-H}=0.93\text{ \AA}$  and  $U_{\text{iso}}(\text{H})=1.2 U_{\text{eq}}(\text{C})$ . Data for **4**, **5**, (*RRS*)-**1**, and (*SSR*)-**1** were collected by using a Bruker D8 Venture (**4** and **5**, 150 K,  $\lambda=1.54178\text{ \AA}$ ) or a Bruker SMART APEX diffractometer ((*RRS*)-**1** and (*SSR*)-**1**, 100 K,  $\lambda=0.71073\text{ \AA}$ ). Data collection and processing were performed by using the programs APEX2<sup>[38]</sup> and SAINT<sup>[39]</sup> and a numerical absorption correction was applied based on indexed crystal faces by using the Crystal Faces plugin in APEX2.<sup>[39]</sup> The structures were solved by direct methods,<sup>[34]</sup> which revealed the position of all non-hydrogen atoms. These atoms were refined on  $F^2$  by a full-matrix least-squares procedure by using anisotropic displacement parameters.<sup>[34]</sup>

**Special details:** For **1**-acetone, **1**-ether, **2**, **3**, **4**, and **5**, all hydrogen atoms were placed in idealized positions and refined by using a riding model. For (*RRS*)-**1** and (*SSR*)-**1**, the solvent masking procedure as implemented in Olex2<sup>[23]</sup> was used to remove the electronic contribution of solvent molecules from the refinement. Each void is postulated to contain  $\approx 1.6$  ((*RRS*)-**1**) or 1.3 ((*SSR*)-**1**) molecules of acetone.

One of the refined phenyl rings in **3** was modeled as split over two positions (59, 41) and geometric and thermal parameter restraints were applied. During the refinement of complex **3**, residual electron density was detected in the lattice associated with solvent molecules. Thus, the data was treated with the SQUEEZE procedure (from PLATON).<sup>[40]</sup> The volume occupied by the solvent was  $1257.4\text{ \AA}^3$  and the number of electrons per unit cell deduced by SQUEEZE was 132, these values were not interpretable as a definitive number of specific solvent molecules.

**Second-harmonic generation (SHG):** The experimental setup used for the TR-SHG measurements was previously published.<sup>[41]</sup> A Nd/YAG Q-switched laser (Quantel) operating at 1.06  $\mu\text{m}$  was used to deliver 360 mJ pulses of 5 ns duration with a repetition rate of 10 Hz. An energy adjustment device made up of two polarizers (P) and a half-wave plate ( $k/2$ ) allowed the incident energy to vary from 0 to  $\approx 200\text{ mJ}$  per pulse. A RG1000 filter was used after the energy adjustment device to remove light from laser flash lamps. The samples (a few mg of powder in a crucible) were placed in a computer-controlled heating-cooling stage (Linkam THMS-600) and were irradiated with a beam (diameter 4 mm). The signal generated by the sample (diffused light) was collected by an optical fiber (500  $\mu\text{m}$  core diameter) and directed onto the entrance slit of a spectrometer (Ocean Optics). A boxcar integrator allowed an average spectrum (spectral range  $\lambda=490\text{--}590\text{ nm}$ ) with a resolution of 0.1 nm to be recorded over 2 s (20 pulses). To avoid problems related to the sublimation of the samples, the heating stage was opened but only during the SHG measurements so it had no significant influence on the temperature regulation. According to the

SHG powder method described by Kurtz and Perry,<sup>[42]</sup> SHG signal intensities were compared to the signal of a reference compound (quartz; 45 lm average size).

**Magnetic measurements:** Magnetic measurements were carried out at the Unitat de Mesures Magnètiques (Universitat de Barcelona) on polycrystalline samples by using a Quantum Design SQUID MPMS-XL magnetometer working in the 2–300 K range. The magnetic fields used in the measurements were 0.03 T (from 2–30 K) and 0.5 T (from 2–300 K). Diamagnetic corrections were evaluated from Pascal's constants. The fit was performed by minimizing the function  $R$  (agreement factor defined as  $\sum[(\chi_m T)^{\text{exptl}} - (\chi_m T)^{\text{calcd}}]^2 / \sum[(\chi_m T)^{\text{exptl}}]^2$ ) TIP and  $\rho$  are defined as temperature-independent parameter and impurities, respectively.

**Theoretical calculations:** Density functional theory methods provide an excellent estimation of the exchange coupling constants by taking into account the very small energy differences computed to extract the exchange coupling constants.<sup>[43]</sup> Because a detailed description of the computational strategy used to calculate the exchange coupling constants in dinuclear and polynuclear complexes is outside the scope of this paper, we will focus our discussion here to its most relevant aspects and a more detailed description can be found elsewhere.<sup>[44–47]</sup> For the calculation of the  $n$  different coupling constants  $J_{ij}$  present in a polynuclear complex, we need to carry out calculations for at least  $n+1$  different spin distributions. Thus, by solving the system of  $n$  equations obtained from the energy differences we can obtain  $n$  coupling constants. For systems in which more than  $n$  spin distributions were calculated, a least-square fitting procedure to obtain the coupling constants must be used. In the specific case of dinuclear  $\text{Fe}^{\text{III}}$  complexes, the  $J$  value is directly obtained from the energy difference between the high-spin state (parallel alignment of the local spins) and the single-determinant low-spin solution (antiparallel alignment of the local spins), usually called broken symmetry, divided by a  $2S_1S_2 + S_1$  term ( $S_1 = 5/2$ ,  $S_2 = 5/2$ ). For the studied symmetric trinuclear  $\text{Fe}_3^{\text{III}}$  complex with two different  $J$  values (the second one between the two terminal  $\text{Fe}^{\text{III}}$  centers), three spin configurations have been calculated, that is, the high-spin one and two  $S = 5/2$  that correspond to the spin inversion of the central and terminal  $\text{Fe}^{\text{III}}$  cations, respectively. In previous studies,<sup>[4]</sup> we found that the hybrid B3LYP functional<sup>[48]</sup> together with the basis sets proposed by Schaefer et al.<sup>[49]</sup> provide  $J$  values in excellent agreement with the experimental ones. We have employed a basis set of triple- $\zeta$  quality as proposed by Schaefer et al. The calculations were performed with the Gaussian 09 code<sup>[50]</sup> using guess functions generated by using the Jaguar 7.5 code.<sup>[51,52]</sup>

## Acknowledgements

We thank CICYT (F.D.S., M.Y.T., F.T., C.V., and J.G.P.: grant CTQ2010-16237; N.A.-A. and E.R.: grant CTQ2012-32247; E.R.: grant CTQ2011-23862-C02-01), Generalitat de Catalunya (F.D.S., M.Y.T., F.T., C.V., and J.G.P.: 2009/SGR/00279; E.R.: 2009SGR-1459) and the CSIC (JAE-doc contract to F.D.S.) for financial support. F.D.S. thanks CONICET for support. M.E.L. and M.B.H. thank the UK Engineering and Physical Science Research Council for support by the X-ray facilities at Southampton. M.B.H. thanks the Leverhulme Trust for the award of an Emeritus Fellowship. M.Y.T. is enrolled in the UAB PhD program. The project "Factoría de Cristalización, CONSOLIDER INGENIO-2010" provided X-ray structural facilities for this work. E.R. gratefully acknowledges the computer resources, technical expertise, and

assistance provided by the CESCO. J.C. acknowledges the CNRS, the University of Rennes 1, and the ANR (12-BS07-0004-METALHEL-01). Michel Gruselle and Jamal Moussa are warmly thanked for fruitful discussions on stereochemical aspects.

**Keywords:** boron • chirality • iron • second-harmonic generation • spontaneous resolution

- [1] a) U. Knof, A. Von Zelewsky, *Angew. Chem.* **1999**, *111*, 312–333; *Angew. Chem. Int. Ed.* **1999**, *38*, 302–322; b) H. Amouri, M. Gruselle, *Chirality in Transition Metal Chemistry: Molecules, Supramolecular Assemblies and Materials*, Wiley, Chichester, **2008**; c) J. Crassous, *Chem. Soc. Rev.* **2009**, *38*, 830–845; d) J. Crassous, *Chem. Commun.* **2012**, *48*, 9684–9692; e) E. B. Bauer, *Chem. Soc. Rev.* **2012**, *41*, 3153–3167.
- [2] a) G. L. J. A. Rikken, E. Raupach, *Nature* **1997**, *390*, 493–494; b) C. Train, R. Gheorghe, V. Krstic, L. M. Chamoreau, N. Ovanesyan, G. Rikken, M. Gruselle, M. Verdaguer, *Nat. Mater.* **2008**, *7*, 729–734; c) C. Train, M. Gruselle, M. Verdaguer, *Chem. Soc. Rev.* **2011**, *40*, 3297–3312.
- [3] For recent examples on metal complexes of 2-(hydroxymethyl)pyridine, see: a) R. Pattacini, P. Teo, J. Zhang, Y. Lan, A. K. Powell, J. Nehrkorn, O. Waldmann, T. S. A. Hor, P. Braunstein, *Dalton Trans.* **2011**, *40*, 10526; b) T. Taguchi, W. Wernsdorfer, K. A. Abboud, G. Christou, *Inorg. Chem.* **2010**, *49*, 10579; c) M. Hubrich, M. Peukert, W. Seichter, E. Weber, *Polyhedron* **2010**, *29*, 1854; d) S. G. Telfer, N. D. Parker, R. Kuroda, T. Harada, J. Lefebvre, D. B. Leznoff, *Inorg. Chem.* **2008**, *47*, 209; e) V. T. Yilmaz, S. Hamamci, C. Thone, *Polyhedron* **2004**, *23*, 841; f) M. Ito, S. Onaka, *Inorg. Chim. Acta* **2004**, *357*, 1039; for complexes of 3- and/or 4-(hydroxymethyl)pyridine, see: g) N. I. Jakab, Z. Vaskova, J. Moncol, B. Gyurcsik, J. Sima, M. Koman, D. Valigura, *Polyhedron* **2010**, *29*, 2262; h) R. Murugavel, S. Kuppuswamy, N. Gogoi, R. Boomishankar, A. Steiner, *Chem. Eur. J.* **2010**, *16*, 994; i) A. Bacchi, M. Carcelli, T. Chiodo, F. Mezzadri, *CrystEngComm* **2008**, *10*, 1916.
- [4] a) V. Terrasson, Y. García, P. Farràs, F. Teixidor, C. Viñas, J. G. Planas, D. Prim, M. E. Light, M. B. Hursthouse, *CrystEngComm* **2010**, *12*, 4109; b) F. Di Salvo, B. Camargo, Y. García, F. Teixidor, C. Viñas, J. G. Planas, M. E. Light, M. B. Hursthouse, *CrystEngComm* **2011**, *13*, 5788; c) F. Di Salvo, C. Paterakis, M. Y. Tsang, Y. García, C. Viñas, F. Teixidor, J. G. Planas, M. E. Light, M. B. Hursthouse, D. Choquesillo-Lazarte, *Cryst. Growth Des.* **2013**, *13*, 1473–1484.
- [5] a) D. Olid, R. Núñez, C. Viñas, F. Teixidor, *Chem. Soc. Rev.* **2013**, *42*, 3318–3336; b) F. Teixidor, C. Viñas in *Science of Synthesis, Vol. 6*, Thieme, Stuttgart, **2005**, p. 1235, and references therein; c) R. N. Grimes, *Carboranes, 2nd ed.*, Elsevier, Amsterdam, **2011**.
- [6] M. Scholz, E. Hey-Hawkins, *Chem. Rev.* **2011**, *111*, 7035, and references therein.
- [7] a) L. Schwartz, L. Eriksson, R. Lomoth, F. Teixidor, C. Viñas, S. Ott, *Dalton Trans.* **2008**, 2379–2381; b) R. Núñez, P. Farràs, F. Teixidor, C. Viñas, R. Sillanpää, R. Kivekäs, *Angew. Chem.* **2006**, *118*, 1292–1294; *Angew. Chem. Int. Ed.* **2006**, *45*, 1270–1272; c) F. Teixidor, R. Núñez, C. Viñas, R. Sillanpää, R. Kivekäs, *Angew. Chem.* **2000**, *112*, 4460–4462; *Angew. Chem. Int. Ed.* **2000**, *39*, 4290–4292.
- [8] F. Di Salvo, F. Teixidor, C. Viñas, J. G. Planas, M. E. Light, M. B. Hursthouse, N. Aliaga-Alcalde, *Cryst. Growth Des.* **2012**, *12*, 5720.
- [9] a) Y.-Y. Zhu, X. Guo, C. Cui, B.-W. Wang, Z.-M. Wang, S. Gao, *Chem. Commun.* **2011**, *47*, 8049–8051; b) E. C. Constable, G. Zhang, C. E. Housecroft, M. Neuburger, J. A. Zampese, *Chem. Commun.* **2010**, *46*, 3077–3079; c) R. Singh, A. Banerjee, E. Colacio, K. K. Rajak, *Inorg. Chem.* **2009**, *48*, 4753–4762.
- [10] C. Train, T. Nuida, R. Gheorghe, M. Gruselle, S. Ohkoshi, *J. Am. Chem. Soc.* **2009**, *131*, 16838–16843.
- [11] W.-Q. Chen, Y.-M. Chen, T. Lei, W. Liu, Y. Li, *Inorg. Chem. Commun.* **2012**, *19*, 4–9.
- [12] K. Butsch, A. Klein, M. Bauer, *Inorg. Chim. Acta* **2011**, *374*, 350 and references therein.
- [13] E. Y. Tshuva, S. J. Lippard, *Chem. Rev.* **2004**, *104*, 987.
- [14] Y. Zang, Y. Dong, L. Que, Jr., K. Kauffmann, E. Münck, *J. Am. Chem. Soc.* **1995**, *117*, 1169.

- [15] I. Shweky, A. Bino, D. P. Goldberg, S. J. Lippard, *Inorg. Chem.* **1994**, *33*, 5161.
- [16] Mercury: visualization and analysis of crystal structures. C. F. Macrae, P. R. Edgington, P. McCabe, E. Pidcock, G. P. Shields, R. Taylor, M. Towler, J. van de Streek, *J. Appl. Crystallogr.* **2006**, *39*, 453–457.
- [17] For simple hmpH structures, see: a) J.-P. Sun, L.-C. Li, X.-J. Zheng, *Inorg. Chem. Commun.* **2011**, *14*, 877–881; b) VOJTAQ, VOJTEU: T. Taguchi, T. C. Stamatatos, K. A. Abboud, C. M. Jones, K. M. Poole, T. A. O'Brien, G. Christou, *Inorg. Chem.* **2008**, *47*, 4095–4108; c) YAZDUY: C. A. Christmas, H.-L. Tsai, L. Pardi, J. M. Kesselman, P. K. Gantzel, R. K. Chadha, D. Gatteschi, D. F. Harvey, D. N. Hendrickson, *J. Am. Chem. Soc.* **1993**, *115*, 12483–12490.
- [18] The average Fe–O bond length (18 bonds) for the four structures for **1** given in this paper is 2.069 Å. The corresponding average for phenyl derivative **3** (8 bonds) is 1.982 Å and that for the 2-methoxyphenyl-hmpH (4 bonds) is 1.971 Å (ETISUW in ref. [12]).
- [19] Note that the sign given refers here to the specific rotation at  $\lambda = 589$  nm in dichloromethane. Indeed, opposite signs have been observed in CD spectra of **oCBhmpH** in dichloromethane between  $\lambda = 230$  and 260 nm and in HPLC conditions (hexane/EtOH 80:20) with a CD detector at  $\lambda = 254$  nm. The specific rotations in dichloromethane also change sign from (S)-(–)-**oCBhmpH** to (SSR)-(+)–**1**.
- [20] F. Delbecq, P. Sautet, *J. Am. Chem. Soc.* **1992**, *114*, 2446–2455.
- [21] H. E. Smith in *Circular Dichroism: Principles and Applications*, 2nd ed., (Eds.: N. Berova, K. Nakanishi, R. W. Woody), Wiley-VCH, Weinheim, **2000**.
- [22] H. D. Flack, *Acta Crystallogr. Sect. A* **1983**, *39*, 876.
- [23] a) J. Jacques, A. Collet, S. H. Wilen, *Enantiomers, Racemates, and Resolutions*, Krieger, Malabar, **1994**; b) G. Coquerel, *Novel Optical Resolution Technologies*, Springer, Berlin, Heidelberg, **2007**, p. 1; c) L. Pérez-García, D. B. Amabilino, *Chem. Soc. Rev.* **2007**, *36*, 941–967.
- [24] a) P. S. Halasyamani, K. R. Poeppelmeier, *Chem. Mater.* **1998**, *10*, 2753–2769; b) K. M. Ok, E. O. Chi, P. S. Halasyamani, *Chem. Soc. Rev.* **2006**, *35*, 710–717.
- [25] Y. Amharar, S. Petit, M. Sanselme, Y. Cartigny, M.-N. Petit, G. Coquerel, *Cryst. Growth Des.* **2011**, *11*, 2453–2462.
- [26] a) K. Kinbara, Y. Hashimoto, M. Sukegawa, H. Nohira, K. Saigo, *J. Am. Chem. Soc.* **1996**, *118*, 3441–3449; b) A. Galland, V. Dupray, B. Berton, S. Morin, M. Sanselme, H. Atmani, G. Coquerel, *Cryst. Growth Des.* **2009**, *9*, 2713–2718.
- [27] O. Kahn, *Molecular Magnetism*, Wiley-VCH, New York, **1993**, pp. 23–26.
- [28] A. Doudouh, C. Woltermann, P. C. Gos, *J. Org. Chem.* **2007**, *72*, 4978.
- [29] COLLECT data collection software, B. V. Nonius, **1998**.
- [30] Z. Otwinowski, W. Minor, *Methods in Enzymology*, Vol. 276: Processing of X-ray Diffraction Data Collected in Oscillation Mode of Macromolecular Crystallography, Part A (Eds.: C. W. Carter, Jr., R. M. Sweet), Academic Press, New York, **1997**, pp. 307–326.
- [31] G. M. Sheldrick, SADABS, Bruker Nonius area-detector scaling and absorption correction, V2.10.
- [32] CrystalClear-SM Expert 2.0 r7 (Rigaku, 2011).
- [33] G. M. Sheldrick, SHELX97, Programs for Crystal Structure Analysis (Release 97-2), University of Göttingen, Göttingen, Germany, **1998**.
- [34] J. Bruno, J. C. Cole, P. R. Edgington, M. Kessler, C. F. Macrae, P. McCabe, J. Pearson, R. Taylor, *Acta Crystallogr. Sect. B* **2002**, *B58*, 389.
- [35] CrysAlis CCD and CrysAlis RED, versions 1.171.33.55; Oxford Diffraction Ltd: Yarnton, Oxfordshire, UK, **2012**.
- [36] O. V. Dolomanov, A. J. Blake, N. R. Champness, M. J. Schröder, *Appl. Crystallogr.* **2003**, *36*, 1283.
- [37] G. M. Sheldrick, SHELXS-97 and SHELXL-97; University of Göttingen: Göttingen, Germany, **1997**.
- [38] Bruker, APEX2 Software, Bruker AXS Inc. V2012.2, Madison, Wisconsin, USA, **2012**.
- [39] Bruker, SAINT, Area Detector Integration Software, Bruker AXS Inc., V8.18c Madison, Wisconsin, USA, **1997**.
- [40] SQUEEZE: P. van der Sluis, A. L. Spek, *Acta Crystallogr. Sect. A* **1990**, *46*, 194–201.
- [41] S. Clevers, F. Simon, V. Dupray, G. Coquerel, *J. Therm. Anal. Calorim.* **2013**, *112*, 271–277.
- [42] For a powder technique for the evaluation of nonlinear optical materials, see: S. K. Kurtz, T. T. Perry, *J. Appl. Phys.* **1968**, *39*, 3798–3813.
- [43] a) E. Ruiz, P. Alemany, S. Alvarez, J. Cano, *J. Am. Chem. Soc.* **1997**, *119*, 1297–1303; b) E. Ruiz, J. Cano, S. Alvarez, *Chem. Eur. J.* **2005**, *11*, 4767–4771; c) E. Ruiz, T. Cauchy, J. Cano, R. Costa, J. Tercero, S. Alvarez, *J. Am. Chem. Soc.* **2008**, *130*, 7420–7426.
- [44] a) E. Ruiz, *Struct. Bonding* **2004**, *113*, 71–102; b) E. Ruiz, S. Alvarez, J. Cano, V. Polo, *J. Chem. Phys.* **2005**, *123*, 164110.
- [45] E. Ruiz, J. Cano, S. Alvarez, P. Alemany, *J. Comp. Chem.* **1999**, *20*, 1391–1400.
- [46] E. Ruiz, A. Rodríguez-Forteza, J. Cano, S. Alvarez, P. Alemany, *J. Comp. Chem.* **2003**, *24*, 982–989.
- [47] E. Ruiz, A. Rodríguez-Forteza, J. Tercero, T. Cauchy, C. Massobrio, *J. Chem. Phys.* **2005**, *123*, 074102.
- [48] A. D. Becke, *J. Chem. Phys.* **1993**, *98*, 5648–5652.
- [49] A. Schäfer, C. Huber, R. Ahlrichs, *J. Chem. Phys.* **1994**, *100*, 5829–5835.
- [50] Gaussian 09, Revision B.01, M. J. Frisch, G. W. Trucks, H. B. Schlegel, G. E. Scuseria, M. A. Robb, J. R. Cheeseman, G. Scalmani, V. Barone, B. Menucci, G. A. Petersson, H. Nakatsuji, M. Caricato, X. Li, H. P. Hratchian, A. F. Izmaylov, J. Bloino, G. Zheng, J. L. Sonnenberg, M. Hada, M. Ehara, K. Toyota, R. Fukuda, J. Hasegawa, M. Ishida, T. Nakajima, Y. Honda, O. Kitao, H. Nakai, T. Vreven, J. A. Montgomery, Jr., J. E. Peralta, F. Ogliaro, M. Bearpark, J. J. Heyd, E. Brothers, K. N. Kudin, V. N. Staroverov, R. Kobayashi, J. Normand, K. Raghavachari, A. Rendell, J. C. Burant, S. S. Iyengar, J. Tomasi, M. Cossi, N. Rega, J. M. Millam, M. Klene, J. E. Knox, J. B. Cross, V. Bakken, C. Adamo, J. Jaramillo, R. Gomperts, R. E. Stratmann, O. Yazyev, A. J. Austin, R. Cammi, C. Pomelli, J. W. Ochterski, R. L. Martin, K. Morokuma, V. G. Zakrzewski, G. A. Voth, P. Salvador, J. J. Dannenberg, S. Dapprich, A. D. Daniels, Ö. Farkas, J. B. Foresman, J. V. Ortiz, J. Cioslowski, D. J. Fox, Gaussian, Inc., Wallingford CT, **2009**.
- [51] *Jaguar 7.0*: Schrödinger, LLC, New York, **2007**.
- [52] G. Vacek, J. K. Perry, J.-M. Langlois, *Chem. Phys. Lett.* **1999**, *310*, 189–194.

Received: August 2, 2013

Published online on December 12, 2013

## Synthesis and Crystallographic Studies of Disubstituted Carboranyl Alcohol Derivatives: Prevailing Chiral Recognition?

Florencia Di Salvo,<sup>†,‡</sup> Christos Paterakis,<sup>†</sup> Min Ying Tsang,<sup>†</sup> Yolanda García,<sup>†</sup> Clara Viñas,<sup>†</sup> Francesc Teixidor,<sup>†</sup> José Giner Planas,<sup>\*,†</sup> Mark E. Light,<sup>‡</sup> Michael B. Hursthouse,<sup>‡,⊥</sup> and Duane Choquesillo-Lazarte<sup>§</sup>

<sup>†</sup>Institut de Ciència de Materials de Barcelona (ICMAB-CSIC), Campus UAB, 08193 Bellaterra, Spain

<sup>‡</sup>School of Chemistry, University of Southampton, Highfield, Southampton SO171BJ, United Kingdom

<sup>⊥</sup>Department of Chemistry, Faculty of Science, King Abdulaziz University, Jeddah 21588, Saudi Arabia

<sup>§</sup>Laboratorio de Estudios Cristalográficos,, IACT-CSIC, Armilla, Granada, Spain.

**S** Supporting Information

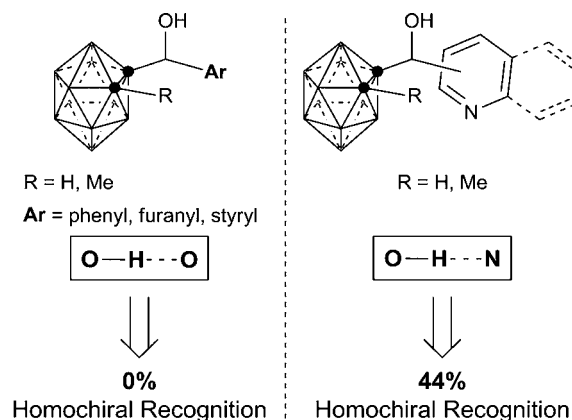
**ABSTRACT:** The syntheses of new *o*-carboranyldiols bearing aromatic rings bis-[R(hydroxy)methyl]-1,2-dicarbocloso-dodecaborane (R = 2-pyridyl **1a**, 3-pyridyl **1b**, 4-pyridyl **1c**, 2-quinolyl **1d**, 4-quinolyl **1e**, phenyl **1f**) are reported. The compounds are obtained as mixtures of meso (*syn*) and racemic (*anti*) stereoisomers with a slight diastereomeric excess (*syn:anti* ratio of 0.7:1) in all cases but in **1b**. The crystal structures of the meso compounds *syn-1a*·2MeOH, *syn-1b*, *syn-1f*·0.25H<sub>2</sub>O and racemic *anti-1a*·MeOH, *anti-1a*·EtOH, and *anti-1d*·2H<sub>2</sub>O are reported. We provide an analysis of these compounds by means of NMR and X-ray crystallography, in the context of crystal engineering and chiral recognition. The results show that the crystal packings for these alcohols are dominated by the supramolecular O–H···N and/or O–H···O hydrogen bonds. Supramolecular analysis of all compounds in this work reveals that homochiral self-assembly, that is, formation of homochiral hydrogen bonded complexes, prevails over heterochiral self-assembly (formation of heterochiral hydrogen bonded complexes).

**■ INTRODUCTION**

The importance of self-assembly and self-organization for the creation of higher order functional structures is evident in natural systems, and the self-assembly of chiral supramolecular species is common in nature.<sup>1</sup> However, the design and preparation of chiral artificial self-assembled systems is an ongoing challenge to the chemist.<sup>1,2</sup> Handshake practice in humans underlines the fact that interactions between pairs of chiral objects depends on their relative handedness. Thus, pairs of right (or left) hands match better than mixed right/left pairs, and, if we force the latter, the grip will be a quite different one. Molecular chirality is a pervasive phenomenon in nature, and an especially striking aspect is the homochirality of life.<sup>1</sup> Homochiral recognition (also termed self-recognition, or homochiral self-assembly)<sup>2,3</sup> of a chiral molecule is a recognition process like a handshake; that is, an enantiomer preferentially recognizes itself to generate homochiral self-assemblies (R···R and S···S). When an enantiomer preferentially recognizes its mirror image (termed heterochiral recognition, self-discrimination, or heterochiral self-assembly),<sup>2,3</sup> it generates heterochiral self-assemblies (R···S). Many examples have been reported of homochiral recognition from the corresponding racemic mixture.<sup>3a,4</sup> Less common is the homochiral self-assembly of *meso*-compounds incorporating both enantiomeric interaction moieties to generate homochiral self-assemblies (R–S···S–R···R–S···).

We have recently synthesized and studied the supramolecular structures of a family of chiral *o*-carboranylalcohols (Scheme 1), which are isolated as racemic mixtures.<sup>6</sup> These molecules, that

**Scheme 1. Summary of Supramolecular Synthons for Previously Reported First Generation of Carboranyl Alcohols and Homochiral Recognition**



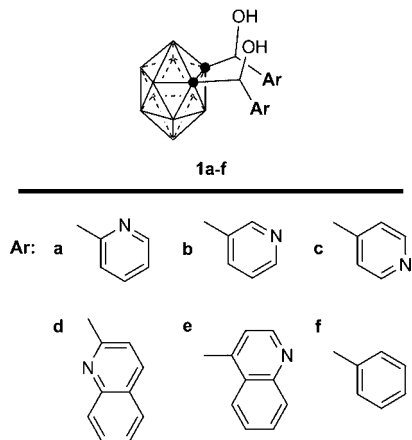
**Received:** October 31, 2012

**Revised:** February 12, 2013

**Published:** February 18, 2013

are prepared in very good yields from one pot reactions and from readily available starting materials, are centered around an *o*-carborane core (*closo*-1,2- $C_2B_{10}H_{10}$ ) with one arm radiating out of one of the cluster carbons, containing a chiral carbon that bears an alcohol and an aromatic moiety. The high thermal and chemical stability, hydrophobicity, acceptor character, ease of functionalization, and three-dimensional nature of the icosahedral carborane clusters make these new molecules valuable ligands in coordination chemistry, and we have just published our first results on the metallosupramolecular chemistry of these ligands.<sup>7</sup> Crystallization of the racemic monosubstituted *o*-carboranylalcohols bearing non-nitrogenated aromatic rings (left of Scheme 1) showed no homochiral recognition. For example, cyclic tetramers sustained by intermolecular O–H...O hydrogen bonds were often observed where *S* and *R* enantiomers alternate.<sup>6b</sup> However, when a nitrogenated aromatic ring was added to the *o*-carboranylalcohols (Scheme 1, right), nearly half of the solved structures (four out of nine) showed homochiral recognition.<sup>6c</sup> In these cases, O–H...N hydrogen bonded homochiral chains (either *S* or *R*) were observed. In our continuing exploration of the synthetic and structural chemistry of the *o*-carboranyl alcohols we now report the synthesis and structures (in solution and solid states) of the disubstituted *o*-carboranylalcohols **1a–f** (Scheme 2). The

Scheme 2. Second Generation of Carboranyl Alcohols



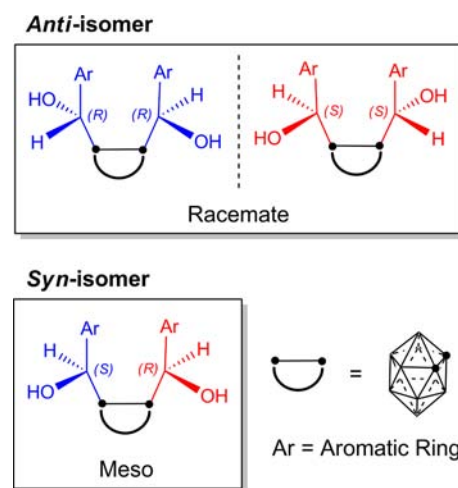
latter constitute a second generation of compounds where two arms radiate out of the cluster carbons with each containing a pyridyl or quinolylmethylalcohol with a chiral carbon. The presence of two chiral carbons per molecule and the different positional isomers offer enough molecular and supramolecular diversity to explore the interactions of molecules in crystal packing. We are particularly interested in the effect that disubstitution may have on crystallization, crystal structures, and networks but also in the potential use of these disubstituted carboranes as ligands in metallosupramolecular chemistry.<sup>8</sup> We show that the aryl(phenyl, pyridyl or quinolyl)methylalcohol moieties in disubstituted *o*-carboranes presented in this paper interact with the surrounding moieties in what it seems a completely enantioselective manner giving homochiral self-assemblies.

## RESULTS AND DISCUSSION

**Synthesis.** Following our previous reports,<sup>6</sup> the new bis-pyridylmethyl or -quinolylmethyl alcohols derived from the *o*-carborane cluster (**1a–f**; Scheme 2; from now on *o*-

carboranyldiols) have been prepared by the reaction of dilithiated *o*-carborane with different aromatic aldehydes at low temperature and isolated in reasonable yields (45–78%). While we were synthesizing this family of new compounds, Nie and co-workers published the synthesis of compound **1a** and the X-ray structure for two different unsolvated polymorphs.<sup>9</sup> However, only partial characterization of **1a** is given in the original publication, and the authors failed to recognize the presence of several stereoisomers in this compound. Therefore, we report here the syntheses and complete full characterization of this new family of diols, including that for **1a**, in solution and solid state. As shown in Scheme 3, *o*-carboranyldiol compounds

Scheme 3. Stereoisomers for Compounds **1a–f**



**1a–f** contain two chiral centers that can adopt either *R* or *S* configuration and therefore could lead to the formation of two diastereoisomers, a meso compound (*RS*; OH groups in a *syn* orientation) and a racemic compound (mixture of *SS* and *RR*; OH groups in an *anti* orientation). In the following discussion we will name *anti* or *syn*-isomers as the racemate or meso compounds, respectively, as shown in Scheme 3.

All new compounds have been fully characterized by standard spectroscopic and analytical techniques, and the data correlated well with that of related alcohols.<sup>6</sup> Table 1 summarizes selected spectroscopic data for all synthesized *o*-carboranyldiols **1a–f** and the ratio of diastereoisomers after work up. As an example, the <sup>1</sup>H NMR spectrum for a mixture of *anti*- and *syn*-diastereoisomers of **1a**, as obtained in the synthesis, shows two sets of signals for the OH and CHOH groups in a 1:0.65 ratio for a mixture of *anti*-**1a** and/or *syn*-**1a**. Proton resonances for the OH and CHOH groups in the mixture appeared in the same range as that for the previously reported monosubstituted alcohols. Accordingly, two sets of <sup>13</sup>C NMR resonances are observed for a mixture of diastereoisomers in solution. OH and CHOH signals for each diastereoisomer have been unequivocally confirmed by a combination of <sup>1</sup>H–<sup>13</sup>C{<sup>1</sup>H} correlation (SI) and X-ray diffraction (XRD) studies. Thus, the *anti*-**1a** diastereoisomer shows proton resonances for the OH and CHOH groups at 6.36 and 5.76 ppm as broad signals, whereas the *syn*-**1a** diastereoisomer signals appear at 6.22 and 5.99 ppm, respectively. The molecule in the *syn*-**1a** diastereoisomer has a mirror symmetry plane that makes both OH and CH equivalent in the NMR spectrum. *Anti*-**1a** diastereoisomer has a

Table 1. Selected  $^1\text{H}$  NMR Signals (ppm) for Diastereoisomers of 1a–f in Acetone- $d_6$  unless Noted

Ar	compound	syn ( <i>meso</i> )		anti ( <i>racemate</i> )		ratio <sup>a</sup> ( <i>anti:syn</i> )
		CH	OH	CH	OH	
2-Py	1a	5.98 (d, 6.3)	6.19 (d, 6.5)	5.75 (d, 6.4)	6.35 (d, 6.5)	(1: 0.65)
3-Py	1b	5.71 (d, 4.9) <sup>b</sup>	6.81 (d, 5.0) <sup>b</sup>	5.59 (d, 5.0) <sup>b</sup>	7.25 (d, 5.5) <sup>b</sup>	(1: 0.78)
4-Py	1c	5.19 (br)	6.40 (br)	5.01 (br)	6.80 (br)	(1: 0.62)
2-Q	1d	6.32 (br)	6.52 (br)	6.04 (br)	6.75 (br)	(1: 0.69)
4-Q	1e	7.00 (br)	c	6.92 (br)		(1: 0.71)
Ph	1f	5.15 (d, 4.9)	6.15 (d, 4.8)	5.01 (d, 5.1)	6.48 (d, 5.1)	(1: 0.71)

<sup>a</sup>Ratio of diastereoisomers estimated by NMR integration of the CH(OH) signals after work up. <sup>b</sup>In DMSO- $d_6$ . <sup>c</sup>Not observed.

2-fold ( $C_2$ ) axis of symmetry that also makes both OH and both CH hydrogen equivalents in this isomer. Similar solubilities and polarities for these two diastereoisomers have prevented, to date, their effective separation. However, certain diastereomeric enrichment has been achieved after preparative TLC trials and although in fairly small amounts, it was enough to run  $^1\text{H}$  NMR experiments. NMR spectra for *anti*-1a and *syn*-1a diastereoisomers and their mixture are shown in the Supporting Information (SI). Effective diastereomer separation has, to date, not been possible in either of the compounds in this work, except in case of the 3-pyridine derivative 1b. Different solubilities of *anti*-1b and *syn*-1b indeed allowed their separation during work up. From Table 1, it can be seen that in all cases a slight diastereomeric excess of the *anti*- over the *syn*-diastereoisomers is observed ( $\sim 1: 0.7$  ratio). The latter probably reflects a higher steric interaction of the OH groups in the *syn*-isomers than in the *anti*-ones which slightly favor the formation of the latter over the former. We are currently working in the separation of *syn*- and *anti*-diastereoisomers for these compounds.

$^{11}\text{B}\{^1\text{H}\}$  NMR spectra for all compounds are consistent with a *closo*-icosahedral geometry for the boron cage.<sup>10</sup>  $^{13}\text{C}\{^1\text{H}\}$  NMR spectra also show characteristic peaks for the two cage-carbon vertices,  $N_{\text{AR}}$  rings and benzyl CH carbons. As for the monosubstituted derivatives, solid state IR spectra for all compounds show diagnostic signals for the OH and BH stretching frequencies in the ranges 3394–3031 and 2630–2561  $\text{cm}^{-1}$ , respectively.

**Molecular Structures.** The molecular structures for compounds *anti*-1a, *syn*-1b, *anti*-1d, and *syn*-1f were unequivocally established by single crystal X-ray diffraction and are in agreement with the NMR data. Six crystal structures have been determined (Figures 1–5), five of them as solvates (*syn*-1a·2MeOH, *anti*-1a·MeOH, *anti*-1a·EtOH, *anti*-1d·2H<sub>2</sub>O, and *syn*-1f·0.25H<sub>2</sub>O) and one without solvent molecules in its lattice (*syn*-1b). Experimental crystal data and structure refinement parameters for the new diols structures reported in this work are listed in Table 2. Due to the critical role that the hydrogen atom of the alcohol function plays in the supramolecular assemblies, its position was determined from the difference map and refined freely without any geometrical or thermal parameter restraints when possible (see Experimental Section for details). Whereas *syn*-1a·2MeOH, *anti*-1a·MeOH, *anti*-1a·EtOH, *anti*-1d·2H<sub>2</sub>O, and *syn*-1f·H<sub>2</sub>O crystallize in centrosymmetric space groups (Table 2), compound *syn*-1b crystallizes in the non-centrosymmetric space group *Pna*2<sub>1</sub>. The molecular structures for all these alcohols show typical icosahedrons with very similar bond distances and angles, and also similar to those in other *o*-carboranyl alcohols.<sup>6</sup> Comparative tables are included in the SI.  $C_{\text{cluster}}-C_{\text{cluster}}$  bond lengths vary from 1.667–1.712 Å and

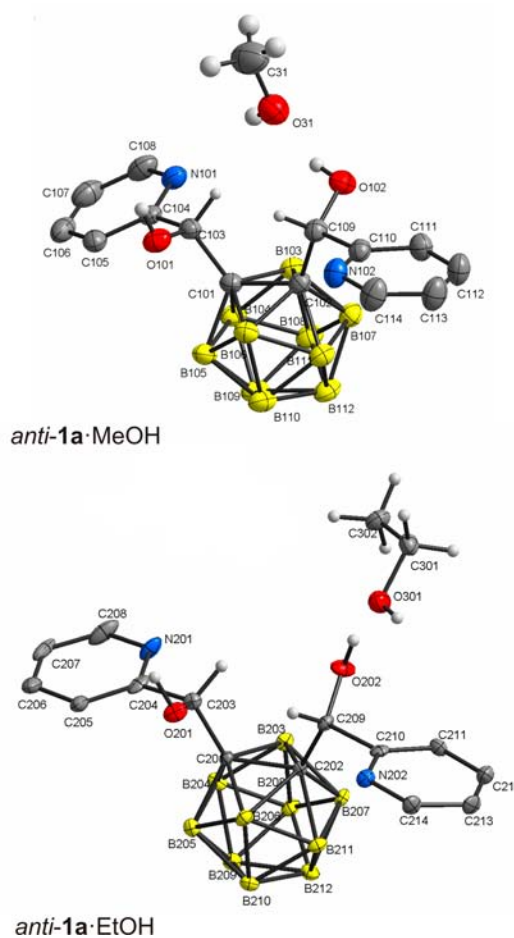
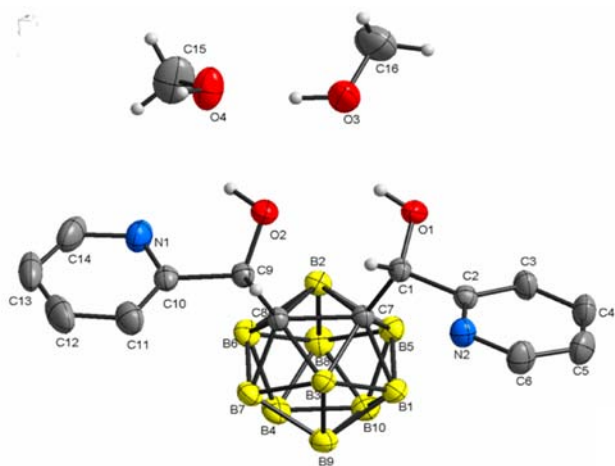
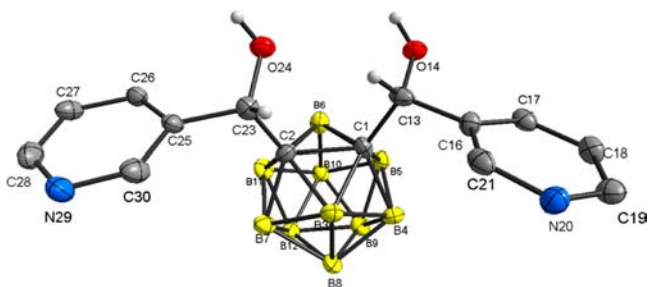


Figure 1. Molecular structures of *anti*-1a·MeOH (top) and *anti*-1a·EtOH (bottom); thermal ellipsoids set at 35% probability (B–H and pyridine hydrogen atoms are omitted for clarity).

being slightly larger than the related monosubstituted derivatives.<sup>6</sup> The latter is well-known to happen in disubstituted *o*-carboranes due to both the electronic and steric nature of the substituents.<sup>11</sup> Carbon–oxygen bond lengths are consistent with a single C–O bond. It is, however, interesting to note that compounds *syn*-1a, *syn*-1a·2MeOH, *anti*-1a·MeOH, *anti*-1a·2EtOH, and *anti*-1d·2H<sub>2</sub>O show shorter C–O bond lengths (1.400–1.409 Å) than *syn*-1b and *syn*-1f·2H<sub>2</sub>O compounds (1.421–1.430 Å). As expected, *syn* isomers show smaller OCCO torsion angles ( $-0.5$  to  $29^\circ$ ) than the *anti* isomers ( $-135$  to  $146^\circ$ ). Refinement of the methanol solvated structure for the *anti*-1a compound deserves some comments. Residual electron density was found in the crystals grown from methanol for this compound. A part of the electron density was modeled



**Figure 2.** Molecular structure of *syn-1a*·2MeOH; thermal ellipsoids set at 35% probability (B–H and pyridine hydrogen atoms are omitted for clarity).



**Figure 3.** Molecular structure of *syn-1b*; thermal ellipsoids set at 35% probability (B–H and pyridine hydrogen atoms are omitted for clarity).

as two methanol molecules per asymmetric unit, one showing two-orientation disorder, but some could not be fully modeled as it was found to be substantially disordered. Therefore, SQUEEZE<sup>12</sup> was utilized to account for the contribution of the extra diffuse electron density to the scattering (see Experimental Section for details).

**Supramolecular Structures.** Crystal structures for all alcohols in this study are based on O–H···N and/or O–H···O hydrogen bonds (Table 3 and Figures 6–11). The distances of all of the observed intra- and/or intermolecular O–H···N/O hydrogen bonds are substantially shorter than the 2.75/2.72 Å

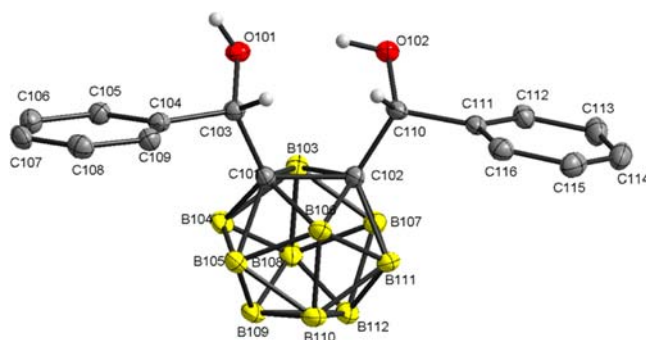


**Figure 5.** Molecular structure of *syn-1f*; thermal ellipsoids set at 35% probability (B–H and phenyl hydrogen atoms are omitted for clarity).

that corresponds to the sum of the van der Waals radii ( $\sum vdw$ ) of hydrogen and nitrogen/oxygen atoms (Table 3), and those intermolecular ones are near-linear. Thus, they qualify as moderate strength hydrogen bonds.<sup>13</sup>

**2-Pyridine Derivative (1a).** As mentioned above, three different solvated structures have been determined for compound **1a**: the meso form *syn-1a*·2MeOH and two different solvates of the racemate *anti-1a*·MeOH and *anti-1a*·EtOH. Their supramolecular structures are shown in Figures 6 and 7. For comparison reasons, the previously reported structure for unsolvated form *syn-1a*<sup>9</sup> will be briefly described here, making special emphasis on those aspects not mentioned in the previous report that are relevant to the following discussion. Compound *syn-1a* forms centrosymmetric dimers in a similar way to that found in the related monosubstituted compound (Scheme 1, right).<sup>6c</sup> Figure 6 shows the formation of dimers of *syn-1a* through two bifurcated O–H···(N)(O) hydrogen bonds, one intra (with nitrogen) and one intermolecular (with oxygen) along a similar direction to that of the *c* axis (Table 3). The remaining OH groups are involved in intramolecular O–H···N hydrogen bonds, and this facilitates intramolecular C–H···O interactions. However, the most relevant feature in the supramolecular structure of *syn-1a* is that their dimers are formed by what it seems self-recognition and therefore provide homochiral dimers (top of Figure 6). This is in contrast with the related monosubstituted 2-pyridine *o*-carboranylalcohol compound that forms heterochiral dimers.<sup>6c</sup> However, in the disubstituted *o*-carboranyldiol *syn-1a* the (*R*)-pyridylmethylalcohol moiety interacts exclusively with (*R*)-moieties, and the (*S*)-moiety interacts with only (*S*)-moieties, to form the observed homochiral dimers. In order to satisfy this homochiral

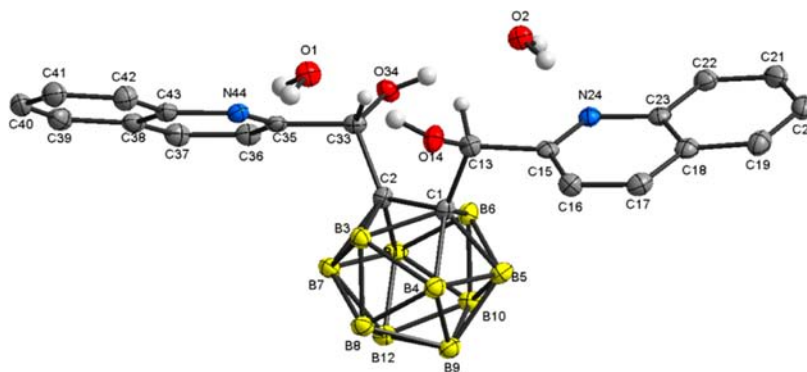


**Figure 4.** Molecular structure of *anti-1d*·2H<sub>2</sub>O; thermal ellipsoids set at 35% probability (B–H and quinoline hydrogen atoms are omitted for clarity).



Table 2. Crystal Data and Refinement Details for Structures of Compounds 1a, 1b, 1d, and 1f<sup>a</sup>

	<i>syn-1a</i> ·2MeOH	<i>anti-1a</i> ·MeOH	<i>anti-1a</i> ·EtOH	<i>syn-1b</i>	<i>anti-1d</i> ·2H <sub>2</sub> O	<i>syn-1f</i> ·0.25H <sub>2</sub> O
empirical formula	C <sub>14</sub> H <sub>22</sub> B <sub>10</sub> N <sub>2</sub> O <sub>2</sub> ·2(CH <sub>3</sub> OH)	C <sub>14</sub> H <sub>22</sub> B <sub>10</sub> N <sub>2</sub> O <sub>2</sub> ·(CH <sub>3</sub> OH) <sub>solv</sub>	C <sub>14</sub> H <sub>22</sub> B <sub>10</sub> N <sub>2</sub> O <sub>2</sub> ·2(CH <sub>3</sub> CH <sub>2</sub> OH)	C <sub>14</sub> H <sub>22</sub> B <sub>10</sub> N <sub>2</sub> O <sub>2</sub>	C <sub>22</sub> H <sub>30</sub> B <sub>10</sub> N <sub>2</sub> O <sub>4</sub>	C <sub>16</sub> H <sub>24</sub> B <sub>10</sub> O <sub>2</sub> ·0.25(H <sub>2</sub> O)
formula weight	422.52	390.48 <sup>b</sup>	404.50	358.44	494.58	1443.82
crystal system	monoclinic	monoclinic	orthorhombic	orthorhombic	monoclinic	triclinic
space group	<i>P</i> 2 <sub>1</sub> / <i>c</i>	<i>C</i> 2/ <i>c</i>	<i>Pbca</i>	<i>Pna</i> 2 <sub>1</sub>	<i>P</i> 2 <sub>1</sub> / <i>c</i>	<i>P</i> $\bar{1}$
unit cell dimensions [Å] and [°]	<i>a</i> = 10.6829(14)  <i>b</i> = 20.759(3)  <i>c</i> = 10.5063(15)  $\beta$ = 90.807(12)	<i>a</i> = 28.260(2)  <i>b</i> = 16.0016(8)  <i>c</i> = 20.5751(16)  $\beta$ = 111.289(9)	<i>a</i> = 16.040(3)  <i>b</i> = 20.284(4)  <i>c</i> = 26.321(6)	<i>a</i> = 14.947(3)  <i>b</i> = 11.1698(19)  <i>c</i> = 11.0133(18)	<i>a</i> = 6.8505(2)  <i>b</i> = 22.9746(8)  <i>c</i> = 15.8013(6)  $\beta$ = 93.117(2)	<i>a</i> = 12.7294(2)  <i>b</i> = 15.8942(3)  <i>c</i> = 20.7959(5)  $\alpha$ = 87.4520(10) $\beta$ = 72.7600(10) $\gamma$ = 85.3720(10)
volume [Å <sup>3</sup> ]	2318.0(6)	8669.3(10)	8564(3)	1838.7(5)	2483.25(15)	4004.43(14)
Z	4	16	16	4	4	2
$\rho_{\text{calcd}}$ [g cm <sup>-3</sup> ]	1.211	1.197	1.255	1.295	1.323	1.197
absorption coeff [mm <sup>-1</sup> ]	0.076	0.072	0.076	0.075	0.640	0.068
<i>F</i> (000)	888	3264	3392	744	1032	1508
crystal	prismatic, colorless	hexagonal, colorless	fragment, colorless	block, colorless	block, clear light orange	block, colorless
crystal size [mm]	0.13 × 0.11 × 0.104	0.26 × 0.19 × 0.108	0.12 × 0.10 × 0.03	0.10 × 0.07 × 0.04	0.14 × 0.08 × 0.06	0.40 × 0.20 × 0.15
$\theta$ range for data collection [°]	3.53–28.95	3.77–7.48	2.97–25.02	2.28–24.20	3.40–66.59	2.96–25.03
reflections collected	32898	28845	41104	8593	13008	79710
independent reflections	5279 [ <i>R</i> <sub>int</sub> = 0.1417]	9613 [ <i>R</i> <sub>int</sub> = 0.0624]	7545 [ <i>R</i> <sub>int</sub> = 0.0847]	2781 [ <i>R</i> <sub>int</sub> = 0.1068]	4330 [ <i>R</i> <sub>int</sub> = 0.0352]	14123 [ <i>R</i> <sub>int</sub> = 0.0862]
completeness to $\theta$ = [°], [%]	27.48°, 99.3%	27.48°, 96.6%	25.02°, 99.8%	24.20°, 98.8%	66.59°, 98.9%	25.03°, 99.8%
max and min transmission	0.9925 and 0.9902	0.987 and 0.982	0.9977 and 0.9910	0.9970 and 0.9925	0.960 and 0.890	0.9899 and 0.9735
largest difference peak and hole [e Å <sup>-3</sup> ]	0.55 and -0.27	0.56 and -0.39	0.712 and -0.428	0.241 and -0.213	0.261 and -0.190	0.535 and -0.348
data/restraints/parameters	5279/0/295	9613/0/552	7545/6/579	2781/1/255	4330/51/387	14123/65/1055
goodness-of-fit on <i>F</i> <sup>2</sup>	1.059	1.053	1.350	0.994	1.043	1.085
final <i>R</i> indices [ <i>F</i> <sup>2</sup> > 2 $\sigma$ ( <i>F</i> <sup>2</sup> )]	<i>R</i> <sub>1</sub> = 0.0701, <i>wR</i> <sub>2</sub> = 0.1780	<i>R</i> <sub>1</sub> = 0.0818, <i>wR</i> <sub>2</sub> = 0.2251	<i>R</i> <sub>1</sub> = 0.1264, <i>wR</i> <sub>2</sub> = 0.2439	<i>R</i> <sub>1</sub> = 0.0638, <i>wR</i> <sub>2</sub> = 0.1263	<i>R</i> <sub>1</sub> = 0.0393, <i>wR</i> <sub>2</sub> = 0.0941	<i>R</i> <sub>1</sub> = 0.0719, <i>wR</i> <sub>2</sub> = 0.1538
<i>R</i> indices (all data)	<i>R</i> <sub>1</sub> = 0.1138, <i>wR</i> <sub>2</sub> = 0.2193	<i>R</i> <sub>1</sub> = 0.1178, <i>wR</i> <sub>2</sub> = 0.2529	<i>R</i> <sub>1</sub> = 0.1382, <i>wR</i> <sub>2</sub> = 0.2499	<i>R</i> <sub>1</sub> = 0.1112, <i>wR</i> <sub>2</sub> = 0.1544	<i>R</i> <sub>1</sub> = 0.0543, <i>wR</i> <sub>2</sub> = 0.1030	<i>R</i> <sub>1</sub> = 0.1065, <i>wR</i> <sub>2</sub> = 0.1688

<sup>a</sup>CCDC 905022 (*syn-1a*·2MeOH), 905023 (*anti-1a*·MeOH), 905021 (*anti-1a*·EtOH), 902365 (*syn-1b*), 902366 (*anti-1d*·2H<sub>2</sub>O), 905020 (*syn-1f*) contain the supplementary crystallographic data for this paper. These data can be obtained free of charge from The Cambridge Crystallographic Data Centre via [www.ccdc.cam.ac.uk/data\\_request/cif](http://www.ccdc.cam.ac.uk/data_request/cif). <sup>b</sup>Squeeze suggests an additional solvent component of 0.125 MeOH per formula unit that has not been included in the refined structure.

self-assembly, carborane cages in the dimers are arranged upside down (this is the only way to shake both hands without crossing arms!). The methanol solvated compound of the later, *syn-1a*·2MeOH, also forms dimers. However, in this case two methanol molecules interrupt the intermolecular hydrogen bonds observed in dimers for the unsolvated *syn-1a*, giving the arrangement shown at the bottom of Figure 6. It is, however, quite interesting to note that the arrangement of chiral pyridylmethanol moieties resemble very much that for the corresponding moieties in the unsolvated *syn-1a* (*R* interacts with *R* and *S* with *S*). As in the monosubstituted derivative, dimers of *syn-1a* are closely packed by intermolecular C–H...O interactions [C(9)–H(9)...O(2) 2.524 Å, CHO 145.9°] leading to the formation of a polymeric chain along the *a* axis (Figure S9 in SI). The solid state structures for the unsolvated *syn-1a* and the methanol solvated *syn-1a*·2MeOH are built by self-assembly of the polymeric hydrogen bonded networks shown in Figure 6, which are dominated by weak dihydrogen and/or hydrophobic interactions (SI).

Crystal structures for racemates *anti-1a*·MeOH and *anti-1a*·EtOH also show dimeric supramolecular structures (Figure

7). Note that although the spacegroups are different, the cell dimensions and the overall crystal structures are also very similar. *o*-Carboranyldiol molecules in each dimer interact by intermolecular O–H...N hydrogen bonds resulting in a R<sub>2</sub>,2(16) ring. This leaves two donors (OH) and two acceptors (N) available in each dimer that can interact with appropriate solvent molecules. Thus, two molecules of methanol or ethanol act as hydrogen bond donors and acceptors to form two D<sub>2</sub>,2(4) patterns. As observed in the previous structures, homochiral self-assembly (*S*–*S*...*S*–*S* and *R*–*R*...*R*–*R* not shown in Figure 7) seems to occur in both *anti-1a*·MeOH and *anti-1a*·2EtOH. More importantly, dimers of the same chirality assemble around a crystallographic 2<sub>1</sub> screw axes (along *c* or *b* in *anti-1a*·MeOH or *anti-1a*·2EtOH, respectively) to generate channels that are occupied by the guest solvents (Figure 7). Channels generated by dimers of different chirality alternate in the 3D structure for these compounds (SI). It is noteworthy that only weak intermolecular forces operate between these two channels.

**3-Pyridine (1b) and Phenyl (1f) Derivatives.** As shown at the top of Figure 8, meso *syn-1b* uses both OH moieties in each molecule to form intermolecular O–H...N hydrogen bonds

**Table 3.** Geometrical Parameters of D–H...A (D: donor; A: acceptor) Contacts (Å, °), Involved in the Supramolecular Construction in *syn-1a*, *syn-1a*·2MeOH, *anti-1a*·MeOH, *anti-1a*·EtOH, *anti-1d*·2H<sub>2</sub>O, and *syn-1f*·0.25H<sub>2</sub>O

compound	D–H...A <sup>a</sup>	d(H...A)	d(O...A)	∠(OHA)
<i>syn-1a</i> <sup>b</sup>	O(2)–H...O(1)	2.07	2.835(2)	155.8
	O(1)–H...N(1) intramol.	2.07	2.591(3)	120.9
	O(2)–H...N(2) intramol.	2.38	2.748(3)	108.0
<i>syn-1a</i> ·2MeOH	O(1)–H...O(3)	2.09	2.808(3)	146.6
	O(2)–H...O(4)(MeOH)	2.26	2.929(3)	138.5
	O(2)–H...N(1) intramol.	2.18	2.668(3)	118.0
	MeO(3)–H...O(4)(MeOH)	1.89	2.706(3)	171.8
	MeO(4)–H...N(2) <sup>i</sup>	2.01	2.828(3)	175.5
<i>anti-1a</i> ·MeOH	O(202)–H...N(102) <sup>ii</sup>	2.04	2.828(2)	161.7
	O(101)–H...N(201) <sup>ii</sup>	2.06	2.847(2)	159.5
	O(201)–H...O(41A)(MeOH) <sup>ii</sup>	1.89	2.674(2)	160.3
	MeO(41A)–H...O(102)	2.18	2.811(2)	134.16
	O(102)–H...O(31)(MeOH)	2.01	2.807(2)	131.5
	MeO(31)–H...N(101)	2.27	2.882(2)	131.5
<i>anti-1a</i> ·EtOH	O(101)–H...N(202) <sup>iii</sup>	1.91	2.831(5)	162.7
	O(201)–H...N(102)	1.93	2.816(5)	154.7
	O(202)–H...O(301)(EtOH)	1.97	2.854(5)	164.5
	O(102)–H...O(301)(EtOH)	1.95	2.697(5)	149.8
	EtO(301)–H...O(401)(EtOH) <sup>iii</sup>	1.86	2.680(5)	164.7
	EtO(401)–H...N(101) <sup>iv</sup>	2.07	2.911(6)	176.9
<i>syn-1b</i>	O(24)–H...N(20) <sup>v</sup>	1.88	2.690(5)	162.2
	O(14)–H...N(29) <sup>vi</sup>	1.97	2.771(5)	161.7
<i>anti-1d</i> ·2H <sub>2</sub> O	O(14)–H...O(1)H <sub>2</sub>	1.96	2.7942(16)	172.00
	O(34)–H...O(2)H <sub>2</sub>	1.89	2.7177(16)	170.50
	HO(1)–H...O(34) <sup>vii</sup>	2.05	2.7926(15)	142.2
	HO(2)–H...O(14) <sup>viii</sup>	2.03	2.7889(16)	144.2
	HO(1)–H...N(44)	2.10	2.9726(18)	170.7
	HO(2)–H...N(24)	1.96	2.8367(17)	170.1
<i>syn-1f</i> ·0.25H <sub>2</sub> O	O(102)–H...O(101)	2.01	2.829(3)	160(2)
	O(201)–H...O(202)	2.02	2.802(3)	153.5(17)
	O(202)–H...O(42B)	2.26	2.875(4)	133(4)
	O(301)–H...O(302)	2.01	2.799(3)	157(3)
	O(302)–H...O(1)W	1.89	2.684(3)	163(4)
	O(401)–H...O(301)	1.97	2.803(3)	170(3)
	O(42)–H...O(401)	2.04	2.802(4)	150
	O(1)W–H...O(102) <sup>ix</sup>	2.01	2.802(4)	161(4)
	O(101)–H...O(201) <sup>x</sup>	1.947	2.777(3)	174(3)

<sup>a</sup>See interactions in Figures 6–10. <sup>b</sup>Reference 8. Symmetry codes: (i)  $-x + 1, -y, -z + 2$ ; (ii)  $-x + 1, -y + 1, -z + 1$ ; (iii)  $-x, y - 1/2, -z + 3/2$ ; (iv)  $-x, y + 1/2, -z + 3/2$ ; (v)  $-x + 1/2, y - 1/2, z - 1/2$ ; (vi)  $-x + 1/2, y + 1/2, z - 1/2$ ; (vii)  $x + 1, y, z$ ; (viii)  $x - 1, y, z$ ; (ix)  $x + 1, y, z$ ; (x)  $x - 1, y, z$ .

with the pyridine nitrogen of two different molecules. This gives rise to the zigzag 2D layer shown in Figure 8. Table 3 lists the salient intermolecular distances and angles. Very interestingly, and as in the previous meso *syn-1a* compound, in *syn-1b* the (*R*)-pyridylmethylalcohol moiety interacts exclusively with (*R*)-moieties, and the (*S*)-moiety interacts with only (*S*)-moieties, to form, in this case, supramolecular layers via homochiral hydrogen bonding chains. Self-assembly of these layers give rise to the 3D structure of *syn-1b*.

The structure for 4(*syn-1f*)·H<sub>2</sub>O is quite interesting since it can be seen as the analogue to *syn-1a* or *1b* but where the nitrogen atoms have been substituted by CH units. As expected, the absence of nitrogen in *syn-1f*, as a hydrogen bond acceptor, greatly influences the supramolecular structure of this compound. Now, only OH moieties of different configuration (*R*–*S*) are available to act as donors and acceptors. As already mentioned in the molecular structure section, one intramolecular O–H...O hydrogen bond is

observed in each molecule. This leaves only one OH group per molecule to act as hydrogen bond donor, and this might complicate the homochiral self-assembly as it was observed in the related monosubstituted derivatives.<sup>6b</sup> However, homochiral self-assembly does take place in the disubstituted *syn-1f* so that (*R*)-phenylmethylalcohol moieties interact exclusively with (*R*)-moieties, and the (*S*)-moiety interacts with only (*S*)-moieties. In order to achieve homochiral self-assembly, four molecules of *syn-1f* and one water molecule form pentameric clusters by intermolecular O–H...O hydrogen bonded clusters (bottom of Figure 8). Stacking of these clusters by weak dihydrogen and/or hydrophobic interactions forms the 3D structure for this compound. Note that in this structure there is replacement of one of the *R,S* molecules of the four in the cluster by an *R,R* molecule (see Experimental Section), and, interestingly, the latter does not form any hydrogen bonds.

**2-Quinoline Derivative (1d).** The molecular structure of *anti-1d* can be related to that of *anti-1a* (2-pyridine based), by

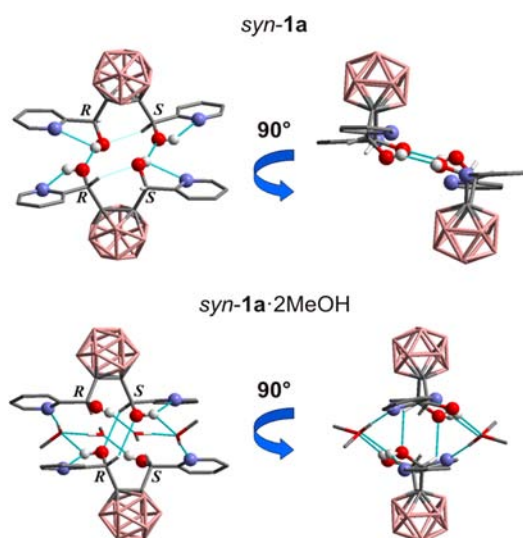


**Figure 6.** Supramolecular assemblies of *syn-1a* (top) and *syn-1a*·2MeOH (bottom). Projections showing 2 molecules of each compound forming hydrogen bonded dimers. Configurations of chiral carbons are indicated. See Table 3 for metric parameters. All hydrogen atoms, except those hydrogen bonded, are omitted for clarity. Color code: B pink; C gray; H white; O red; N blue.

adding a phenyl ring to each pyridine moiety. This clearly increases the bulkiness around the nitrogen atoms of the aromatic rings in *anti-1d* and consequently it should affect the formation of intermolecular O–H...N hydrogen bonds. This is what actually happens in the monosubstituted derivatives where only intramolecular O–H...N hydrogen bonds were observed.<sup>6c</sup> Organization of molecules in the *o*-carboranyldiol *anti-1d*·2H<sub>2</sub>O involves the formation of cyclic, tetrameric (two *anti-1d* + two H<sub>2</sub>O molecules) intermolecular O–H...O hydrogen bond arrangements shown in Figure 10. In addition, the remaining H atom of the water molecules forms intermolecular O–H...N hydrogen bonds. Molecules along the *a* axis are linked by these intermolecular O–H...O and O–H...N hydrogen bonds into homochiral chains, that is, formed by association of one of the two possible enantiomers (only RR is shown in Figure 9). Homochiral chains of *anti-1d*·2H<sub>2</sub>O are closely packed by intermolecular C–H...O interactions [C(13)–H...O(1) 2.400 Å, CHO 136.53°] leading to the formation of racemic columns along the *a* axis (Figure 11A). Self-assembly of these racemic columns by weak interactions forms the 3D structure of *anti-1d*·2H<sub>2</sub>O as shown in Figure 11B. It is however noteworthy that the racemic columns are packed in a way to form parallel homochiral layers that alternate through the 3D structure. In fact, contiguous molecules of the same chirality in a plane interdigitate their quinoline rings (Figure 10B, left), and this provides homochiral layers that are sustained by hydrophobic and/or dispersion forces.

**Discussion of Crystallization Outcomes and Supramolecular Structures.** In the crystallization of racemic compounds (mixtures for *R* and *S* enantiomers or racemate), three possible outcomes are possible according to Figure 11.<sup>14</sup> The most frequent is the formation of racemic crystals where both enantiomers are intimately mixed (A). Another common phenomenon is the formation of racemic crystals but where some degree of enantiomer separation occurs within the crystals, as shown in Figure 11 (process B). And finally,

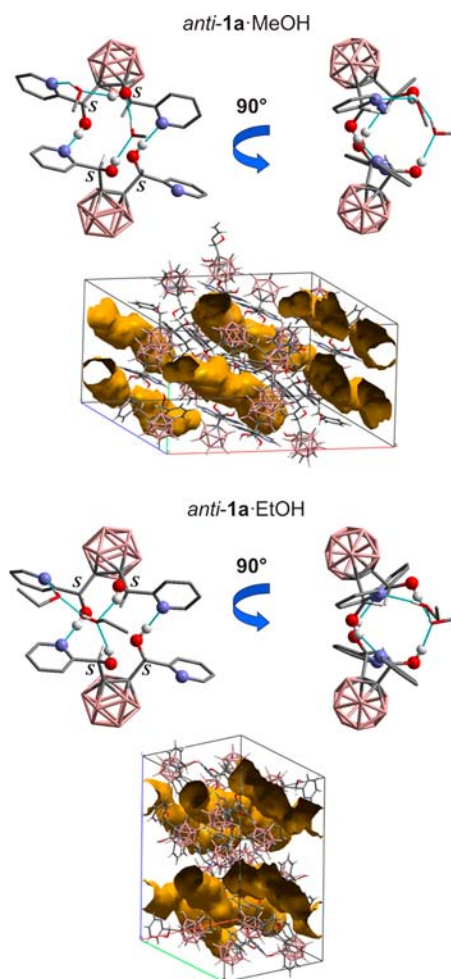


**Figure 7.** Supramolecular assemblies of *anti-1a*·MeOH (top) and *anti-1a*·EtOH (bottom). Projections showing two molecules of each compound forming hydrogen bonded dimers and a comparative unit cell packing showing the well-defined channels (yellow-orange) in both compounds. Configurations of chiral carbons are indicated. See Table 3 for metric parameters. All hydrogen atoms, except those hydrogen bonded, and solvent molecules in the channels are omitted for clarity. Color code: B pink; C gray; H white; O red; N blue.

spontaneous resolution takes place when complete separation of enantiomers occurs on crystallization (process C).<sup>3a</sup> The different crystallization outcomes (A, B, or C in Figure 11) determine the degree to which enantiomers become separated in the crystallization process and whether racemic or conglomerate material will be formed.<sup>13</sup> It is certainly surprising that there are few reports on crystallization outcome B in the solid state despite its inherent interest.<sup>13a</sup>

A wide range of diols are known to form channel structures that incorporate guest species capable of fitting within the space available. These include helical tubuland diols or thin acetylenic or flat oligothiophene spaced diols.<sup>13,15</sup> The new *o*-carboranyldiol compounds represent a new diol system that differs structurally from the previous examples. These novel molecules combine a hydrophobic carborane cluster, two alcohol functionalities, and two nitrogenated aromatic rings and represent one of the few examples of nonflexible C<sub>2</sub>-symmetric 1,4-diols.<sup>16</sup> Crystallization in all *anti*-isomers leads to outcome B in Figure 11, that is, racemic crystals where some degree of separation occurs within the crystal. Thus, self-assembly in *anti-1a*·MeOH and *anti-1a*·2EtOH leads to the formation of

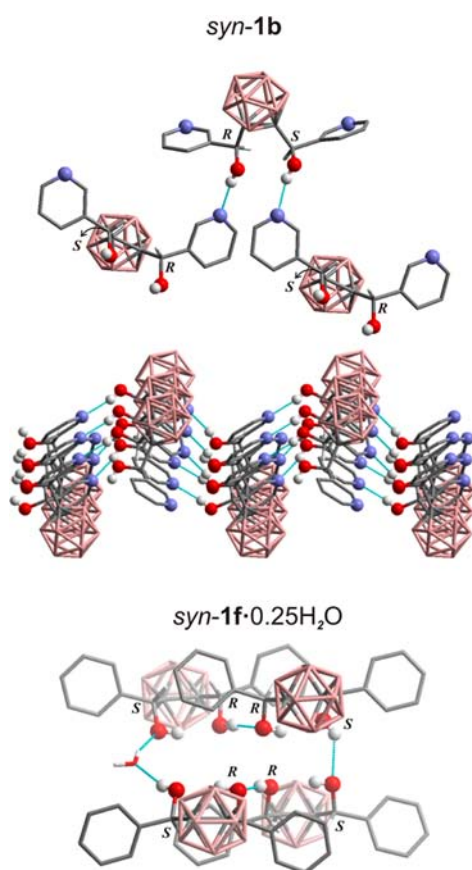


**Figure 8.** Supramolecular assemblies of *syn-1b* and *syn-1f*·0.25H<sub>2</sub>O. Top: Two projections showing 3 or 15 molecules of *syn-1b* forming hydrogen bonded zigzag layers. Bottom: Projection showing four molecules of *syn-1f* and one molecule of water forming a hydrogen bonded cluster. Configurations of chiral carbons are indicated. See Table 3 for metric parameters. All hydrogen atoms, except those hydrogen bonded, are omitted for clarity. Color code: B pink; C gray; H white; O red; N blue.

discrete homochiral channels (Figure 7 and SI). As previously mentioned, dimers of the same chirality in both compounds self-assemble around a crystallographic  $2_1$  screw axes (along  $c$  or  $b$  in *anti-1a*·MeOH and *anti-1a*·2EtOH, respectively) to generate channels that are occupied by the guest solvents. Mercury<sup>17</sup> was used to remove the solvents in both structures to enable direct comparison between channels. These channels present several important features. The channel size enlarges in proportion to the size of the solvent included. The channel volume of the unit cell in *anti-1a*·MeOH is estimated to be 1065.81 Å<sup>3</sup> (12.3% of unit cell), whereas that for *anti-1a*·2EtOH is 1119.70 Å<sup>3</sup> (13.1% of unit cell). Although the solvents included in the channels in these two structures are not chiral, they are generated exclusively by homochiral dimers (Figures 7 and SI). This is even more surprising when one realizes that no strong interactions are observed between the homochiral dimers. The latter suggests that formation of homochiral channels is driven by weak hydrophobic and/or dihydrogen bond interactions, and this explains that channel size can be adjusted to the size of the solvent included in it. Another important consequence of the fact that only weak interactions are operating between homochiral channels of different handedness is that conglomerate behavior (outcome C in Figure 11) is likely to occur under the appropriate

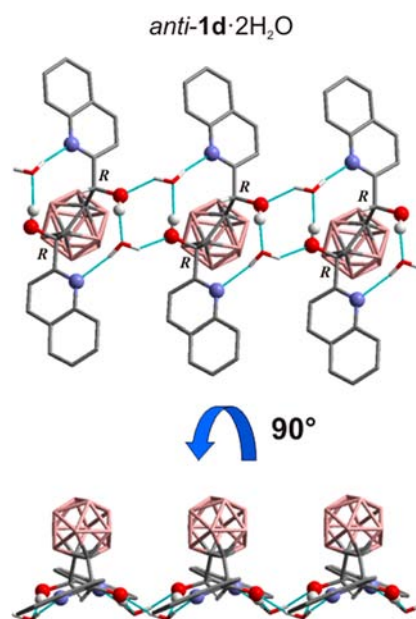


**Figure 9.** Supramolecular assembly of *anti-1d*·2H<sub>2</sub>O. Two projections showing three molecules of *anti-1d* forming O–H···O and O–H···N hydrogen bonded chains that include water molecules along the  $a$  axis. Configurations of chiral carbons are indicated. See Table 3 for metric parameters. All hydrogen atoms, except those hydrogen bonded, are omitted for clarity. Color code: B pink; C gray; H white; O red; N blue.

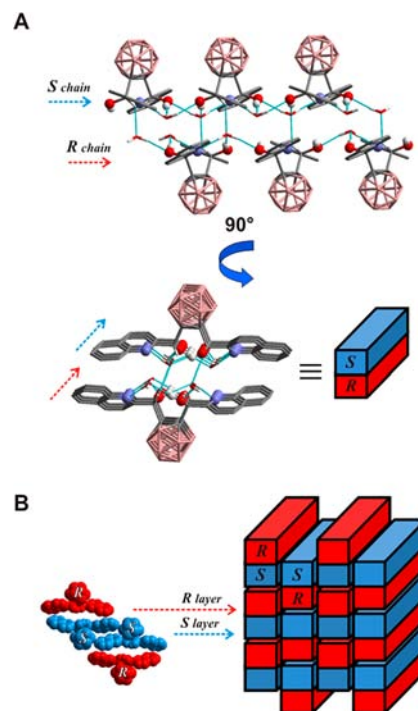


**Figure 10.** (A) Comparative views of self-assembled supramolecular homochiral chains (indicated by arrows) of *anti-1d*·2H<sub>2</sub>O, perpendicular (top) and along the O–H···O and O–H···N hydrogen bonds (bottom) giving racemic columns (represented as red/blue rectangular prism). Color code: B pink; C gray; H white; O red; N blue. (B) A pictorial representation of the 3D assembly of racemic columns of *anti-1d*·2H<sub>2</sub>O.

crystallization conditions. We are currently exploring the clathrating properties of this *o*-carboranyldiol as well as the

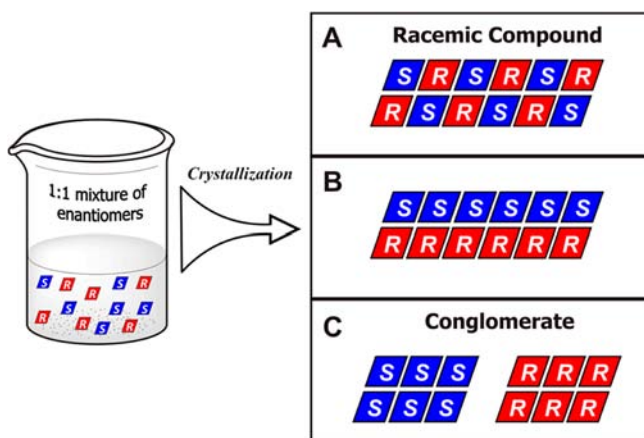


**Figure 11.** Three common outcomes observed on crystallization of a 1:1 mixture of enantiomers. Rhomboids represent enantiomeric molecules. (A) Formation of racemic crystals containing an intimate mix of enantiomers. (B) Formation of racemic crystals containing enantiomers separated into discrete domains. (C) Complete separation of the enantiomers into individual homochiral crystals (a conglomerate).

possibility for it to act as a soft porous molecular material.<sup>18</sup> The crystallization outcome for the 2-quinoline derivative *anti*-**1d**·2H<sub>2</sub>O deserves some comments. It is obvious that formation of homochiral chains, sustained by moderate O–H···O and O–H···N hydrogen bonds, would correspond to crystallization outcome B (Figure 11). Then, homochiral chains of opposite handedness are then packed through weak C–H···O interactions to form racemic columns along the *a* axis (Figure 10A). However, as already discussed above, racemic columns close pack by hydrophobic and/or dispersion forces in a way to provide homochiral layers (Figure 10B).

Supramolecular structures for the unsolvated structures for *syn*-**1a** and **1b** are in agreement with the corresponding monosubstituted derivatives.<sup>6</sup> All hydrogen bond donors and acceptors are satisfied in both structures. As seen in the monosubstituted derivatives, intramolecular O–H···N hydrogen bonds are formed in the 2-pyridine derivative **1a**. The latter is not possible in the 3-pyridine derivative **1b**, and consequently only intermolecular O–H···N interactions are observed, giving rise to zigzag 2D layers (Figure 8). Supramolecular analysis of all *o*-carboranyldiol compounds in this work reveals that formation of homochiral hydrogen bonded complexes prevails over heterochiral hydrogen bonded, independently of whether the compounds are in their *syn*-(meso) or *anti*-(racemate) forms (Figures 6–10). (*R*)-Pyridylmethylalcohol moieties interact exclusively with (*R*)-moieties, and (*S*)-moieties interact with only (*S*)-moieties in all structures described in this work. This seems to suggest that homochiral recognition (self-recognition) is favored over heterochiral recognition (self-discrimination) in these compounds. This raises some interesting questions. If self-recognition is taking place, what would be the recognition mechanism?. It could be due to stereoselective intermolecular O–H···N/O hydrogen bonding. If that is the case, we find quite interesting that in two of the reported structures, molecules are hydrogen bonded (dimers in *syn*-**1a**·2MeOH, Figure 6 or layers in *anti*-**1d**·2H<sub>2</sub>O) through solvent molecules and not directly. Still, arrangements of chiral pyridylalcohol moieties are in a way that (*R*)-moieties are closer to (*R*)-moieties, and (*S*)-moieties to (*S*)-moieties. This can be clearly observed when comparing unsolvated and solvated *syn*-

**1a** structures (Figure 6). This suggests that, in the case of a stereoselective hydrogen bonding mechanism, homochiral recognition takes place in solution (like in solid *syn*-**1a**; top of Figure 6), and then methanol molecules interact with these dimers to give the observed structure for *syn*-**1a**·2MeOH in a sort of solvent mediated self-recognition. In the case of *anti*-**1d**·2H<sub>2</sub>O (Figure 10), the observed supramolecular arrangement could be explained by a stepwise self-recognition/discrimination/recognition process in solution. However, we have no experimental evidence for a stereoselective hydrogen bonding mechanism for self-recognition in these compounds. The other possibility, which was raised by one reviewer during the evaluation process of this paper, is that spatial requirements for the carborane cluster cages in these molecules might favor closer proximity of homochiral groups over heterochiral. We cannot exclude, at the moment, any of these possibilities, and this certainly shows that the self-recognition and self-discrimination phenomena are complex and we are still far from the comprehension of it.

## CONCLUSIONS

A series of novel bis-pyridylmethyl, -quinolylmethyl, or -phenyl alcohols derived from the *o*-carborane cluster **1a–f** (Scheme 2) have been synthesized and characterized. The latter family constitutes our second generation of compounds where two arms (one in the first generation) radiate out of the cluster carbons, and each contains *n*-pyridylmethylalcohol (*n* = 2, **1a**; 3, **1b**; 4, **1c**), *n*-quinolylmethylalcohol (*n* = 2, **1d**; 4, **1e**), or phenylmethylalcohol (**1f**) fragments. All compounds contain two chiral centers that can adopt either *R* or *S* configuration and therefore have been isolated as a mixture of two diastereoisomers, a meso compound (*RS*; OH groups in a *syn* orientation) and a racemic compound (*SS* and *RR* enantiomers; OH groups in an *anti* orientation). A slight diastereomeric excess is observed in all compounds (*syn*:*anti* ratio of 0.7:1), except in the case of the 3-pyridine derivative **1b** where diastereoisomers separate by precipitation during work up.

*Syn* and *anti*-stereoisomers crystallized separately from their mixtures (except **1b**), and crystal structures for three *syn*- and three *anti*-stereoisomers have been determined. Supramolecular structures are dominated by O–H···N and/or O–H···O hydrogen bonds. Supramolecular analysis of all compounds in this work reveals that formation of homochiral hydrogen bonded complexes prevails over heterochiral hydrogen bonded complexes. Complete homochiral self-assembly is always observed, independently of whether the compounds are in their *syn*-(*RS* configurations) or *anti*-(*RR* and *SS* configuration) forms. Homochiral self-assembly in *anti*-**1a**·MeOH and *anti*-**1a**·2EtOH leads to the formation of discrete homochiral channels whose size enlarges in proportion to the size of the solvent included. Crystallization in all *anti*-isomers leads to outcomes where enantiomers, although forming racemic crystals, are separated into discrete domains.

## EXPERIMENTAL SECTION

**General Remarks.** Reactions were carried out under a nitrogen atmosphere in round-bottomed flasks equipped with a magnetic stirring bar, capped with a septum. THF and diethyl ether were distilled from Na/benzophenone and CH<sub>2</sub>Cl<sub>2</sub> over CaH<sub>2</sub>. All the other chemicals were commercially available and used as received. TLC analyses were performed on Merck silica gel 60 F<sub>254</sub> TLC plates (0.5 mm thickness). IR ATR spectra were recorded on a Perkin–Elmer

Spectrum One spectrometer.  $^1\text{H}$ ,  $^{13}\text{C}$ , and  $^{11}\text{B}$  spectra were recorded respectively at 300, 75, and 96 MHz with a Bruker Advance-300 spectrometer in deuterated acetone, unless denoted, and referenced to the residual solvent peak for  $^1\text{H}$  and  $^{13}\text{C}$  NMR or to  $\text{BF}_3\cdot\text{OEt}_2$  as an external standard for  $^{11}\text{B}$  NMR. Chemical shifts are reported in ppm and coupling constants in Hertz. Multiplets nomenclature is as follows: s, singlet; d, doublet; t, triplet; br, broad; m, multiplet. Elemental analyses were obtained by a CarboErba EA1108 microanalyzer (Universidad Autónoma de Barcelona). The mass spectra were recorded in the negative ion mode using a Bruker Biflex MALDI-TOF-MS [N<sub>2</sub> laser;  $\lambda_{\text{exc}}$  337 nm (0.5 ns pulses); voltage ion source 20.00 kV (Uis1) and 17.50 kV (Uis2)] with 3,5-dimethoxy-4-hydroxycinnamic acid as matrix.

**General Procedure for the Synthesis of the *o*-Carboranyl-diols 1a–f.** We followed a procedure analogous to that previously reported by us.<sup>6</sup> In general, THF or diethyl ether can be used as solvents with very slight variation in yields. Diethyl ether seems to facilitate the work up while avoiding the formation of oily residues, although THF is preferred in the synthesis of **1b** due to the spontaneous separation of diastereoisomers.

**1,2-Bis(pyridin-2'-yl)methanol-1,2-dicarba-closo-dodecaborane (1a).** *n*-BuLi (1.75 mL, 1.6 M in hexane, 2.8 mmol) was added dropwise to a solution of *o*-carborane (201.4 mg, 1.4 mmol) in diethyl ether (10 mL) at 0 °C (ice/water bath) under nitrogen atmosphere. The mixture was stirred for 30 min at low temperature and for a further 1.5 h at room temperature to give a clear, pale yellow suspension. The flask was then cooled to –84 °C (ethylacetate/liquid N<sub>2</sub>), whereupon a solution of the 2-pyridinecarboxaldehyde (303.3 mg, 0.27 mL, 2.8 mmol) in diethyl ether (1 mL) was added. The resulting pale-yellow solution was stirred at –84 °C, and the reaction was monitored by TLC. When the reaction had reached completion (after about 4 h), a saturated aqueous solution of NH<sub>4</sub>Cl (10 mL) was added at –84 °C, and then the mixture was taken out of the cooling bath and allowed to warm naturally to room temperature while stirring. The aqueous phase was then extracted with Et<sub>2</sub>O (3 × 20 mL), and the organic phases were dried over MgSO<sub>4</sub>, filtered, and evaporated to dryness. The resultant dark yellow oil was washed with *n*-pentane (2 × 10 mL). Fresh *n*-pentane was added and the mixture was treated with ultrasound for c.a. 15 min, and the slightly colored pentane supernatant was removed afterward. The same procedure was repeated until a light yellow solid was obtained (4–5 times). After the solvent was removed, the yellow solid was dried under vacuum affording pure **1a** (361.82 mg, 1 mmol, 72.1%). NMR experiments confirmed the presence of the two different diastereoisomers *anti*-**1a** and *syn*-**1b** in a 44:56 proportion (see Figure 1).  $^1\text{H}$  NMR of the mixture: 8.63–8.58 (m, 2H, C<sub>5</sub>H<sub>4</sub>N *syn*- and *anti*-isomers), 7.96–7.89 (m, 2H, C<sub>5</sub>H<sub>4</sub>N *syn*- and *anti*-isomers), 7.66 (apparent t,  $J = 8.3$  Hz, 2H, C<sub>5</sub>H<sub>4</sub>N *syn*- and *anti*-isomers), 7.46–7.41 (m, 2H, C<sub>5</sub>H<sub>4</sub>N *syn*- and *anti*-isomers), 6.34 (brs, 1H, OH *anti*-isomer), 6.19 (brs, 1H, OH *syn*-isomer), 5.98 (brs, 1H, CHOH *syn*-isomer), 5.75 (brs, 1H, CHOH *anti*-isomer).  $^{13}\text{C}$  NMR: 159.5 and 159.4, 149.1 and 149.0, 138.0, and 137.9 (C<sub>5</sub>H<sub>4</sub>N *syn*- plus *anti*-isomers), 124.9 (C<sub>5</sub>H<sub>4</sub>N *syn*- plus *anti*-isomers), 123.6 and 123.4 (C<sub>5</sub>H<sub>4</sub>N *syn*- plus *anti*-isomers), 86.37 and 86.24 (C<sub>cluster</sub> *syn*- plus *anti*-isomers), 74.3 (CHOH *syn*-isomer)\*, 73.53 (CHOH *anti*-isomer)\* (\*values assigned by  $^1\text{H}$ – $^{13}\text{C}$  correlation (Figure S1 in SI)).  $^{11}\text{B}$  NMR: –2.9 (d,  $J_{\text{B,H}} = 145$ , 2B), –10 a –11 (m, 8B). IR (ATR; only assigned bands are listed here; see SI for complete spectrum):  $\nu$  3197 (OH), 2599, 2573 (BH). MALDI-TOF,  $m/z$ : M: 359.27 [M + H]<sup>+</sup>.

**Crystallization.** The isomers mixture was dissolved in an ether-methanol solution and left in a barely opened vial. After ca. 24 h pyramidal colorless crystals were obtained. Single crystal XRD experiments confirmed their identity, the less soluble isomer with the *syn* conformation, *syn*-**1a**·2MeOH. After about 48 h, hexagonal bipyramidal colorless crystals were also observed; single crystal XRD experiments confirmed they corresponded to the *anti* isomer, *anti*-**1a**·MeOH.

$^1\text{H}$  NMR of *syn*-**1a**: 8.61 (ddd,  $J = 4.8, 1.7, 1.0$ , 2H, C<sub>5</sub>H<sub>4</sub>N), 7.91 (td,  $J = 7.8, 1.8, 2\text{H}$ , C<sub>5</sub>H<sub>4</sub>N), 7.43 (d,  $J = 7.9, 2\text{H}$ , C<sub>5</sub>H<sub>4</sub>N), 7.43 (ddd,

$J = 7.5, 4.8, 1.1, 2\text{H}$ , C<sub>5</sub>H<sub>4</sub>N), 6.19 (d,  $J = 6.5, 2\text{H}$ , OH), 5.98 (d,  $J = 6.3, 2\text{H}$ , CHOH).

$^1\text{H}$  NMR of *anti*-**1a**: 8.61 (ddd,  $J = 4.8, 1.8, 1.0$  Hz, 2H, C<sub>5</sub>H<sub>4</sub>N), 7.92 (td,  $J = 7.8, 1.8, 2\text{H}$ , C<sub>5</sub>H<sub>4</sub>N), 7.65 (d,  $J = 7.9, 2\text{H}$ , C<sub>5</sub>H<sub>4</sub>N), 7.44 (ddd,  $J = 7.5, 5.6, 1.0, 2\text{H}$ , C<sub>5</sub>H<sub>4</sub>N), 6.35 (d,  $J = 6.5, 2\text{H}$ , OH), 5.75 (d,  $J = 6.4, 2\text{H}$ , CHOH).

**1,2-Bis(pyridin-3'-yl)methanol-1,2-dicarba-closo-dodecaborane (1b).** The general procedure described for **1a** was followed, using *o*-carborane (205 mg, 1.42 mmol), *n*-BuLi (1.9 mL, 1.56 M in hexane, 2.99 mmol), THF (20 mL) and 3-pyridinecarboxaldehyde (312 mg, 0.27 mL, 2.9 mmol), and an acetone/liquid N<sub>2</sub> cooling bath (–94 °C). The reaction reached completion after 4 h and was treated with a saturated aqueous solution of NH<sub>4</sub>Cl (10 mL) at –94 °C, and then the mixture was taken out of the cooling bath and allowed to warm naturally to room temperature while stirring.

Then diethyl ether (15 mL) was added while stirring and a very insoluble white solid was obtained after 15–20 min. The white solid was separated by filtration, washed with methanol, and dried under a vacuum to afford pure *syn*-**1b** (155.0 mg, 0.43 mmol, 30.5%). Work up of the remaining two phase solution as in **1a** gave a light yellow solid that was dried under a vacuum to afford pure *anti*-**1b** (200 mg, 0.56 mmol, 39.3%).

(*syn*-**1b**):  $^1\text{H}$  NMR (DMSO): 8.70 (brs, 2H, C<sub>5</sub>H<sub>4</sub>N), 8.57 (d,  $J = 4.5, 2\text{H}$ , C<sub>5</sub>H<sub>4</sub>N), 7.91 (brd,  $J = 8.0, 2\text{H}$ , C<sub>5</sub>H<sub>4</sub>N), 7.46 (dd,  $J = 7.7, 4.9, 2\text{H}$ , C<sub>5</sub>H<sub>4</sub>N), 6.81 (d,  $J = 5.0, 2\text{H}$ , OH)\*\* (\*\*these signals oscilate from 7 to 6.8 ppm, probably due to concentration changes between NMR experiments). 5.71 (d,  $J = 4.9, 2\text{H}$ , CHOH).  $^{13}\text{C}$  NMR (DMSO): 149.39, 148.49, 136.98, 135.02, and 123.20 (C<sub>5</sub>H<sub>4</sub>N), 87.86 (C<sub>cluster</sub>), 68.75 (CHOH).  $^{11}\text{B}$  NMR (DMSO) –2.58 (bs, 4B), –9.43 (m, 8B). IR (ATR; only assigned bands are listed here):  $\nu$  2989 (OH), 2618, 2605, 2569, 2544 (BH). MALDI-TOF,  $m/z$ : M: 359.27 [M + H]<sup>+</sup>.

(*anti*-**1b**):  $^1\text{H}$  NMR (DMSO): 8.62 (d,  $J = 1.8, 2\text{H}$ , C<sub>5</sub>H<sub>4</sub>N), 8.58 (dd,  $J = 4.7, 1.5, 2\text{H}$ , C<sub>5</sub>H<sub>4</sub>N), 7.86 (brd,  $J = 8.0, 2\text{H}$ , C<sub>5</sub>H<sub>4</sub>N), 7.47 (dd,  $J = 7.9, 4.8, 2\text{H}$ , C<sub>5</sub>H<sub>4</sub>N), 7.25 (d,  $J = 5.5, 2\text{H}$ , OH), 5.59 (d,  $J = 5.50, 2\text{H}$ , CHOH).  $^{13}\text{C}$  NMR (DMSO): 149.61, 148.09, 136.65, 134.86, and 123.45 (C<sub>5</sub>H<sub>4</sub>N), 86.71 (C<sub>cluster</sub>), 68.87 (CHOH).  $^{11}\text{B}$  NMR (DMSO) –3.4 (m, 4B), –10.4 (m, 8B). IR (ATR from the mixture containing an excess of **3a**); only assigned bands are listed here):  $\nu$  3071, 2989 (OH), 2628, 2614, 2587, 2545 (BH). MALDI-TOF,  $m/z$ : M: 359.26 [M + H]<sup>+</sup>.

**Crystallization.** Isomer *syn*-**1b** was dissolved in DMSO in a vial, and then it was left open to the air. Colorless crystal were obtained after several days.

**1,2-Bis(pyridin-4'-yl)methanol-1,2-dicarba-closo-dodecaborane (1c).** The general procedure described for **1b** was followed, using *o*-carborane (208 mg, 1.44 mmol), *n*-BuLi (1.8 mL, 1.6 M in hexane, 2.88 mmol), THF (20 mL) and 4-pyridinecarboxaldehyde (317 mg, 0.28 mL, 2.9 mmol), and an acetone/liquid N<sub>2</sub> cooling bath (–94 °C). Work up gave a light yellow solid that was dried under a vacuum to afford a mixture of *syn*- and *anti*-**1c** (297 mg, 0.83 mmol, 57.6%). NMR of the latter showed an *anti*/*syn*-**1c** ratio of 62/38.  $^1\text{H}$  NMR of the mixture: 8.64 (brd,  $J = 4.0, 4\text{H}$ , C<sub>5</sub>H<sub>4</sub>N *syn*- and *anti*-isomers), 7.54 (d,  $J = 6.1, 2\text{H}$ , C<sub>5</sub>H<sub>4</sub>N *syn*-isomer), 7.47 (d,  $J = 6.1, 2\text{H}$ , C<sub>5</sub>H<sub>4</sub>N *anti*-isomer), 7.26 (d,  $J = 5.4, 1\text{H}$ , OH *anti*-isomer), 6.86 (d,  $J = 5.2, 1\text{H}$ , OH *syn*-isomer), 5.67 (d,  $J = 5.2, 1\text{H}$ , CHOH *syn*-isomer), 5.48 (d,  $J = 5.4, 1\text{H}$ , CHOH *anti*-isomer).  $^{11}\text{B}$  NMR: –3.7 (m, 2B), –9.9 (m, 8B). IR (ATR; only assigned bands are listed here; see SI for complete spectrum):  $\nu$  3053, (OH), 2555 (BH). MALDI-TOF,  $m/z$ : M: 359.18 [M + H].

**1,2-Bis(quinolin-2'-yl)methanol-1,2-dicarba-closo-dodecaborane (1d).** The general procedure described for **1b** was followed, using *o*-carborane (219 mg, 1.52 mmol), *n*-BuLi (2.25 mL, 1.35 M in hexane, 3.04 mmol), THF (20 mL) and 2-quinolinecarboxaldehyde (492.2 mg, 3.06 mmol), and an acetone/liquid N<sub>2</sub> cooling bath (–94 °C). Work up gave a light orange solid that was dried under a vacuum to afford a mixture of *syn*- and *anti*-**1d** (402 mg, 0.88 mmol, 57.7%). NMR of the latter showed an *anti*/*syn*-**1d** ratio of 61/39.  $^1\text{H}$  NMR of the mixture: 8.49 (t,  $J = 7.8, 2\text{H}$ , C<sub>8</sub>H<sub>6</sub>N *syn*- and *anti*-isomers), 8.07 (m, 4H, C<sub>8</sub>H<sub>6</sub>N *syn*- and *anti*-isomers), 7.84 (m, 4H, C<sub>8</sub>H<sub>6</sub>N *syn*- and

*anti*-isomers), 7.68 (m, 4H, C<sub>8</sub>H<sub>6</sub>N *syn*- and *anti*-isomers), 6.75 (brs, 1H, OH *anti*-isomer), 6.52 (brs, 1H, OH *syn*-isomer), 6.32 (brs, 1H, CHOH *syn*-isomer), 6.04 (brs, 1H, CHOH *anti*-isomer). <sup>13</sup>C NMR: 150.6 and 150.3, 136.4 and 136.3, 127.3 and 127.2, 120.3 and 120.2, 119.1, 118.2, 117.8, 117.3 (C<sub>9</sub>H<sub>6</sub>N *syn*- plus *anti*-isomers), 76.0 and 75.5 (C<sub>cluster</sub> *syn*- plus *anti*-isomers), 63.3 and 63.1 (CHOH *syn*-isomer plus *anti*-isomers). <sup>11</sup>B NMR: -2.7 (d, J = 138, 2B), -7 to -15 (m, 8B). IR (ATR; only assigned bands are listed here; see SI for complete spectrum):  $\nu$  3197 (OH), 2599, 2573 (BH). MALDI-TOF, *m/z*: M: 460.46 [M + 2H]<sup>+</sup>.

**Crystallization.** The isomers mixture was dissolved in DMF in a vial, and then it was left open to the air. After about 7 days light yellow needles were obtained.

**1,2-Bis(quinolin-4'-yl)methanol-1,2-dicarba-closo-dodecaborane (1e).** The general procedure described for **1b** was followed, using *o*-carborane (222 mg, 1.53 mmol), *n*-BuLi (2.00 mL, 1.53 M in hexane, 3.06 mmol), THF (20 mL) and 4-quinolinecarboxaldehyde (498.4 mg, 3.08 mmol), and an acetone/liquid N<sub>2</sub> cooling bath (-94 °C). Work up gave a light yellow solid that was dried under a vacuum to afford a mixture of *syn*- and *anti*-**1e** (341.7 mg, 0.75 mmol, 48.7%). NMR of the latter showed an *anti*/*syn*-**1e** ratio of 59/41. <sup>1</sup>H NMR of the mixture: 9.01 (d, J = 4.2, 2H, C<sub>8</sub>H<sub>6</sub>N *syn*- and *anti*-isomers), 8.57 (brs, 1H), 8.52 (brs, 1H), 8.14 (brd, J = 8.4, 2H, C<sub>8</sub>H<sub>6</sub>N *syn*- and *anti*-isomers), 7.93 (m, 2H, C<sub>8</sub>H<sub>6</sub>N *syn*- and *anti*-isomers), 7.86-7.68 (m, 6H, C<sub>8</sub>H<sub>6</sub>N *syn*- and *anti*-isomers), 7.00 (brs, 1H, CHOH *syn*-isomer), 6.92 (brs, 1H, CHOH *anti*-isomer). <sup>13</sup>C NMR: 150.8, 149.3 and 149.1, 147.8, 146.4, 131.1 and 130.9, 130.3, 127.9, 127.0, 125.3 and 124.9, 122.2, and 121.7 (C<sub>9</sub>H<sub>6</sub>N *syn*- plus *anti*-isomers), 86.0 and 85.1 (C<sub>cluster</sub> *syn*- plus *anti*-isomers), 69.8 and 69.2 (CHOH *syn*-isomer plus *anti*-isomers).

<sup>11</sup>B NMR: -2.3 (d, J = 134, 2B), -7 to -15 (m, 8B). IR (ATR; only assigned bands are listed here; see SI for complete spectrum):  $\nu$  3073 (OH), 2567 (BH). MALDI-TOF, *m/z*: M: 459.46 [M + H]<sup>+</sup>.

**1,2-Bis(phenylmethanol)-1,2-dicarba-closo-dodecaborane (1f).** The general procedure described for **1b** was followed, using *o*-carborane (200 mg, 1.39 mmol), *n*-BuLi (1.8 mL, 1.6 M in hexane, 2.88 mmol), THF (20 mL), and benzaldehyde (0.29 mL, 2.86 mmol) to obtain **1f** as a white solid (367 mg, 1.03 mmol, 74%) by column chromatography (eluent: hexane/ethylacetate 4:1, R<sub>f</sub> = 0.25). NMR of the latter showed an *anti*/*syn*-**1f** ratio of 58/42. <sup>1</sup>H NMR of the mixture: 7.05-6.91 (m, 10H, C<sub>6</sub>H<sub>5</sub>), 6.48 (d, J = 5.1, 1.2H, OH *anti*-**1f**), 6.15 (d, J = 4.8, 0.8H, OH *syn*-**1f**), 5.15 (d, J = 4.9, 0.8H, CHOH *anti*-**1f**), 5.01 (d, J = 5.1, 1.2H, CHOH *syn*-**1f**). <sup>11</sup>B NMR (CDCl<sub>3</sub>): -1.9 (d, J = 161.8, 2B), -9.2 to -11.8 (br m, 8B). <sup>13</sup>C NMR: 139.5 and 138.6, 129.7 and 129.5, 128.7 and 128.6, 127.7, and 127.3 (C<sub>5</sub>H<sub>4</sub>N *syn*- plus *anti*-isomers), 84.4 and 83.5 (C<sub>cluster</sub> *syn*- plus *anti*-isomers), 74.8 and 74.3 (CHOH *syn*- plus *anti*-isomers). IR (KBr, cm<sup>-1</sup>): 3307 (OH), 2561 (BH), 1974, 1958, 1899, 1885, 1818, 1614, 1587, 1495, 1456, 1428, 1357, 1318, 1261, 1278, 1200, 1117, 1088, 1061, 1029, 1011, 914, 847, 804, 768, 751, 718, 702, 664, 592, 544. Anal. Calcd for C<sub>16</sub>B<sub>10</sub>H<sub>24</sub>O<sub>2</sub>·0.5H<sub>2</sub>O(365.47): C 52.58, H 6.89; found C 52.75, H 6.96.

**Crystallization.** The isomers mixture was dissolved in a CH<sub>2</sub>Cl<sub>2</sub>/hexane mixture in a vial, and then it was left open to the air. White blocks grown after several days.

**Single Crystal Studies.** Single crystal intensity data for and *syn*-**1f** were collected at 120 K on a Bruker Nonius KappaCCD area detector mounted at the window of a rotating Mo anode ( $\lambda$ (Mo K $\alpha$ ) = 0.71073 Å) (Table S2). Data collection and processing were performed using the programs COLLECT<sup>19</sup> and DENZO,<sup>20</sup> and a multiscan absorption correction was applied using SADABS.<sup>21</sup> Data for *anti*-**1a**·2EtOH were collected at 100 K on a Rigaku AFC12 goniometer equipped with an enhanced sensitivity (HG) Saturn724+ detector mounted at the window of an FR-E+ SuperBright molybdenum rotating anode generator ( $\lambda$ (Mo K $\alpha$ ) = 0.71073 Å) with HF Varimax optics (100  $\mu$ m focus). Data collection and processing, including a multiscan absorption correction, were performed using CrystalClear.<sup>22</sup> The structures were solved via direct methods<sup>23</sup> and refined by full matrix least-squares<sup>24</sup> on F<sup>2</sup>. X-ray reflections for *anti*-**1a**·MeOH, *syn*-**1a**·2MeOH and **2** were collected at 298 K on an Oxford Xcalibur

Gemini Eos CCD diffractometer using Mo K $\alpha$  radiation ( $\lambda$  = 0.7107 Å). Data collection and processing, including a multiscan absorption correction were performed using *CrysAlisPro* (version 1.171.33.55),<sup>25</sup> and OLEX2-1.2<sup>26</sup> and SHELXL97<sup>27</sup> were used for structure solution and refinement. For these structures, several H atoms (especially OH) were detected at approximate locations in a difference Fourier map and then refined freely. Those for BH and some CH were placed in idealized positions and refined using a riding model, with C-H = 0.93 Å and U<sub>iso</sub>(H) = 1.2U<sub>eq</sub>(C). Data for *syn*-**1b** was collected at 100 K on a Bruker SMART APEX diffractometer ( $\lambda$  = 0.71073 Å) whereas for *anti*-**1d** was collected at 100 K on a Bruker D8 Venture diffractometer ( $\lambda$  = 1.54178 Å). Data collection and processing were performed using the programs APEX2<sup>28</sup> and SAINT,<sup>29</sup> and a multiscan absorption correction was applied using SADABS.<sup>30</sup> The structures were solved by direct methods,<sup>21</sup> which revealed the position of all non-hydrogen atoms. These atoms were refined on F<sup>2</sup> by a full-matrix least-squares procedure using anisotropic displacement parameters.<sup>22</sup> All hydrogen atoms were located in difference Fourier maps and included as fixed contributions riding on attached atoms with isotropic thermal displacement parameters 1.2 times those of the respective atom.

**Special Details.** Two molecules of MeOH were observed in *anti*-**1a**·MeOH, one of them showing some disordered atoms. During refinement, residual electron density was detected in the lattice associated with other solvent molecules. Thus, the data were treated with the SQUEEZE procedure (from PLATON).<sup>11</sup> The volume occupied by the solvent was 288.9 Å<sup>3</sup>, and the number of electrons per unit cell deduced by SQUEEZE was 36. Considering that the approximate volume of a methanol molecule would be ca. 80-100 Å<sup>3</sup> and the electron count, the residual electron density corresponds to 2-3 methanol molecules distributed within the unit cell. One of the refined methanol molecules was modeled as split over 2 positions (66, 34) and geometric and thermal parameter restraints were applied. For all but the disordered solvent molecule, the OH positions were clear in the difference map, and while the O-H distance was constrained the torsion angles were allowed to refine to coincide with the electron density maxima. The OH hydrogen atoms in *syn*-**1a**·MeOH were treated in an identical fashion. *anti*-**1a**·2EtOH: The hydrogen of the solvent alcohol group was treated as riding on the parent oxygen, but the torsion was allowed to refine. this placed the hydrogen at the position of an observed maxima in the difference map. The remaining OH hydrogens were clearly visible in the difference map and freely refined. 4(*syn*-**1f**)·H<sub>2</sub>O: One of the ligand sites in one of the four independent RS molecules has ca. 37% occupancy of an R ligand in the S site. Thermal parameter constraints and geometrical restraints were applied. All OH (with the exception of those in the low occupancy part) were refined using O-H distance restraints (0.84) and U<sub>eq</sub> = 1.5 those of their parents' atoms.

## ■ ASSOCIATED CONTENT

### 📄 Supporting Information

Spectroscopic and crystallographic data. This material is available free of charge via the Internet at <http://pubs.acs.org/>.

## ■ AUTHOR INFORMATION

### Corresponding Author

\*E-mail: jginerplanas@icmab.es.

### Present Address

#(F.D.S.) Departamento de Química Inorgánica, Analítica, y Química Física, Facultad de Ciencias Exactas y Naturales, Universidad de Buenos Aires, INQUIMAE-CONICET, Ciudad Universitaria, Pabellón 2, C1428EHA Buenos Aires, Argentina.

### Notes

The authors declare no competing financial interest.

## ■ ACKNOWLEDGMENTS

We thank CICYT (Project CTQ2010-16237), Generalitat de Catalunya (2009/SGR/00279), and CSIC (JAE-doc contract to FDS) for financial support. F.D.S. thanks CONICET for support. M.E.L. and M.B.H. thank the UK Engineering and Physical Science Research Council for support of the X-ray facilities at Southampton. M.B.H. thanks the Leverhulme Trust for the award of an Emeritus Fellowship. M.Y.T. is enrolled in the UAB PhD program. The project "Factoría de Crystalización, CONSOLIDER INGENIO-2010" provided X-ray structural facilities for this work.

## ■ REFERENCES

- (1) See for example: (a) Lehn, J.-M. *Supramolecular Chemistry: Concepts and Perspectives*; VCH: Weinheim, 1995; (b) Whitesides, G. M.; Grzybowski, B. *Science* **2002**, *295*, 2418. (c) Guijarro, A.; Yus, M. *The Origin of Chirality in the Molecules of Life. A Revision from Awareness to the Current Theories and Perspectives of this Unsolved Problem*; The Royal Society of Chemistry: Cambridge, U.K., 2009.
- (2) See for example: (a) Cornelissen, J. J. L. M.; Rowan, A. E.; Nolte, R. J. M.; Sommerdijk, N. A. J. M. *Chem. Rev.* **2001**, *101*, 4039. (b) Pérez-García, L.; Amabilino, D. B. *Chem. Soc. Rev.* **2002**, *31*, 342. (c) Mateos-Timoneda, M. A.; Crego-Calama, M.; Reinhoudt, D. N. *Chem. Soc. Rev.* **2004**, *33*, 363. (d) Pérez-García, L.; Amabilino, D. B. *Chem. Soc. Rev.* **2007**, *36*, 941. (e) Hembury, G. A.; Borovkov, V. V.; Inoue, Y. *Chem. Rev.* **2008**, *108*, 1. (f) Crassous, J. *Chem. Soc. Rev.* **2009**, *38*, 830. (g) Blanco, F.; Alkorta, I.; Rozas, I.; Elguero, J. J. *Phys. Org. Chem.* **2010**, *23*, 1155. (h) Tahara, K.; Yamaga, H.; Ghijssens, E.; Inukai, K.; Adipoejoso, J.; Blunt, M. O.; De Feyter, S.; Tobe, Y. *Nat. Chem.* **2011**, *3*, 714.
- (3) (a) Jaques, J.; Collet, A.; Wilen, S. H. *Enantiomers, Racemates, and Resolutions*; Krieger Publishing, FL, 1994. (b) Safont-Sempere, M. M.; Osswald, P.; Radacki, K.; Würthner. *Chem.—Eur. J.* **2012**, *16*, 7380 and references therein.
- (4) See for example: (a) Telfer, S. G.; Sato, T.; Kuroda, R.; Lefebvre, J.; Leznoff, D. B. *Inorg. Chem.* **2004**, *43*, 421. (b) ten Cate, A. T.; Dankers, P. Y. W.; Kooijman, H.; Spek, A. L.; Sijbesma, R. P.; Meijer, E. W. *J. Am. Chem. Soc.* **2003**, *125*, 6860. (c) Weissbuch, L.; Bolbach, G.; Zepik, H.; Shavit, E.; Tang, M.; Frey, J.; Jensen, T. R.; Kjaer, K.; Leiserowitz, L.; Lahav, M. *J. Am. Chem. Soc.* **2002**, *124*, 9093. (d) Ishida, Y.; Aida, T. *J. Am. Chem. Soc.* **2002**, *124*, 14017. (e) Isaacs, L.; Witt, D. *Angew. Chem., Int. Ed.* **2002**, *41*, 1905. (f) Murguly, E.; McDonald, R.; Branda, R. N. *Org. Lett.* **2000**, *2*, 3169. (g) Prins, L. J.; Huskens, J.; de Jong, F.; Timmerman, P.; Reinhoudt, D. N. *Nature* **1999**, *398*, 498.
- (5) (a) Takahashi, S.; Jukurogi, T.; Katagiri, T.; Uneyama, K. *CrystEngComm* **2006**, *8*, 320. (b) Takahashi, S.; Katagiri, T.; Uneyama, K. *CrystEngComm* **2006**, *8*, 132. (c) Takahashi, S.; Katagiri, T.; Uneyama, K. *Chem. Commun.* **2005**, 3658.
- (6) (a) Terrasson, V.; Planas, Prim, D.; Viñas, C.; J.G.; Teixidor, F.; Light, M. E.; Hursthouse, M. B. *J. Org. Chem.* **2008**, *73*, 9140. (b) Terrasson, V.; García, Y.; Farràs, P.; Teixidor, F.; Viñas, C.; Planas, J. G.; Prim, D.; Light, M. E.; Hursthouse, M. B. *CrystEngComm* **2010**, *12*, 4109. (c) Di Salvo, F.; Planas, J. G.; Camargo, B.; Garcia, Y.; Teixidor, F.; Viñas, C.; Light, M. E.; Hursthouse, M. B. *CrystEngComm* **2011**, *13*, 5788.
- (7) Di Salvo, F.; Teixidor, F.; Viñas, C.; Planas, J. G.; Light, M. E.; Hursthouse, M. B.; Aliaga-Alcalde, N. *Cryst. Growth Des.* **2012**, *12*, 5720.
- (8) (a) Rys, E. G.; Lönnecke, P.; Stadlbauer, S.; Kalinin, V. N.; Hey-Hawkins, E. *Polyhedron* **2009**, *28*, 3467. (b) Maulana, I.; Lönnecke, P.; Hey-Hawkins, E. *Inorg. Chem.* **2009**, *48*, 8638. (c) Stadlbauer, S.; Frank, S.; Maulana, I.; Lönnecke, P.; Kirchner, B.; Hey-Hawkins, E. *Inorg. Chem.* **2009**, *48*, 6072.
- (9) Peng, B.; Nie, Y.; Miao, J.; Zhang, Z.; Xu, M.; Sun, G. *J. Mol. Struct.* **2012**, *1007*, 214.
- (10) Todd, L. J. *Prog. NMR Spectrosc.* **1979**, *13*, 87.
- (11) (a) Oliva, J. M.; Allan, N. L.; Schleyer, P. v. R.; Viñas, C.; Teixidor, F. *J. Am. Chem. Soc.* **2005**, *127*, 13538. (b) Llop, J.; Vinas, C.; Oliva, J. M.; Teixidor, F.; Flores, M. A.; Kivekas, R.; Sillanpaa, R. *J. Organomet. Chem.* **2002**, *657*, 232. (c) Llop, J.; Vinas, C.; Oliva, J. M.; Teixidor, F.; Victori, L.; Kivekas, R.; Sillanpaa, R. *Organometallics* **2001**, *20*, 4024. (d) Kivekäs, R.; Teixidor, F.; Viñas, C.; Nuñez, R. *Acta Crystallogr.* **1995**, *C51*, 1868.
- (12) SQUEEZE: Sluis, P. v.d.; Spek, A. L. *Acta Crystallogr.* **1990**, *A46*, 194–201.
- (13) See for example: (a) Desiraju, G. R. *Crystal Engineering. The Design of Organic Solids*; Elsevier Science Publishers B. V., Amsterdam, 1989; (b) Etter, M. C. *Acc. Chem. Res.* **1990**, *23*, 120. (c) Desiraju, G. R.; Steiner, T. *The Weak Hydrogen Bond in Structural Chemistry and Biology*; Oxford University Press: Oxford, 2001; (d) Steiner, T. *Angew. Chem.* **2002**, *114*, 50; *Angew. Chem., Int. Ed.* **2002**, *41*, 48. (e) Atwood, J. L.; Steed, J. W. *Encyclopedia of Supramolecular Chemistry*; Marcel Dekker: New York, 2004; (f) Metrangolo, P.; Neukirch, H.; Pilati, T.; Resnatti, G. *Acc. Chem. Res.* **2005**, *38*, 386. (g) Kitagawa, S.; Uemura, K. *Chem. Soc. Rev.* **2005**, *34*, 109. (h) Britz, D. A.; Khlobystov, A. N. *Chem. Soc. Rev.* **2006**, *35*, 637. (i) Steed, J. W.; Atwood, J. L., *Supramolecular Chemistry*, 2nd ed.; Wiley: Chichester, 2009.
- (14) (a) Nguyen, V. T.; Chan, I. Y. H.; Bishop, R.; Craig, D. C.; Scudder, M. L. *New. J. Chem.* **2009**, *33*, 1736. (b) *Enantiomer Separation: Fundamentals and Practical Methods*; Toda, F., Ed.; Springer: Berlin, 2004. (c) Collet, A. The Homochiral versus Heterochiral Packing Dilemma, in *Problems and Wonders of Chiral Molecules*; Simonyi, M., Ed.; Akadémiai Kiadó: Budapest, 1990; pp 91–109.
- (15) Bishop, R. *Chem. Soc. Rev.* **1996**, *25*, 311.
- (16) Bhowmick, K. C.; Joshi, N. N. *Tetrahedron Asymmetry* **2006**, *17*, 1901.
- (17) Macrae, C. F.; Bruno, I. J.; Chisholm, J. A.; Edgington, P. R.; McCabe, P.; Pidcock, E.; Rodriguez-Monge, L.; Taylor, R.; van de Streek, J.; Wood, P. A. *J. Appl. Crystallogr.* **2008**, *41*, 466.
- (18) Horike, S.; Shimomura, S.; Kitagawa, S. *Nat. Chem* **2009**, *1*, 695.
- (19) COLLECT data collection software: Nonius B. V., 1998.
- (20) Otwinowski, Z.; Minor, W. Processing of X-ray Diffraction Data Collected in Oscillation Mode. *Methods in Enzymology*, Carter, C.W., Jr., Sweet, R.M., Eds.; Academic Press: New York, 1997; Vol. 276: Macromolecular Crystallography, part A, pp 307–326.
- (21) Sheldrick, G. M. *SADABS - Bruker Nonius Area Detector Scaling and Absorption Correction*, V2.10.
- (22) *CrystalClear-SM Expert 2.0 r7*; Rigaku: The Woodlands, TX, 2011.
- (23) *SHELX97: Programs for Crystal Structure Analysis*, Release 97-2; Sheldrick, G. M., Institut für Anorganische Chemie der Universität, Göttingen, Germany, 1998.
- (24) Bruno, I. J.; Cole, J. C.; Edgington, P. R.; Kessler, M.; Macrae, C. F.; McCabe, P.; Pearson, J.; Taylor, R. *Acta Crystallogr.* **2002**, *B58*, 389.
- (25) CrysAlis CCD and CrysAlis RED, versions 1.171.33.55; Oxford Diffraction Ltd: Yarnton, Oxfordshire, UK., 2011.
- (26) Dolomanov, O. V.; Blake, A. J.; Champness, N. R.; Schröder, M. *J. Appl. Crystallogr.* **2003**, *36*, 1283.
- (27) Sheldrick, G. M. *SHELXS-97 and SHELXL-97*; University of Göttingen: Göttingen, Germany, 1997.
- (28) *Bruker, APEX2 Software*, V2012.2; Bruker AXS Inc.: Madison, Wisconsin, USA, 2012.
- (29) *Bruker, SAINT, Area Detector Integration Software*, V8.18c; Bruker AXS Inc.: Madison, Wisconsin, USA, 1997.
- (30) Sheldrick, G. M. *SADABS - Bruker Nonius Area Detector Scaling and Absorption Correction*, V2.10.





---

## Articles in Preparation



# High Hydrophobicity, Water Stability and Methane Affinity in a MOF Exhibiting Pores Decorated with Carborane Clusters

Min Ying Tsang,<sup>†</sup> Kyriakos C. Stylianou,<sup>§</sup> Francesc Teixidor,<sup>†</sup> Clara Viñas,<sup>†</sup> Duane Choquesillo-Lazarte,<sup>◇</sup> Cristóbal Verdugo Escamilla,<sup>◇</sup> Daniel MasPOCH<sup>§,#</sup> and José Giner Planas<sup>†</sup>

<sup>†</sup> Institut de Ciència de Materials de Barcelona (ICMAB-CSIC), Bellaterra, Spain

<sup>§</sup> ICN2 (ICN-CSIC), Institut Català de Nanociència i Nanotecnologia, Esfera UAB, 08193 Bellaterra, Spain

<sup>◇</sup> Laboratorio de Estudios Cristalográficos, IACT, CSIC-Universidad de Granada, Av. de las Palmeras 4, E-18100 Armilla, Granada, Spain

<sup>#</sup> Institució Catalana de Recerca i Estudis Avançats (ICREA), 08100 Barcelona, Spain

**Abstract.** The decoration of the internal pore surface of a MOF with carboranes yields a hydrophobic and porous material in which water molecules cannot diffuse within its pores to destruct the MOF structure. The generation of unsaturated metal sites upon activation, combined with the presence of the carborane core within the channels leads in the isolation of a material with high affinity for methane at low and high coverage (19.6 – 23.1 kJ/mol) which is one the highest values reported to date.

A metal organic framework (MOF) is an infinite network of metal ions or metal ion clusters bridged by organic ligands through covalent bonds into a porous extended structure. The range of potential structures encompassed by this area is vast as different structures and properties can be obtained not only by the judicious choice of metal and multifunctional ligand but also by the connectivity of the structure (different pore sizes and shapes) and which groups decorate their pore surface. This has led to the discovery of a broad array of highly porous MOF materials with various topologies and compositions, displaying record surface areas up to 7000 m<sup>2</sup>/g, high void volumes (up to 90%) and low densities (down to 0.19 g/cm<sup>3</sup>). The ability to chemically modify the ligand either pre- or post-synthesis and introduce desired functional

groups within their pores, combined with the potential for open metal sites allows the generation of catalytic centers and specific interactions with tailored internal surfaces for applications such as gas separation and provides exceptional figures of merit for “standard” porous materials applications such as gas storage. Although MOFs are very attractive for many applications, one of their major drawback is their low hydrolytic stability preventing their use for many industrial processes such as the direct capture of CO<sub>2</sub> from flue gas, water purification and others. In order to enhance their hydrolytic stability, many different strategies have been developed and most of them lie on the incorporation of hydrophobic molecules: a. through ligand design and the introduction of hydrophobic groups within a ligand, b. the encapsulation of hydrophobic molecules and c. the coating of MOF crystals with hydrophobic polymers. The presence of hydrophobic groups within MOFs cannot only improve their hydrolytic stability but it can be also used to introduce strong interactions with non-polar molecules such as methane. Recent reports revealed that the CH<sub>4</sub> adsorption and how strong it interacts with the pore surface it depends mainly on the ligand

functionalities and/or generation of unsaturated metal sites.

Carborane based ligands were used to construct MOFs by Mirkin *et al.* and they serve many advantages compared to other conventional ligand based MOFs, as carborane based MOFs are robust, rigid with high thermal and chemical stabilities and they can be hydrophobic. To date, carborane based MOFs have shown great potential for application in gas storage – H<sub>2</sub> and CH<sub>4</sub> storage, and CO<sub>2</sub> capture. However, most of the carborane based MOFs reported in the literature are based on para-substituted carborane cores and although they show intriguing properties for gas storage applications, they are hugely expensive. In contrast, the ortho-substituted carborane core is cheap however, reports on its functionalisation are not exhaustive and they have not yet been used for the construction of MOFs.

Herein, we show that the reaction of a cheap and newly synthesised carborane ligand functionalised with pyridyl groups at *ortho*-positions (*anti*-oCB-L) with Zn(II) and 1,4-benzene dicarboxylic acid (H<sub>2</sub>bdc) results in the isolation of **oCB-MOF-1**: ortho-carborane-MOF-1, which is resistant to water. This behaviour is mainly attributed to the presence of the carborane core pointing towards the pores preventing thus, water molecules to diffuse within the pores, attack the Zn<sub>4</sub>-cluster, displace the ligands and destroy the structural integrity of **oCB-MOF-1**. **oCB-MOF-1** is porous to CO<sub>2</sub> at 195 K with a surface area of 296 m<sup>2</sup>/g and it has high affinity for CH<sub>4</sub> at low coverage as well as at high loadings.

The reaction of Zn(NO<sub>3</sub>)<sub>2</sub>·6H<sub>2</sub>O, H<sub>2</sub>bdc, 1,2-Bis((pyridin-3-yl)methanol)-1,2-dicarba-closo-dodecaborane (*anti*-oCB-L) and 2-methylimidazole (2-Hmim) in a 1:1 mixture of ethanol:dimethylformamide (EtOH:DMF) V<sub>t</sub> = 2 mL, at 85 °C for 48 hours gave rise to a pure phase of

**oCB-MOF-1** with formula of [Zn<sub>4</sub>(bdc)<sub>2</sub>(*anti*-oCB-L)<sub>2</sub>(μ<sub>3</sub>-O)<sub>2</sub>(DMF)<sub>2</sub>](DMF)<sub>4</sub>. The purity of **oCB-MOF-1** was confirmed by elemental analysis as well as by powder X-ray diffraction (PXRD). Note that addition of 2.5 equivalents of 2-Hmim was necessary in order to avoid the formation of **MOF-5** and **oCB-MOF-1** mixtures.

**oCB-MOF-1** is a 3D framework built up from 2D Zn<sub>4</sub>(bdc) layers interconnected by the *anti*-oCB-L ligand. A tetranuclear Zn cluster is formed in which there are two distinct Zn(II) coordination modes – tetrahedral (Zn#1) and octahedral (Zn#2). Zn#1 coordinates to two carboxylate O atoms from the bdc ligand, one μ<sub>3</sub>-O atom and one N atom from the *anti*-oCB-L ligand whereas Zn#2 binds to two carboxylate O atoms from the bdc ligand, two μ<sub>3</sub>-O, one N atom from the *anti*-oCB-L ligand and the sixth position is completed by the coordination of DMF through the oxygen atom. 1,4-bdc ligands coordinate with the Zn-cluster to form a square grid 2D layer as shown in **Figure xx**, and the *anti*-oCB-L act as bridging linkers to connect the 2D layers and form the 3D network. It is important to highlight here, that the carborane core is pointing towards the channels; this is due to the specific coordination of *anti*-oCB-L ligand around the Zn<sub>4</sub> cluster. **oCB-MOF-1** is porous along the *c*-axis with pore dimensions of **3.5 x 6.5 Å**. The accessible volume of **oCB-MOF-1** is 28 % as calculated by PLATON giving thus a pore volume of 0.21 cm<sup>3</sup>/g.

The behavior of **oCB-MOF-1** over H<sub>2</sub>O prompted us to check the hydrophobicity of **oCB-MOF-1** by firstly measuring the contact angle – a useful tool that indicates the wettability of the materials by a liquid, and water vapor isotherms. Activated **oCB-MOF-1** was initially grinded to a fine powder and packed by a glass slide to create a flat surface, for contact angle (θ<sub>c</sub>) measurements. The θ<sub>c</sub> was found to be 138° suggesting that **oCB-MOF-1** is within the group of hydrophobic materials. Vapour

H<sub>2</sub>O adsorption revealed that the hydrophobic **oCB-MOF-1** exhibits low water uptake of 0.025 g/g at high relative humidity. **oCB-MOF-1** has a comparable sorption behavior with that of the hyper-hydrophobic **ZIF-8** and its isorecticular hydrophilic **SIM-1**. The low adsorption clearly suggests that the pore surface of **oCB-MOF-1** is hydrophobic and thus water is not favored to diffuse within the pores and thus destruct the structure.

**oCB-MOF-1** does not collapse when is soaked in liquid H<sub>2</sub>O at room temperature (RT) for 15 hours and also in boiling liquid H<sub>2</sub>O (B) for 0.5 hours. The PXRD pattern of the **H<sub>2</sub>O\_RT@oCB-MOF-1** shows that the low angle reflections shift in higher 2-theta degrees indicating that there is a small change (shrinkage) of the unit cell and it is very comparable with that of **MeOH@oCB-MOF-1**. The pattern corresponding to **H<sub>2</sub>O\_B@oCB-MOF-1** shows a remarkable reduction of crystallinity and the Bragg reflections were broaden indicating the generation of a highly distorted material. The IR spectra of **H<sub>2</sub>O\_RT@oCB-MOF-1** and **H<sub>2</sub>O\_B@oCB-MOF-1** are almost identical with that of **oCB-MOF-1** suggesting that the MOF retains its structural integrity. **oCB-MOF-1** can be recovered when **H<sub>2</sub>O\_B@oCB-MOF-1** was immersed in liquid DMF for 15 hours at room temperature which is a further proof that **H<sub>2</sub>O\_B@oCB-MOF-1** does not collapse. In order to further study the influence of H<sub>2</sub>O on **oCB-MOF-1**, we have soaked bulk material in liquid D<sub>2</sub>O and the 1H NMR spectrum revealed that the DMF molecules diffuse in the aqueous phase. In addition, we have quantitatively checked the content of free Zn(II) ions content by ICP/MS when pure **oCB-MOF-1** was soaked in liquid H<sub>2</sub>O – considering that **oCB-MOF-1** collapses. Interestingly, 15 mg/L of Zn(II) was observed after 4 days of immersion and we found a weight loss of

12.8 % in terms of the weight of the material. **oCB-MOF-1** was also immersed at different pH solutions pH 2, 4, 6, 8, 10 and 12 (pH adjusted with HCl or NaOH) at room temperature for 15 hours and their corresponding PXRD patterns show a remarkable coincidence and are very comparable with that of **H<sub>2</sub>O\_RT@oCB-MOF-1** highlighting its structural integrity and robustness.

The thermal stability of **oCB-MOF-1** was investigated by thermogravimetric analysis and it is found that the guest and coordinated to Zn(II) DMF molecules were removed in the temperature range of 30-250 °C with the total loss to be 24.0 %. The weight loss observed in TGA is in a good agreement with that calculated from elemental analysis (24.5 %). **oCB-MOF-1** is stable up to 380 °C and its decomposition occurs immediately after this temperature in a single step. **oCB-MOF-1** is stable in standing in air as this confirmed by PXRD.

In order to gently activate **oCB-MOF-1** without damaging its integrity and remove the guest and coordinated to Zn(II) molecules, several different conditions were tried but the optimal conditions were at 100 °C overnight at 10<sup>-3</sup> mbar. Elemental analysis revealed that the activated **oCB-MOF-1'** is free of guest DMF molecules and also coordinated DMF molecules, yielding thus **oCB-MOF-1'** with readily available pores and unsaturated Zn(II) ions. The pores of **oCB-MOF-1'** are bifunctional functionalised as both the hydrophobic carborane core and exposed open Zn(II) sites are pointing towards the channels. **oCB-MOF-1'** is non-porous to N<sub>2</sub> at 77 K and 1 bar as confirmed by the type II isotherm and this is due to the smaller pore window of **oCB-MOF-1'** than the kinetic diameter of N<sub>2</sub> (3.6 Å). Contrawise, carbon dioxide isotherms collected on **oCB-MOF-1'** at 195 K and 0.8 bar showed a type I behavior characteristic of microporous materials. The Brunauer-Emmett-Teller (BET) model applied over

$p/p^0 = 0.05 - 0.3$  gives a surface area of  $296 \text{ m}^2/\text{g}$  and pore volume (calculated using the DR equation) of  $0.18 \text{ cm}^3/\text{g}$  which is slightly smaller than the calculated pore volume from the static single crystal structure of **oCB-MOF-1'** ( $0.21 \text{ cm}^3/\text{g}$ ). This is entirely consistent with the PXRD pattern of **oCB-MOF-1'** as we have observed shifts of Bragg reflections at higher 2-theta values suggesting the shrinkage of the unit cell parameters.

$\text{CO}_2$  and  $\text{CH}_4$  sorption isotherms on **oCB-MOF-1'** collected at 273 K and 298 K at 1 bar show reversible type I behavior. **oCB-MOF-1'** adsorbs 26.1 and  $13.1 \text{ cm}^3/\text{g}$  of  $\text{CO}_2$  and  $\text{CH}_4$  respectively at 273 K and 1 bar. Isothermic heats of adsorption,  $Q_{st}$ , for  $\text{CO}_2$  and  $\text{CH}_4$  on **oCB-MOF-1'** were derived using the Clausius-Clapeyron equation using the adsorption branches of the isotherms measured at 273 K and 298 K. The  $Q_{st}$  of **oCB-MOF-1'** for  $\text{CO}_2$  was calculated to be  $33.6 \text{ kJ/mol}$  at low coverage and this decreases to  $27.6 \text{ kJ/mol}$  at high coverage. The relatively high  $Q_{st}$  is thought to be due to the presence of open Zn(II) ions pointing towards the channels introducing strong interactions with  $\text{CO}_2$  molecules. This observation is entirely consistent with other MOFs containing open metal sites such as the HKUST-1, Al-MIL-96 and Al-MIL-53. The  $Q_{st}$  for  $\text{CH}_4$  for **oCB-MOF-1'** at low coverage was found to be  $19.6 \text{ kJ/mol}$  and it increases at high loadings to  $23.1 \text{ kJ/mol}$ . This is among the highest value reported for highly porous MOFs that are promising for methane storage applications (i.e. Ni-MOF-74 –  $21.4 \text{ kJ/mol}$ ,  $\text{Co}_9\text{-INA}$  –  $19.4 \text{ kJ/mol}$ , PCN-14 –  $18.7 \text{ kJ/mol}$ ). A Raman spectroscopic investigation of  $\text{CH}_4$  adsorption in the isoreticular IRMOF family demonstrates the critical role that the ligands play in the adsorption behavior of methane in these MOFs, thus revealing that the selection of appropriate ligands with the highest

affinity for methane will provide an optimal storage material. In addition, the high affinity of Ni-MOF-74 for  $\text{CH}_4$  is mainly due to the presence of unsaturated metal sites. The high affinity thus of **oCB-MOF-1'** for  $\text{CH}_4$  is thought to be attributed to its bifunctional pore functionalization as both the hydrophobic carborane core and open metal sites are pointing towards the channels and it can interact with both the carborane core and unsaturated Zn(II) sites. Despite the fact that **oCB-MOF-1'** is not as highly porous as for example the Ni-MOF-74 or PCN-14, it is a water resistant material and shows high  $Q_{st}$  for methane which can be further tested for the purification of natural gas.

To conclude, a neutral pyridyl containing carborane-based ligand interlinks the Zn-bdc 2D layers to form a 3D and water stable **oCB-MOF-1**. **oCB-MOF-1** is stable in air and does not collapse when is treated with several organic solvents nor at liquid water at room temperature nor at boiling water. The activated **oCB-MOF-1'** has a bifunctional pore character as both the carborane core and open metal sites are pointing towards the channels and this is found to be of great importance for the introduction of strong interactions with  $\text{CO}_2$  and  $\text{CH}_4$ . The  $Q_{st}$  of **oCB-MOF-1'** for  $\text{CH}_4$  is found to be at  $19.6\text{-}23.1 \text{ kJ/mol}$  which is one of the highest values reported to date. Our future efforts will focus on testing **oCB-MOF-1** as a stationary phase for the purification of natural gas (composed primarily of  $\text{CH}_4$ ,  $> 95 \%$ , with the remaining fraction a mixture of ethane and heavier hydrocarbons,  $\text{N}_2$ , and  $\text{CO}_2$ ), a process which requires the usage of robust materials and be selective to  $\text{CH}_4$  for the efficient  $\text{CO}_2/\text{CH}_4$  separation.

## Experimental Section

### Materials and Characterization

Zinc(II) nitrate hexahydrate, 1,4-benzenedicarboxylate(bdc) and 2-methylimidazole were purchased from Sigma Aldrich and used as received. The ligand 1,2-Bis((pyridin-3-yl)methanol)-1,2-dicarba-closo-dodecaborane (*anti-oCB-L*) was synthesized according to the reported method. [1]

IR ATR spectra were recorded on a Perkin-Elmer Spectrum One Spectrometer. Elemental analyses were obtained by a CarboErba EA1108 microanalyzer (Universidad Autonoma de Barcelona). Powder X-ray Diffraction (PXRD) was recorded at room temperature on an X'Pert PRO MPD $\theta/\theta$  powder diffractometer (PanAnalytical; configuration: convergent beam; radius: 240 nm) equipped with a focalizing mirror and a transmission geometry with a silicon sample holder, for Cu K $\alpha$  radiation ( $\lambda = 1.5418 \text{ \AA}$ ). Thermogravimetric Analysis (TGA) were performed in air, on a nSTA 449 F1 Jupiter-Simultaneous TGA-DSC from (NETZSCH; heating rate: 5 °C/min; temperature range: 25 °C to 500 °C). Gas sorption (CH<sub>4</sub>/273 K and 298 K; CO<sub>2</sub>/273 K and 298 K; and N<sub>2</sub>/77K) measurements were performed using an AutosorbIQ after activating the **oCB-MOF-1** at 100 oC and 10<sup>-3</sup> mbar.

Synthesis of [Zn<sub>4</sub>(1,4-bdc)<sub>2</sub>(**L3**)<sub>2</sub>( $\mu$ -O)<sub>2</sub>](DMF)<sub>2</sub>(**oCB-MOF-1**) was reported [1]. <sup>1</sup>H NMR (DMSO): 8.62 (d, *J* = 1.8, 2H, C<sub>5</sub>H<sub>4</sub>N), 8.58 (dd, *J* = 4.7, 1.5, 2H, C<sub>5</sub>H<sub>4</sub>N), 7.86 (brd, *J* = 8.0, 2H, C<sub>5</sub>H<sub>4</sub>N), 7.47 (dd, *J* = 7.9, 4.8, 2H, C<sub>5</sub>H<sub>4</sub>N), 7.25 (d, *J* = 5.5, 2H, OH), 5.59 (d, *J* = 5.50, 2H, CHOH). <sup>13</sup>C NMR (DMSO): 149.61, 148.09, 136.65, 134.86 and 123.45 (C<sub>5</sub>H<sub>4</sub>N), 86.71 (*C<sub>cluster</sub>*), 68.87 (CHOH). <sup>11</sup>B NMR (DMSO) -3.4 (m, 4B), -10.4 (m, 8B). IR (ATR from the mixture containing an excess of **3a**); only assigned bands are listed here):  $\nu$  3071, 2989 (OH), 2628, 2614, 2587, 2545 (BH). MALDI-TOF, *m/z*: M: 359.26 [M+H]<sup>+</sup>

Crystalline solid **oCB-MOF-1** was obtained by mixing Zn(NO<sub>3</sub>)<sub>2</sub>·6H<sub>2</sub>O (16.6 mg, 0.56mmol), *anti-oCB-L* (10 mg, 0.027mmol), 2-methylimidazole (4.6mg, 0.054mmol) and 1,4-bdc (4.6mg, 0.027mmol) in 2 mL of DMF/ethanol (1:1). This mixture was sonicated until all solids were dissolved, followed by heating at 85 °C for 48 hours. Pale yellow crystalline solid of **oCB-MOF-1** was collected and washed with DMF (24.3 mg, yield 56%). IR (ATR; selected bands):  $\nu$  3419 (OH); 2927, 2881 (CH); 2520 (BH); 1652 (C=O from DMF); 1602 (C=O from carboxylate). Elemental analysis (%) calculated for [Zn<sub>4</sub>(C<sub>8</sub>H<sub>4</sub>O<sub>4</sub>)<sub>2</sub>(C<sub>14</sub>B<sub>10</sub>N<sub>2</sub>O<sub>2</sub>H<sub>22</sub>)<sub>2</sub>( $\mu$ -O)<sub>2</sub>](DMF)<sub>6</sub>·(H<sub>2</sub>O)<sub>2.5</sub>: C: 40.82, H: 5.58, N: 7.68; Found: C: 40.90, H: 5.5, N: 7.6.



## Single-Crystal X-ray Diffraction

Table S1. Crystal data and structural refinement for **oCB-MOF-1**

Crystal Data	<b>oCB-MOF-1</b>
Empirical formula	C <sub>25</sub> H <sub>33</sub> B <sub>10</sub> N <sub>3</sub> O <sub>8</sub> Zn <sub>2</sub>
Formula weight	742.38
Crystal system	Triclinic
Space group	P-1
Temperature/K	100.0
Wavelength/Å	0.79480
Unit cell dimensions	a = 12.0317(10) Å b = 13.8465(10) Å c = 15.5341(9) Å α = 110.362(6)° β = 109.511(7)° γ = 92.299(7)°
Volume/ Å <sup>3</sup>	2250.8(3) Å <sup>3</sup>
Z	2
Density (calculated)/ Mg/m <sup>3</sup>	1.095
Absorption coefficient/ mm <sup>-1</sup>	1.491
F(000)	756
Theta range for data collection/deg	1.93 to 27.87
Index ranges	-15 ≤ h ≤ 15 -19 ≤ k ≤ 18 -18 ≤ l ≤ 21
Reflections collected/unique	16441/6997 [R(int) = 0.0584]
Max. and min. transmission	1.00000 and 0.39923
Final R indices [I > 2σ(I)]	R1 = 0.0898, wR2 = 0.2787
R indices (all data)	R1 = 0.0977, wR2 = 0.2923
Largest diff. peak and hole	1.019 and -1.063 e.Å <sup>-3</sup>

Table S2. Selected bond lengths and angles for **oCB-MOF-1**

Zn(1)-O(1)	1.945(4)	O(1)-Zn(1)-Zn(2)#1	89.18(14)
Zn(1)-Zn(2)#1	3.1174(9)	O(1)-Zn(1)-N(19)	103.8(2)
Zn(1)-O(8)	1.927(4)	O(1)-Zn(1)-O(34)	108.51(19)
Zn(1)-N(19)	2.023(5)	O(8)-Zn(1)-O(1)	115.15(18)
Zn(1)-O(34)	1.963(3)	O(8)-Zn(1)-Zn(2)#1	41.48(11)

---

Zn(2)-Zn(1)#1	3.1174(9)	O(8)-Zn(1)-N(19)	117.6(2)
Zn(2)-O(8)#1	2.105(4)	O(8)-Zn(1)-O(34)	106.60(16)
Zn(2)-O(8)	2.101(3)	N(19)-Zn(1)-Zn(2)#1	159.03(17)
Zn(2)-N(27)	2.103(5)	O(34)-Zn(1)-Zn(2)#1	86.37(13)
Zn(2)-O(29)	2.172(4)	O(34)-Zn(1)-N(19)	104.48(19)
Zn(2)-O(36)#1	2.118(4)	C(30)#1-O(1)-Zn(1)	118.5(4)
Zn(2)-O(40)	2.155(4)	O(8)#1-Zn(2)-Zn(1)#1	37.32(11)
		O(8)-Zn(2)-Zn(1)#1	104.88(11)
		O(8)-Zn(2)-O(8)#1	80.28(17)
		O(8)-Zn(2)-N(27)	95.14(17)
		O(8)-Zn(2)-O(29)	87.32(15)
		O(8)#1-Zn(2)-O(29)	93.09(15)
		O(8)-Zn(2)-O(36)#1	171.79(15)
		O(8)#1-Zn(2)-O(36)#1	91.69(15)
		O(8)#1-Zn(2)-O(40)	93.18(16)
		O(8)-Zn(2)-O(40)	90.75(15)
		N(27)-Zn(2)-Zn(1)#1	147.47(14)
		N(27)-Zn(2)-O(8)#1	174.82(17)
		N(27)-Zn(2)-O(29)	89.09(17)
		N(27)-Zn(2)-O(36)#1	92.81(17)
		N(27)-Zn(2)-O(40)	84.42(18)
		O(29)-Zn(2)-Zn(1)#1	66.95(11)
		O(36)#1-Zn(2)-Zn(1)#1	68.93(11)
		O(36)#1-Zn(2)-O(29)	94.86(16)
		O(36)#1-Zn(2)-O(40)	87.99(16)
		O(40)-Zn(2)-Zn(1)#1	120.01(13)
		O(40)-Zn(2)-O(29)	173.04(17)
		Zn(1)-O(8)-Zn(2)	126.88(18)
		Zn(1)-O(8)-Zn(2)#1	101.19(16)
		Zn(2)-O(8)-Zn(2)#1	99.72(17)
		C(18)-N(19)-Zn(1)	121.3(5)
		C(20)-N(19)-Zn(1)	118.2(4)
		C(26)-N(27)-Zn(2)	119.4(3)
		C(28)-N(27)-Zn(2)	121.9(4)
		C(30)-O(29)-Zn(2)	139.9(4)
		C(35)-O(34)-Zn(1)	121.2(4)
		C(35)-O(36)-Zn(2)#1	137.5(3)
		C(41)-O(40)-Zn(2)	128.2(5)

---

Symmetry transformations used to generate equivalent atoms:

#1 x+1,y+1,z+1    #2 x+1,y+1,z    #3 x,y+1,z+1    #4 x+1,y,z+1

# 1. Representative Views and structural description of *oCB-MOF-1*

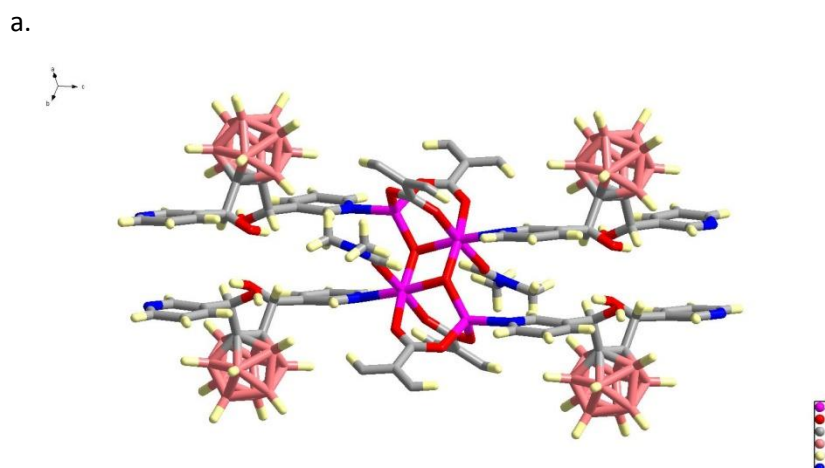


**Figure S1:** Illustration shows the coordination of the connection of *anti-oCB-L* with the tetra-nuclear Zn core.

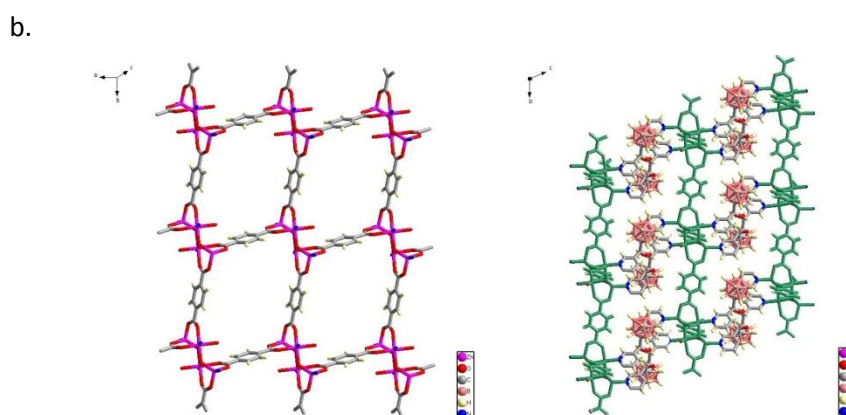


**Figure S2:** The 2D layer constructed by 1,4-bdc (grey) and the Zn core (purple). The linkage between the 2D layers by *anti-oCB-L*.

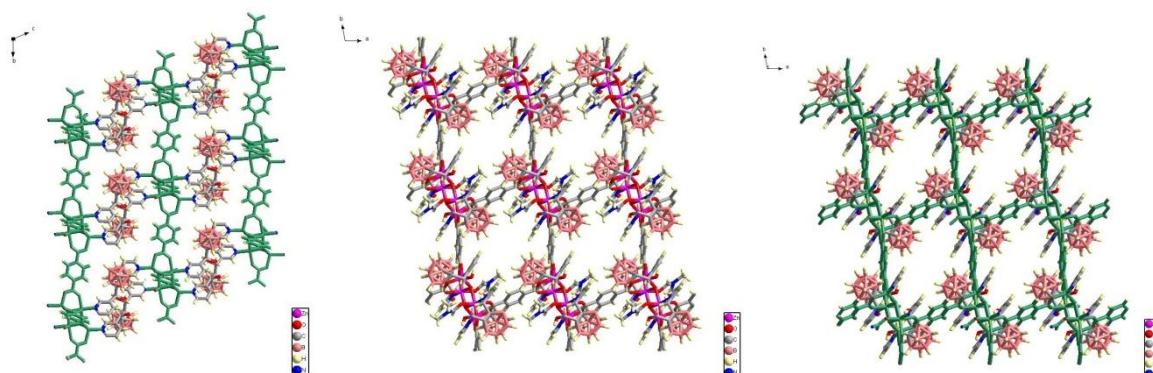


**Figure S3:** The organization of the *anti-oCB-L* around the 2D-Zn(II)-based layer that produces the 3D network, in which the carborane cages are pointed towards the pores (along the *c*-axis).

### Powder X-ray Diffraction (PXRD) of **oCB-MOF-1**

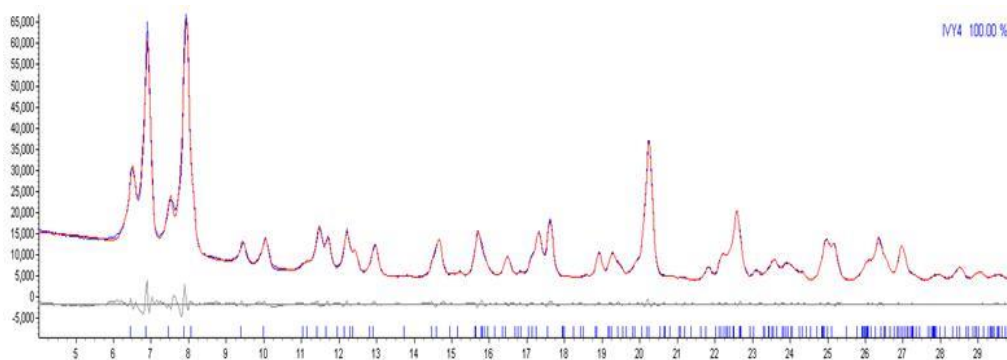


**Figure S4:** PXRD patterns of **oCB-MOF-1** that prepared by solvothermal method. The data are in good agreement with the refined simulated pattern derived from the corresponding single-crystal structure data.

### Infrared Spectra (ATR) of **oCB-MOF-1**

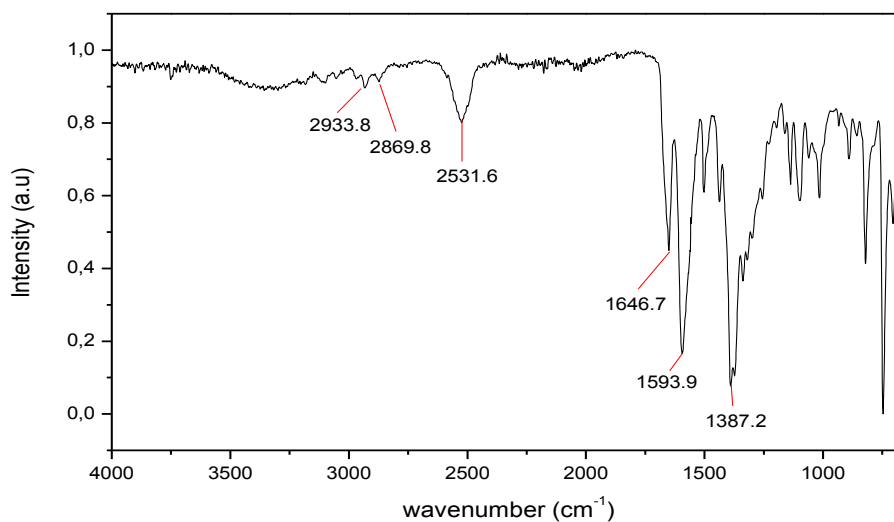


**Figure S5:** ATR spectra of **oCB-MOF-1** and **L3**. The B-H signals of **oCB-MOF-1** are in good agreement with the corresponding *anti*-**oCB-L**.

## Thermogravimetric Analysis (TGA) of **oCB-MOF-1**

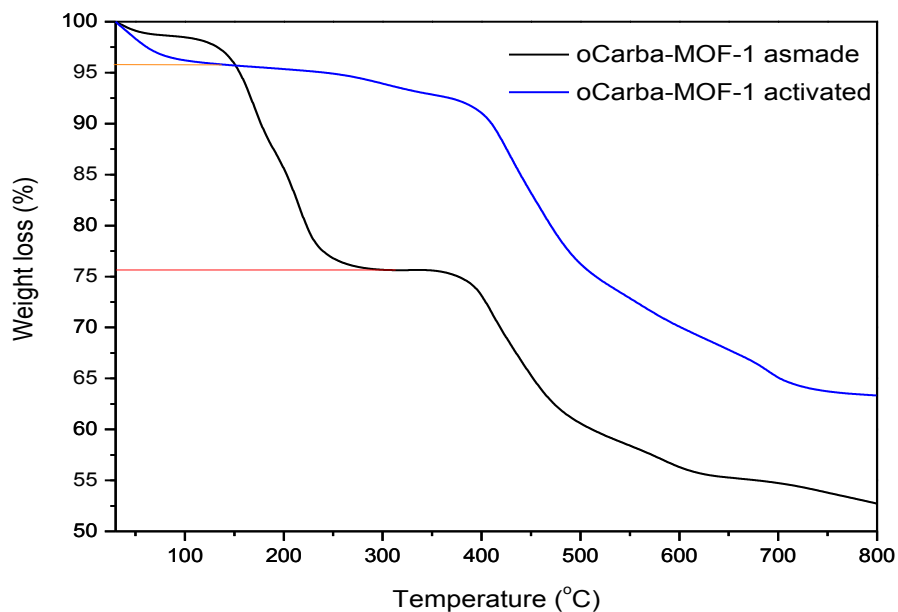


**Figure S6:** TGA curves for **oCB-MOF-1** asmade, activated **oCB-1-MOF-1'**, water treated **oCB-MOF-1** and boiling water treated **oCB-MOF-1** (heating rate: 5 °C/min; temperature range: 30 to 800 °C). The asmade **oCB-1-anti** shows weight loss of 24% from 30 °C to 250 °C, which corresponds to the loss of guest DMF molecules; and is stable up to 400 °C; then decomposes stepwise about 400 °C. The TGA curve of the activated **oCB-1-anti** shows almost no loss of weight from 30 °C to 400 °C, which confirms that **oCB-MOF-1** is free of guest molecules. The final product corresponds to the ZnO and B<sub>2</sub>O<sub>3</sub>.

Solvent (MeOH, CHCl<sub>3</sub> and acetone) treatment

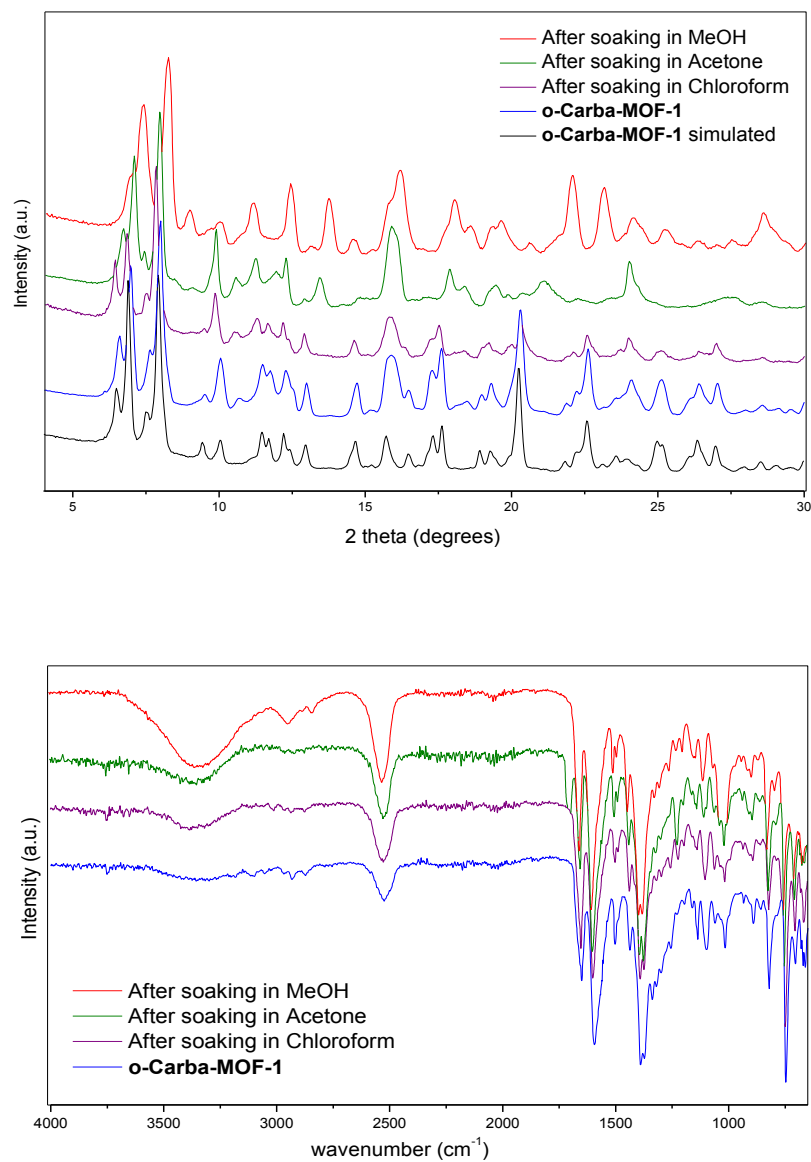


**Figure S7:** **oCB-MOF-1** after soaking in methanol, acetone and chloroform respectively for 15 h. (a) PXRD patterns (b) ATR spectrum. The signals of **oCB-MOF-1** are in good agreement with the corresponding materials.

## Water treatment

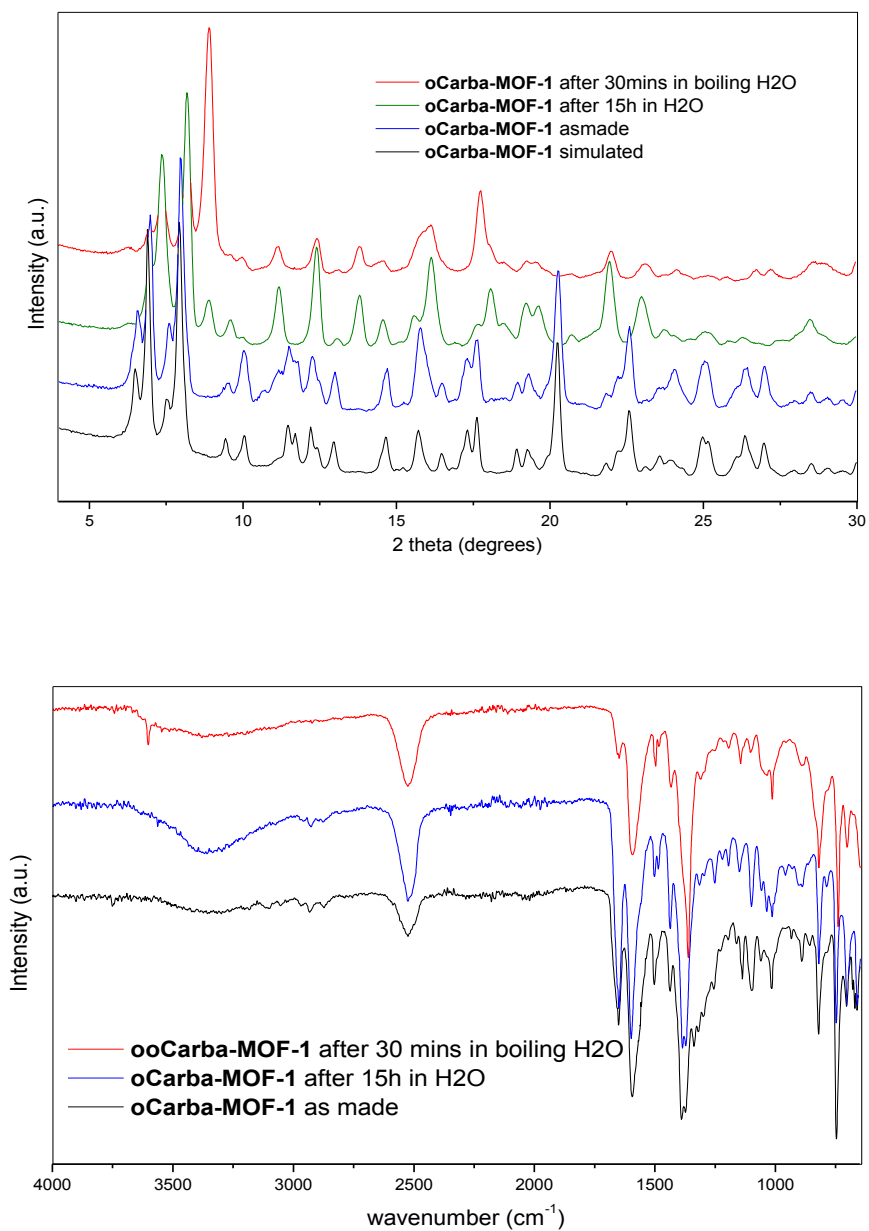


**Figure S8:** oCB-MOF-1 after treating with water and boiling water. (a) PXRD patterns. (b) ATR spectrum. The signals of oCB-MOF-1 are in good agreement with the corresponding materials.

## Reversibility of **oCarba-MOF-1** after water treatment

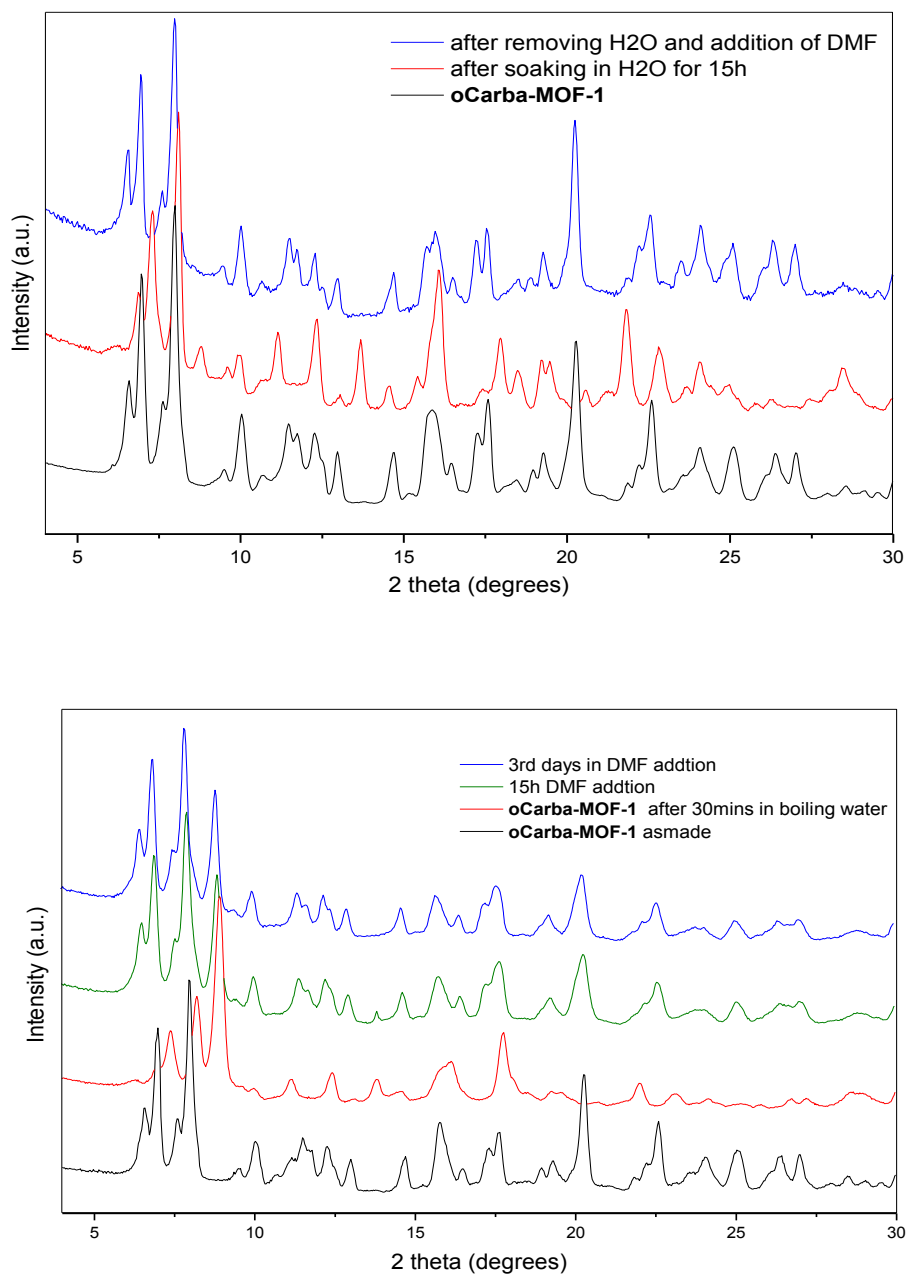


**Figure S9: oCB-MOF-1** after treated with water and reversibility test with DMF. (a) PXRD patterns of room temperature water treatment. (b) PXRD patterns of boiling water treatment.



## pH solution treatment

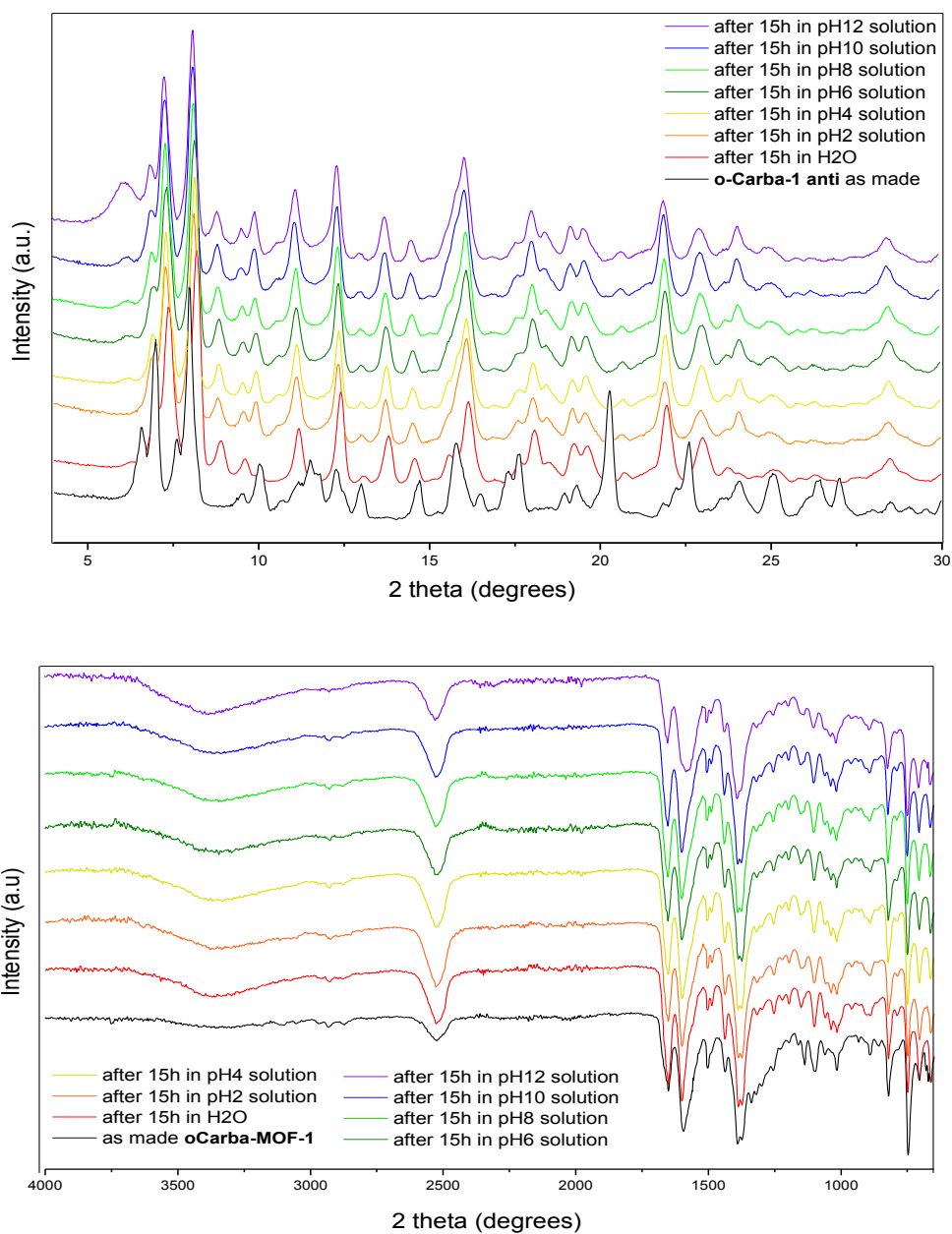


**Figure S10:** *o*CB-MOF-1 after treated with different pH solutions. (a) PXRD patterns. (b) ATR spectrum. The signals of *o*CB-MOF-1 are in good agreement with the corresponding materials.

## Hydrophobicity tests

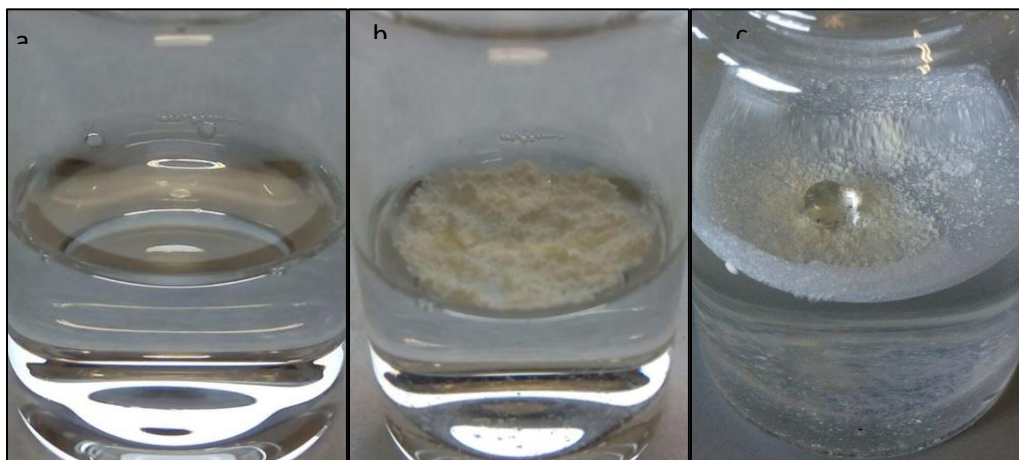


**Figure S11:**(a) Pure water, (b) addition of **oCarba-MOF-1** powder, (c) a drop of pure water on top of the powder.

## Contact angle

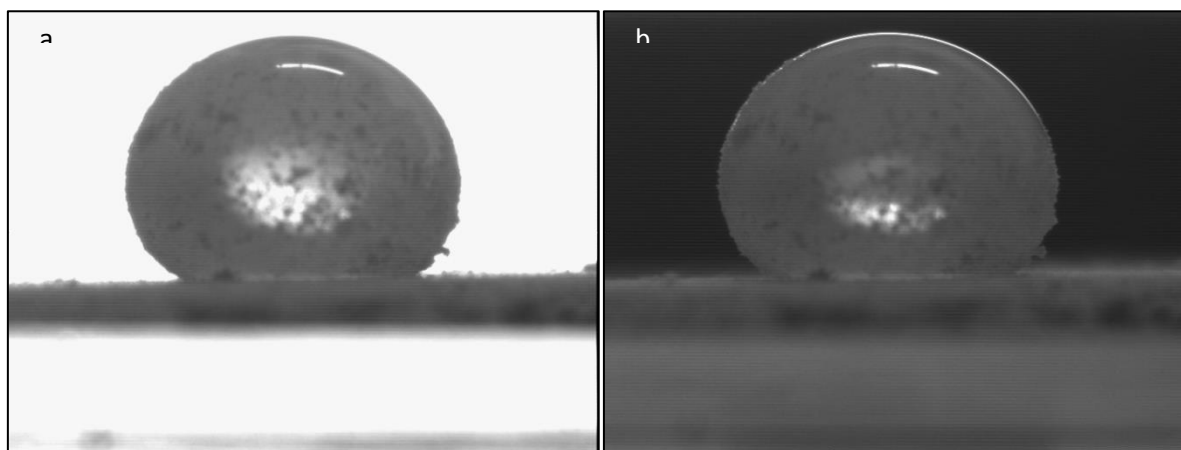


**Figure S12:** Image of the contact angle measurement of **oCarba-MOF-1** compacted powder. (a) is in white background and (b) is in black background.

# Carborane based-Coordination Polymers: Synthesis, Crystal Structure and Water Stability

Min Ying Tsang,<sup>a</sup> Sabina Rodríguez-Hermida,<sup>b</sup> Kyriakos C. Stylianou,<sup>b</sup> Francesc Teixidor,<sup>a</sup> Clara Viñas,<sup>a</sup> Duane Chosquesillo-Lazarte,<sup>c</sup> Cristóbal Verdugo Escamilla,<sup>c</sup> Inhar Imaz,<sup>b</sup> Daniel Maspoch<sup>b,d\*</sup> and José Ginel Planas<sup>a\*</sup>

<sup>a</sup>Institut de Ciència de Materials de Barcelona (ICMAB-CSIC), Campus UAB, 08193 Bellaterra, Spain.

<sup>b</sup>ICN2 – Institut Català de Nanociència i Nanotecnologia, Campus UAB, 08193 Bellaterra (Barcelona), Spain.

<sup>c</sup>Laboratorio de Estudios Cristalográficos, IACT-CSIC, Armilla, Granada, Spain.

<sup>d</sup>Institució Catalana de Recerca i Estudis Avançats (ICREA), 08100 Barcelona, Spain.

## Supporting Information Placeholder

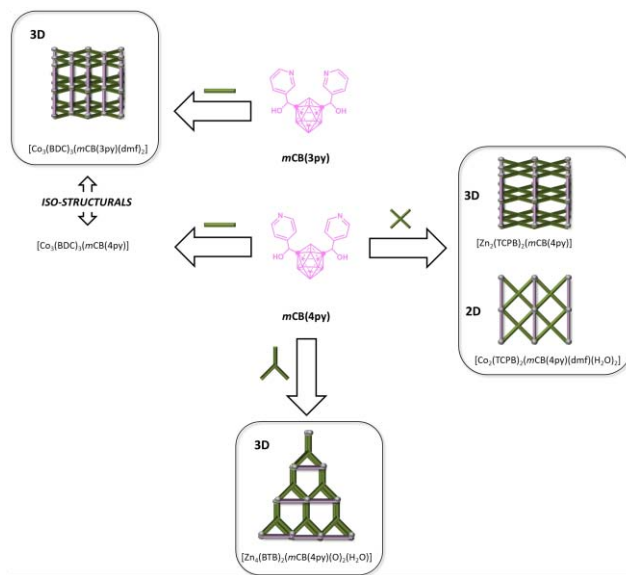
**ABSTRACT:** We report the synthesis of metal-organic frameworks (MOFs) based on M(II), di-, tri- and tetra-carboxylate linkers and two novel carborane/pyridine ligands.

## INTRODUCTION

Herein, we report the synthesis of two novel carboranylalcohol ligands (*m*CB(3py) and *m*CB(4py)) and the combination of these ligands with different di-, tri- and tetra-topic carboxylic acids to form six new extended coordination polymers (Scheme 1). The *m*CB ligands can adopt a linear conformation or a U-shape disposition, showing their structural flexibility. For example, in MOF1 and MOF4, the conformation of the *m*CB(4py) ligand is crucial to obtain 3D or 2D structures, respectively. Gas sorption measurements of the porous structures were performed, but show non-permanent porosity, indicating structural re-arrangements during the activation and/or sorption processes. Water stability tests were also performed and show that the introduction of carborane entities increase the water stability of the materials, in the cases of absence of Unsaturated Metal Centers (UMCs).

## EXPERIMENTAL SECTION

**Materials and Characterization.** Syntheses for the carboranylalcohol ligands were carried out under a nitrogen atmosphere in round-bottomed flasks equipped with a magnetic stirring bar, capped with a septum. THF was distilled from Na/benzophenone. MOF syntheses were done in air. All chemicals were commercially available and used as received. IR ATR spectra were recorded on a Perkin–Elmer Spectrum One spectrometer. <sup>1</sup>H, <sup>13</sup>C and <sup>11</sup>B spectra were recorded respectively at 300, 75 and 96 MHz with a Bruker Advance-300 spectrometer in deuterated dimethylsulfoxide, unless denoted, and referenced to the residual solvent peak for <sup>1</sup>H and <sup>13</sup>C NMR or to BF<sub>3</sub>.OEt<sub>2</sub> as an external standard for <sup>11</sup>B NMR. Chemical shifts are reported in ppm and coupling constants in Hertz. Multiplets nomenclature is as follows: s, singlet; d, doublet; t, triplet; br, broad; m, multiplet. Elemental analyses were obtained by a CarboErba EA1108 microanalyzer (Universidad Autónoma de Barcelona). The mass spectra were recorded in the negative ion mode using a Bruker Biflex MALDI-TOF-MS [N<sub>2</sub> laser; λ<sub>exc</sub> 337 nm (0.5 ns pulses); voltage ion



Scheme 1. Coordination modes of adenine within **1** (7Hade, left) and **2** (9Hade, right). In both MOFs, adenine is neutral. However, it acts as a bidentate (through N3 and N9) terminal linker in **1**, whereas it acts as a bidentate (through N3 and N7) bridging linker in **2**, being responsible of the formation of 1D Co(II)-adenine chains.

source 20.00 kV (Uis1) and 17.50 kV (Uis2)] with 3,5-dimethoxy-4-hydroxycinnamic acid as matrix. TGA-DSC from NETZSCH (heating rate: 10 °C/min; temperature range: 25 to 800°C). Gas sorption (CO<sub>2</sub>/195K and N<sub>2</sub>/77K) measurements for **2'** were performed using an AutosorbIQ (Quantachrome Instruments). Field-Emission Scanning Electron Microscopy (FE-SEM) images were collected using a Quanta 650F Environmental Scanning Electron Microscopy (Field Emission Inc, USA). The samples were metallized with 10 nm of platinum in an EM ACE600 High-Vacuum Coater (Leica, Germany). Powder X-ray Diffraction (PXRD) patterns were recorded at room temperature on an X'Pert PRO MPD diffractometer (PanAnalytical) for Cu Kα (λ = 1.5405 Å).

## Synthesis of the ligands

**Synthesis of 1,2-bis{(pyridin-3'-yl)methanol}-1,7-dicarba-closo-dodecaborane (mCB(3Py)).** nBuLi (1.02 mL, 1.44 M in hexane, 1.47 mmol) was added dropwise to a solution of m-carborane (105.8 mg, 0.73 mmol) in diethyl ether (10 mL) at 0 °C (ice/water bath) under nitrogen atmosphere. The mixture was stirred for 30 min at low temperature and for a further 1 h at room temperature to give a clear, pale yellow suspension. The flask was then cooled to -63 °C (chloroform/liquid N<sub>2</sub>), whereupon a solution of the 3-pyridinecarboxaldehyde (157.1 mg, 0.14 mL, 1.47 mmol) in THF (1 mL) was added. The resulting pale-yellow solution was stirred at -63 °C for 4 h. Then a saturated aqueous solution of NH<sub>4</sub>Cl (10 mL) was added at -63 °C and then the mixture was taken out of the cooling bath and allowed to warm naturally to room temperature while stirring. The aqueous phase was then extracted with Et<sub>2</sub>O (3 x 20 mL) and the organic phases were dried over MgSO<sub>4</sub>, filtered, and evaporated to dryness. The resultant dark yellow oil was washed with n-pentane (2 x 10 mL). Fresh n-pentane was added and the mixture was treated with ultrasound for c.a. 30 minutes, and the slightly colored pentane supernatant was removed afterwards. The same procedure was repeated until a light yellow solid was obtained (2-3 times). After removing the solvent, the yellow solid was dried under vacuum affording pure mCB(3Py) (200.9 mg, 0.56 mmol, 77 %). <sup>1</sup>H NMR: 8.50 (brs, 2H, C<sub>5</sub>H<sub>4</sub>N), 7.64 (brs, 2H, C<sub>5</sub>H<sub>4</sub>N), 7.63 (d, J = 7.8, 2H, C<sub>5</sub>H<sub>4</sub>N), 7.36 (dd, J = 8.1 Hz, 4.8 Hz, 2H, C<sub>5</sub>H<sub>4</sub>N), 6.58 (d, J = 5.1 Hz, 2H, OH), 4.89 (d, J = 5.4 Hz, 2H, CHOH). <sup>11</sup>B NMR: 0 to -20 ppm (br, 10B). <sup>13</sup>C NMR: 148.9 (C<sub>5</sub>H<sub>4</sub>N), 147.8 (C<sub>5</sub>H<sub>4</sub>N), 136.9 (C<sub>5</sub>H<sub>4</sub>N), 134.0 (C<sub>5</sub>H<sub>4</sub>N), 123.3 (C<sub>5</sub>H<sub>4</sub>N), 81.8 (C<sub>cluster</sub>), 71.2 (CHOH). IR (ATR),  $\nu$  [cm<sup>-1</sup>] = 3070 (br, OH), 2602(m, BH), {only selected bands reported}. MALDI-TOF, m/z: M: 358.4 [M]<sup>+</sup>. Elemental analysis (%) calculated for B<sub>10</sub>C<sub>14</sub>O<sub>2</sub>N<sub>2</sub>H<sub>22</sub> (M: 358.44 g mol<sup>-1</sup>) C 46.9, H 6.2, N 7.8; found C 46.7, H 6.4, N 7.5.

**Synthesis of 1,2-bis{(pyridin-4'-yl)methanol}-1,7-dicarba-closo-dodecaborane (mCB(4Py)).** The general procedure described above was followed, nBuLi (4.49 mL, 1.55 M in hexane, 7.0 mmol), THF (25 mL), m-carborane (502.4 mg, 3.5 mmol) and 4-pyridinecarboxaldehyde (0.7 mL, 7.0 mmol), and an acetonitrile/liquid N<sub>2</sub> cooling bath (-41 °C). The resulting pale-yellow solution was stirred at -41 °C for 4 h. Then a saturated aqueous solution of NH<sub>4</sub>Cl (10 mL) was added at -41 °C and then the mixture was taken out of the cooling bath and allowed to warm naturally to room temperature while stirring. Then diethyl ether (15 mL) was added while stirring. A white solid precipitated after about 25-20 minutes, that was filtrated, washed with water and diethyl ether and dried under vacuum affording pure mCB(4Py) (1.16 g, 3.23 mmol, 92.3 %). <sup>1</sup>H NMR 8.53 (d, J = 6.0 Hz, 4H, C<sub>5</sub>H<sub>4</sub>N), 7.23 (d, J = 6.0 Hz, 4H, C<sub>5</sub>H<sub>4</sub>N), 6.64 (d, J = 5.1 Hz, 2H, OH), 4.83 (d, J = 5.1, 2H, CHOH). <sup>11</sup>B NMR: -11.36 (br, 10B). <sup>13</sup>C NMR: 149.9 (C<sub>5</sub>H<sub>4</sub>N), 149.3 (C<sub>5</sub>H<sub>4</sub>N), 127.8 (C<sub>5</sub>H<sub>4</sub>N), 81.0 (C<sub>cluster</sub>), 72.2 (CHOH). IR (ATR),  $\nu$  [cm<sup>-1</sup>] = 3093 (br, OH), 2590 (m, BH), {only selected peaks bands are reported}. MALDI-TOF, m/z: M: 359.4 [M+H]<sup>+</sup>. Elemental analysis (%) calculated for B<sub>10</sub>C<sub>14</sub>O<sub>2</sub>N<sub>2</sub>H<sub>22</sub> (M: 358.44 g mol<sup>-1</sup>) C 46.9, H 6.2, N 7.8; found C 46.5%, H 6.2%, N 7.6.

### Synthesis of the Coordination Compounds

**Synthesis of [Zn<sub>2</sub>(TCPB)(mCB(4Py))]·8dmf (mCarba-MOF-1).** Single crystals of mCarba-MOF-1 were obtained by mixing Zn(NO<sub>3</sub>)<sub>2</sub>·6H<sub>2</sub>O (16.6 mg, 0.056 mmol), mCB(4Py) (10 mg, 0.027 mmol) and H<sub>4</sub>TCPB (15.6 mg, 0.027 mmol) in 4 mL of DMF/ethanol (1:1). This mixture was sonicated until all solids were uniformly dispersed, followed by heating at 80°C for 72 hours. Few pale yellow crystals of mCarba-MOF-1 were filtered

and washed with DMF. Insufficient crystals were obtained for elemental analysis or meaningful estimation of yield.

**Synthesis of [Co<sub>3</sub>(1,4-BDC)<sub>3</sub>(mCB(3Py)(dmf)<sub>2</sub>]·2dmf (mCarba-MOF-2).** Co(NO<sub>3</sub>)<sub>2</sub>·6H<sub>2</sub>O (48.7 mg, 0.167 mmol) was mixed with mCB(3Py) (20 mg, 0.054 mmol) and 1,4-BDC (13.8 mg, 0.167 mmol) in 4 mL of DMF/ethanol (1:1). This mixture was sonicated until all solids were uniformly dispersed, followed by heating at 100 °C for 24 hours. Violet flake-liked crystals of mCarba-MOF-2 were collected and washed with DMF (45.3 mg, 68.5%). IR (ATR; selected bands):  $\nu$  3426 (OH); 2931, 2861 (CH); 2531 (BH); 1657 (C=O from DMF); 1617 (C=O from carboxylate). Elemental analysis (%) calculated for [Co<sub>3</sub>C<sub>50</sub>H<sub>62</sub>B<sub>10</sub>N<sub>6</sub>O<sub>18</sub>] C: 45.5, H: 4.7, N: 6.4; Found: C: 45.0, H: 4.6, N: 6.2.

**Synthesis of [Co<sub>3</sub>(1,4-BDC)<sub>3</sub>(mCB(4Py)(dmf)<sub>2</sub>]·3dmf·6H<sub>2</sub>O (mCarba-MOF-2B).** mCarba-MOF-2B was obtained by mixing Co(NO<sub>3</sub>)<sub>2</sub>·6H<sub>2</sub>O (48.7 mg, 0.167 mmol), mCB(4Py) (20 mg, 0.054 mmol) and 1,4-BDC (13.8 mg, 0.167 mmol) in 4 mL of DMF/ethanol (1:1). This mixture was sonicated until all solids were uniformly dispersed, followed by heating at 100°C for 24 hours. Violet flake-liked crystals of mCarba-MOF-2B was collected and washed with DMF (50 mg). IR (ATR; selected bands):  $\nu$  3200 (OH); 2963, 2923, 2885 (CH); 2617 (BH); 1656 (C=O from DMF); 1598 (C=O from carboxylate). Elemental analysis (%) calculated for [Co<sub>3</sub>C<sub>53</sub>H<sub>81</sub>B<sub>10</sub>N<sub>7</sub>O<sub>25</sub>] C: 42.4, H: 5.4, N: 6.5; found: C: 42.0, H: 5.0, N: 7.0.

**Synthesis of [Zn<sub>4</sub>(BTB)<sub>2</sub>(mCB(4Py)(OH)<sub>2</sub>(H<sub>2</sub>O)<sub>2</sub>]·5H<sub>2</sub>O·4dmf (mCarba-MOF-3).** mCarba-MOF-3 was obtained by mixing Zn(NO<sub>3</sub>)<sub>2</sub>·6H<sub>2</sub>O (33.2 mg, 0.112 mmol), mCB(4Py) (10 mg, 0.027 mmol) and H<sub>3</sub>BTB (23.6 mg, 0.054 mmol) in 2 mL of DMF/ethanol/H<sub>2</sub>O (2:1:1). This mixture was sonicated until all solids were uniformly dispersed, followed by heating at 85 °C for 48 hours. Transparent square crystals of mCarba-MOF-3 was collected and washed with DMF (48.5 mg, 89%). IR (ATR; selected bands):  $\nu$  3350 (OH); 2933, 2964, 2865 (CH); 2617, 2554 (BH); 1660 (C=O from DMF); 1610, 1585 (C=O from carboxylate). Elemental analysis (%) calculated for [Zn<sub>4</sub>C<sub>80</sub>H<sub>88</sub>O<sub>23</sub>B<sub>10</sub>N<sub>6</sub>] C: 49.5, H: 4.9, N: 4.3; Found: C: 50.0, H: 4.7, N: 4.7.

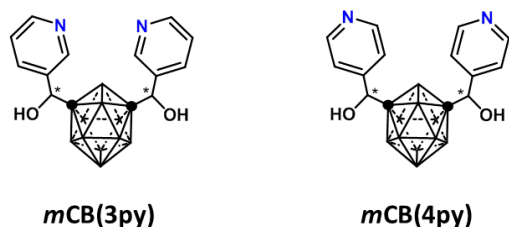
**Synthesis of [Co<sub>2</sub>(TCPB)(mCB(4Py)(H<sub>2</sub>O)( $\mu$ -H<sub>2</sub>O)(dmf)]·2.7dmf (mCarba-MOF-4).** mCarba-MOF-4 was obtained by mixing Co(NO<sub>3</sub>)<sub>2</sub>·6H<sub>2</sub>O (16.3 mg, 0.056 mmol), mCB(4Py) (10 mg, 0.027 mmol) and H<sub>4</sub>TCPB (15.6 mg, 0.027 mmol) in 4 mL of DMF/ethanol (1:1). This mixture was sonicated until all solids were uniformly dispersed, followed by heating at 85°C for 48 hours. Pale yellow crystals of mCarba-MOF-4 was collected and washed with DMF. Insufficient crystals were obtained for elemental analysis or meaningful estimation of yield.

**Crystallography.** Crystallographic data for MOF3 was collected at 100K at XALOC beamline at ALBA synchrotron ( $\lambda$  = 0.82653 Å). Data were indexed, integrated and scaled using the XDS<sup>17</sup> and IMOSFLM<sup>18</sup> programs. Absorption corrections were not applied. The structure was solved by direct methods and subsequently refined by correction of F<sup>2</sup> against all reflections, using SHELXS2013<sup>21</sup> and SHELXL2013<sup>22</sup> within the WinGX package.<sup>23</sup> All non-hydrogen atoms were refined with anisotropic thermal parameters by full-matrix least-squares calculations on F<sup>2</sup> using the program SHELXL2013. Hydrogen atoms were inserted at calculated positions and constrained with isotropic thermal parameters. The disorder associated with the oxygen atom of the crystallization water molecule hindered the localization of its hydrogen atoms. The contribution of four crystallized dmf mole-

cules to the diffraction pattern could not be rigorously included in the model and were consequently removed with the SQUEEZE routine of PLATON.

## RESULT AND DISCUSSION

**Synthesis and Characterization.** Two novel *mCB* ligands derived from *m*-carborane and pyridinecarboxyaldehyde have been synthesized in good yield. They have been characterized by  $^1\text{H}$ -,  $^{13}\text{C}$ - and  $^{11}\text{B}$ -nuclear magnetic resonance, infrared spectroscopy, elemental analysis and mass spectrometry (MALDI-TOF). They exhibit two N donor atoms connected to the hydrophobic carborane moiety through a quiral hydroxyl centre (Scheme 1). The ligands are flexible, as evidence from the crystal structure of the MOFs, *vide infra*.



Scheme 1. Representation of *mCB*(3py) and *mCB*(4py), showing the quiral centres (\*) and the binding N atoms (blue).

Solvothermal reactions between the corresponding *mCB* and di-, tri- and tetra-carboxylic ligands with metallic nitrate salts give rise to single crystals after 24 h at 100 °C, excepting for **MOF-1** that it is at 80 °C during 75h. Unfortunately no suitable single crystals of **MOF-2B** were obtained, and insufficient crystals of **MOF-1** and **MOF-4** were obtained. **MOF-2**, **MOF-2B** and **MOF-3** have been obtained in good yield as pure phases: the experimental powder X-ray diffraction pattern matches the simulated from the corresponding crystal structure (Figure SXXX), and the SEM images show homogeneity in the bulk material (Figure SXXX). IR spectra show the characteristic band of the B-H stretching from the carborane (centered at  $\sim 2615\text{ cm}^{-1}$  and  $\sim 2555\text{ cm}^{-1}$ ), and the C=O vibration of the carboxylic groups and the dmf solvent molecules. The thermal stability of these materials has been studied. The TGA diagrams (Figure SXXX) of **MOF-2** and **MOF-2B** show a first weight loss, which corresponds with the release of the solvent molecules and a second step that starts with the decomposition of the materials at  $\sim 350\text{ }^\circ\text{C}$ . From r.t. to 300 °C, **MOF-2** and **MOF-2B** show a weight loss of 22.6 % and 31.2 %, attributable to the dmf (calc. 22.4 %) and, dmf and water molecules (calc. 31.8 %), respectively. For **MOF-3**, it is possible to distinguish three weight loss steps: 1) from r.t. to 94 °C with a weight loss of 4.9 % (that corresponds with the 5 crystallized water molecules; calc. 4.6 %); 2) from 94 °C to 260 °C it losses 13.7 %, attributable to the uncoordinated dmf molecules (calc. 15.2 %) and 3) the decomposition of the framework.

**Structural Study of MOF-2 and MOF-2B.** Single crystal analysis of **MOF-2** shows that this compound is a 3D framework based on the trinuclear cluster namely Co1-Co2-Co1 which is formed by two crystallographically independent hexacoordinated metal centres. Co(1) is  $\{\text{NO}_5\}$  octahedrally coordinated to one *mCB*(3py) ligand, to four oxygen atoms from three BDC<sup>2-</sup> and to one oxygen atom belonging to one dmf molecule. Co(2) is  $\{\text{O}_6\}$ -coordinated to six neighboring BDC<sup>2-</sup> ligands (Figure XXa). There are two distinct carboxylate ligands regarding their coordination modes. One exhibits the bridge bidentate  $\mu\text{-}\kappa\text{O}:\kappa\text{O}'$  coord-

ination mode, and the other one connects four metal centres *via* the  $\mu\text{-}\kappa^2\text{O}_2\text{O}':\kappa\text{O}'$  bridge bidentate chelate binding mode (Figure XXb). Trinuclear cluster and BDC<sup>2-</sup> ligands create layers extended in the *ac* plane, which are further 3D-connected through the *mCB*(3py) ligand (Figure XXc), giving rise to a compact structure. The hydroxyl groups of the *mCB*(3py) ligand are disposed in an *anti* configuration and establish H-bonds with the crystallized dmf molecules. The ligand moiety is almost linear with a N-N distance of 12.15 Å, and it is the responsible for the three-dimensional arrangement.

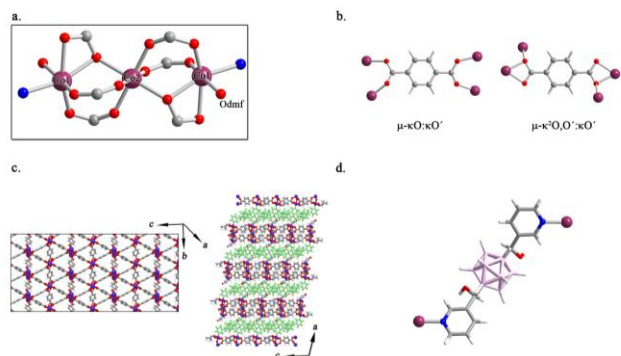
Attempts to obtain suitable single crystals for **MOF-2B** were unsuccessful; however it is possible to obtain the unit cell parameters from the powder pattern by comparison with the PXRD of **MOF-2**, assuming that both compounds crystallize in the monoclinic *C2/c* space group. Since the *mCB*(3py) ligand connects  $\{\text{Co}_3\text{-BDC}\}$  layers along the *a* axis in **MOF-2**, the N position in *mCB*(4py) ligand may be the responsible for the 3.36 Å of enhancement in the *a* parameter in **MOF-2B** (Table XX).

Table 1. Crystal and Structure Refinement data.					
Compound	MOF-1	MOF-2	MOF-2B	MOF-3	MOF-4
Empirical formula	$C_{72}H_{96}B_{10}N_{10}O_{18}Zn_2$	$C_{50}H_{62}B_{10}N_6O_{18}Co_3$		$C_{68}H_{45}B_{10}N_2O_{17}Zn_4$	$C_{59.10}H_{67.90}B_{10}N_{5.70}O_{15.70}Co_2$
Formula weight	1628.42	1319.95		1540.71	1335.25
Crystal system	Triclinic	Monoclinic	Monoclinic	Monoclinic	Monoclinic
Space group	P-1	C2/c	C2/c	Pn	P2 <sub>1</sub> /c
CCDC ref					
Unit cell dimensions					
a (Å)	11.6364(5)	34.542(7)	37.907	18.5945(10)	16.2470(9)
b (Å)	15.5850(6)	9.5651(19)	9.066	8.0800(5)	21.0403(9)
c (Å)	18.8230(8)	18.011(4)	17.420	30.2904(19)	22.8395(11)
$\alpha$ (deg)	86.4230(18)				
$\beta$ (deg)	82.8690(19)	97.71(3)	95.135	90.819(2)	105.811(2)
$\gamma$ (deg)	89.7220(19)				
V (Å <sup>3</sup> )	3380.6(2)	5897(2)	5962.6	4550.5(5)	7512.1(6)
Z	2	4		2	4
F (000)	1704	2716		1564	2768
$\theta$ (range)	2.370-66.598	2.46-28.05		1.277-25.023	2.334-25.060
Max. / min. transmission	0.7528 / 0.6338	0.7467 / 0.4052		0.7452 / 0.2826	0.7452 / 0.2826
Ind refln (R <sub>int</sub> )	11752 (0.0509)	5155 (0.0594)		15879 (0.1216)	
Final R indices	R1 = 0.0736	R1 = 0.0781		R1 = 0.0759	R1 = 0.0678
[I > 2 $\sigma$ (I)]	wR2 = 0.1979	wR2 = 0.2264		wR2 = 0.1858	wR2 = 0.1790

**Structural Study of MOF-3 and MOF-3B.** MOF-3 crystallizes in the monoclinic *Pn* space group with four crystallographically independent Zn(II) metal centers forming tetranuclear entities. Zn(1) and Zn(3) are hexacoordinated with a {O<sub>6</sub>} and {NO<sub>5</sub>} environments, respectively. Zn(1) is coordinated to four oxygen atoms belonging to three different BTB<sup>3-</sup> ligands and to two oxygen atoms from OH groups. Zn(3) is coordinated to one *m*CB(4py) ligand, to three oxygen atoms from BTB<sup>3-</sup> ligands, to

the OH group and to a water molecule (Figure XXa). Zn(1) and Zn(4) are {NO<sub>3</sub>}- and {O<sub>4</sub>}-tetracoordinated. These metal centers are coordinated to two oxygen atoms from BTB<sup>3-</sup> ligands, to one OH group and to *m*CB(4py) ligand (for Zn(1)) or to one water molecule (for Zn(4)). Each {Zn<sub>4</sub>} cluster coordinate six BTB<sup>3-</sup> ligands and two *m*CB(4py) ligands. There are two distinct BTB<sup>3-</sup> ligands that exhibits three different coordination modes: monodentate ( $\kappa O$ ), bridge bidentate ( $\mu-\kappa O:\kappa O'$ ) and bridge bidentate chelate ( $\mu-\kappa^2 O,O':\kappa O'$ ). The two distinct BTB<sup>3-</sup> ligands share two {Zn<sub>4</sub>} clusters, connecting a total of four {Zn<sub>4</sub>} units. (Figure

XXb). The association between  $\{Zn_4\}$  entities and  $BTB^{-3}$  ligands creates a 3D honeycomb like network, where  $mCB(4py)$  bridges two  $\{Zn_4\}$  units in an almost linear disposition with a N-N dis-



**Figure XX.** a) Trinuclear cluster and coordination environment of the Co metal centres, b) Coordination modes of  $BDC^{2-}$ , c) Co-BDC layers (coordinated dmf molecules are omitted for clarity) and the 3D supramolecular association achieved through the  $mCB(3py)$  represented in pink, d) disposition of  $mCB(3py)$  within the structure.

tance of 12.20 Å, but without taking place in the dimensionality. The hydroxyl groups of the carborane are pointed to the interior of the honeycomb pores maybe establishing H-bonds with the squeezed solvent molecules (Figure XXc).

**Structural Study of MOF-1 and MOF-4.** These complexes will be described together since they are built from the same organic ligands, molar ratio and solvent mixture, but with different reaction time and metal centers: 72h and Zn(II) for **MOF-1**, and 48 h and Co(II) for **MOF-4**. **MOF-1** is a 3D-framework, whereas **MOF-4** is a 2D-network, both based on M(II) atoms, tetratopic carboxylic and  $mCB(4py)$  linkers. Coordinated and crystallization solvent molecules are also present. In **MOF-1**, zinc atoms are  $\{NO_4\}$ -pentacoordinated and the values of the Addison parameter  $\tau$  suggest that the metal center adopt a square pyramidal geometry (0.054 for Zn1 and 0.059 for Zn2), with the oxygen atoms of four  $TCPB^{-4}$  linkers in the basal position and the nitrogen atom of the  $mCB(4py)$  in the apex with a Zn-N distance of 2.030(4) Å (Figure XXa). **MOF-4** crystallizes in the monoclinic  $P2_1/c$  space group with two crystallographically independent cobalt atoms. Both metal centers are  $\{NO_5\}$ -hexacoordinated, but with different coordination spheres. Co(1) is coordinated to one nitrogen atom from one  $mCB(4py)$  ligand, to one terminal water molecule, to a dmf molecule, to two oxygen atoms belonging to two  $TCPB^{-4}$  ligands and to one oxygen atom from a bridge water molecule. Co(2) is coordinated to four neighbouring  $TCPB^{-4}$  ligands, to one nitrogen atom from a  $mCB(4py)$  ligand and to the bridge water molecule.

In both compounds, the carboxylate ligand is fully deprotonated, but adopts different coordination modes. In **MOF-1**,  $TCPB^{-4}$  coordinates four Zn-paddle wheels in a bridge bidentate mode ( $\mu-\kappa O:\kappa O'$ ) and in **MOF-4** exhibits also the monodentate ( $\kappa O$ ) modes connecting six Co atoms. Although the coordination modes of the ligands are different in each CP, their orientation creates layers in the  $ab$  plane in both **MOF-1** and **MOF-4**. The main difference between the two structures is the conformation adopted by  $mCB(4py)$  ligand. The selected structural parameters are listed in Table XX. In **MOF-1**, the ligand acts as pillar linkers connect-

ing  $\{Zn_2(TCPB)\}$  layers with a Zn-Zn distance of  $\sim 16$  Å, affording to a final 3D-framework that shows 2-fold interpenetration. Contrariwise, in **MOF-4**, the U-shape orientation of the pyridine arms to the same side creates a convergent coordination, where  $mCB(4py)$  bridges two Co(II) atoms of the same layer with a Co-Co distance of  $\sim 11$  Å, preventing a three-dimensional arrangement through coordination bonds. In this case, the framework is 3D H-bonded through the O-H...O interaction established between the coordinated water molecule and the oxygen atom of a carboxylic group (Table XX).

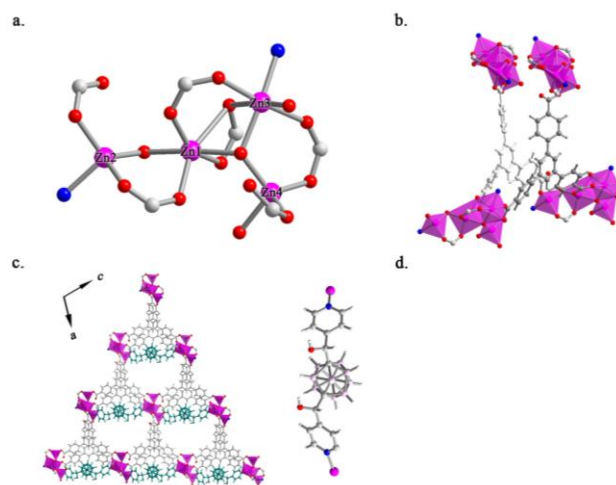


**Figure XX.** a) Tetranuclear cluster and coordination environment of the Zn metal centres, b) Two  $BTB^{-3}$  ligands connect four  $\{Zn_4\}$  units, c) left: 3D-honeycomb net ( $mCB(4py)$  is represented in green), right: disposition of  $mCB(4py)$  ligand in **MOF3**, d)

**Water stability.** One of the problems in the MOF field is their water stability. Metal-ligand bonds can be hydrolyzed or ligands can be displaced during the MOF reaction with water, leading to the collapse of the structure or prevent or decrease their adsorption capacity. One approach to solve this problem is focused on the modification of the linker to have a hydrophobic character.

With this in mind, water stability test has been studied in the reported CB-MOFs, by immersion the materials in liquid  $H_2O$  for 24 hours. By PXRD, we have found that **MOF2** collapses. On the other hand, **MOF3** remains stable after 24 hours of liquid  $H_2O$ -exposure. This stability can be explained due to the hydrophobic character of the pores

**Sorption properties.**

**Conclusions**

## ASSOCIATED CONTENT

### Supporting Information

This material is available free of charge via the Internet at <http://pubs.acs.org>.

### AUTHOR INFORMATION

#### Corresponding Author

E-mail: [jginerplanas@icmab.es](mailto:jginerplanas@icmab.es).

#### Funding Sources

This work was supported by the MINECO-Spain under the project PN MAT2012-30994 and EU FP7 ERC-Co 615954.

#### Notes


The authors declare no competing financial interests.

### ACKNOWLEDGMENT

I.I. and K.C.S. are grateful to MINECO, for a Ramón y Cajal grant, and to the EU, for a Marie Curie Fellowship (300390 NanoBioMOFs FP7-PEOPLE-2011-IEF), respectively. ICN2 acknowledges support of the Spanish MINECO through the Severo Ochoa Centers of Excellence Program under Grant SEV-2013-0295.

### REFERENCES

Table 1. Structural parameters of the carboranyl moiety within the MOFs

Compound	MOF-1	MOF-2	MOF-3	MOF-4
Carboxylate ligand	TCPB	BDC	BTB	TCPB
M(II)	Zn	Co	Zn	Co
mCB ligand	4py	3py	4py	4py
				
N-N dist. (Å)	12.04	12.15	12.20	9.42
CCCB torsion angles (deg)	82.0, 137.8	151.4, -139.6	145.1, -114.3	56.1, -89.9
Angle between the py rings (deg)	62.1	41.3	77.3	79.8
Coordinated to	Dinuclear paddle wheel	Trinuclear unit	Tetranuclear unit	Dinuclear unit
Involved in dimensionality	YES	YES	NO	NO

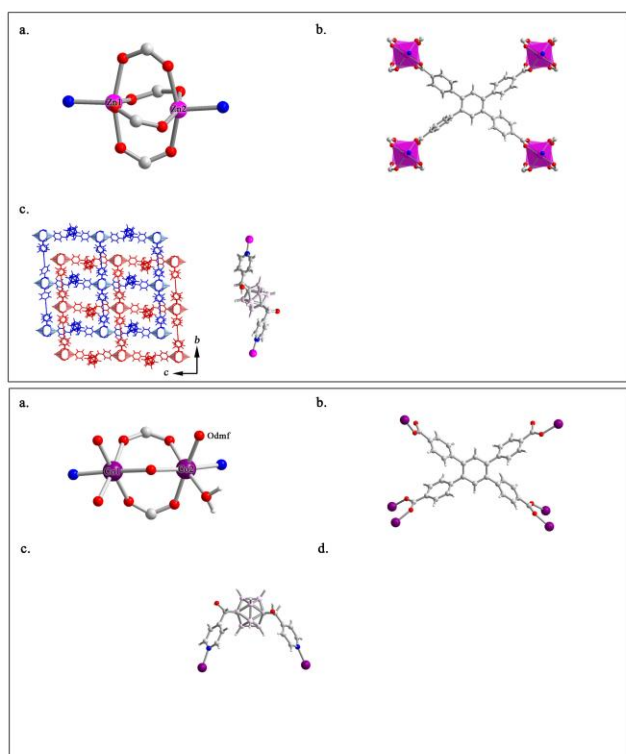


Figure XX.



# Inclusion compounds of a palladacyclic carboranyldiol: a supramolecular soup!

Min Ying Tsang,<sup>†</sup> Clara Viñas,<sup>†</sup> Francesc Teixidor,<sup>†</sup> José Giner Planas,<sup>\*,†</sup> Duane Choquesillo-Lazarte.<sup>§</sup>

<sup>†</sup>Institut de Ciència de Materials de Barcelona (ICMAB-CSIC), Campus UAB, 08193 Bellaterra, Spain. <sup>§</sup> Laboratorio de Estudios Cristalográficos, IACT-CSIC, Armilla, Granada, Spain.

E-mail: jginerplanas@icmab.es

**Abstract:** The title compound produced eight different types of solvent lattice inclusion crystals having a OH...O and xxx interactions with the solvents. The hydrogen bonded solute-solvent units are organized in four different packing modes. **To be completed.**

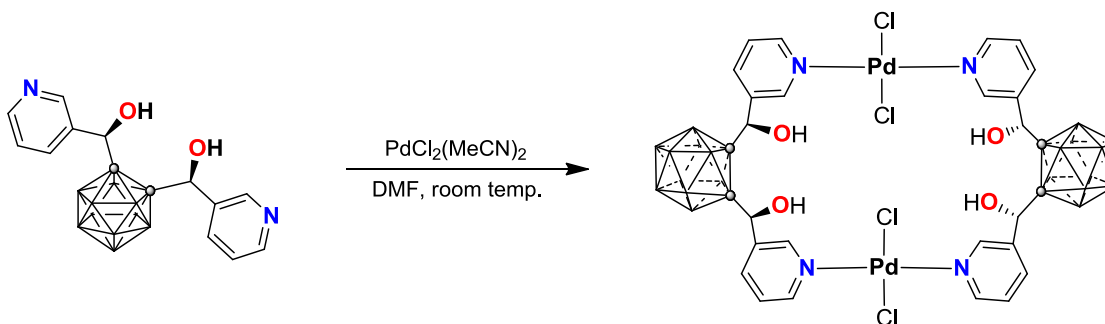
## Introduction

**To be completed.**

In the present work we report eight different inclusion compounds for a sole host (caboranylalcoholbases palladacycle; Chart 1) with exceptionally high host/guest stoichiometric ratios of 1:n (n = 6, 7 and 8). Polymorphs and pseudopolymorphs are observed for two host-guest compounds and combinations of hosts forms two more host-guest compounds.

## Results and discussion

Reaction of equimolar amounts of  $[\text{PdCl}_2(\text{CH}_3\text{CN})_2]$  with ligand **1** gave the corresponding neutral dipalladium(II) complex **2** as shown in xxx.



Since the palladacyclic dimer possesses four hydroxyl groups that are not involved in the complex formation, it was expected that compound **2** shows inclusion behavior. Compound **2** is insoluble in water, acetone, acetonitrile, 1,4-dioxane, diethyl ether, dichloromethane or n-hexane. It is however

slightly soluble in very polar organic solvents and does form inclusion compounds from DMF, DMSO, THF and EtOAc. The different inclusion compounds were obtained by changing the solvent system used for crystallization. In a typical crystallization experiment, the host **2** (ca. xxx mg) was dissolved in 5 mL of solvent (guest) and the clear solution was allowed to evaporate slowly over a period of 2-4 days. This procedure afforded crystals for eight inclusion compounds: **2**·DMF-I, **2**·DMF-II, **2**·DMF·H<sub>2</sub>O, **2**·DMSO-I, **2**·DMSO-II, **2**·DMF/DMSO, **2**·EtOAc and **2**·THF. The structures for all inclusion compounds have been unequivocally established by X-ray crystallography. Crystallization solvent, host/guest stoichiometry, space group, calculated density and guest accessible volume are given in Table 1. Crystal and data collection details can be found in Table 2 and experimental section.

**Table 1.** Details for crystallization solvent, Host:Guest Stoichiometry, Space Group, Calculated Density ( $D$ ; mg/m<sup>3</sup>), Guest accessible volume ( $V$ ; % unit cell)<sup>a</sup>.

Inclusion Compound	Solvent of crystallization	Host/guest	Space Group	$D$	$V$
<b>2</b> ·DMF-I	DMF	1:6	$P-1$	1.454	36
<b>2</b> ·DMF-II	DMF	1:6	$P2_1/n$	1.390	42
<b>2</b> ·DMF·H <sub>2</sub> O	DMF	1:6	$P2_1/c$	1.433	42
<b>2</b> ·DMSO-I	DMSO	1:8	$P-1$	1.490	47
<b>2</b> ·DMSO-II	DMSO	1:7 <sup>b</sup>	$P2_1/n$	1.485	41
<b>2</b> ·DMF/DMSO	DMF + DMSO	1:2:4 <sup>b</sup>	$P-1$	1.470	36
<b>2</b> ·EtOAc	EtOAc	1:7 <sup>b</sup>	$P-1$	1.360	53
<b>2</b> ·THF	THF	1:6	$P2_1/c$	1.441	39

<sup>a</sup> Calculated in Mercury (Probe radius 1.2; Grid spacing 0.7 Å). <sup>b</sup> Olex2 was used to remove the electronic contribution of disordered solvent molecules per host: 5 DMSO molecules in **2**·DMSO-II, 2 DMSO molecules in **2**·DMF/DMSO and 3 EtOAc molecules in **2**·EtOAc.

**X-ray Crystal Structures Analysis.** A comparison of the crystal structures of the inclusion compounds of **2** revealed a remarkably constant conformation of the host molecule **2** in all the structures (see ESI for molecular overlap, Fig. SX)). Figure 1 shows a molecule of the host from the structure **2**·DMF-I where it can be seen the disposition of the carborane clusters and the hydroxyl moieties. Describe the carboranes blab la bla. The hydroxyl groups???

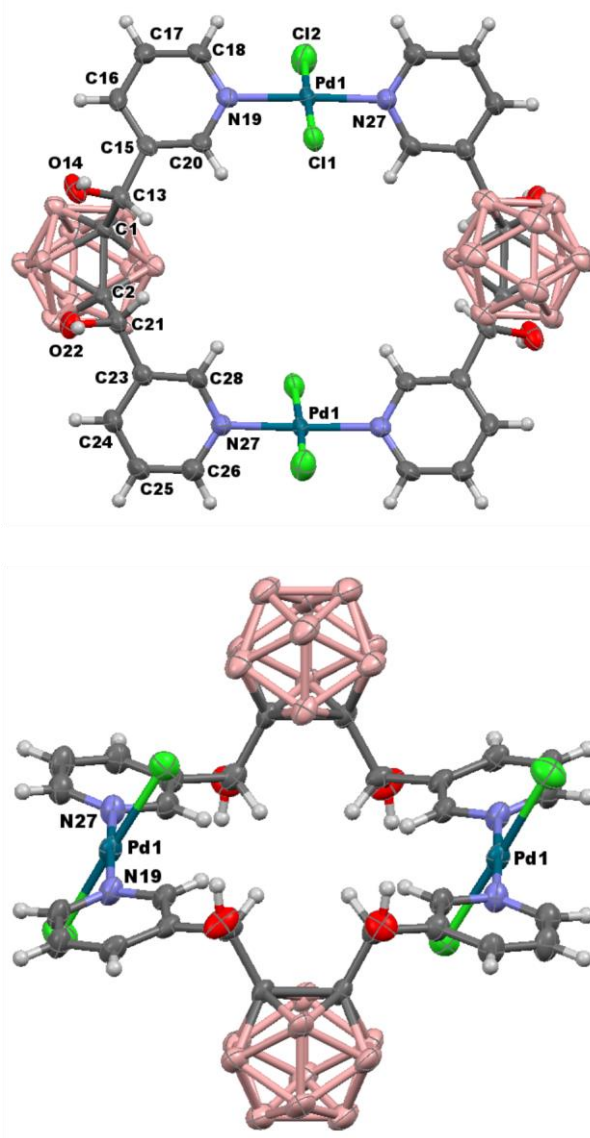
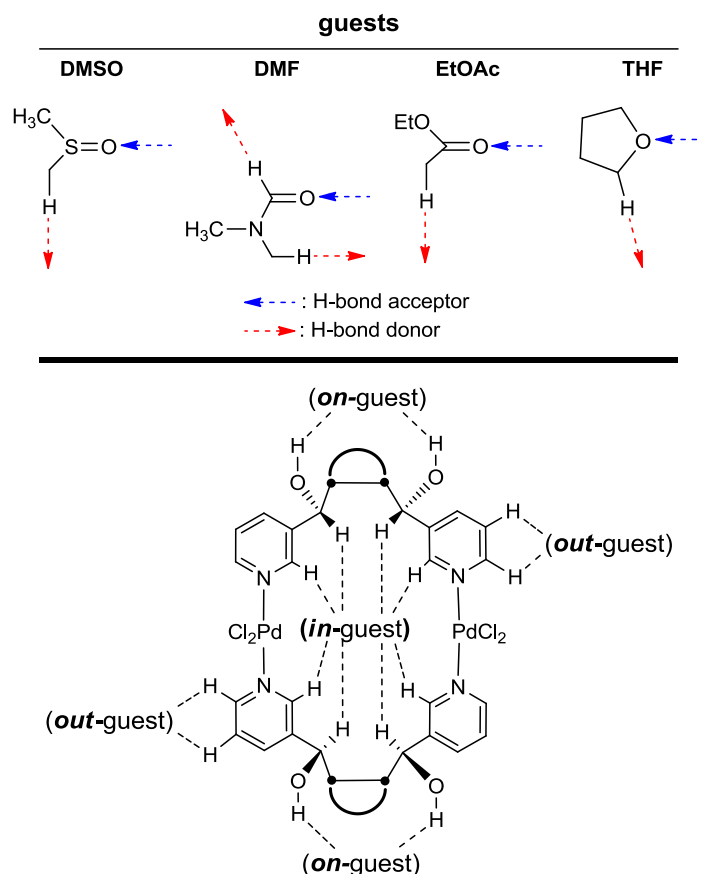


**Figure 1.** Labelled ORTEP diagrams for two different views of **2**·DMF-I. The thermal ellipsoids are shown at the 80% probability level and the H atoms as fixed-size spheres of 0.18 Å. The DMF molecules and H atoms attached to Boron (pink) are omitted for clarity. Selected bond lengths (Å) and angles (°); xxxxx

The solid state structures for the eight inclusion compounds presented in this work constitute examples of lattice inclusion compounds with small molecular guests. Due to the presence of four

alcohol moieties per host molecule, and the significant, although variable, proton donor and/or acceptor ability of the guests (Scheme 1), O–H···O and C–H···O hydrogen bonding is expected to play a dominant role in the molecular recognition and packing. One remarkable point is the host/guest stoichiometric ratios of 1:6 and 1:7, which are exceptionally high respect to the guest component. The latter indicates a high efficiency of guess accommodation. In order to shade some light into the inclusion properties of this new host we have analyzed, blab la bla and divided in three isostructural groups that are described bellow.



**Group 1.** The inclusion compounds **2**·DMF-I, **2**·DMSO-I, **2**·DMF/DMSO and **2**·EtOAc are isostructural, all crystallizing in the space group *P*-1 with *Z* = 1 and **similar cell dimensions** (Figure 2 and Table 1-2). The guests in the **2**·DMF-I, **2**·DMF/DMSO and **2**·EtOAc are found in two locations, one on the hydroxyl groups (*on-guest* in Scheme 1) and inside the palladacycle (*in-guest*). In case **2**·DMSO-I, *out-guest* (Scheme 1) solvent molecules are also found in addition to *on*- and *in-guest* molecules. As expected, guest molecules are acting as hydrogen bond acceptors, being the *on-guest* molecules involved in (host)O–H···O(guest) moderate hydrogen bonds and the *in*- and *out-guest* ones are interacting with the host by weaker hydrogen bonds of the type (host)C–H···O/S(guest). The details of hydrogen bonding for all structures are shown in Table 3. O–H···O

hydrogen bonds with O...O distances and OHO angles in the range xxxx-xxx and xxx are found in these four structures. Significant guest-guest hydrogen bonding is also observed in the structures via (host)C-H...O(host) interactions as well as guest-host C-H...Cl and dihydrogen bond interactions.

**Figure 2.** xxxxx

The inclusion compound **2**·DMF/DMSO deserves some comments as it contains two guest molecules of different nature. As shown in Table 1, this inclusion compound contains two DMF molecules and four DMSO ones (two were removed with Olex2) per host molecule. In this particular structure, DMF and DMSO are acting as *on-guest* and *in-guest*, respectively. This means that the more polar and better hydrogen bond acceptor DMSO guest is occupying the site dominated by weak hydrogen bonding, whereas a somewhat worse hydrogen bond acceptor such as DMF is occupying the moderate hydrogen bonding sites. Explain???

The packing of the structure **2**·DMF-I, which is representative of all four structures in this group, is shown in Figure 3 (See ESI for packing diagrams for all structures). Xxxxx. The host molecules are packed in a segregated columnar mode, leading to interstitial channels of approximate cross-section xxx

**Group 2.** Inclusion compounds **2**·DMF-II and **2**·DMSO-II are also isostructural, all crystallizing in the space group  $P2_1/n$  with  $Z = 2$  and **similar cell dimensions**. The guests in these compounds are also found in two locations, *on-guest* and *in-guest* (Scheme 1). The guests positions do not differ from those in the related **2**·DMF-I and **2**·DMSO-I. Interestingly, **2**·DMF-I and **2**·DMF-II show the same host/guest ratio and are true polymorphs.

The packing of the structure **2**·DMF-II, which is representative of both structures in this group, is shown in Figure xx.

**Group 3.** Inclusion compounds **2**·THF crystallized in the space group  $P2_1/c$  with  $Z = 2$ . Explain this in detail (out-guest!!!!) and related to Desiraju ChemComm.

**Table 3.** Geometrical parameters of D–H···A (A = O, H) contacts (Å, °), involved in the supramolecular construction in **1-2**.

Compound	D–H···A <sup>[a]</sup>	<i>d</i> (D···A)	<i>d</i> (H···A)	<(DHA)	<(HHB)
<b>2·DMF-I</b>	O(22)–H···O(41) <sup>i</sup>	2.742(3)	1.90	176.6	-
	O(14)–H···O(31) <sup>i</sup>	2.777(3)	2.04	146.8	-
	C(13)–H···O(31) <sup>ii</sup>				-
	C(13)–H···O(51) <sup>iii</sup>				-
	C(20)–H···O(51) <sup>i</sup>				-
	C(21)–H···O(51) <sup>ii</sup>				-
	C(28)–H···O(51) <sup>ii</sup>				-
	C(32)–H···O(41) <sup>ii</sup>				-
	C(52)–H···O(31) <sup>ii</sup>				-
	C(54)–H(B)···H–B(8) <sup>ii</sup>				-
<b>2·DMF-II</b>	O(22)–H···O(31) <sup>i</sup>	2.651(2)	1.82	172.0	-
	O(14)–H···O(41) <sup>i</sup>	2.714(2)	1.90	163.6	-
	C(13)–H···O(51) <sup>ii</sup>				-
	C(20)–H···O(51) <sup>i</sup>				-
	C(28)–H···O(51) <sup>ii</sup>				-
	C(32)–H···O(14) <sup>ii</sup>				-
	C(42)–H···O(51) <sup>ii</sup>				-
	C(44)–H(C)···Cl(2) <sup>ii</sup>				-
B(3)–H(B)···O(51) <sup>ii</sup>				-	
<b>2·DMF·H<sub>2</sub>O</b>	O(14)–H···O(31) <sup>i</sup>	2.755(3)	1.92	170.8	-
	O(22)–H···O(1) <sup>i</sup>	2.670(4)	1.86	161.7	-
	O(1)–H(A)···O(31) <sup>i</sup>	2.802(4)	1.94	169.2	-
	O(1)–H(B)···O(41) <sup>i</sup>	2.696(4)	1.86	161.5	-
	C(20)–H···O(51) <sup>iii</sup>				-
	C(21)–H···O(51) <sup>ii</sup>				-
	C(28)–H···O(51) <sup>ii</sup>				-
	C(34)–H(C)···O(1) <sup>ii</sup>				-
	B(3)–H···O(51) <sup>ii</sup>				-
C(42)–H···Cl(1) <sup>ii</sup>				-	
<b>2·DMSO-I</b>	O(14)–H···O(32) <sup>i</sup>	2.628(3)	1.81	164.8	-
	O(22)–H···O(2) <sup>i</sup>	2.760(3)	1.93	169.9	-
	C(20)–H···O(2) <sup>ii</sup>				-
	C(21)–H···O(2) <sup>iii</sup>				-
	C(28)–H···O(2) <sup>i</sup>				-
	C(00)–H(B)···O(14) <sup>ii</sup>				-
	C(00)–H(D)···O(22) <sup>ii</sup>				-
	C(4)–H(A)···O(42) <sup>ii</sup>				-
	C(4)–H(C)···Cl(2) <sup>ii</sup>				-
	C(3)–H(C)···Cl(1) <sup>ii</sup>				-
C(3)–H(C)···H–B(3) <sup>ii</sup>				-	
<b>2·DMSO-II</b>	C(13)–H···O(2) <sup>ii</sup>				-
	C(20)–H···O(2) <sup>iii</sup>				-
	C(21)–H···O(2) <sup>ii</sup>				-

	C(28)–H···O(2) <sup>ii</sup>				-
	C(3)–H(C)···H–B(3) <sup>ii</sup>				
2·DMF/DMSO	O(14)–H···O(41) <sup>i</sup>	2.787(5)	1.97	162.4	-
	O(22)–H···O(41) <sup>i</sup>	2.688(5)	1.93	150.0	-
	C(13)–H···O(31) <sup>ii</sup>				-
	C(20)–H···O(31) <sup>i</sup>				-
	C(21)–H···O(31) <sup>ii</sup>				-
	C(21)–H···O(41) <sup>ii</sup>				-
	C(28)–H···O(31) <sup>ii</sup>				-
	C(33)–H(A)···H–B(6) <sup>ii</sup>				-
2·EtOAc	O(22)–H···O(41) <sup>i</sup>	2.747(2)	1.91	172.1	-
	C(13)–H···O(31) <sup>iii</sup>				-
	C(20)–H···O(31) <sup>i</sup>				-
	C(21)–H···O(31) <sup>ii</sup>				-
	C(28)–H···O(31) <sup>ii</sup>				-
	C(43)–H(A)···O(22) <sup>ii</sup>				-
2·THF	O(22)–H···O(29) <sup>i</sup>	2.737(5)	1.90	171.6	-
	C(20)–H···O(39) <sup>i</sup>				-
	C(21)–H···O(39) <sup>ii</sup>				-
	C(25)–H···O(34) <sup>ii</sup>				-
	C(26)–H···O(34) <sup>ii</sup>				-
	C(41)–H(B)···Cl <sup>ii</sup>				-
	C(43)–H(A)···H–B(3) <sup>ii</sup>				-

[a] O–H bond lengths are not normalised to neutron distances. Symmetry codes (i)  $-x+1, -y+1, -z+1$  (ii)  $x, -1+y, z$  (iii)  $-x, -y, -z$  (iv)  $-0.5+x, 0.5-y, 0.5+z$  (v)  $0.5-x, -y, -0.5+z$  (vi)  $x, -0.5-y, -0.5+z$  (vii)  $2-x, 1-y, -z$  (viii)  $0.5+x, y, 0.5-z$  (ix)  $0.5-x, 0.5+y, z$  (x)  $2-x, -0.5+y, 0.5-z$  (xi)  $2-x, -y, 1-z$  (xii)  $1-x, -0.5+y, 0.5-z$  (xiii)  $-0.5+x, -0.5+y, z$  (xiv)  $0.5-x, -0.5+y, 0.5-z$  (xv)  $2.5-x, 0.5+y, 0.5-z$  (xvi)  $2.5-x, -0.5+y, 0.5-z$  (xvii)  $x, y, 1+z$  (xviii)  $-x, 2-y, 2-z$  (xix)  $0.5-x, -0.5+y, 1.5-z$  (xx)  $1-x, 0.5+y, 1-z$  (xxi)  $-x, -0.5+y, 1-z$  (xxii)  $-1+x, y, z$  (xxiii)  $1+x, y, z$  (xxiv)  $1+x, y, 1+z$  (xxv)

**Discussion.** Although crystallizations were left over a 2-4 days period, crystals for the inclusion compounds of **2** often appeared after 2-4 hours at room temperature. This is remarkable, in particular for the higher boiling point solvents of the series. This remarkable “rapid” crystallization is a first indication that host **2** crystallizes as a solvate. Then, the high host/guest stoichiometric ratios found in the structures (Figures x-x), indicates a high efficiency of guest accommodation. Overall, the host **2** shows three types of structural organizations, involving always solvents as hosts. An schematic representation of crystal packing patterns is shown in Figure xxx. Describe it.

Figure packing patterns

In spite of our efforts we were not able to obtain an unsolvated form of **2** (the apohost). The awkward shape of host **2** does not facilitate the self-assembly xxx. In a hypothetical apohost, host-host interactions would be likely OH/Cl. Such interactions are only found in the THF inclusion

compound **2**·THF (Figures xxx). An examination of supramolecular network for this inclusion compound already reveals that a dense packing for an apohost would be difficult.

### **Thermal stability and desolvation behavior.**

The thermal data clearly shows an enormous effect of the guest in the inclusion compound. Heating of the inclusion compounds showed chemical decomposition of the host on guest release. Melting point measurements and TGA analyses (ESI) for the inclusion compounds reveals that weight loss starts in the range 100-150 °C

Only both DMF polymorphs **2**·DMF-I and **2**·DMF-II were stable enough in air and after grinding as confirmed by PXRD. Fast lost of crystallinity was observed in all other cases.

Polymorphs **2**·DMF-I and **2**·DMF-II were concomitant and variable temperature XRD confirms that those are not interconverted. Explain Duane.

### **Experimental Section**

**General Remarks:** Reactions were carried out under a nitrogen atmosphere in round-bottomed flasks equipped with a magnetic stirring bar, capped with a septum. THF and diethyl ether were distilled from Na/benzophenone and CH<sub>2</sub>Cl<sub>2</sub> over CaH<sub>2</sub>. All the other chemicals were commercially available and used as received. TLC analyses were performed on Merck silica gel 60 F<sub>254</sub> TLC plates (0.5 mm thickness). IR ATR spectra were recorded on a Perkin–Elmer Spectrum One spectrometer. <sup>1</sup>H, <sup>13</sup>C and <sup>11</sup>B spectra were recorded respectively at 300, 75 and 96 MHz with a Bruker Advance-300 spectrometer in deuterated acetone, unless denoted, and referenced to the residual solvent peak for <sup>1</sup>H and <sup>13</sup>C NMR or to BF<sub>3</sub>·OEt<sub>2</sub> as an external standard for <sup>11</sup>B NMR. Chemical shifts are reported in ppm and coupling constants in Hertz. Multiplets nomenclature is as follows: s, singlet; d, doublet; t, triplet; br, broad; m, multiplet. Elemental analyses were obtained by a CarboErba EA1108 microanalyzer (Universidad Autónoma de Barcelona). The mass spectra were recorded in the negative ion mode using a Bruker Biflex MALDI-TOF-MS [N<sub>2</sub> laser; λ<sub>exc</sub> 337 nm (0.5 ns pulses); voltage ion source 20.00 kV (Uis1) and 17.50 kV (Uis2)] with 3,5-dimethoxy-4-hydroxycinnamic acid as matrix. ESI-MS spectra were recorded in a Thermo Quest Finigan Navigator LC/MS apparatus.

ASSOCIATED CONTENT



Supporting information. Spectroscopic and crystallographic data. This material is available free of charge via the internet at <http://pubs.acs.org>.

#### ACKNOWLEDGMENTS

We thank CICYT (Project CTQ2010-16237), Generalitat de Catalunya (2009/SGR/00279) and CSIC (JAE-doc contract to FDS) for financial support. FDS thanks CONICET for support. MEL and MBH thank the UK Engineering and Physical Science Research Council for support of the X-ray facilities at Southampton. MBH thanks the Leverhulme Trust for the award of an Emeritus Fellowship. M. Y. Tsang is enrolled in the UAB PhD program. The project “Factoría de Cristalización, CONSOLIDER INGENIO-2010” provided X-ray structural facilities for this work.

#### REFERENCES